Czech Technical University in Prague
Faculty of Electrical Engineering

Doctoral Thesis

August 2014

Michal Janošek

Czech Technical University in Prague
Faculty of Electrical Engineering
Department of Measurement

A precise gradiometer suitable for space applications

Doctoral Thesis

Michal Janošek

Prague, August 2014

Ph.D. Programme:	Electrical Engineering and Information Technology
Branch of study:	Measurement and Instrumentation

Supervisor:	Prof. Ing. Pavel Ripka, CSc.
Supervisor-Specialist:	Doc. Ing. Antonín Platil, Ph.D.

Acknowledgement

I would like to express my thanks to everybody who has contributed to this work with his help, advice or feedback; mainly to my supervisor prof. Pavel Ripka and the supervisor-specialist Antonín Platil. My thanks also go to my former student and colleague Jan Vyhnánek for his significant contribution to the AMR related work. Finally, I wish to appreciate the support and patience of my family.

The research presented here has been performed in collaboration with the following institutions:

Technische Universität Braunschweig, Braunschweig, Germany
Institute of Physics, Slovak Academy of Sciences, Slovakia
Institute of Geophysics, Academy of Sciences of the Czech Republic
Czech Metrology Institute, Laboratory of Fundamental Metrology, CZ
Newmont Mining Corp., CO, USA
Vector Magnetics LLC., NY, USA
Billingsley Aerospace & Defense Inc., MD, USA

The research has been funded, or partially funded, by following grants:

Technology Agency of the Czech Republic
TA01010298 “Fluxgate gradiometer for space application”
Czech Science Foundation
GAP102/12/2177 Nanostructured soft magnetic materials for sensors
GA102/08/0743 - Fluxgate effect in thin layers
Ministry of Education, Youth and Sports of the Czech Republic
MSM6840770012 "Transdisciplinary Research in the Area of Biomedical Engineering II"
7AMB12SK027 - Metallic ribbons for magnetic sensors
Czech Technical University in Prague
SGS10/205/OHK3/2T/13 “Compact sensors of magnetic field gradient – development and applications”

Abstract

This thesis has addressed the theoretical and design problems associated with the development and construction of a compact, low-noise magnetic gradiometer suitable for the space environment. The demands of industrial and space applications defined the required gradiometer parameters: gradiometric base below 40 mm and noise below 1 $nT \cdot m^{-1} \cdot Hz^{-0.5}$. A low gradiometric base is required due to constructional constraints or the need for a precise estimate of the magnetic gradient. It is also advantageous in detection of the fast-decaying response of small and weak magnetic field sources in the environmental noise which can have gradient character.

The sensor types for the non-cryogenic, low-noise compact gradiometer were selected as anisotropic magnetoresistors (AMR) and fluxgate, both suitable also for space environment. I have studied the crossfield effect for both fluxgate and AMR's, which I have verified by measurements. I have addressed the high crossfield response of race-track fluxgates with planar, etched cores for the first time. I have also participated in deriving a novel algorithm to suppress the crossfield response of AMR's.

At first, I have used off-the-shelf AMR and fluxgate sensors for compact gradiometers. I have developed an original dB_x/dy PCB fluxgate gradiometer for magnetic field mapping and a novel mine-detector with AC excitation based on a 4×4 array of dB_z/dz AMR gradiometers. I have also calibrated and astatized a state-of-the-art axial fluxgate gradiometer, where I have proposed an unconventional astatization method.

To meet the specifications, I have developed two miniaturized low-noise fluxgate sensors - a novel, 20×11×2 mm^3 race-track and a 20×20×8 mm^3 ring-core sensor. Field annealing of the 12-mm diameter ring-core enabled its magnetic noise to be decreased down to 7 $pT \cdot Hz^{-0.5}$@ 1 Hz - this is the lowest noise of sensor of this size and type found in literature. I have also tested the parameters of the developed sensors (noise, offset) and confirmed their suitability for space-grade applications. The size of the developed sensors allowed to reduce the gradiometric base below 40 mm and also to propose a 46×46×46 mm^3 full-tensor gradiometer.

Significant part of the research is designated to the development of a novel, original concept of gradient feedback, which has been used in two types of fluxgate gradiometer to overcome the stability problems of the state-of-the-art, compact instruments. The "single-core" gradiometer had a gradiometric base of 40-mm and the original "dual-core" gradiometer with 30-mm base has finally met the noise requirement of 1 $nT \cdot m^{-1} \cdot Hz^{-0.5}$ @ 1 Hz. Gradiometer astatization has been carried out with the novel method and real-world measurements are presented. Up to 90 dB CMRR has been achieved which also using the gradiometer allows in applications faced by high common-mode fields, as in UXO detection and biomedicine.

Abstrakt

Disertační práce se zabývá teoretickými a konstrukčními aspekty při vývoji kompaktního, nízkošumového gradiometru využitelného v kosmickém výzkumu. Požadavky z průmyslové sféry a kosmického výzkumu definovaly cílové parametry gradiometru: gradiometrická báze menší než 40 mm a šum gradiometru pod 1 $nT \cdot m^{-1} \cdot Hz^{-0.5}$ @ 1 Hz. Malá báze gradiometru je dána konstrukčními omezeními nebo potřebou precizního odhadu magnetického gradientu jako veličiny. Je také výhodou při detekci rychle slábnoucí odezvy od slabých zdrojů magnetického pole v zarušeném prostředí s možným gradientním šumem.

Pro nekryogenní, nízkošumový kompaktní gradiometr jsem vybral anizotropické magnetorezistory (AMR) a sondy fluxgate, oba typy vyhoví pro kosmické prostředí. Studoval jsem tzv. crossfield efekt u obou typů senzorů; u AMR jsem jeho průběh potvrdil měřeními. Zaměřil jsem se na velkou odezvu oválných fluxgate sond s planárním jádrem, kterou jsem poprvé vysvětlil. Také jsem se podílel na odvození nového algoritmu pro potlačení crossfield efektu u senzorů AMR.

V počáteční fázi jsem se zabýval vývojem kompaktních gradiometrů s dostupnými magnetickými senzory. Vyvinul jsem původní dB_x/dy fluxgate gradiometr pro magnetická mapování se senzory vyrobenými metodou tištěných spojů a minohledačku se střídavým buzením, nově založenou na poli dB_z/dz AMR gradiometrů. Dále jsem kalibroval a astatizoval precizní, axiální fluxgate gradiometr; kde jsem navrhl netradiční, zjednodušenou metodu astatizace.

Za účelem dosažení stanovených parametrů jsem vyvinul dva miniaturizované typy nízkošumových fluxgate sond: originální sondu s oválným jádrem „race-track“ ($20 \times 11 \times 2$ mm^3) a sondu s kruhovým jádrem o průměru 12 mm ($20 \times 20 \times 8$ mm^3). Díky žíhání v magnetickém poli bylo dosaženo snížení magnetického šumu kruhové sondy pod 7 $pT \cdot Hz^{-0.5}$ @ 1 Hz, což je nejnižší šum publikovaný v literatuře pro tento typ a rozměr sondy. Z testování parametrů vyvinutých sond (šum, offset) jsem potvrdil jejich vhodnost pro kosmické aplikace. Rozměry vyvinutých senzorů dovolily snížení gradiometrické báze pod 40 mm a umožnily také navrhnout tenzorový gradiometr s rozměry $46 \times 46 \times 46$ mm^3.

Významnou část výzkumu jsem věnoval vývoji gradientní zpětné vazby – tento nový, originální koncept byl použit ve dvou typech fluxgate gradiometrů a umožnil překonat problémy se stabilitou současných kompaktních gradiometrů. S jejím využitím jsem vyvinul tzv. „jednojádrový“ fluxgate gradiometr s gradiometrickou bází 40 mm a nový, „dvoujádrový“ gradiometr s bází 30 mm, který splnil požadovanou specifikaci šumu 1 $nT \cdot m^{-1} \cdot Hz^{-0.5}$ @ 1 Hz. Gradiometry byly astatizovány vyvinutou metodou a jsou prezentovány výsledky z jejich nasazení mimo laboratoř. Potlačení souhlasných polí je až 90 dB což umožňuje využití gradiometrů i v aplikacích, kde jsou takováto pole přítomna, jako vyhledávání min a nevybuchlé munice a také v biomedicíně.

Contents

1. Introduction

This thesis is motivated by the need for a compact, stable, low-noise magnetic gradiometer with a gradiometric base less than 40 mm that is usable for geophysical exploration, NDT/UXO detection, biomedicine and space applications.

The magnetic gradient as a quantity is estimated only by difference measurements – the smallest possible sensor spacing (the gradiometric base) should be used to estimate the gradient tensor components precisely. The gradiometric base may also be limited by the restricted operational area of the gradiometer. An example is the vertical drilling application of Vector Magnetics Inc. Their need is to fit the gradiometer to the 40-mm borehole diameter. Another example of size restriction was the NASA/ESA application of an onboard service gradiometer for the LISA project [Jennrich 2009]. The tensor gradiometer should fit into a cube of $46\times46\times46$ mm^3 in this case – it was supposed to replace the cubic test-mass during magnetic cleanliness testing. In NDT, geophysical prospecting, archaeology and UXO detection, a small gradiometric base and thus small overall sensor size is a benefit if the gradiometers are to be towed or moved. A sensor array can be formed: the scanning time decreases as the scanning area increases [Stolz 2006].

A small gradiometric base will also improve the performance of the gradiometers for detecting magnetic particles in biomedicine in unshielded environments due to better attenuation of environmental noise which can have gradient character. However, the magnetic moment of a single Fe particle may be as low as 10^{-12} A·m^2, which leads to the use of SQUID gradiometers with low gradiometric bases in magnetopneumography [Bohánková 2003]. If the ferromagnetic dusts in lungs were magnetized with a strong DC field, their remanent magnetic moment increased up to 10^{-4} A·m^2 in the case of strongly exposed objects [Stroink 1982, Navrátil 1999]. This made possible to use a 10-cm gradiometric base fluxgate gradiometer in magnetopneumography [Tomek 2006]. The response of super-paramagnetic particles used as markers in biomedicine is several orders of magnitude lower, and generally requires SQUID gradiometers [Pankhurst 2003]. [Ludwig 2005] has shown that the relaxation Neel amplitude is as low as 1 nT for 1 μl of the DC-magnetized Fe nanoparticles, which was however successfully measured with a fluxgate gradiometer in an unshielded environment.

If the gradiometric base is decreased, both the sensor size and its noise have to be decreased. As an example, the LISA instrument should have gradient noise PSD less than 0.3 nT·m^{-1}·Hz$^{-0.5}$ at 1 Hz. The down-hole drilling application has a relaxed requirement of 1 nT·m^{-1}·Hz$^{-0.5}$ [Ripka 2012]. As the gradiometric base is limited at the same time in both cases, the overall size of each sensor is limited to 20 mm to fulfill the requirements. Assuming a 30-mm base, the 1-Hz sensor noise cannot be greater than 20 pT·Hz$^{-0.5}$ in the down-hole drilling application, and for LISA it should be smaller than 7 pT·Hz$^{-0.5}$. This is a tough requirement and requires further development of compact, low-noise magnetic sensors.

1.1 Theoretical background

1.1.1 Magnetic field gradient

As a result of the Maxwell equation $\nabla \times \boldsymbol{H} = 0$, supposing a current-source free application and a vacuum, we can define the magnetic flux density vector $\boldsymbol{B}$ in orthogonal coordinates [Ida 2004]:

$$\boldsymbol{B} = \left(B_x, B_y, B_z\right) = \mu_0 \boldsymbol{H} = \mu_0 \left(-\nabla \psi\right) = -\nabla F \qquad [\mathrm{T}] \qquad (1.1)$$

The magnetic flux density $\boldsymbol{B}$ is thus a negative gradient of the scalar potential F, and can therefore be considered as zero-order gradient tensor.

If we define the magnetic gradient as a spatial derivative of the $\boldsymbol{B}$ vector, we get the (first order) 3×3 gradient tensor matrix:

$$\nabla \boldsymbol{B} = \boldsymbol{G} = \begin{bmatrix} \frac{\partial B_x}{\partial x} & \frac{\partial B_y}{\partial x} & \frac{\partial B_z}{\partial x} \\ \frac{\partial B_x}{\partial y} & \frac{\partial B_y}{\partial y} & \frac{\partial B_z}{\partial y} \\ \frac{\partial B_x}{\partial z} & \frac{\partial B_y}{\partial z} & \frac{\partial B_z}{\partial z} \end{bmatrix} \qquad [\mathrm{T.m^{-1}}] \qquad (1.2)$$

Considering again $\nabla \times \boldsymbol{H} = 0$ in the absence of currents, we get the following properties of the tensor matrix elements

$$\frac{\partial B_x}{\partial y} - \frac{\partial B_y}{\partial x} = 0, \; \frac{\partial B_x}{\partial z} - \frac{\partial B_z}{\partial x} = 0, \; \frac{\partial B_y}{\partial z} - \frac{\partial B_z}{\partial y} = 0 \qquad (1.3, 1.4, 1.5)$$

As a result, the gradient matrix has off-diagonal symmetry ($\partial B_i/\partial j = \partial B_j/\partial i$).

Further, as a consequence of the Maxwell equation $\nabla \cdot \boldsymbol{B} = 0$, we can write

$$\frac{\partial B_x}{\partial x} + \frac{\partial B_y}{\partial y} + \frac{\partial B_z}{\partial z} = 0 \qquad (1.6)$$

Thus the gradient tensor contains only 5 independent components. For example, only the following components are required to describe the gradient tensor completely:

$$\left\{\frac{\partial B_x}{\partial x}, \frac{\partial B_y}{\partial y}, \frac{\partial B_x}{\partial y}, \frac{\partial B_x}{\partial z}, \frac{\partial B_y}{\partial z}\right\}. \tag{1.7}$$

By applying the ∇ operation also to the magnetic gradient (1.2), we get higher order gradients.

An important case to be considered is the magnetic field created by a dipole source. The scalar potential created by a dipolar field in vacuum can be written as:

$$F(\boldsymbol{r}) = \frac{\mu_0 \cdot \boldsymbol{m} \cdot \boldsymbol{r}}{4\pi \cdot r^3} \tag{1.8}$$

Where $\boldsymbol{r}$ is the position vector, its size $|\boldsymbol{r}| = \sqrt{x^2 + y^2 + z^2}$ is the radial distance from the dipole source and $\boldsymbol{m}$ is the magnetic moment of the dipole.

Then for example for $\boldsymbol{m} = (0, 0, m_z)$, and a position vector $\boldsymbol{r} = (0, 0, z)$ with a distance $|\boldsymbol{r}| = z$, we get using Eq. 1.1:

$$B_z = -\nabla\left(\frac{\mu_0 \cdot m_z \cdot z}{4\pi \cdot z^3}\right) = -\nabla\left(\frac{\mu_0 \cdot m_z}{4\pi \cdot z^2}\right) = \frac{2\mu_0 \cdot m_z}{4\pi \cdot z^3} \tag{1.9}$$

If we further apply the ∇ operation to Eq. 1.9, we get for the $\partial B_z/\partial z$ component of the gradient tensor:

$$\frac{\partial B_z}{\partial z} = -\nabla\left(\frac{\mu_0 \cdot m_z}{2\pi \cdot z^3}\right) = \frac{-3\mu_0 \cdot m_z}{2\pi \cdot z^4} \tag{1.10}$$

As a consequence, the dipolar field decreases with the 3rd power of the distance *z*, but the dipolar field gradient decreases with the 4th power.

1.1.2 Gradient estimation by magnetic field measurement

The components of the magnetic field vector used for calculating the magnetic gradient are measured with vectorial magnetic sensors, either standalone or in orthogonal triplets. In the real world, due to finite sensor size and noise, the magnetic gradient components are however only approximated by the difference of two spatially separated sensor readings - see Fig. 1.1. For example for two sensors in the x axis at a distance $d=x_1-x_2$ (the so-called gradiometric base), which are reading B_{x1} and B_{x2}, we can approximate the gradient component using the derivative definition:

$$\frac{\partial B_x}{\partial x} = \lim_{d \to 0} \frac{B_{x1} - B_{x2}}{(x_1 - x_2)} \cong \frac{B_{x1} - B_{x2}}{d} = \frac{\Delta B_x}{\Delta x} \tag{1.11}$$

The size of the gradiometric base clearly influences the estimate of the magnetic gradient, mainly if the magnetic field has higher order spatial derivates. An important case is the field of a magnetic dipole (Eq. 1.8).

For a single-axis gradiometer, [Merayo 2001] introduced a correction term which takes into account the gradiometric base d and the distance z from the dipolar source aligned in the z-direction:

$$\frac{\partial B_z}{\partial z} \cong \frac{B_{x1} - B_{x2}}{d} \left(1 + \frac{5}{6} \left(\frac{d}{z} \right)^2 + \frac{7}{16} \left(\frac{d}{z} \right)^4 + \ldots \right) \tag{1.12}$$

For example, an instrument with a gradiometric base of 50 cm will for a 50-cm distance from the dipolar field source exhibit an error greater than 220 %. For less than 10 % error, the required z/d fraction is >3.

The influence of finite sensor distances on the tensor gradiometer for a tensor gradiometer constructed from 7 and 10 sensors, respectively, was studied by [Huang 2010], who showed that in order to decrease the error, a common crossing point of all gradiometric bases should exist. Huang proved that 7 is the minimum number of vectorial magnetic sensors needed to measure all gradient tensor components, if arranged according to Fig. 1.2. The size of the cube is the gradiometric base d, and Huang showed that for the distance $z = 100$ m a gradiometric base $d = 2$ m would yield 8 % error in the magnetic gradient but up to 30 % error in dipole localization.

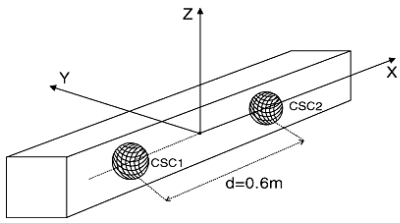

Fig. 1.1 – A gradiometer using two orthogonal sensor triplets, from [Merayo 2001]

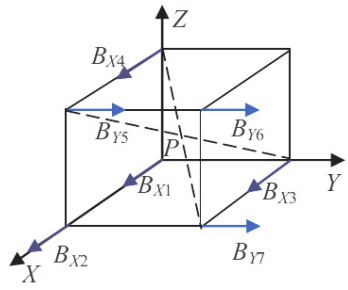

Fig. 1.2 – A 7-sensor tensor gradiometer, from [Huang 2010]

1.1.3 Gradiometer performance

As a result of Eq. 1.11, the sensitivity of a gradiometer is limited by the finite resolution of vectorial sensors and by the gradiometric base *d*. In addition, sensor-to-sensor matching and misalignments of their sensitive axes limit the performance of a gradiometer in large common-mode fields.

1.1.3.1 Gradiometric base selection

The gradiometric base is selected as a compromise between gradiometer performance and its application. Sensor noise and sensor size are reasons for increasing the gradiometric base in order to increase the detection limit, if the errors arising from Eq. 1.12 can be tolerated or corrected.

A. The effect of sensor size.

The size of a sensor may vary from fractions of a millimetre for magnetoresistive sensors, Hall sensors and other chip-scale sensors to several centimeters for bulk fluxgate sensors [Ripka 2010]. In this case the packaging size determines the smallest gradiometric base, which is then limited to $d = \frac{1}{2}(l_{i1} + l_{i2})$, where l_{i1} and l_{i2} are the sensor dimensions in the respective axis. Sensor size not only determines the minimum gradiometric base, but also causes integration of the spatial derivative across the sensor element volume, which in turn decreases the sensitivity [Rühmer 2012]. In the case of a tensor gradiometer, sensor size also restricts the configuration of other sensors in the gradiometer head (Fig. 1.2).

B. The influence of sensor noise.

Sensor noise poses a limitation due to the basic equation Eq. 1.11. In the case of uncorrelated white noise, the noise of the gradient component can be rewritten as

$$\frac{\Delta B_{Nx}}{\Delta x} = \frac{\sqrt{B_{NX1}{}^2 + B_{NX2}{}^2}}{d} \tag{1.13}$$

and if the noise is equal, it simplifies to

$$\frac{\Delta B_{NX}}{\Delta x} = \frac{\sqrt{2} B_{NX}}{d} \tag{1.14}$$

For example, a 10 pT uncorrelated white noise of each sensor in a distance d = 1 m results in 14 pT·m^{-1}·Hz$^{-0.5}$ white gradient noise. For equally performing sensors with d = 0.1 m, however, the noise is 10× higher. For correlated sensor noise, the situation is more complicated: if there were perfect noise correlation, the gradiometer noise would be zero, but this is only a theoretical situation.

1.1.3.2 Gradiometer errors

All gradiometers are affected by finite suppression of homogeneous fields, i.e. a finite common mode rejection ratio, due to differences in the sensor-to-sensor gain factor, A/D conversion errors and, above all, due to geometrical imperfections of sensor orientations. For an axial gradiometer, these errors were analyzed in [Merayo 2001].

Considering an axial gradiometer ($\partial B_i/\partial i$) with a parasitic response ΔB_P due to the presence of the aligned common-mode field B_{CM} (or a projection of an unaligned common-mode field), we can define the common-mode rejection ratio:

$$CMRR = 20 \cdot \log \frac{B_{CM}}{\Delta B_p} = 20 \cdot \log \frac{B_{CM}}{G_P \cdot d} \tag{1.15}$$

It is evident that when decreasing the gradiometric base d, higher CMRR of the gradiometer is necessary to keep the same parasitic response G_P (in gradient units). As a consequence, as the gradiometric base decreases, the requirements on sensor matching and alignment rise. In addition, the CMRR of the signal processing electronics and ADCs will introduce further errors.

The most usual common-mode field is the Earth's field, with a magnetic gradient less than 15 pT·m^{-1} [Campbell 2003] and intensity around 50,000 nT in the northern hemisphere. When moving the gradiometer in the Earth's field, e.g. in airborne or manual geomagnetic measurements, these errors may be large enough to mask the required instrument response.

The effect of finite gradiometer CMRR is shown in [Chwala 2012]. In the airborne, highly balanced SQUID towed gradiometer with a gradiometric base of 35 mm, the 80 dB CMRR, as defined by precision lithography, increased after compensation with the least-squares fit for each tensor component to more than 130 dB. This would yield 2 nT·m^{-1} error using Eq. 1.15 for 50 μT common-mode field variation.

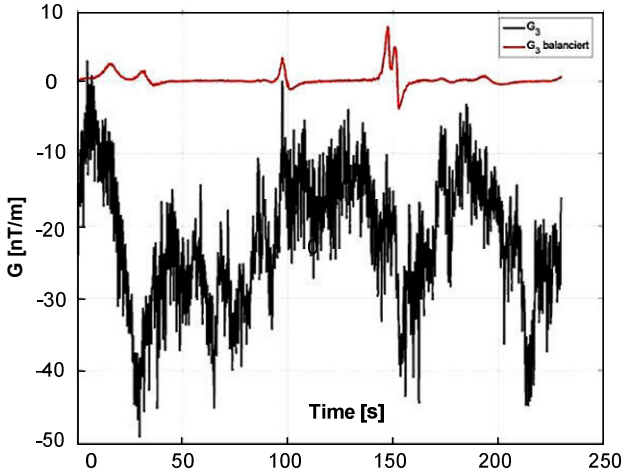

Fig. 1.3 – The effect of finite CMRR on a SQUID gradiometer, redrawn from [Chwala 2012]. Black – raw data, red – after balancing

1.1.3.3 Gradiometer astatization

Astatization of the gradiometer, i.e. minimizing the response to common-mode fields, is the key issue in real-world measurements with large common-mode fields. Balance is usually obtained mechanically. [Merayo 2001] used adjustable screws at the second sensor head for his fluxgate gradiometer.

Misalignments of the sensors can also be calibrated and compensated using redundant information about the disturbing homogeneous field. A "redundant" triaxial magnetometer is commonly used, as shown in [Chwala 2012], [Pei 2009] and in [Kumar 2005]. The calibration technique mostly relies on least-squares fit or scalar-calibration [Merayo 2005]. However, the calibration relies on the presence of a homogeneous magnetic field without any magnetic gradients.

For a mechanically fixed gradiometer detecting a mobile anomaly/dipole source, the problem is only the common-mode magnetic noise, which can be more than 3 orders of magnitude smaller than the Earth's magnetic field, even in a laboratory environment. Fig. 1.4 shows the homogeneous noise (black) and the difference noise ΔB_z (red, without further corrections) during day-time and night-time in a noisy laboratory environment measured by the author (1-sample differences are shown to suppress the offset change). The two spacing between the two fluxgate sensors was 10 cm.

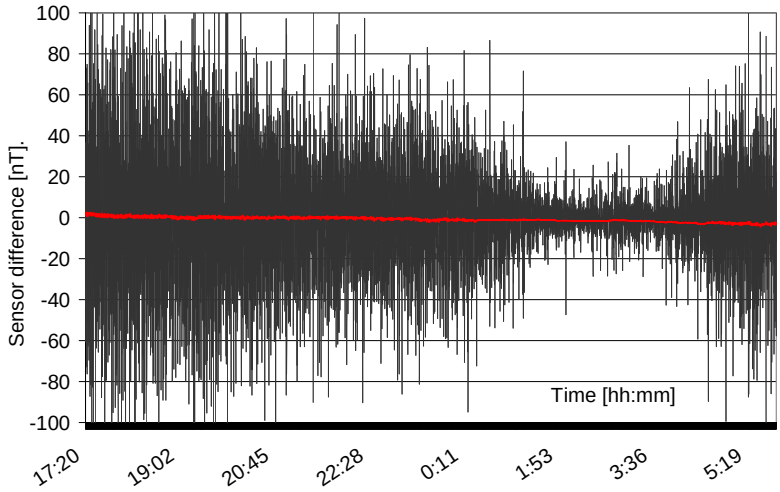

Fig. 1.4 – Magnetic noise in a laboratory surrounded by DC-traction traffic.

In this case, the CMRR was only 30 dB, but this enabled difference signals as low as 2 nT (20 nT·m^{-1} with a 10-cm gradiometric base) to be measured without any correction procedure in daytime.

1.2 Gradiometer applications

Most applications of gradiometers make use of the following properties of the gradient tensor:

1. For a spatially homogeneous magnetic field, all tensor components are zero (Eq. 1.2).
2. The tensor components measured at a single point describe the magnetic dipole strength and its location – Eq. 1.10
3. The attenuation of the dipolar field gradient scales with the 4th power of distance, as compared to the third power in the case of the dipolar field (Eq. 1.9 and 1.10)
4. The magnetic field generated by a long current-carrying conductor can be described by the respective tensor components – $\nabla \times \boldsymbol{H} = I$
5. The mechanical force acting on a ferromagnetic object is caused by the spatial gradient of the magnetic field.

The first and second of these properties are used to detect ferromagnetic (or even superparamagnetic) objects, or magnetic anomalies in general.

The third property provides a further advantage of gradiometry over magnetometry in higher attenuation of distant disturbing dipole field sources.

The fifth application of the magnetic gradient is used in susceptibility measurements using the Faraday method, where the gradient is kept constant [Wecker 2006]:

$$F = V\chi H\frac{\Delta H}{\Delta y} \tag{1.16}$$

where F is the force on the sample with volume V and susceptibility χ, and H is the applied magnetic field with gradient in the y-direction.

1.2.1 Full-tensor gradiometers

Full-tensor information is used mainly in geophysical prospecting and in security/military applications, because it offers the possibility to localize the magnetic disturbance [Beiki 2012], [Clark 2012] or to discriminate between information from the tensor components [Schneider 2013]. The gradiometer for the European Space Agency's LISA project was assumed to determine the disturbing force due to the magnetic gradients by measuring the gradient tensor in the spacecraft. In this case, existing magnetic gradients could affect precise distance measurements, due to the force applied to the test mass (Eq. 1.16) – the cube with composition of 75% Au and 25% Pt would have a susceptibility of -2×10^{-5} [Jennrich 2009].

In addition to the proposed 7-sensor configuration by [Huang 2010] and the 10-sensor arrangement used also by [Griffin 2012], another widely used solution for establishing a full gradient tensor involves using three or more triaxial magnetometers (magnetometer heads) to provide redundancy [Pei 2009].

The gradient is usually calculated numerically from the individual sensor outputs; however this method suffers from finite ADC resolution. Alternatively, magnetic sensors can be biased by a common feedback field provided either by a separate triaxial head [Kumar 2005] or by a combination of sensor readings [Anderson 2002].

1.2.2 Gradiometers measuring tensor components

For a specific application, however, only a limited number of gradient tensor components can provide the needed information: the gradiometer design can be simplified. The use of more sensors leads to redundancy in this case.

Single-component ∂Bi/∂i or ∂Bi/∂j type gradiometers are typically used for detecting magnetic disturbances in the presence of a large disturbing common-mode field (which can be the Earth's field, a magnetizing field, or common-mode noise). Applications include non-destructive testing [Grüger 2003], geophysics [Bevan 2013], UXO detection [Kumar 2005], archaeology [Bevan 2013] and biomedicine [Tomek 2006], [Seki 2009], [Ludwig 2005]. They are typically constructed using

two or more magnetic field sensors, or a coil-pair in the case of SQUID sensors [Stolz 2000].

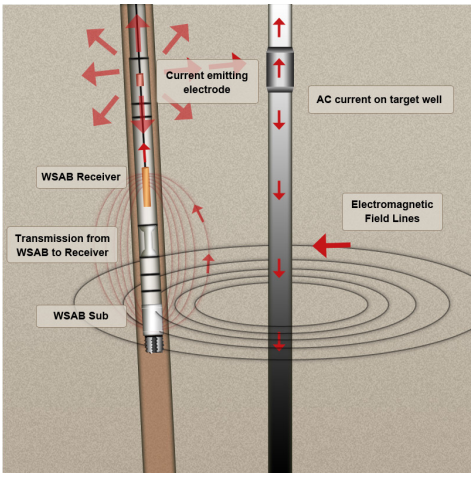

Fig. 1.5 – Down-hole drilling with magnetic field guidance. From the Vector Magnetics website.

The relation between magnetic gradient and electric current is used in down-hole drilling by Vector Magnetics Inc. (the magnetic division now at Halliburton) [Kuckes 1994]. The electric current carrying defective pipe serves for navigating the drilling head, which keeps a specified distance and orientation in relation to that pipe during relief well drilling, see Fig. 1.5. In this case of electric current aligned in the vertical z-direction, only two gradient tensor components are non-zero: $\partial B_y/\partial y$ and $\partial B_x/\partial y$. The distance can then be calculated from the nonzero components.

1.2.3 "Scalar" gradiometers

The so-called "scalar gradiometer" measures the gradient of the total field $|\mathbf{B}|$. The components in this case are limited to:

$$\boldsymbol{G}_{|\boldsymbol{B}|} = \left\{ \frac{d|\boldsymbol{B}|}{dx}, \frac{d|\boldsymbol{B}|}{dy}, \frac{d|\boldsymbol{B}|}{dz} \right\}$$

Two scalar magnetometers are used to obtain the respective component; typically they are Proton, Overhauser or optically pumped magnetometers having high accuracy (better than 10 pT). Although this setup is widely used in practical applications due to its high sensitivity and accuracy and its low heading error, it has been proved that the "scalar gradient" does not provide as much information as the gradient tensor components [Schmidt 2006]. However, for space applications, the usage of scalar magnetometers in a mixed vectorial-scalar setup is helpful for enabling in-flight magnetometer calibration and for suppressing the spacecraft magnetic signature [Primdahl 2006].

Scalar gradiometers are not further considered in this thesis.

2 State-of-the-art

Generally, the most sensitive commercial gradiometers use fluxgate sensors having a $0.6 \div 1$ m gradiometric base - (Schonsted GA52, Foerster Ferex, GeoscanFM256, Bartington GRAD601 axial gradiometers) - or use cryogenic SQUID magnetometers which allow for short gradiometric bases [Chwala 2012]. This in turn makes them bulky and impractical in restricted areas, although the SQUID systems can achieve excellent performance. For example, the full-tensor SQUID gradiometer of [Chwala 2012] achieved a noise as low as 10 $pT \cdot m^{-1} \cdot Hz^{-0.5}$ @ 1Hz after gradiometer balancing, however its consumption was about 15 W and the mass of the towed system was 100 kg [Braginski 2009].

On the other hand, miniaturized, non-cryogenical solutions tend to be limited to compact gradiometers for NDT or magnetic particle detection with a liftoff to the dipole source or disturbance in fractions of a millimetre. These devices are either micro-fluxgates [Grüger 2003] or GMR gradiometers [Leitao 2013]. They exhibit noise several magnitudes larger than fluxgate gradiometers, which prevents other practical uses. [Pelkner 2011] shows a detection limit of about 5 μT of the integrated gradiometer (Sensitec, Germany), which after recalculation on the 0.25 mm gradiometric base gives a detection limit of 20 $mT \cdot m^{-1}$ in gradient units.

As the compact gradiometer falls between the two above limiting cases, the following overview of relevant state-of-the-art instruments is based on slightly relaxed parameters than the thesis objective. Instruments having gradiometric base less than 30 cm and gradient noise less than 5 $nT \cdot m^{-1} \cdot Hz^{-0.5}$ @ 1Hz, or showing a perspective to achieve this goal, are presented.

2.1 Full-tensor gradiometers

An SDT gradiometer for NDT and UXO detection consisting of an array of 6x9 SDT sensors was presented by NVE [Anderson 2002]. SDT sensors were arranged on all six faces of a cube - Fig. 2.1. The initial version [Wold 1998] had noise of 1 $nT \cdot Hz^{-0.5}$@ 1 Hz, resulting in gradient noise of 4.5 $nT \cdot m^{-1} \cdot Hz^{-0.5}$ @ 1 Hz with the 30-cm gradiometric base of the device. The final 2002 version did not include further data.

The gradiometer presented by [Wiegert 2007] used four sensors, each comprised of two triaxial fluxgate magnetometers. A so called “Magnetic Scalar Triangulation and Ranging” technology was used to calculate scalar functions rather than classical gradient tensor components to locate UXO or mines. The published sensor noise was 0.25 nT p-p which would yield 1.2 $nT \cdot m^{-1}$ p-p gradient noise (30-cm base).

Underwater autonomous vehicles with tensor gradiometers for detecting anomalies in military applications have been presented by [Allen 2005], [Kumar 2005] and by [Pei 2009]. Allen used off-the-shelf Billingsley sensor heads. To decrease the large common mode appearing to the analog-to-digital converters that were used, an auxiliary triaxial head served to compensate most of the homogeneous field by the gradiometer sensors – see Fig. 2.2. The noise shown in [Allen 2005] was about 300 $pT \cdot m^{-1} \cdot Hz^{-0.5}$ @ 1 Hz after compensating the underwater vehicle noise, with a gradiometric base again of approx. 30 cm.

[Griffin 2012] has shown a tensor gradiometer developed for the LISA project. The gradiometer uses 10×2 rod-cores (Vacquier fluxgate sensor), and the pick-up coils of the gradient sensor pairs are connected anti-serially. The field is apparently partially compensated by a D/A converter to obtain a reasonably low differential signal. Due to the construction of the sensor, only $\partial B_i/\partial i$ terms were calibrated – the unavailability of precise calibrating coils for other gradient components makes calibration challenging. The noise was shown to be 0.3 $nT \cdot m^{-1} \cdot Hz^{-0.5}$ @1Hz for the $\partial B_i/\partial i$ pairs. No other parameters or construction details are given, however, and this makes the results questionable.

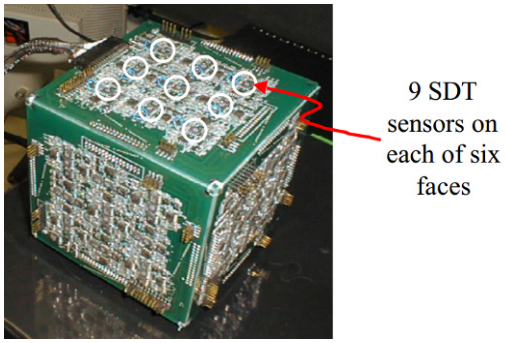

Fig. 2.1 – SDT gradiometer for UXO classification, from [Anderson 2002]

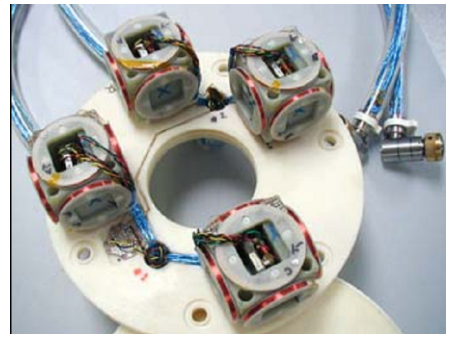

Fig. 2.2 – Four Billingsley triaxial fluxgate heads, from [Kumar 2005]

2.2 Axial gradiometers

[Merayo 2001] constructed a 20-cm base gradiometer with two 17-mm ring-core sensors, with an overall sensor size of 24×24×7 mm^3 [Nielsen 1991]. The sensors were astatized with non-magnetic screws, and a correction term for sensor non-orthogonalities was proposed. The accuracy of the instrument was 0.3 $nT \cdot m^{-1}_{RMS}$. Merayo measured the cross-coupling of the sensors and found a 250-ppm scale change, even for the 20-cm gradiometric base. Later, he constructed a better performing gradiometer, but with a 60-cm gradiometric base [Merayo 2002].

In his portable gradiometer, which is also available with a 25-cm gradiometric base, [Forster 1983] uses two rod-core fluxgate sensors with their cores attached to a non-magnetic string that is kept under tension. However, the pick-up coils are mounted on a tube, where the string is attached axially, see Fig. 2.3. The sensing direction of a rod core fluxgate with a low demagnetization factor and high permeability is defined by its core axis rather than by the pick-up coil [Musmann 2010]. In this manner, almost perfect alignment of the probes is achieved, resulting in high CMRR of the gradiometer.

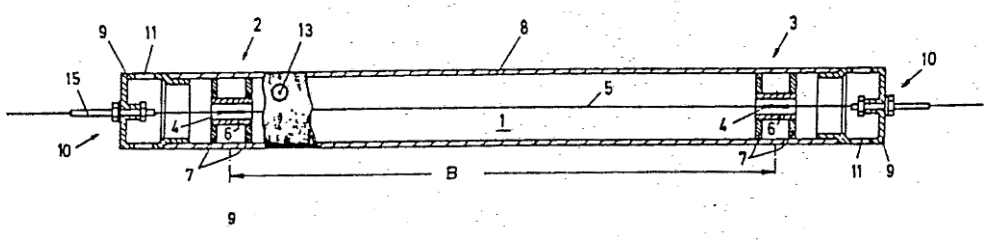

Fig. 2.3 – The Forster gradiometer with the sensor cores (4) on a string (5), from [Forster 1983]

For magnetopneumography, [Tomek 2009] used an axial gradiometer composed of 25–mm ring-core fluxgate sensors with 10 cm spacing. The noise was better than 350 $pT \cdot m^{-1} \cdot Hz^{-0.5}$ @ 1 Hz and the suppression of the homogeneous field was 0.035 $(T \cdot m^{-1}) \cdot T^{-1}$ corresponding to a CMRR of approx. 30 dB [Platil 2010].

[Sunderland 2009] obtained noise as low as 0.2 $nT \cdot m^{-1} \cdot Hz^{-0.5}$ @ 1 Hz in a so-called direct-string gradiometer. The sensor dimensions were 300×30×30 mm^3. In principle, the deflection of a conductive current carrying string is measured. The force due to the magnetic field gradient deflects the string in second order mode, causing a change in the string vibration amplitude (the string is fed with an AC current at second harmonic of the string). This gradiometer was later also tested in a space-like environment [Sunderland 2008]. However the susceptibility of the gradiometer parts initially limited the accuracy of the system [Sunderland 2007].

[Sasada 2014] has presented a fluxgate gradiometer consisting of two 30-mm long low-noise, fundamental harmonics operated sensors, with antiserially connected pickups. Astatization is achieved by tuning the excitation DC-current, which in turn results in changing the sensitivity of each sensor. With a gradiometric base of 50 mm (overall sensor length), he claims that he achieved 150 $pT \cdot m^{-1} \cdot Hz^{-0.5}$ @ 1 Hz in the open-loop operated gradiometer. This very good result is a consequence of the low demagnetization factor of the magnetic core and the fundamental-mode operation [Sasada 2002].

2.2.1 Single core fluxgate gradiometers

In the case of fluxgate sensors, the axial gradiometer can be simplified to the so-called single-core gradiometer, which was introduced by [Berkman 1960]. Its basic operating principle is shown in Fig. 2.4. The magnetic field gradient generates a gradient in the core flux Φ_B of the magnetic core and thus the (anti-serially connected) pick-up coils W_2' and W_2'' at positions L_1 and L_2 measure the difference between H_1 and H_2. The gradiometric base d is then defined as the pick-up coils distance $d=L_1-L_2$.

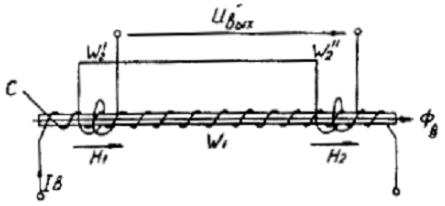

Fig. 2.4 – The single-core gradiometer from [Berkman 1960]

[Mermelstein 1988] introduced a similar gradiometer that used a magnetostrictive material to facilitate sensor excitation, see Fig. 2.5. The gradiometric base was 30 mm, and the noise when recalculated was approx. 1 nT·m^{-1}·Hz$^{-0.5}$ @ 1 Hz. However, its CMRR was only around 20 dB, even for homogeneous fields of only 50-nT magnitude. Later, the improved design used three coils [Mermelstein 1990]. [Ripka 1993] constructed a race-track fluxgate gradiometer with a 70-mm long race-track sensor having a 37.5 mm gradiometric base, also using three detection coils (2 for the gradient, 1 for the homogeneous channel), see Fig. 2.6. The 1-Hz noise was 1.2 nT·m^{-1}·Hz$^{-0.5}$, but the basic problem was the instability of the sensor due to open-loop operation. Later the coils were split into sections to reduce the instability due to coil capacitance, and the gradiometer was successfully used in magnetopneumography [Ripka 1997].

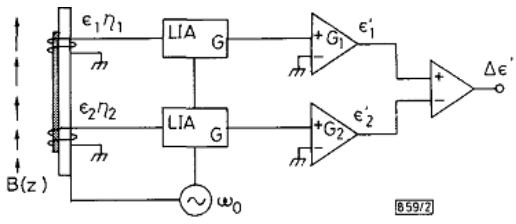

Fig. 2.5 – Magnetostrictive gradiometer [Mermelstein 1988]

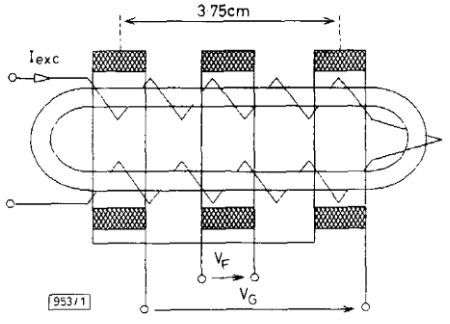

Fig. 2.6 – Race-track fluxgate gradiometer [Ripka 1993]

3 Thesis objectives and organization

The main goal of the thesis is the research and development of a low-noise magnetic gradiometer ($\leq 1\ \mathrm{nT \cdot m^{-1} \cdot Hz^{-0.5}}$ @ 1 Hz) with a small gradiometric base (≤ 40 mm), which would be usable for geophysical exploration, UXO detection, biomedicine and space applications.

Developing a gradiometer with a short gradiometric base poses several challenges, which are addressed as thesis objectives:

I. *Magnetic sensor selection and evaluation.* The best, off-the-shelf available magnetic sensors should be selected and possible limitations of their performance in a gradiometer should be studied.

II. *Gradiometer performance with available magnetic sensors.* Magnetic gradiometer with the above off-the-shelf sensors should be designed and its performance evaluated.

III. *Gradiometer astatization.* For small gradiometric bases, the same geometric misalignments result in higher angular deviations and thus in lower CMRR (Eq. 1.15). Appropriate astatization should increase the CMRR.

IV. *A compact, low-noise magnetic sensor.* The performance of the magnetic sensor for the use in a compact gradiometer is to be improved: its size should be reduced, if possible without influencing the sensor noise.

V. *Further development of the single-core gradiometer concept.* Low CMRR and unstable operation was one of the main problems with the instrument proposed by [Berkman 1960] and later presented by [Ripka 1997]. Offset drift and sensor gain instability were a consequence of open-loop operation, and the large uncompensated common-mode field made astatization difficult.

The thesis is organized as a reprint of relevant publications in journal papers and conference proceedings on a total of 55 pages accompanied with 32 pages of introductory, explanatory and also extension text, if required by the condensed form of the articles. The chapters are organized on the basis of the objectives:

- *Objective I.* Chapter 4 (Magnetic sensors for a compact gradiometer)
  Chapter 5 (Crossfield effect of AMR and fluxgate)
- *Objective II.* Chapter 6 (A PCB fluxgate gradiometer)
  Chapter 7 (A gradiometer with AMR sensors)
- *Objective III.* Chapter 8 (Axial gradiometer calibration and astatization).
- *Objective IV.* Chapter 9 (A compact, low-noise fluxgate sensor).
- *Objective V.* Chapter 10 (A gradiometer with 30-mm gradient base).
- In addition, a tensor gradiometer with the newly-developed sensors is proposed in Chapter 11. Chapter 12 discusses the prospects of the developed gradiometer.

4 Magnetic sensors for a compact gradiometer

The author co-authored the following review article *"Advances in Magnetic Field Sensors"* [J7] published in IEEE Sensors Journal in 2010. He mainly focused on recent trends in AMR and fluxgate sensors, which are shown in the Conclusions to be clear favorites because of their performance: size, noise and temperature stability.

Advances in Magnetic Field Sensors

Pavel Ripka, *Member, IEEE*, and Michal Janošek

***Abstract*—The most important milestone in the field of magnetic sensors was when AMR sensors started to replace Hall sensors in many applications where the greater sensitivity of AMRs was an advantage. GMR and SDT sensors finally found applications. We also review the development of miniaturization of fluxgate sensors and refer briefly to SQUIDs, resonant sensors, GMIs, and magnetomechanical sensors.**

***Index Terms*—Magnetic field sensors, magnetic sensors, magnetometers, magnetoresistors.**

I. Introduction

IN THIS PAPER, we make a review of recent advances in the technology and applications of magnetic sensors, which have appeared in the past seven years following the publication of a comprehensive book on magnetic sensors and magnetometers [1]. Here, we concentrate primarily on thin-film devices, as magnetic sensors based on bulk functional magnetic materials were recently reviewed in [2].

In recent years, anisotropic magnetoresistive (AMR) sensors with integrated flipping and feedback coils have become standard off-the-shelf devices for use in medium-accuracy applications such as compasses for mobile devices. After many years of development, giant magnetoresistive (GMR) sensors have finally found applications in angular sensing. Spin-dependent tunneling (SDT) devices are used for applications that require the smallest sensor size. Exciting improvements have been achieved in the sensitivity of resonance magnetometers, but most of the new devices are still in the laboratory phase. Despite the recent achievements in giant magnetoimpedance (GMI) sensors and orthogonal fluxgates, these devices are still far from the parameters achieved by classical longitudinal fluxgate sensors.

The development of magnetic sensor technology has been slow and gradual. Most breaking news about nanosensors with picotesla resolution has turned out to be a bubble. Exaggerated advertisements have resulted in inflated parameters for magnetic devices; we will try to show which factors are critical for real applications of magnetic sensors.

II. Flux Concentrators

Flux concentrators made of high-permeability material increase the sensitivity of any magnetic sensor. At present, they are integrated into the package of some Hall sensors and magnetoresistors. They can also be used to deflect the sensing direction so that the Hall sensor is sensitive to the in-plane field [3]. Similar concentrators are used to shield inactive sensors connected in a Wheatstone bridge in some GMR sensors.

The weak points of flux concentrators include remanence, nonlinearity, the danger of saturation, and temperature dependence. It is important to use high-permeability material and not excessively high magnetic gain, so that the temperature dependence of the gain factor is low.

An extreme case of a high-gain setup is a low-noise Hall sensor with 20-cm long concentrators having a 100 μm air gap [4]. The magnetic gain is 600, and the achieved noise level is 100 $\mathrm{pT}/\sqrt{\mathrm{Hz}}$@1 Hz. Such a sensor is a rarity, as much smaller fluxgates have lower noise. However, a similar sensor configuration was successfully used in one device in combination with an induction magnetometer to measure also the dc component [5].

Modulation of the permeability of the material by an excitation field may help to shift the signal frequency out of the $1/f$ noise range of the Hall sensor. The miniature sensor described in [6] uses permeability modulation of the 5-mm-long wire concentrator and the achieved noise level is 8 $\mathrm{nT}/\sqrt{\mathrm{Hz}}$@1 Hz. Modulation of the dc field can also be achieved by periodically moving the concentrator using an Microelectromechanical System (MEMS) [7]. However, compared to field modulation by changing the permeability (which is also used in fluxgate sensors), this approach is rather complicated. Until now, competitive results have not been achieved. It is also possible to modulate the permeability by increasing the temperature above the Curie point [8], but this is rather impractical, as the working temperature of such a device is limited.

Flux concentration can be also performed by a super-conducting loop (a flux-to-field transformer), which has been successfully used in GMR-mixed sensors [9]; the achieved gain factor was 1000. However, to achieve 100 $\mathrm{pT}\sqrt{\mathrm{Hz}}$@1 Hz the device requires 4.2 K temperature. For 77 K temperature, the noise is increased to 600 $\mathrm{pT}\sqrt{\mathrm{Hz}}$@1 Hz.

III. Hall Sensors

Most of the magnetic sensors that are produced use the Hall effect. The Hall sensitivity of silicon sensors is typically 1 mV/mT for a 1 mA current. Higher sensitivity can be achieved with thin-film InSb (typ. 5 mV/mT) or InAs (typically, 2 mV/mT). InAs exhibits lower temperature dependence of the Hall voltage compared to Si and InSb, and the working range of InAs devices is also superior: it exceeds the -40 °C to $+150$ °C range required for automotive applications. A promising Hall sensor was made using silicon-on-insulator (SOI) technology: 1 $\mu\mathrm{T}/\sqrt{\mathrm{Hz}}$@1 Hz noise was achieved for an 80-μm wide, 50-nm thick sensor [11].

Manuscript received October 02, 2009; revised December 16, 2009; accepted February 07, 2010. Current version published April 07, 2010. This is an expanded paper from the IEEE SENSORS 2008 Conference. The associate editor coordinating the review of this paper and approving it for publication was Dr. Patrick Ruther.

The authors are with the Department of Measurement, Czech Technical University, Faculty of Electrical Engineering, Technicka 2, 166 27 Praha 6, Czech Republic (e-mail: ripka@fel.cvut.cz; janosem@fel.cvut.cz).

Color versions of one or more of the figures in this paper are available online at http://ieeexplore.ieee.org.

Digital Object Identifier 10.1109/JSEN.2010.2043429

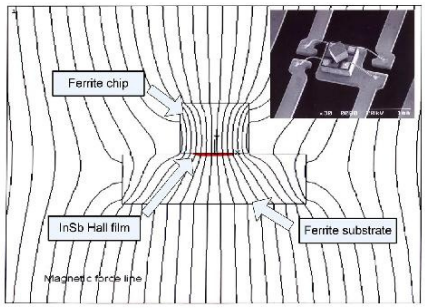

Fig. 1. Magnetic force lines of field concentrators for a thin-film Hall sensor (FEM simulation), courtesy of Asahi Kasei Electronics.

Two-dimensional quantum-well multilayer heterostructures based on GaAs are promising for low-noise Hall sensors: 100 $\mathrm{nT}/\sqrt{\mathrm{Hz}}$@1 Hz noise was achieved with external spinning-current electronics [10], which was further improved threefold by using leakage-free switches.

Fig. 1 shows an off-the-shelf InSb Hall sensor with an integrated ferrite concentrator (Asahi Kasei, BW series): the InSb thin-film Hall sensor is sandwiched between two ferrite pieces. The figure shows the flux lines simulated by FEM and a microphotograph of the device.

The integrated CMOS[1] micro-Hall plate sensor with an active area of 2.4 μm × 2.4 μm supplied by the spinning current has noise of 300 $\mathrm{nT}/\sqrt{\mathrm{Hz}}$@1 Hz [12]. CMOS technology allows to make intelligent Hall sensors with an on-chip digital signal processing part, these sensors can communicate digitally and perform sophisticated error corrections. One example is the ability to compensate not only the temperature dependence of the sensor itself, but also the temperature dependence of the magnetic circuit enclosing the sensor (temperature coefficient of the permeability, changes in the airgap, etc.)

IV. AMR Sensors

Single-domain ferromagnetic thin films exhibit AMR: their electric resistance is higher by about 2% in the direction of the magnetization than in the perpendicular direction (this effect exists in non-magnetic metals, but it is much weaker). AMR sensors are more sensitive than Hall sensors, and they exhibit better offset stability because they do not suffer from the piezo effect. The development of AMR sensors was driven by the need to replace inductive reading heads in hard disks. In this application, they were later replaced by GMR and SDT sensors, as these allowed higher storage densities due to their smaller size. Linear AMR sensors are at present produced mainly by NXP (Philips), Honeywell and Sensitec. They can have 10 nT resolution, but, unlike Hall sensors, the driving and signal processing electronics cannot be integrated on the same chip.

Almost all commercially available AMR sensors use a "barber pole" structure, in which aluminum stripes sputtered on permalloy strips deflect the direction of the current by 45° and make the characteristics linear. Four such meander-shaped elements are connected into a Wheatstone bridge.

[1]Complementary Metal-Oxide-Semiconductor.

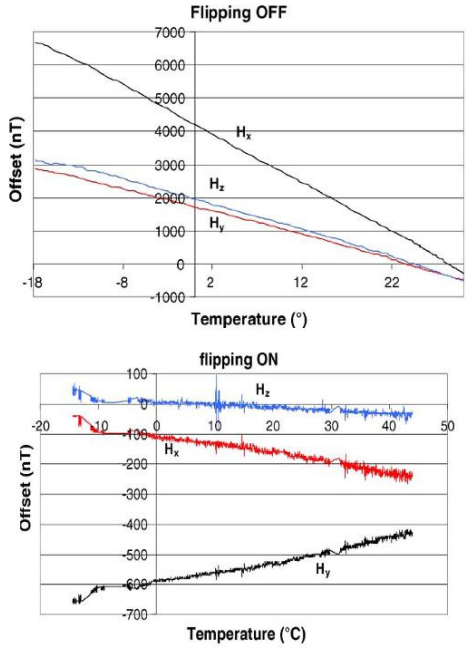

Fig. 2. (Top) Temperature offset drift of three Honeywell HMC 1001 AMR sensors without flipping, from [17]. (Bottom) Temperature offset drift of three Honeywell HMC sensors 1001 with periodical flipping, from [17].

The principles of AMR sensors are described in [13], comparative measurements of the noise of various magnetoresistors are shown in [14]. The best AMR sensors have a noise of 200 $\mathrm{pT}/\sqrt{\mathrm{Hz}}$@1 Hz [15]; however, it is difficult to achieve pT noise values with the whole AMR magnetometer; realistic resolution is 10 nT [16].

A. Flipping

The proper function of an AMR sensor is based on the single-domain state of the magnetic layer. A good technique for guaranteeing this is periodical "flipping" – remagnetization of the sensor structure by short pulses into a coil (which is usually integrated on the chip). Bipolar flipping is used for low-field sensors, because it also reduces the sensor offset and crossfield error. Fig. 2 shows the offset drift of flipped sensors in a tri-axial AMR magnetometer: without flipping, the drift was typically 100 $\mathrm{nT}/°\mathrm{C}$.

B. Magnetic Feedback

Another technique for improving the accuracy of any magnetic sensor is feedback compensation of the measured field. Modern AMR sensors have an integrated flat feedback coil, which simplifies the magnetometer design, but may also cause new design problems, as the compensating field is much less homogeneous than that of a solenoid–this may cause linearity error. The temperature coefficient of sensitivity of a typical

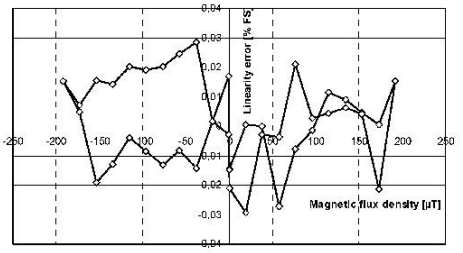

Fig. 3. Linearity error of a Philips KMZ 51 AMR sensor, feedback compensated by using an internal coil. Hysteresis is also visible from the measurement cycle [18].

AMR sensor may be reduced from 0.25%/K to 0.01%/K by using negative feedback with a sufficient gain; the remaining temperature dependence is due to the temperature coefficient of the field factor of the feedback coil. The temperature coefficient of the offset remains the same (typically 10 nT/K, but varies from piece to piece, even between sensors from the same batch), as feedback has no effect on this parameter. With feedback compensation, the linearity error may be below 300 ppm of the full-scale, as shown in Fig. 3 [18].

C. Crossfield Error

AMR sensors suffer from cross-field error: the output voltage V depends not only on the measured field H_Y, but also on the field component H_X, perpendicular to the sensing direction

$$V = 2I\Delta R\frac{H_Y}{H_X + H_0}$$

where ΔR is the maximum resistance change and I is the bridge current.

From the previous equation, we can see that the cross-field error (response to H_x) is zero for $H_y = 0$. The magnetic feedback that automatically compensates H_y can achieve this (Method 1). However, in some cases this is not possible due to limitations of power, circuit complexity or speed. Honeywell has released new sensors with "reduced cross-field error" by increasing the H_0 (Method 2); but this also reduces sensitivity and thus increases sensor noise in field units.

Cross-field error may cause a 2.4-degree azimuth error for the AMR compass. This error can be compensated numerically if we know H_0 and measure the field in two directions, or better in three directions (Method 3) [19]. If periodic flipping is used and each output is read separately, the cross-field error can be suppressed simply by averaging the outputs for the "SET" and "RESET" flipping polarities (Method 4). More complicated calculations may lead to better correction of the crossfield error (Method 5), and, in some cases, two components of the external field can even be measured using a single sensor [20]. Methods for suppressing the cross-field error are summarized in Table I.

TABLE I
METHODS FOR REDUCING THE CROSSFIELD ERROR IN AMRS

Method	Advantage	Disadvantage
Feedback compensation of the measured field H_y	Fully analog method	Non-homogeneity of the compensation field. Power consumption
Increasing H_0	Implemented during sensor production, no postprocessing	Decreased sensitivity, increased noise
Numerical correction using 3 sensors	Flipping not necessary, lowest power consumption	Requires complicated calibration. Digital processing necessary
Flipping and averaging	Simple, can be analog	Residual error (typically 1%)
Flipping and calculation	Small error	Digital processing required

V. GMR AND SDT SENSORS

GMR and SDT magnetoresistors are made of magnetic multilayers separated by very thin non-magnetic conducting (GMR) or insulating (SDT) layers. The electrical resistance of these structures depends on the direction of their magnetization. In general, if the magnetic layers are magnetized in the same direction, the resistance is smaller than for layers magnetized in opposite (antiparallel) directions. The external measured field usually controls the magnetization direction in the "free" layer, while the other "pinned" layer has fixed magnetization.

In order to compensate the basic temperature sensitivity, these devices are made as Wheatstone bridges. A bipolar response of the GMR bridge branches can be achieved by a DC bias field or, in the case of a spin valve, by changing the orientation of the magnetization of the magnetically hard pinning layer [21].

The most promising industrial application of GMR sensors is in angular sensing. The magnetization direction of the free layer of the spin-valve is rotated by the permanent magnet. If the free layer is saturated, the sensor output does not depend on the magnet distance, only on the measured angle.

Recently developed GMR sensors have increased their temperature stability: Hitachi has reported only a 20% sensitivity change between -40 °C to $+120$ °C, and 30 minutes of survival at 250 °C. However, large magnetic fields—especially at elevated temperatures—can destroy GMR spin valves due to changes in the magnetization of the pinning layer. This danger does not exist for Hall sensors and AMR magnetoresistors.

In the case of SDT sensors, high coercivity and low linearity remain a serious problem [22]; however, a digital magnetometer with a SDT sensor reported in [23] exhibited 1 μT resolution and a linear range of ± 1 mT.

GMR and SDT sensors have $1/f$ noise with cutoff frequency in the order of MHz, and the reported noise levels are quite high [24]. Picotesla-detection predictions are usually based only on thermal noise, and they did not take magnetic $1/f$ noise into account [25]. Fig. 4 shows that magnetoresistors in general have much higher noise than fluxgate sensors. However, their main advantage, especially in the case of SDT sensors, is their small

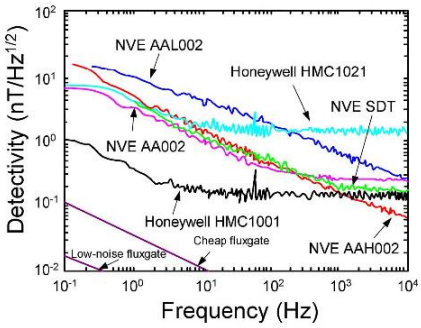

Fig. 4. Noise spectrum of magnetoresistors and fluxgate sensors. HMC 1001 and 1021 are AMR magnetoresistors, NVE AAxx are GMR magnetoresistors, and NVE SDT is a prototype of a spin-dependent tunelling device. The data for a "cheap fluxgate" represent typical noise of Applied Physics Model 533 and similar devices. The data for "low-noise fluxgate" is taken from [27]. Adopted from [14].

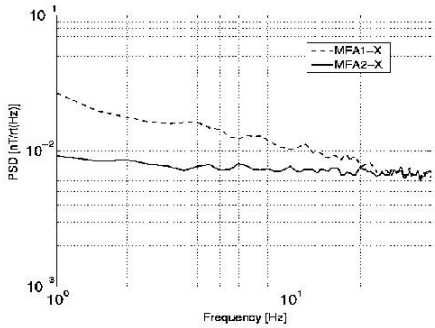

Fig. 5. Noise of a fully digital fluxgate magnetometer with CMOS ASIC electronics – without (top trace) and with dynamic offset cancellation (bottom trace)– from [33].

size and thus high spatial resolution. This is critical when measuring small objects such as magnetic microbeads for medical applications [26], and also where a small distance from the magnetic source is required.

VI. Fluxgate Sensors

Fluxgate sensors measure DC and low-frequency AC fields up to approximately 1 mT with a resolution of 100 pT and with linearity-error less than 10 ppm. Their operation is based on modulation of the permeability of the soft magnetic core, which creates changes in the dc flux ("flux-gating") of the pickup coil wound around the sensor core. The output voltage is on the second harmonics of the excitation frequency, as permeability reaches its minimum and maximum twice in each excitation cycle.

Most fluxgates have a ring core and the same direction of the excitation and measured fields [27]. The Vacquier-type fluxgate, which has two straight cores and solenoidal windings, was studied in [28]. Another form of core material is magnetic wire. Despite the higher noise, the Vacquier-type fluxgate has the following important advantages: 1) due to very low demagnetization, the sensor is insensitive to perpendicular fields and 2) unlike ring-core sensors, the sensing direction is well defined by the direction of the core. This is utilized in gradiometers, which require very high directional stability.

In order to achieve low remanence (or a small perming effect, which is an offset change after the sensor is subjected to a magnetic shock), the excitation should very deeply saturate the core of the sensor. In order to achieve this with reasonable power consumption, nonlinear excitation tuning is often used. The resonance tank consists of the excitation coil and the parallel capacitor. In resonance, the coil current has very high peaks (typically, 1 to 4 A): once the core is saturated, the impedance of the excitation coil drops and the capacitor is discharged through this coil. Despite the high peaks, the rms value of the current is small (typically, 10 to 50 mA).

The standard method for fluxgate signal processing is phase-sensitive detection of the second harmonic component of the output voltage. Precise magnetometers developed at the Danish Technical University utilize (short-circuited) current output [29].

The best fluxgate magnetometers use a so-called Compact Spherical Coil (CSC) with three orthogonal windings for the feedback. In order to achieve a homogeneous field, the coil is wound on the surface of a sphere, as the ideal spherical coil has a homogeneous field throughout the volume inside. The external magnetic field is completely compensated, so that the three orthogonally mounted fluxgate sensors inside the coil system are in a magnetic vacuum and thus do not suffer from cross-field errors. The disadvantages of CSC are as follows:

— large volume: in order to reduce the size of the CSC the fluxgate sensors are mounted in close vicinity and influence each other;
— high price: complex mechanics;
— the sensors cannot be removed without breaking the coils.

The best reported offset stability in the -18 °C to $+63$ °C range is ± 0.6 nT [30]. Nishio *et al.* investigated sensitivity, offset and noise in a wide-temperature range [31]: with a ceramic core bobbin, the offset variations were below ± 3 nT in the -180 °C to $+220$ °C range.

Digital fluxgate magnetometers [32] use two basic approaches, which can be combined:

— replacing the analog synchronous detector by digital signal processing;
— replacing the analog feedback loop by a delta-sigma or some other digital feedback scheme.

Digital magnetometers still do not achieve the parameters of the top analog magnetometers [33], but they are very flexible and allow for the future integration of electronics into a single ASIC chip. Using dynamic offset compensation of the input stage, the noise was lowered to 9 pT/$\sqrt{\text{Hz}}$@1 Hz (Fig. 5), which is sufficient for most applications in the presence of the Earth's field [34].

A. Miniature Fluxgates

As common fluxgate sensors can be quite large (diameter in units of cm for low-noise, ring-core devices), many miniaturiza-

tion approaches have been tried. Three basic types of miniature fluxgate are: 1) CMOS-based devices with flat coils; 2) sensors with microfabricated solenoids; and 3) PCB-based devices with solenoids made by tracks and vias.

CMOS microfluxgates are based on a strip of soft magnetic material on top of a flat coil system made with a metallic layer of a standard CMOS process. These flat coils serve both to excite the strip core, which is either a sputtered or an electrodeposited permalloy or a shaped amorphous material. These devices may have low-power sensor electronics integrated on the same chip. A 4 × 4 mm, 2-axial sensor for a wristwatch compass was reported to achieve 15 $\mathrm{nT}/\sqrt{\mathrm{Hz}}$@1 Hz noise with 92 V/T sensitivity and 10 mW power consumption [35]. A similar design using a sputtered, 1-μm-thick Vitrovac ($H_c = 100$ A/m), achieved 7.4 $\mathrm{nT}/\sqrt{\mathrm{Hz}}$@1 Hz. With increased power consumption, the sensitivity was 450 V/T and the linearity was 1.15% in the $\pm$50-μT range [36].

A flat coil of CMOS fluxgates has, in principle, high resistance and poor magnetic coupling with the core. The efficiency of the flat coil is therefore much worse than that of a solenoid. The UV-LIGA[2] process enables the production of MEMS single-layer solenoids with 25 turns/mm [37]. A microfluxgate made using such a technology is reported in [38]. The sensor with a 30-μm electroplated permalloy core has 56 excitation turns with a total resistance of 2 Ω and 11 sensing turns. A sensitivity of 650 V/T was achieved for a 5.5-mm-long sensor with 14 mW power consumption. The noise is 32 $\mathrm{nT}/\sqrt{\mathrm{Hz}}$@1 Hz, and the practical resolution is 1 μT, which is still worse than the resolution of the best AMR sensors. To reduce the size of the sensor, the authors used the "localized core saturation" method, which led to large perming because only a part of the sensor core was saturated: 30 μT perming was observed for a 200 mT shock.

PCB-based fluxgates achieved low noise (24 $\mathrm{pT}/\sqrt{\mathrm{Hz}}$ @1 Hz) and good temperature stability (20 nT in the -20 °C to $+70$ °C range), but the minimum size achievable with this technology is about 10 mm [39].

As miniature fluxgates may have only a limited number of turns of the pickup coil, the sensitivity is lower than that of a traditional wire-wound fluxgate. This is often compensated by a higher excitation frequency (typically, 300 kHz compared to 20 kHz). Proper fluxgate excitation should deeply saturate the sensor core in order to reduce "perming" (offset the change after the sensor is exposed to a large field). The low number of turns of the excitation coil of the integrated fluxgate necessitates the use of large excitation current peaks. As the cross-sectional area of the magnetic core is small, the quality factor of the excitation coil is low in comparison with large-size fluxgates. Nonlinear excitation tuning is therefore no longer possible. One way to reduce the power consumption in the excitation circuit is to use short excitation current pulses instead of a sinewave or square-wave [40].

B. Orthogonal Fluxgates

The main advantage of an orthogonal fluxgate is that it needs no excitation coil – the sensor is excited directly by the current flowing through the core. As is usual for fluxgate sensors, the output is at the second harmonic of the excitation frequency. The orthogonal fluxgate effect in ferromagnetic wire was known since the 1950s. Some authors have observed this effect during magnetoimpedance studies, and they use the term "nonlinear magnetoimpedance" for the same effect. This effect has been studied at high frequencies in tapes [41] and in wires [42], [43]; the observed output variable was calculated as the "MI ratio," which does not keep phase information and thus does not allow the field polarity to be recognized. The use of phase-sensitive detection of the output voltage (which is a standard technique for a fluxgate) gives a clear advantage for the performance of the sensor. The disadvantage of an orthogonal fluxgate is that the necessary excitation current is usually high (typically, 20 to 100 mA). As the magnetic field in the inner part of the conductor is low, which causes perming, a favorable design is a nonmagnetic conductor covered by a magnetically soft thick layer.

A miniature orthogonal fluxgate with a planar structure, formed by a Permalloy layer electrodeposited on a rectangular copper conductor, is reported in [44]. The sensor core is only 1 mm in length, and the sensor has two flat 60-turn pickup coils. The overall dimension of the sensor chip is 1.8 × 0.8 mm, the sensitivity is 0.5 $\mathrm{mV}/\mu\mathrm{T}$ in a $\pm$200 μT linear operating range. The noise was 95 $\mathrm{nT}/\sqrt{\mathrm{Hz}}$@1 Hz with 8 mW net excitation power consumption.

The "fundamental mode" orthogonal fluxgate uses DC biased excitation; the output is on the same frequency as the excitation. As this sensor is saturated only in one polarity, the basic offset stability is poor and it can be improved by periodic switching of the excitation bias. The authors in [45] achieved a sensitivity of 1.8 $\mathrm{mV}/\mu\mathrm{T}$, offset stability of 1.2 nT/hour and a noise level of about 100 $\mathrm{pT}/\sqrt{\mathrm{Hz}}$@1 Hz with periodic bias switching (20 pT without it). In [46], the temperature coefficient of sensitivity was reduced from 6500 to 100 ppm/K using feedback compensation. A triaxial device was reported in [47], having three 38-mm-long U-shaped legs made of a single amorphous wire (125 μm diameter). The sensor achieved a noise level of 360 $\mathrm{pT}/\sqrt{\mathrm{Hz}}$@1 Hz with 4 mA excitation and 20 mA DC bias current. Another fundamental-mode fluxgate with an unusual, 5-cm-long, amorphous tubular core was presented in [48]. The orthogonal excitation field was created by a toroidal coil, which reduced the necessary excitation current to 6 mA. For a 60-mA DC-bias current, the noise achieved was 10 $\mathrm{pT}/\sqrt{\mathrm{Hz}}$@1 Hz. However, this configuration is no longer mechanically simple, which is the main advantage of the classical orthogonal configuration.

The so called "coil-less fluxgate" has no pickup coil: the sensor output is the second harmonic voltage induced between the wire terminals. The operation is based on helical anisotropy, which creates an off-diagonal component of the permeability tensor: the field in the axial direction creates axial flux and thus the longitudinal component of the induced voltage. The sensitivity achieved for a 38-mm-long sensor is 0.2 $\mathrm{mV}/\mu\mathrm{T}$ [49].

VII. Other Devices

In this short review paper, we will mention SQUID [3] magnetometers only briefly. DC SQUIDS are less noisy than the RF SQUIDS. These devices are based on a superconducting

[2]UltraViolet Lithographie, Galvanoformung, Abformung.

[3]Superconducting Quantum Interference Devices.

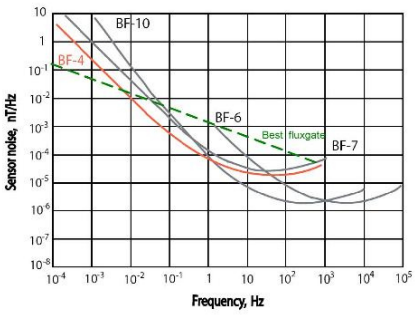

Fig. 6. Noise of popular EMI induction sensors and a low-noise fluxgate – adapted from a Schlumberger datasheet [54].

ring with two Josephson junctions [1]. In order to increase the sensitivity, a flux transformer is often used. SQUID in fact measures only field changes, not the absolute field. The noise level of a low-Tc SQUID with a flux-transformer can be as low as 1 $\mathrm{fT}/\sqrt{\mathrm{Hz}}$ and a high-Tc system can have white noise of 36 $\mathrm{fT}/\sqrt{\mathrm{Hz}}$, as shown in the excellent review by Robbes [50].

Resonant magnetometers (proton magnetometers, Overhauser magnetometers and optically pumped magnetometers) are usually very stable scalar devices which measure the absolute field value regardless of the field direction [1]. While optical magnetometers are based on Zeeman splitting, classical proton magnetometers measure the precession frequency of a proton or electron. It is known that any scalar magnetometer can be made vectorial by adding a rotating bias field and demodulating the output, but this technique degrades the sensor performance both in bandwidth and in noise. The 1 $\mathrm{fT}/\sqrt{\mathrm{Hz}}$@10 Hz noise of the spin-exchange relaxation-free (SERF) magnetometer is noticeable: the main idea of this magnetometer is to reduce spin-exchange broadening of the Zeeman resonance. SERF may reach SQUID-level performance without cryogenic cooling. This magnetometer is a vectorial one: to obtain the remaining two vectors, the field has to be again modulated. The SERF magnetometer operates only in a near-zero field, and the vapor cell must be heated. Magnetic fields higher than about 10 nT should be vectorially compensated. A recent review of these "optical atomic magnetometers," which are still experimental devices, has been presented by Budker *et al.* [51].

Induction magnetometers are based on the Faraday induction law; thus they measure the flux derivative. Instead of measuring open-circuited induced voltage, some induction magnetometers evaluate the short-circuited coil current, which in ideal conditions is proportional to the flux [1]. Induction magnetometers naturally cannot measure dc fields, but at frequencies higher than 0.01 Hz they may have lower noise than a fluxgate, if sensor dimension and mass is not an issue. Fig. 6 shows the noise spectra of several commercially available induction coils manufactured by EMI (a division of Schlumberger) [52], compared to a typical low-noise fluxgate. The length of the BF-4 sensor, which has the smallest noise at low frequencies, is 142 cm, and its mass is 8 kg. BF-6 and BF-10 are similar in size, but these coils are optimized for higher frequencies; the 104 cm long BF-7 sensor weighs only 2 kg. A small induction sensor was described in [53], it is 10 cm in length and weighs only 11 g; its noise is 2 $\mathrm{pT}/\sqrt{\mathrm{Hz}}$@1 Hz. In [54], the authors constructed a 3-axial satellite induction magnetometer using similar sensors with 17-cm-long cores, and the overall mass weight of the 3-axial probe, including the holder device, was only 600 g. The frequency range was 0.1 Hz to 10 kHz, keeping the noise level of 2 $\mathrm{pT}/\sqrt{\mathrm{Hz}}$@1 Hz. A detailed review of induction magnetometers appeared recently in [55].

The GMI effect is based on the field-dependent change of the penetration depth [56]. The effect has only limited practical applications, as it is temperature dependent, gives low sensitivity and the characteristics are nonlinear and unipolar. The temperature dependence of the GMI effect is analyzed in [57]–[59]. GMI sensors are used in compass modules for some mobile phones [59], but the achievable accuracy is not clearly specified. The lowest achieved noise level extrapolated to 1 Hz (using $1/f$ noise rule) is 100 $\mathrm{pT}/\sqrt{\mathrm{Hz}}$@1 Hz for a 10-mm-long device presented in [60]. Due to the small diameter of the wire core, these sensors may have high spatial resolution and thus serve for detecting microbeads [61]. The disadvantage of GMI and similar sensors compared to a fluxgate is the perming effect, because the ferromagnetic core is usually not demagnetized during sensor operation.

A synthetic **magneto-electric sensor** with 130 V/T sensitivity was presented in [62]. It contains a sandwich made from magnetostrictive and piezoelectric materials. The measured field causes strain in the magnetostrictive layer. This strain is coupled to the piezoelectric layer, where the output voltage is generated. The achieved sensitivity for a 10-cm-long Metglas-PZT fiber laminate was 3000 V/T [63].

Other sensors are based on changing the **resonance frequency** of free-standing elements manufactured by MEMS technology. The preliminary results on large-scale models of a "xylophone magnetometer" were promising, but until now low noise has not been achieved on a small scale using MEMS polysilicon technology [64].

The micromachined **Lorentz force magnetic sensor** achieved field resolution of 10 $\mathrm{nT}/\sqrt{\mathrm{Hz}}$ for a 100 μA measuring current [65]. The Lorentz force, which is proportional to the measured field and the measuring current, deflects the free-standing MEMS structure. The motion is made periodic by applying an AC measuring current, usually at mechanical resonance frequency. The advantage of Lorentz force magnetometers is their high linearity and the possibility to change their range widely by selecting the measuring current. The sensor can work up to 50 T [66]. A detailed discussion on these sensors can be found in [67].

Magnetic sensors used for measuring electric **current, position, and mechanical torque** are described in [68], and therefore do not appear in this review. The most important achievements in these devices are the AMR gradient bridge for current sensors and polarized-band torque sensors for automotive applications. Sensors for magnetic **nondestructive testing** have been reviewed in [69].

TABLE II
PROPERTIES OF COMMON MAGNETIC FIELD SENSORS

	Hall with field concentrators (Sentron CSA-1VG)	AMR (Philips KMZ 51, Honeywell, HMC1001)	AMR flipped feedback (KMZ 51 [18])	Fluxgate Billingsley TFM100
linear range	5 mT	300 μT	300 μT	100 μT
size	6 mm	6 mm	6 mm	15 mm
linearity	0.1 < 0.2 %	1 %	40 ppm	20 ppm
sensitivity TC	200 ppm/K	600 ppm/K	20 ppm/K	20 ppm/K
offset @ 25°C	50 μT	< 10 μT	< 1 μT	10 nT
offset TC	600 nT/K	100 nT/K	2 nT/K	0.2 nT/K
$noise_{RMS}$ (0.1-10 Hz)	1 μT	10 nT(1 nT)	10 nT	<100 pT
perming, hysteresis	1 μT	300 nT	10 nT	< 1 nT
BW	100 kHz	100 kHz	100 Hz	3.5 kHz
power consumption	55 mW	30 mW	100mW	350 mW

VIII. CONCLUSION

We have briefly referred to the main recent advances in magnetic field sensors. So far, there is always a tradeoff between the size of a sensor and its parameters. The progress of miniaturization is not likely to be skipped by novel nanosized sensors without using new physical principles. In many applications, such as detection of magnetic microbeads, micromagnetic scanning or NDT, sensor size is an issue and is often the only selection criterion, either because of the need for spatial resolution or because of the weak point-like sources. However, in cases where a large detection distance cannot be avoided, parameters such as noise (detectivity) become more important. In more demanding applications, such as precise compasses, positioning and tracking devices, the linearity, temperature coefficients and even cross-field sensitivity of the sensor also start to be more important than noise, which is often the only parameter that is mentioned .

Table II compares important parameters of the most popular solid-state magnetic field sensors. We give values for some of the best commercially-available sensors in each class.

REFERENCES

[1] *Magnetic Sensors and Magnetometers*, P. Ripka, Ed.. New York: Artech, 2001.

[2] P. Ripka, "Sensors based on bulk soft magnetic materials: Advances and challenges," *JMMM*, vol. 320, pp. 2466–2473, 2008.

[3] R. S. Popovic, *Hall Effect Devices*. London, U.K.: Institute of Physics, 2004.

[4] P. Leroy, C. Coillot, V. Mosser, A. Roux, and G. Chanteur, "Use of magnetic concentrators to highly improve the sensitivity of Hall effect sensors," *Sensor Lett.*, vol. 5, pp. 162–166, 2007.

[5] P. Leroy *et al.*, "An ac/dc magnetometer for space missions: Improvement of a Hall sensor by the magnetic flux concentration of the magnetic core of a searchcoil," *Sens. Act. A*, vol. 142, pp. 503–510, 2008.

[6] A. Quasimi, C. Dolabdjian, D. Bloyet, and V. Mosser, "Improvement of the mu-hall magnetic sensor sensitivity at low frequency," *IEEE Sensors J.*, vol. 4, pp. 160–166, 2004.

[7] O. Arif, E. R. Nowak, A. S. Edelstein, G. A. Fischer, C. A. Nordman, and S. F. Cheng, "Magnetic-field dependence of the noise in a magnetoresistive sensor having MEMS flux concentrators," *IEEE Trans. Magn.*, vol. 42, pp. 3306–3308, 2006.

[8] W. Wang and J. Zhenye, "Thermally modulated flux concentrator for minimizing 1/f noise in magnetoresistance-based field sensors," *IEEE Trans. Magn.*, vol. 44, pp. 4003–4006, 2008.

[9] M. Pannetier-Lecoeur *et al.*, "RF response of superconducting-GMR mixed sensors, application to NQR," *IEEE Trans. Appl. Superc.*, vol. 2, pp. 598–601, 2007.

[10] A. Kerlain and V. Mosser, "Low frequency noise suppression in III-V Hall magnetic microsystems with integrated switches," *Sensors Lett.*, vol. 5, pp. 192–195, 2007.

[11] Y. Haddab, V. Mosser, M. Lysowec, J. Suski, L. Demeus, C. Renaux, S. Adriensen, and D. Flandre, "Low-noise SOI Hall devices," *Proc. SPIE.*, vol. SPIE-5115, pp. 196–203, May 2003.

[12] P. Kejik *et al.*, "An integrated micro-Hall probe for scanning magnetic microscopy," *Sens. Act. A*, vol. 129, pp. 212–215, 2006.

[13] S. Tumanski, *Thin Flm Magnetoresistive Sensors*. Bristol, U.K.: IOP Publishing, 2001.

[14] N. A. Stutzke *et al.*, "Low-frequency noise measurements on commercial magnetoresistive magnetic field sensors," *J. Appl. Phys.*, vol. 7, no. 10: Art. 10Q107, 2005.

[15] E. Zimmermann, A. Verweerd, W. Glaas, A. Tillmann, and A. Kemna, "An AMR sensor-based measurement system for magnetoelectrical resistivity tomography," *IEEE Sensors J.*, vol. 5, pp. .233–241, 2005.

[16] A. Bertoldi *et al.*, "Magnetoresistive magnetometer with improved bandwidth and response characteristics," *Rev. Sci. Instrum.*, vol. 76, pp. 065106-1–065106-6, 2005.

[17] J. Včelák, P. Ripka, A. Platil, J. Kubík, and P. Kašpar, "Errors of AMR compass and methods of their compensation," *Sens. Actuators A*, vol. 129, pp. 53–57, 2006.

[18] M. Vopálenský, P. Ripka, and A. Platil, "Precise magnetic sensors," *Sens. Actuators A*, vol. 106, pp. 38–42, 2003.

[19] J. Kubik, J. Vcelak, and P. Ripka, "On cross-axis effect of the anisotropic magnetoresistive sensors," *Sens. Actuators A*, vol. 129, pp. 15–19, 2006.

[20] P. Ripka, M. Janošek, and M. Butta, "Using the crossfield error in AMR," in *Intermag 2009 Digests*, 2009, pp. 129–130.

[21] M. Pannetier-Llecoeur, C. Fermon, A. Devismes, E. Kerr, and L. Vieuxrochaz, "Low noise magnetoresistive sensors for current measurement and compasses," *J. MMM*, vol. 316, pp. e246–e248, 2007.

[22] A. Jander, C. A. Nordman, A. V. Pohm, and J. M. Anderson, "Chopping techniques for low-frequency nanotesla spin-dependent tunneling field sensors," *J. Appl. Phys.*, vol. 93, pp. 8382–8384, 2003.

[23] J. Deak, A. Jander, E. Lange, S. Mundon, D. Brownell, and L. Tran, "Delta-sigma digital magnetometer utilizing bistable spin-dependent-tunneling magnetic sensors," *J. Appl. Phys.*, vol. 99, pp. 08B320–08B320-3, 2006.

[24] R. Ferreira, P. Wisniowski, P. P. Freitas, J. Langer, B. Ocker, and W. Maass, "Tuning of MgO barrier magnetic tunnel junction bias current for picotesla magnetic field detection," *J. Appl. Phys.*, vol. 99, pp. 08K706–08K706-3, 2006.

[25] P. P. Freitas, R. Ferreira, S. Cardoso, and F. Cardoso, "Magnetoresistive sensors," *J. Phys. Condens. Matter*, vol. 19, p. 165221, 2007.
[26] L. Xu, H. Yu, S.-J. Han, S. Osterfeld, R. L. White, N. Pourmand, and S. X. Wang, "Giant magnetoresistive sensors for DNA microarray," *IEEE Trans. Magn.*, vol. 44, pp. 3989–3991, 2008.
[27] P. Ripka, "Advances in fluxgate sensors," *Sens. Actuators A*, vol. 106, pp. 8–14, 2003.
[28] C. Moldovanu, P. Brauer, O. V. Nielsen, and J. R. Petersen, "The noise of the Vacquier type sensors referred to changes of the sensor geometrical dimensions," *Sens. Act. A: Phys.*, vol. 81, no. 1–3, pp. 197–199, 2000.
[29] F. Primdahl, J. M. G. Merayo, and P. Brauer, "Fluxgate magnetometry for precise mapping of the Earth's field," *Sensors Lett.*, vol. 5, pp. 110–112, 2007.
[30] F. Primdahl, T. Risbo, J. M. G. Merayo, P. Brauer, and L. Tøffner-Clausen, "In-flight spacecraft magnetic field monitoring using scalar/vector gradiometry," *Meas. Sci. Technol.*, vol. 17, no. 6, pp. 1563–1569, 2006.
[31] Y. Nishio, F. Tohyama, and N. Onishi, "The sensor temperature characteristics of a fluxgate magnetometer by a wide-range temperature test for a Mercury exploration satellite," *Meas. Sci. Technol.*, vol. 18, pp. 2721–2730, 2007.
[32] A. Cerman, A. Kuna, P. Ripka, and J. M. G. Merayo, "Digitalization of highly precise fluxgate magnetometers," *Sens. Actuators A*, vol. 121/2, pp. 421–429, 2005.
[33] W. Magnes *et al.*, "A sigma-delta fluxgate magnetometer for space applications," *Meas. Sci. Technol.*, vol. 14, pp. 1003–1012, 2003.
[34] W. Magnes *et al.*, "Highly integrated front-end electronics for space-borne fluxgate sensors," *Meas. Sci. Technol.*, vol. 19, no. Article 115801, 2008.
[35] P. M. Drljaca, P. Kejik, F. Vincent, D. Piguet, and R. S. Popovic, "Low-power 2-D fully integrated CMOS fluxgate magnetometer," *IEEE Sensors J.*, vol. 5, pp. 909–915, 2005.
[36] A. Baschirotto *et al.*, "A fluxgate magnetic sensor: From PCB to micro-integrated technology," *IEEE Trans. Instrum. Meas*, vol. 56, pp. 25–31, 2007.
[37] M. Woytasik, J.-P. Grandchamp, E. Dufour-Gergam, J.-P. Gilles, S. Megherbi, E. Martincic, H. Mathias, and P. Crozat, "Two- and three-dimensional microcoil fabrication process for three-axis magnetic sensors on flexible substrates," *Sens. Act. A: Phys.*, vol. 132, pp. 2–7, 2006.
[38] P.-M. Wu and C. H. Ahn, "Design of a low-power micromachined fluxgate sensor using localized core saturation method," *IEEE Sensors J.*, vol. 8, pp. 308–313, 2008.
[39] J. Kubík, L. Pavel, and P. Ripka, "PCB racetrack fluxgate sensor with improved temperature stability," *Sens. Act. A Phys.*, vol. 130, pp. 184–188, 2006.
[40] J. Kubik, L. Pavel, P. Ripka, and P. Kaspar, "Low-power printed circuit board fluxgate sensor," *IEEE Sensors J.*, vol. 7, pp. 179–183, 2007.
[41] A. Garcia-Arribas *et al.*, "Non-linear magnetoimpedance in amorphous ribbons: Large asymmetries and angular dependence," *Sens. Act. A, Phys.*, vol. 129, pp. 275–278, 2006.
[42] G. V. Kurlyandskaya, A. Garcia-Arribas, and J. M. Barandiaran, "Advantages of nonlinear giant magnetoimpedance for sensor applications," *Sens. Act. A*, vol. 106, pp. 234–239, 2003.
[43] J. G. S. Duque *et al.*, "The effect of helical magnetoelastic anisotropy on magnetoimpedance and its second harmonic component in amorphous wires," *JMMM*, vol. 271, pp. 390–395, 2004.
[44] O. Zorlu, P. Kejik, and R. S. Popovic, "An orthogonal fluxgate-type magnetic microsensor with electroplated Permalloy core," *Sens. Act. A, Phys.*, vol. 135, pp. 43–49, 2007.
[45] K. Goleman and I. Sasada, "High sensitive orthogonal fluxgate magnetometer using a Metglas ribbon," *IEEE Trans. Magn.*, vol. 42, pp. 3276–8, 2006.
[46] A. Plotkin, E. Paperno, A. Samohin, and I. Sasada, "Compensation of the thermal drift in the sensitivity of fundamental-mode orthogonal fluxgates," *J. Appl. Phys.*, vol. 99, pp. 08B305–08B305-3, 2006.
[47] K. Goleman and I. Sasada, "A triaxial orthogonal fluxgate magnetometer made of a single magnetic wire with three U-shaped branches," *IEEE Trans. Magn.*, vol. 43, pp. 2379–2381, 2007.
[48] E. Paperno, E. Weiss, and A. Plotkin, "A tube-core orthogonal fluxgate operated in fundamental mode," *IEEE Trans. Magn.*, vol. 44, pp. 4018–4031, 2008.
[49] M. Butta, P. Ripka, S. Atalay, F. E. Atalay, and X. P. Li, "Fluxgate effect in twisted magnetic wire," *JMMM*, vol. 320, pp. e974–e978, 2008.
[50] D. Robbes, "Highly sensitive magnetometers—A review," *Sens. Act. A, Phys.*, vol. 129, pp. 86–93, 2006.
[51] D. Budker and M. V. Romalis, "Optical magnetometry," *Nature Phys.*, vol. 3, pp. 227–234, 2007.
[52] BF EM4 Datasheet, Schlumberger: EMI Technology Center. [Online]. Available: http://www.slb.com/content/about/technology/emi_bf_sensor.asp
[53] C. Coillot, J. Moutoussamy, P. Leroy, G. Chanteur, and A. Roux, "Improvements on the design of search coil magnetometer for space experiments," *Sensor Lett.*, vol. 5, pp. 167–170, 2007.
[54] A. Roux *et al.*, "The search coil magnetometer for THEMIS," *Space Sci. Rev.*, vol. 141, pp. 265–275, 2008.
[55] S. Tumanski, "Induction coil sensors," *Measure. Sci Technol.*, vol. 18, pp. R31–R46, 2007.
[56] K. Knobel, M. Vázquez, and L. Kraus, "Giant Magnetoimpedance," in *Handbook of Magnetic Materials*, K. H. J. Buschow, Ed. New York: Elsevier, 2003, vol. 15, pp. 497–563.
[57] M. Michal, R. Pavel, and K. Ludek, "Temperature offset drift of GMI sensors," *Sens. Act. A*, vol. 147, pp. 415–418, 2008.
[58] B. Hernando, J. Olivera, M. L. Sanchez, V. M. Prida, and R. Varga, "Temperature dependence of magnetoimpedance and anisotropy in nanocrystalline finemet wire," *IEEE Trans. Magn.*, vol. 44, pp. 3965–3968, 2008.
[59] Y. Nakamura, T. Uchiyama, C. M. Cai, and K. Mohri, "PWM-type amorphous wire CMOS IC magneto-impedance sensor having high-temperature stability," *IEEE Trans. Magn.*, vol. 44, pp. 3981–3984, 2008.
[60] D. Robbes, C. Dolabdjian, and Y. Monfort, "Performances and place of magnetometers based on amorphous wires compared to conventional magnetometers," *J. Mag. Mag. Mat.*, vol. 249, pp. 393–397, 2002.
[61] D. Kim, H. Kim, S. Park, W. Lee, and W. Y. Jeung, "Operating field optimization of giant magneto impedance (GMI) devices in micro scale for magnetic bead detection," *IEEE Trans. Magn.*, vol. 44, pp. 3985–3988, 2008.
[62] N. H. Duc and D. T. Huong, "Magnetic sensors based on piezoelectric–magnetostrictive composites," *J. Alloys and Compounds*, vol. 449, pp. 214–218, 2008.
[63] J. Zhai, S. Dong, Z. Xing, and J. Li, "Viehland: Geomagnetic sensor based on giant magnetoelectric effect," *Appl. Phys. Lett.*, vol. 91, p. 123513, 2007.
[64] D. K. Wickenden *et al.*, "Micromachined polysilicon resonating xylophone bar Magnetometer," *Acta Astronautica.*, vol. 52, pp. 421–425, 2003.
[65] J. Kyynäräinen *et al.*, "3D micromechanical compass," *Sensor Lett.*, vol. 5, pp. 126–129, 2007.
[66] F. Keplinger, S. Kvasnica, A. Jachimowicz, F. Kohl, J. Steurer, and H. Hauser, "Lorentz force based magnetic field sensor with optical readout," *Sens. Act. A: Phys.*, vol. 110, no. 1–3, pp. 112–118, 2004.
[67] A. L. Herrera-May *et al.*, "A resonant magnetic field microsensor with high quality factor at atmospheric pressure," *J. Micromech. Microeng.*, vol. 19, no. Art.Nr. 015016, 2009.
[68] P. Ripka and K. Závěta, "Magnetic sensors," in *Handbook of Magnetic Materials*, J. Buschow, Ed. New York: Elsevier, 2010, to be published.
[69] G. Vertesy and A. Gasparics, "Nondestructive material evaluation by novel electromagnetic methods," *Mater. Sci. Forum*, vol. 414–4, pp. 343–352, 2003.

Pavel Ripka (M'00) received the Engineering degree in 1984, the C.Sc. (equivalent to Ph.D.) in 1989, Docent degree in 1996 and in 2002 Professor degree at the Czech Technical University, Prague, Czech Republic.

During 1991–1993, he was a Visiting Researcher at the Danish Technical University and during 2001 he was Marie Curie Fellow at the National University of Ireland, Galway. From 2005 to 2006, he was a Visiting Researcher at the Institute for the Protection and the Security of the Citizen, Ispra, Italy. Currently, he is Head of the Department of Measurement, Faculty of Electrical Engineering, Czech Technical University, Prague. He is lecturing in measurements, engineering magnetism and sensors. He is a author and coauthor of 6 books, >80 journal papers and 5 patents. His main research interests are magnetic sensors, especially fluxgate and MR, eddy current detectors and their applications.

Prof. Ripka is a member the Elektra Society, Czech Metrological Society, Czech National IMEKO Committee, Eurosensors Steering Committee, and the Advisory Board of SMM Conferences. From 2001 to 2005, he served as an Associated Editor of the IEEE SENSORS JOURNAL. He was a General Chairman of the Eurosensors XVI Conference held in Prague in 2002.

5 Crossfield effect of AMR and fluxgate

The so-called crossfield effect, which is the non-zero response of a magnetic sensor to perpendicular fields, is inherent to AMR [Pant 2005], [Ripka 2009] and it is also observed in fluxgate sensors [Brauer 1997]. If the sensors are arranged to form a gradiometer and the sensors are perfectly matched, this effect can be suppressed if it is caused by an uncompensated component of the large homogeneous field.

5.1 Crossfield sensitivity in AMR sensors

For AMRs, the theoretical response was derived in [Ripka 2009]. If the AMR is flipped, the crossfield response remains the same, but the sign of the voltage due to the measured field is changed: if both the output polarities are used, the sensitivity to crossfield is reduced. In the case of HMC 1001 sensor and a 20 μT measured field with 50 μT crossfield, the error was shown to be reduced from 1 μT down to 100 nT [Ripka 2009]. The equation describing the theoretical response was later improved by [Mohamadabadi 2013] who also verified compensation of this effect when using orthogonal sensors.

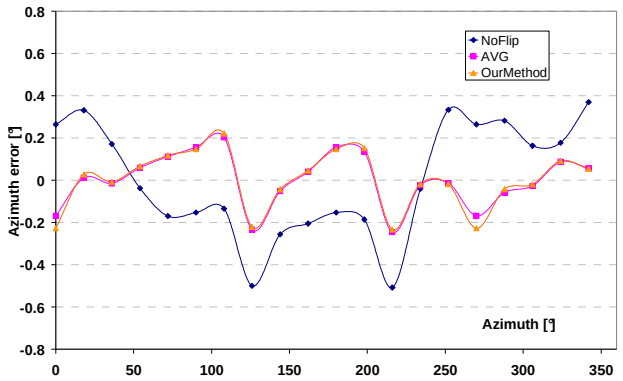

Fig. 5.1 – Unflipped and flipped azimuth error with KMZ 51.

In Fig. 5.1, the azimuth error due to the crossfield effect, if the KMZ 51 is used in a compass, is shown as measured by the author. The second, orthogonal sensor, needed for azimuth calculation, was synthetic – perfect mutual orthogonality was assumed. The error is less than ±0.4° without flipping and improves to ±0.2° with the proposed signal processing. For HMC 1001, the error was up to ±1° without flipping and below ±0.2° with flipping and signal processing after [Ripka 2009]. The recent method of [Mohamadabadi 2013] could further decrease the azimuth error of such AMR compass. These measurements were presented at the Symposium on AMR sensors, Wetzlar, Germany in 2009 and did not appear in the following paper due to its limited scope.

The following paper *"Crossfield sensitivity in AMR sensors"* [J9] was published in IEEE Transactions on Magnetics in 2009. It shows the theoretical response (derived earlier) of Honeywell HMC 1001 sensor compared with real measurements which were performed by the author. Author took part also in deriving the method to reduce the crossfield response using the flipped AMR output.

4514 IEEE TRANSACTIONS ON MAGNETICS, VOL. 45, NO. 10, OCTOBER 2009

Crossfield Sensitivity in AMR Sensors

Pavel Ripka, Michal Janošek, and Mattia Butta

Department of Measurement, Faculty of Electrical Engineering, Czech Technical University in Prague, 166 27 Praha 6, Czech Republic

We discuss the origin of the crossfield sensitivity of AMR sensors, the way how this error may influence the performance of an AMR compass and methods for its correction. Finally, we confirm the simple formulas experimentally. Crossfield may cause compass error up to 2.6 deg., depending on the compass orientation. The most effective way to suppress the crossfield error is using magnetic feedback, however this is not always possible. We suggest a method of processing of the SET/RESET sensor outputs which is more efficient than the usual averaging.

***Index Terms*—AMR, crossfield sensitivity, magnetic sensors, magnetoresistance.**

I. Introduction

CROSSFIELD effect (or crossfield error) is defined as an unwanted non-linear sensitivity to small fields perpendicular to the sensing direction [1]. This effect can be found in any sensor containing ferromagnetic material. While in fluxgate this error can be minimized by proper design, for AMR sensors the crossfield sensitivity is their inherent property, as it is caused by the basic sensor principle.

If the crossfield is large, it causes irreversible changes: in case of AMR, the single domain state is broken and the anisotropy dispersion occurs [2]. We do not consider this situation in this paper.

We also do not speak about the linear part of the crossfield sensitivity: it can be easily corrected by rotating the sensor. Nonlinear dependence effectively means that one cannot find a universal "insensitive" direction as such direction is field-dependent. The first widely published technical description of this problem was made by Pant and Caruso [3]. The problem is serious: for a sensitive AMR used in magnetic compass a maximum crossfield error in the Earth's field is 1100 nT, which may cause an azimuth error of 2 degrees [4]. Some manufacturers reacted to this challenge by changing the design. By increasing anisotropy field they reduced the crossfield error, but also decreased the sensor sensitivity and thus degraded the noise performance. In this paper we will show that crossfield error is easy to understand and we also discuss methods on how to suppress or eliminate this error without compromising the other parameters of AMR sensor.

The simplified formula for the sensor output is [3]:

$$V_1 \approx \frac{H_y}{H_x + H_0} \tag{1}$$

where H_y is the measured field, H_x is the crossfield, and H_0 is the anisotropy field.

This formula shows that the effect is not present if $H_y = 0$.

We will show how (1) is derived and what are the simplifications leading to this formula. But before that we will show the influence of the crossfield error on AMR compass.

Manuscript received March 06, 2009. Current version published September 18, 2009. Corresponding author: P. Ripka (e-mail: ripka@fel.cvut.cz).

Color versions of one or more of the figures in this paper are available online at http://ieeexplore.ieee.org.

Digital Object Identifier 10.1109/TMAG.2009.2022051

II. Compass Error Caused by Crossfield

Small and low-cost magnetic compasses are required for cars, ships and mobile devices. Digitally gimbaled compass is using three-axial magnetic sensor and information about actual roll and pitch of the device to calculate azimuth in every position. Precise compass devices usually use classical fluxgate sensors, which are quite large, expensive and power consuming. There are many commercially available compass systems with AMR sensors and inclinometers, but these systems usually have azimuth error of a few degrees. More sophisticated AMR compasses have integrated compensation of offset and sensitivities of individual sensors as well as their angular misalignment. As there are usually six sensors (three magnetic sensors and three accelerometers) in the system, the calibration and error correction algorithm is rather complicated [5]. We suppose that the mentioned errors are compensated and we concentrate on the effect of the crossfield error.

In our application example we use Honeywell HMC 1001 sensor with $H_0 = 1000$ A/m (i.e., $B_0 = 800$ μT). We can estimate the influence of crossfield error using (1).

If we use horizontally aligned two-axial compass at equator, where the horizontal component of the Earth's field is approx. 50 μT, the crossfield causes maximum azimuth error of 2.4 deg. In arbitrary position this error can reach 2.5 deg [4], [6].

III. The Origin of the Simplified Formula

We will try to review how (1) was derived in order to find out which simplifications were made.

Let us suppose an ideal single-domain magnetically soft AMR strip having uniaxial anisotropy with easy direction x and effective field of H_0. We assume only coherent rotation of magnetization.

Let us consider a crossfield H_x present simultaneously to the measured field H_y. For the total energy density of a single domain of anisotropic material in the magnetic field H we may write

$$E = E_A + E_H = \frac{1}{2}\mu_0 M_S H_0 \sin^2\varphi - \mu_0 M_S H \cos\alpha \tag{2}$$

where M_s is the saturation magnetization, α is an angle between the magnetization M_s and external field $H = (H_x, H_y)$ and φ is an angle between the magnetization M_s and easy direction x.

In order to find the energy minimum we solve the equation $\mathrm{dE}/\mathrm{d}\varphi$ and if the external field H is much smaller than the anisotropy field: $|H_\mathrm{x}|, |H_\mathrm{y}| \ll |H_0|$ we will find [2]

$$\sin\varphi = \frac{H_y}{H_x + H_0}. \tag{3}$$

The resistance in x direction is calculated, e.g., in [2]

$$R(H_Y) = R_0 + \Delta R\left[1 - \left(\frac{H_Y}{H_x + H_0}\right)^2\right] = R_0 + \Delta R\cos^2\varphi. \tag{4}$$

Using Barber poles the resistance equation becomes

$$R = R_0 + \Delta R\cos^2(\varphi + 45°) \tag{5}$$

from that we will derive the following formula for the strip resistance:

$$R = R_0' + \Delta R\frac{H_Y}{H_x + H_0}\sqrt{1 - \left(\frac{H_y}{H_x + H_0}\right)^2} \tag{6}$$

where

$$R_0' = R_0 + \frac{\Delta R}{2}.$$

For $|H_\mathrm{x}|, |H_\mathrm{y}| \ll |H_0|$ we finally arrive to

$$R = R_0' + \Delta R\frac{H_Y}{H_0} \qquad V_1 \approx \frac{H_y}{H_x + H_0}. \tag{7}$$

IV. Methods to Eliminate the Crossfield Sensitivity

A. Feedback Compensation

From (1) it is clear that there is no response to crossfield H_x when the measured field H_y is zero. That is why the crossfield sensitivity is erased by feedback compensation of the measured field. The limitation of this approach is the homogeneity of the compensation field, which is questionable for flat compensation coil used in case of integrated sensors. However practically achieved linearity of the feedback-compensated KMZ51 was 0.1%, which is sufficient for most applications [7].

Other drawbacks of compensation include increased power consumption and decreased bandwidth.

Ideal compensation is to completely remove the total field. For 3-axial magnetometers this can be achieved by using external 3-axial compensation coil [8], however such solution is very expensive.

B. Increasing H_0

We already mentioned that increasing H_0 improves the linearity in uncompensated mode, and reduces crossfield effect, but decreases sensitivity. H_0 is an effective anisotropy field, which is a result of both shape anisotropy and induced anisotropy. Thus we can change H_0 by changing the strip thickness or by magnetic field annealing. The price we pay for this solution is an increase of the sensor noise (in the magnetic field units) which is proportional to the decrease of the sensitivity. Thus in general this solution is effective only for low-end sensors.

C. Numerical Correction in Multi-Axial Systems

From the readings of two perpendicular sensors which measure H_x and H_y we can calculate corrected field values supposing that we know the value of H_0. The equation has no analytical solution, but it can easily be solved numerically. The procedure is in detail described in [3]. The only problem is the knowledge of H_0. It is not easy to measure it, but fortunately the sensitivity to this parameter is not critical [4].

D. Crossfield Suppression by Flipping and Averaging

After flipping (i.e. reversing the remanent magnetization of the AMR strip) the output voltage is changed from V_1 to V_2:

$$V_2 \approx \frac{H_y}{H_x - H_0}. \tag{8}$$

Standard technique used in AMR magnetometers is to sample V_1 and V_2 and subtract them still in the analog form. The resulting voltage V is then

$$V \approx \frac{H_y}{H_x + H_0} - \frac{H_y}{H_x - H_0} = \frac{-2H_yH_0}{H_x^2 - H_0^2}. \tag{9}$$

The sensitivity of V to the crossfield H_x is largely reduced, as H_x is typically much lower than H_0.

Using this technique, the residual error in our example (HMC 1001 in $\mathrm{B} = 50\ \mu\mathrm{T}$ for the measured field $\mathrm{B_y}$ of 20 μT) was reduced from 1000 to 100 nT [6].

E. Separate Processing of V_1 and V_2

We proposed a simple original method to directly calculate both H_y and H_x (if we know H_0) [9]:

$$\text{for } \mathrm{V}_1 \neq \mathrm{V}_2 : H_x \approx H_0\frac{(V_1 + V_2)}{(V_1 - V_2)},\ H_y \approx \frac{2H_0(V_1 \cdot V_2)}{(V_2 - V_1)}$$
$$\text{for } \mathrm{V}_1 = \mathrm{V}_2 : H_\mathrm{y} = 0.$$

Using this method the crossfield effect is suppressed much more effectively. The uncertainty of estimation of both H_y and H_x is not the same. For practical values of the anisotropy field H_0 the sensitivity to H_y is much higher than sensitivity to H_x. The uncertainty of H_x caused by the magnetic noise depends on H_y. In the best case the H_x noise for HMC 1001 is 16-times higher than noise for H_y—approximatelly 80 nT p-p. In the worst case we cannot measure H_x when H_y is zero ($\mathrm{V}_1 = -\mathrm{V}_2$). However, this novel method can be used for simple compass applications and also in two- and three-axial systems to effectively correct for the crossfield error.

This method can be used only for AMR sensors with medium or low value of H_0, such as Honeywell HMC 1001 ($H_0 = 0.8\ \mathrm{mT}$) and it is limited to the environment with low magnetic noise.

F. Flipping in Multiaxial Systems

Flipping can also be used for numerical correction in multiaxial sensor systems. Pant and Caruso have shown that flipping and averaging V_1 and V_2 in two-axial or triaxial system leads to much faster iterations during the finding of H_y [3]. Also this

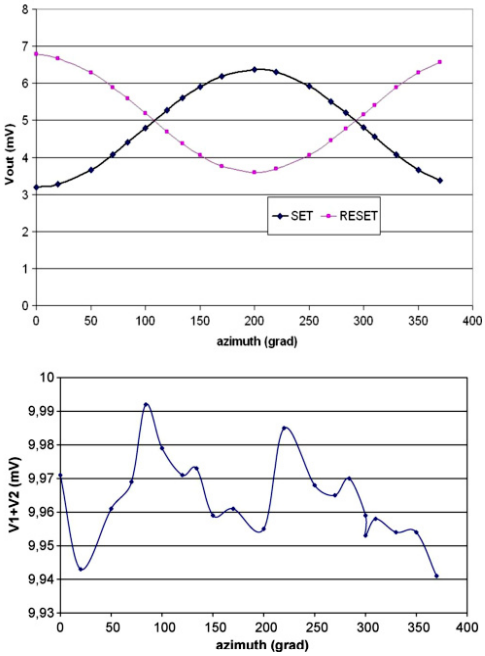

Fig. 1. (a) KMZ 51 sensor V_1 (SET) and V_2 (RESET) outputs for rotation in the horizontal plane. (b) KMZ51—$V_1 + V_2$ as a function of azimuth.

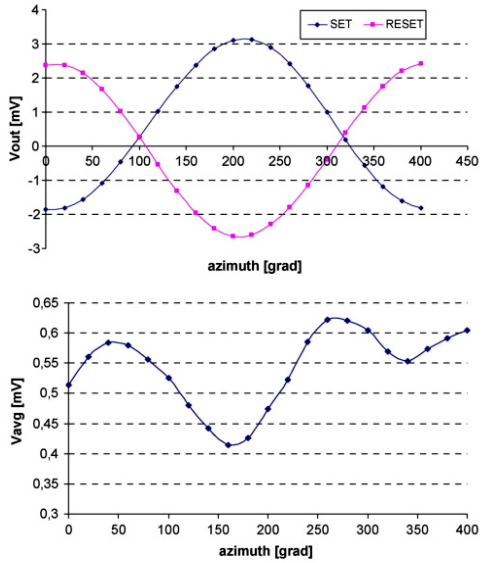

Fig. 2. (a) HMC 1001—V_1 (SET) and V_2 (RESET) outputs for rotation in the horizontal plane. (b) HMC 1001: $V_{avg} = V_1 + V_2$ as a function of azimuth.

method requires complex numerical processing and knowledge of H_0. However, if we do not average but process V_1 and V_2 for each sensor, we have 6 equations and we need no apriori information about H_0.

G. Using Redundant Sensors

We can use 6 sensors in 3-axial AMR magnetometer: XY, YX, XZ, ZX, YZ, ZY. The first letter denotes the sensing direction, the second letter denotes the crossfield direction. Two letters define the plane in which the sensor chip is mounted. Even without flipping we obtain 6 equations which allow us to compensate for the crossfield error without the knowledge of H_0. When flipping we can increase the number of equation to 12. Increasing the number of sensors also increases the complexity of the mentioned scheme for the compensation of angular misalignments.

V. Experimental Verification

Fig. 1(a) shows the output voltages V_1 and V_2 as a function of azimuth, measured for Philips KMZ 51 AMR sensor which is used as one axis in magnetic compass. If $V_1 - V_2$ value is used, the deviation from sinewave caused by the crossfield effect is practically invisible. However it may cause up to 1 grad compass error. $V_1 + V_2$ value is normally considered to be a sensor offset, which is partly suppressed by flipping procedure. However, if we measure this value as a function of azimuth for a compass sensor rotating in the Earth's horizontal field of 20 000 nT (Fig. 2(b)), we observe a double-peak waveform confirming the simplified formulae (1) and (8). The observed p-p variation of 50 μV corresponds to 274 nT. Using the simplified formulae this variation gives a rough estimate of $H_0 = 3.2$ mT for this sensor.

Fig. 2(a) shows V_1 (SET) and V_2 (RESET) outputs of Honeywell HMC 1001 sensor (bridge current 6 mA) rotated in azimuth. Together with the $V_1 + V_2$ function in Fig. 2(b), it indicates smaller value of H_0 than in KMZ51—this corresponds well with $H_0 = 0.8$ mT measured in [4].

In Fig. 3(a), the cross-axis direction of HMC1001 is oriented upwards, so that Hx is in the rotation axis and therefore constant, Hx $= 40$ μT. In agreement with derived equations the V_1 and V_2 responses are sinewaves with only slightly different amplitudes. $V_{diff} = V_1 - V_2$ in this case is close to sinewave (Fig. 3(b)), according to (9). Here we can conclude that the design of HMC 1001 is on the limit of linear AMR sensors: H_0 is only 16-times higher than the Earth's field.

VI. Conclusion

In this paper we analyzed the crossfield sensitivity of barberpole AMR sensor. Crossfield sensitivity of unbiased AMR elements can also be utilized to measure field in two directions [10].

The measured results confirm the fact that in small field region, for which the single-domain structure of the AMR sensor is not broken, simple formulas for crossfield response are valid.

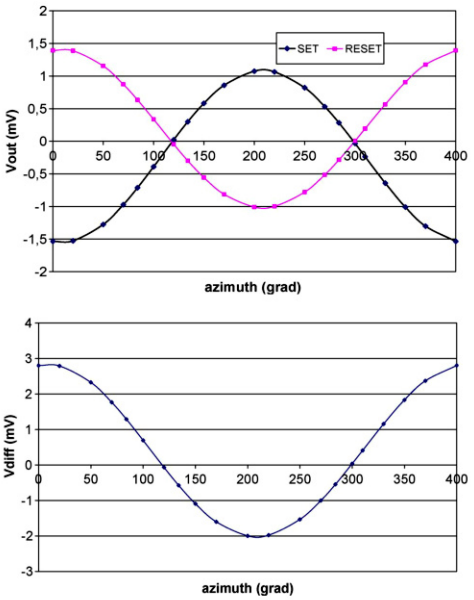

Fig. 3. (a) HMC-1001 sensor's V_1 (SET) and V_2 (RESET) outputs for rotation around the crossfield axis x, which was pointing upwards. Notice that for this measurement the sensor was oriented differently than for Figs. 5 and 6. (b) HMC-1001: $\mathrm{Vdiff} = V_1 - V_2$ as a function of rotation around crossfield axis.

We have shown that separate processing of the V_1 and V_2 voltages instead of simple averaging leads to more efficient correction of the crossfield error. This is easy in digital magnetometers such as [11]. However, if field compensation is possible, such processing is not necessary.

It would be desirable to design more sensitive AMR sensors. One of the possible approaches would be to decrease H_0. Such sensor would no longer be linear and would have a large crossfield sensitivity, but both these errors can be easily compensated or corrected.

ACKNOWLEDGMENT

This work was supported by the research program No. MSM6840770015 sponsored by the Ministry of Education, Youth and Sports of the Czech Republic.

REFERENCES

[1] P. Ripka, *Magnetic Sensors and Magnetometers*. Boston, MA: Artech, 2001.
[2] S. Tumanski, *Thin Film Magnetoresistive Sensors*. New York: IoP Pub., 2001.
[3] B. B. Pant and M. Caruso, Magnetic Sensor Cross-Axis Effect, AN 205 Honeywell.
[4] J. Kubik, J. Vcelak, and P. Ripka, "On cross-axis effect of the anisotropic magnetoresistive sensors," *Sens. Actuators A*, vol. 129, pp. 15–19, 2006.
[5] J. Včelák, P. Ripka, A. Platil, J. Kubík, and P. Kaňpar, "Errors of AMR compass and methods of their compensation," *Sens. Actuators A*, vol. 129, pp. 53–57, 2006.
[6] P. Ripka and M. Butta, "Origin of the crossfield effect in AMR sensors," presented at the EMSA 2008 Conf., to appear in *Sensors Lett.*.
[7] M. Vopálenský, P. Ripka, and A. Platil, "Precise magnetic sensors," *Sens. Actuators A*, vol. 106, pp. 38–42, 2003.
[8] F. Primdahl and P. A. Jensen, "Compact spherical coil for fluxgate magnetometer vector feedback," *J. Phys. E: Sci. Instrum.*, vol. 15, pp. 221–226, 1982.
[9] P. Ripka and M. Janosek, "Crossfield sensitivity in AMR sensors and its compensation," in *10th Symp. Magnetoresistive Sensors and Magnetic Systems*, Wetzlar, 2009.
[10] B.-Z. Kaplan, E. Paperno, and D. Flunn, "In-plane vector magnetometer employing a single unbiased magnetoresistor," *IEEE Trans. Magn.*, vol. 34, pp. 253–258, 1998.
[11] A. Bertoldi, D. Bassi, and L. Ricci *et al.*, "Magnetoresistive magnetometer with improved bandwidth and response characteristics," *Rev. Sci. Instrum.*, vol. 76, p. 065106, 2005.

5.2 Crossfield response of a race-track fluxgate sensor

For fluxgate sensors, the error depends on the structure of the sensor [Ripka 2000b] – a negligible effect was measured for rod-core Vacquier sensors. The crossfield error of tape-wound sensors depends on the field direction: the demagnetization factor of the tape differs for perpendicular and transverse directions**.** However, as was shown in the following article, in the case of a single-sheet, etched magnetic core, the demagnetization factor parallel to the core is very low and the effect is therefore much more pronounced in this case. The response of early printed circuit board sensors with etched cores was studied by [Kubík 2006].

The following article *"Two sources of crossfield error in race-track fluxgate"* [J8], was published in Journal of Applied Physics in 2010. The article describes the measurements with PCB race-track sensors the author carried out and addresses the origin of the large crossfield response. The fluxgate was attached to a non-magnetic theodolite and two Helmholtz coils were used to create the main and perpendicular fields. The high response shown in the article can be improved – we have shown in agreement with [Auster 2000] that it can be decreased by better alignment of the sensor core and coil, and also by modifying the time-domain processing of the fluxgate output signal.

The final crossfield response of the PCB fluxgate, shown in Fig. 5.2 was not presented in the article (the data was not available at the time of paper submission) but was published later in Journal of Electrical Engineering however with inferior graphic quality [R2]. The measurements were carried out in the "Magnetsrode" magnetic calibrating facility of TU Braunschweig, Germany with the kind help of Dr. Ingo Richter. The possibility to cancel the Earth's magnetic field and apply a synthetic magnetic field was used. The result confirmed the high crossfield response for the in-plane direction, presented in the article below [J8].

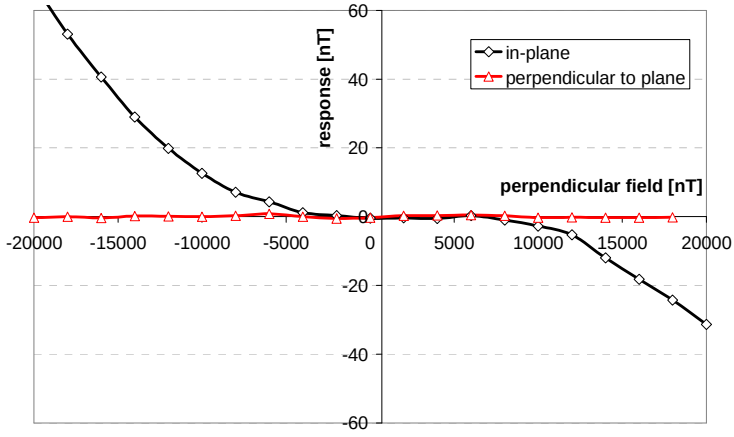

Fig. 5.2 – Crossfield response of the PCB fluxgate, from [R2]

JOURNAL OF APPLIED PHYSICS **107**, 09E713 (2010)

Two sources of cross-field error in racetrack fluxgate

M. Janosek,[a] M. Butta, and P. Ripka
Department of Measurement, Faculty of Electrical Engineering, Czech Technical University in Prague, Technicka 2, 166 27 Praha, Czech Republic

(Presented 21 January 2010; received 31 October 2009; accepted 17 November 2009; published online 30 April 2010)

This contribution covers cross-field response of fluxgate sensors with a flat, single-sheet race-track core, which to our knowledge has not been studied yet. In the case of race-track shape, it was commonly believed that the error is automatically lower than for the ringcore due to the shape anisotropy. Instead we observed that the exact geometry of the race track (i.e., ratio between the longitudinal and upright section) and the position of the coils start to play a significant role, not only the core homogeneity—there is no more symmetry as in the case of a ring core. We found the cross-field response dependent on defining the perpendicular angle, either to the sensor's core axis or to the axis of the feedback coil; these two axes were misaligned by up to 1°. When arranging the cross field to be perpendicular to the feedback coil axis, we were able to verify results previously published in literature: we obtained 60 nT response for 50 μT cross-field. © *2010 American Institute of Physics*. [doi:10.1063/1.3337721]

I. INTRODUCTION

The cross-field effect (or transverse-field effect) in magnetic sensors is described in literature as an unwanted sensitivity or linearity error due to fields perpendicular to the sensor's sensitive axis. In the case of anisotropic magnetoresistors, the effect is now well understood[1,2] and may be suppressed by operating in feedback loop (field in the sensitive axis is zero). However in fluxgate sensors, the error is still present even in feedback loop and can be effectively suppressed only by vectorial compensation.[3,4]

The cross-field effect of fluxgate sensors was first observed in 1980s, later Brauer[5] identified the core in nonhomogeneity as the possible error source for ring-core fluxgates. Brauer described the cross-field error as a residual nonlinearity of the sensor, which reached ±5 nT for ±50 μT cross field. Ripka and Billingsley[6] described the cross-field effect of a race-track fluxgate also as a quadratic decrease in sensor's sensitivity. While Vacquier sensors are by nature almost free of such an error due to their large shape anisotropy (the cross-field response is lower than measurement uncertainty), sensors with race-track core should theoretically combine advances of both designs. In this case, it was commonly believed that the error can be lower than for the ring core due to the shape. On the contrary, we observed that the geometry of the race track (i.e., ratio between the longitudinal and upright sections) and the position of the coils start to play a significant role—there is no more symmetry as in the case of a ring core (Fig. 1).

We therefore started to investigate the cross-field error of fluxgate sensors with a race-track core ($34\times16\times0.9$ mm^3), consisting of one sheet Vitrovac 6025x amorphous material, encapsulated in a printed-circuit board (PCB).[7] The signal processing used gated integrators and the sensors were operating in the feedback loop. It is worth to notice, that the pick-up coil served also as a feedback coil.

II. SYSTEM SETUP

We placed the race-track, PCB fluxgate on an iron-free theodolite (50 cc accuracy) in a dual-axis Helmholtz coils system: the X-axis served for generating the cross-field, the Y-axis for simulating different operating conditions (actual measured field)—Fig. 2. We tried two approaches to find the perpendicular position.

A. By using the sensor's pick-up coil as a search coil

We applied a low-frequency (to avoid eddy currents in the core) ac field and measured the response in two different angles, read on the theodolite (e.g., 10° and 45°). From the cosine dependence giving a set of two equations, it was possible to calculate the main and perpendicular angle. The other approach was to find with a lock-in amplifier the sign threshold of the rectified output voltage, indicating the zero crossing. The latter method provided repeatable results, however we observed following effect: when the core was saturated by a dc field provided by injecting dc current into the

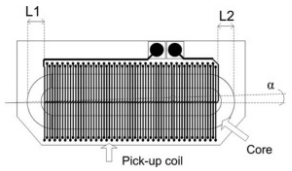

FIG. 1. PCB fluxgate sensor—depicting the geometric aspects: angular difference between core and coil axis (α) and longitudinal shift (L1 ≠ L2). The upright sections of the core are clearly visible as not covered by the pick-up/compensating coil.

[a]Author to whom correspondence should be addressed. Tel.: + (420) 2 2435 3964. FAX: +(420) 2 3333 9929. Electronic mail: janosem@fel.cvut.cz.

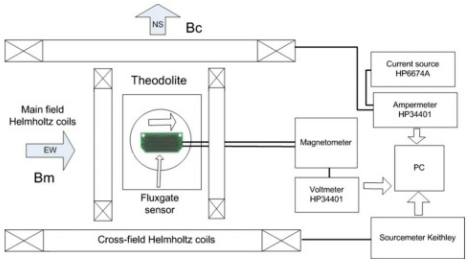

FIG. 2. (Color online) Measurement setup used for determining the cross-field response. Sensor (not to scale) shown having the main-field Bm in sensitive direction and the cross-field Bc in perpendicular direction.

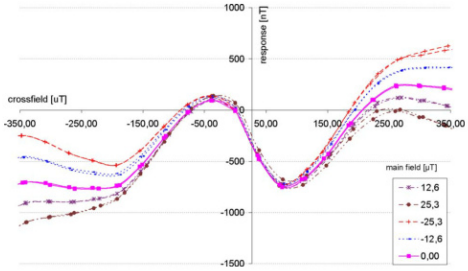

FIG. 3. (Color online) Cross-field response (perpendicular direction to the sensor core) shown for five different fields in main direction, offset due to main field removed.

excitation coil, the perpendicular angle was changed by 0.8°–1.5°, depending on the respective sensor. We explain this difference as a direct result of angular misalignment between the axes of the core and the pickup coil (Fig. 1).

B. By measuring the response of magnetometer with respective sensor

We measured the dependence of the fluxgate magnetometer output voltage on sweeps of the perpendicular field while rotating the sensor along the horizontal axis. For deviations from the sensitive axis other than 90°, the sensitivity is ≠0 and changes the sign with crossing the perpendicular direction. Finding the zero-crossing point of sensitivity equals finding the perpendicular direction. The response is significantly changed even with 0.05° rotation measured by the theodolite. When taking into account broader (±300 μT) or narrower (±50 μT) range for determining the sensitivity, we obtain again the two perpendicular angles: one related to the effective core direction and the other to the compensating-coil direction. The perpendicular angle of the feedback-coil direction was approximately 1° less than of the core, simmilar as determined in method 1.

III. EXPERIMENTAL RESULTS

First, we measured the sensor linearity—the error was below ±2 nT in ±50 μT range—and then the sensor was rotated to the perpendicular direction to the core axis previously measured. The cross-field error in field units was several magnitudes larger than the sensor nonlinearity even for small perpendicular fields and was verified for three sensors and two measurement setups. The shape of the response for limited field is similar to a sinewave (Fig. 3), similar shape was presented in Ref. 6. However in this case, the magnitude of the error is huge (up to 1 μT for 100 μT cross field).

We have found that this was only an artificial result of measuring at the direction perpendicular to the core axis. When the sensor was moved to the perpendicular direction to the coil axis (−1°), the response resulted in approximately ±60 nT for ±50 μT cross field (Fig. 4). The same result was obtained, when the response from Fig. 3 was linearized around zero, and the linear part removed. The remaining near-zero sensitivity for small cross-field magnitudes (i.e., ±20 μT) has physical sense and is in a good agreement with results published in Ref. 5.

Brauer identified the cross-field response as a direct result of the core inhomogeneity, but we have to note that the ring core is geometrically symmetric with constant demagnetization factor in all directions. Although we obtained very similar shape of the response, we believe that its elevated amplitude is caused not only by the inhomogeneity of the sensor's core, but also by geometric imperfections (Fig. 1). These include the longitudinal shift and angular misalignment of the pick-up/feedback coil: if the contribution of the upright sections is asymmetric (shifted pick-up coil), also the cross-field response is asymmetric. Angular misalignment alone brings symmetric cross-field response. This was demonstrated in Fig. 3; the compensating field, which was not in the direction of the perpendicular field, caused the sinewave-like response of the sensor. It was a direct measure of the misalignment from perpendicular direction of the compensating-coil axis.

However, it should be stated that the material inhomogeneity will be in this case several times larger as for wound cores in Refs. 5 and 6—the sensor core consists of one sheet of the 25 μm material and thus the material imperfections cannot be averaged out as in the tape-wound ones.

We also expressed the cross-field error as a change in the sensitivity of the fluxgate sensor—Fig. 5—and found it with

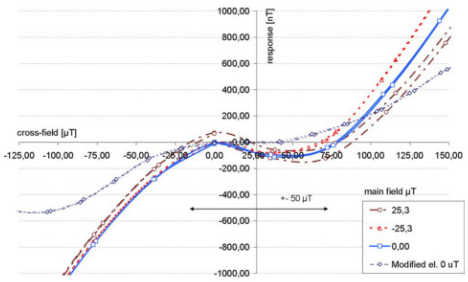

FIG. 4. (Color online) Cross-field response (perpendicular direction to the pick-up coil) shown for three different fields in main direction, and also for modified detection electronics (thin trace).

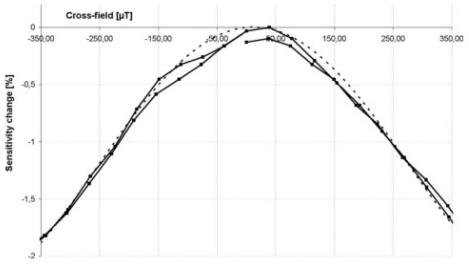

FIG. 5. The same data as in Fig. 3, but expressed as sensitivity change on applied cross-field.

a good agreement with results in Ref. 6. For calculation, the same data as in Fig. 4 were used; sensitivity was calculated for every change in cross-field, knowing the changes in the main field. The result in Fig. 5 shows a 0.4% sensitivity decrease for ± 100 μT cross-field range.

IV. SUPPRESSION OF THE CROSS-FIELD RESPONSE

We increased the excitation amplitude (from 550 mA pp) and did not notice any significant difference, indicating that the sensor's core was saturated enough. We also used modified method of signal extraction, where only one part of the voltage pulse (during the switch on and on time of excitation current) was used. This approach resulted in decreased sensitivity of the magnetometer, however, when recalculated to the field units, decreased also the cross-field response (Fig. 4—last trace). Numerical compensation would also be possible, as we obtained for several sensors of the same series similar response. As there is huge difference in the behavior of the response being 1° off the main axis (cf. Figs. 3 and 4), even perfect suppressing the perpendicular field would not help: any field 1° off would case different response. Modeling the cross-field response is due to this nature difficult, therefore is not presented in this paper. However, the model presented by Brauer is by comparison valid for the perpendicular direction of the feedback coil. This means that the response may be further suppressed by proper geometrical configuration: separating the pick-up and feedback coils, while shortening the pick-up one (not to cover the upright sections of the core); and also enlarging the compensation coil to assure homogeneous compensating field in the whole core volume. For sensors with larger ratio of the longitudinal/upright branches of the race-track core (in this case 1:7), the response is expected to be lower; this was confirmed experimentally for 10-cm-large fluxgate sensor, derived from presented one, with a ratio of 1:10.

V. CONCLUSION

We directly measured the cross-field response of race-track fluxgate sensors and found a good agreement with previously published results. However, for slight deviation from the perpendicular direction of the pick-up coil (1°), the difference in the response is dramatic. We believe to have identified the source of this difference experimentally as geometric imperfections of the sensor's configuration—its core and pick-up coil misalignment. The cross-field response of a flat, pulse-excited PCB race-track fluxgate sensor was lower than 60 nT for 50 μT cross-field applied and with modified signal extraction, we lowered this response at elevated cross fields.

ACKNOWLEDGMENTS

This work was supported by the Grant Agency of Czech Republic, Grant No. 102/08/0743, "Fluxgate effect in thin layers."

[1]J. Kubik, J. Vcelak, and P. Ripka, Sens. Actuators, A **129**, 15 (2006).
[2]P. Ripka, M. Janosek, and M. Butta, IEEE Trans. Magn. **45**, 4514 (2009).
[3]F. Primdahl andP. A. Jensen, J. Phys. E: J. Sci. Instrum. **15**, 221 (1982).
[4]H. U. Auster, K. H. Glassmeier, W. Magnes, O. Aydogar, W. Baumjohann, D. Constantinescu, D. Fischer, K. H. Fornacon, E. Georgescu, P. Harvey, O. Hillenmaier, R. Kroth, M. Ludlam, Y. Narita, R. Nakamura, K. Okrafka, F. Plaschke, I. Richter, H. Schwarzl, B. Stoll, A. Valavanoglou, and M. Wiedemann, Space Sci. Rev. **141**, 235 (2008).
[5]P. Brauer, J. M. G. Merayo, O. V. Nielsen, F. Primdahl, and J. R. Petersen, Sens. Actuators, A **59**, 70 (1997).
[6]P. Ripka and S. W. Billingsley, Sens. Actuators, A **81**, 176 (2000).
[7]M. Janošek and P. Ripka, Sens. Actuators, A **151**, 141 (2009).

6 A PCB fluxgate gradiometer

6.1 PCB fluxgate sensors

The author developed the printed-circuit board (PCB) fluxgate sensor used in the gradiometer [J20] – see Fig. 6.1. It exhibits 1-Hz noise of 20 $pT \cdot Hz^{-0.5}$ (higher than incorrectly stated in [Janošek 2007]), and the sensor size is $30 \times 8 \times 1$ mm^3. Due to the low thickness of the sensor (Fig. 6.2), a $\partial B_i/\partial j$ type gradiometer with a very small gradiometric base can easily be constructed. Square-wave pulse excitation [Kubík 2005] is used to keep power consumption low - excitation tuning [Ripka 2002] is not possible because of the poor quality factor of the excitation coil (low inductance and high resistance). The detection electronics relied on gated-integrators [Kubík 2007]. The sensitivity of PCB fluxgates is low, approx. $70\ V \cdot T^{-1}$ at 10 kHz excitation frequency [J20]. It is limited by the core cross-section and by the number of pickup-coil turns. This in turn results in low SNR at the demodulator, even with a low-noise pre-amplifier

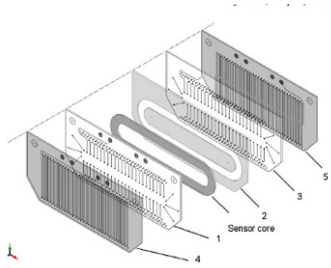

Fig. 6.1 – Structure of the PCB fluxgate - from [J17]

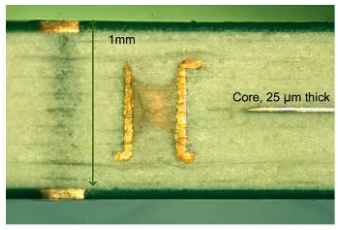

Fig. 6.2 – PCB fluxgate vertical cut – the magnetic core can be seen, and also the excitation and pick-up through-hole vias.

In fluxgates with wire-wound sensors, the so-called current-output is used mainly to suppress the pick-up coils capacitances, allowing for longer cabling to the sensors and to increase sensor stability – the pick-up coil is effectively short-circuited. Also, a simplified phase-sensitive detector with gated integrators can be used [Primdahl 1991]. As a result, using the current-output in PCB fluxgates can improve the SNR due to their low pick-up coil resistance.

The next article *"Current-Output of PCB fluxgates"* [J10] was published in Sensors Letters in 2009 after presenting at the EMSA 2008 conference as a majority work of the author. The low resistance of the pick-up coil was found as an advantage in current-output mode providing sufficient SNR as shown in the article. The noise of the PCB fluxgates however did not improve. In our case, the noise was of magnetic origin– it is inherent to the design where the magnetic core is under mechanical stress caused by the manufacturing process of bonding the five PCB layers together – see Fig. 6.2.

SENSOR LETTERS
Vol. 7, 1–4, 2009

Current-Output of PCB Fluxgates

M. Janosek[1,*] and P. Ripka[1]

[1] *Faculty of Electrical Engineering, Department of Measurement, Czech Technical University in Prague, Technicka 2, 166 27 Praha, Czech Republic*

(Received: 19 February 2008. Accepted: 1 February 2009)

Current-output mode of PCB fluxgate sensors is presented. As the short-circuited output current sensitivity is inversely proportional to the number of turns of the pickup coil, PCB fluxgates should perform well in this mode. In order to avoid serial tuning of the sensor's output, sufficiently large series capacitor must be used mainly for pickup-coils with very low impedance. The sensitivities (with sinewave excitation and 2nd harmonic detection) have been found as 32 and 86 A/T for sensor IIIA and IIB, respectively. The noise values remain the same as in the voltage mode; however the linearity of the uncompensated sensor shows differences from the voltage mode. Sensor IIB with pickup-coil covering only one third of racetrack length (centred) showed improvement from 0.5% in voltage mode to 0.23% in the current-output mode. Sensor IIIA with long pickup-coil covering also the core ends has good linearity in the voltage mode (0.3%), however in the current-output regime it was worsened down to 3.5% nonlinearity of 100 μT full-scale.

Keywords: Current Output, Fluxgate, PCB, Sensor.

RESEARCH ARTICLE

1. INTRODUCTION

Fluxgate sensors can be made very temperature stable and resistant against other environmental influences including vibrations and radiation.[1,2] PCB (Printed Circuit Board) fluxgate sensors are, due to low-cost manufacturing and miniature design, promising alternative to classical fluxgate sensors with wire-wound coils.[3] PCB design creates solenoids by the use of two metallic layers connected by vias. This design can be further miniaturized by using microtechnology.[4,5] The main advantage of solenoid coils compared to flat coils is much better coupling with the sensor core—thus the excitation efficiency and sensitivity are much higher.[6] However, miniaturization results in low number of turns of the pickup coil, which decreases voltage sensitivity, compared to classical wire-wound fluxgate sensors.[7]

The low number of turns should be an advantage in the current-output mode of the sensor, as introduced in Ref. [8]. As the output current is inversely proportional to the number of turns of the pickup winding, limited only by the winding resistance, PCB fluxgates should be ideal candidates for short-circuited, current-output mode of operation. Another advantage would be integrating the current-to-voltage converter directly on the sensor, which would allow driving long, shielded cables with no impedance and interference problems of the sensor's output. Sensitivity and noise parameters can be further improved by using serial-tuning of the pick-up coil,[8] however it was not considered in this paper.

Two race-track PCB fluxgate sensors developed at our department have been used in order to compare the achieved results. Race-track shape shows better sensitivity compared to classical ring-core[12] and we are using amorphous core material with much better magnetic properties than any electrodeposited permalloy.[11] Two-layer sensor IIB[15] has pickup coil with 37 turns, located in the middle of the sensor (shown in Fig. 1). Four-layer sensor IIIA has pick-up coil with 68 turns, covering the whole length of the sensor.

2. CURRENT-OUTPUT MODE

2.1. Principle of Operation

The current-output mode together with calculations of the output current has been described by Primdahl.[9] The output current is there handled as equivalent coil current, which would create field equal to the measured one:

$$B_{eq} = \mu_0 \frac{N}{l} i_{eq} \quad (1)$$

*Corresponding author; E-mail: janosem@fel.cvut.cz

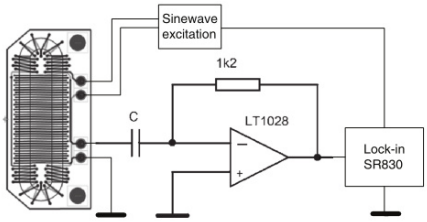

Fig. 1. Block diagram of current-output operation.

The real measured output current will have always an error mainly caused by the non-zero resistance of the pick-up coil. The non-zero input impedance of the current-to-voltage converter is of the minor importance. Another source of error is the fact that the B_{eq} field is non-homogenous. The resistance of the pickup-coils varies according to PCB technology used (2 or 4 layers, track widths and diameters of through-hole vias). For sensor IIIA, it was measured as 4.8 Ω, while sensor IIB with lower number of turns and only 2 PCB layers with wider tracks had 1.48 Ω pickup coil resistance.

As we used sinewave excitation, the model described by Primdahl for pulse excitation was not in a good agreement with the experimental results. We presently work on a Matlab model based on the circuit equation and simplified hysteresis curve for Vitrovac6025x; preliminary results show a good agreement with the measurements. Existing models of this type describe only voltage output.[13]

2.2. Experimental Setup

The pick-up coil of the fluxgate sensor was short-circuited by a current-to-voltage converter consisting of single operational amplifier (Fig. 1). The resulting voltage swing is then proportional to the feedback resistor. Series capacitance is necessary to cut the path for the DC and low-frequency input bias current, which could affect the sensor offset and also influence the noise parameters. The input current noise, which has flicker character, would create equivalent noise field in the pickup coil.

Two sensors—IIB and IIIA as described above have been used, in order to verify the inverse proportionality between number of turns and current-output sensitivity. The sensors were excited with 10 kHz sinewave current of 350 mA p–p, which was previously verified as the best mode of operation in sinewave mode.

The output of the I/V converter was led to lock-in amplifier SR-830 and the 2nd harmonic detection has been used. The resulting current-waveform is shown in Figure 2 for sensor IIB. In order to observe true current waveform related to the external field, it was necessary to numerically correct for two applied field magnitudes, opposite in sign. As the peak–peak current is exceeding 20 mA for 60 μT

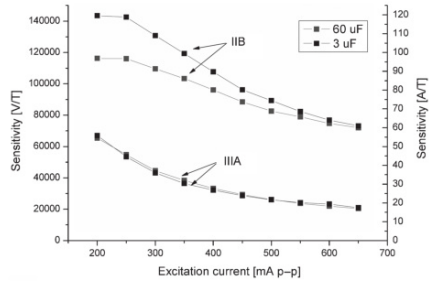

Fig. 2. Sensitivity of PCB fluxgates versus excitation current and series capacitance.

applied field, we had to replace the feedback resistor in the I/V converter for smaller value of 510 Ω in order to reduce the excessive voltage swing and corresponding power losses of the operational amplifier. Further, the larger resistance also caused nonlinearity problems for large input currents.

3. RESULTS AND DISCUSSION

3.1. Sensitivity

We found the sensitivity decreasing with the excitation current (Fig. 3). This dependence is related to the changes of the current waveform; however, sensitivity is often not the most important parameter: larger excitation current decreases sensor perming. The sensitivity also depends on the series capacitor used, as it can cause serial output tuning—this is the case of sensor IIB with low impedance of the pickup-coil, where sufficiently large capacitance (51 μF) has to be used. The sensitivity at 350 mA p–p was 32 A/T for sensor IIIA and 86 A/T for sensor IIB, respectively (Table I). The number of turns of sensor's IIIA pickup-coil (68) is 1.8-times higher than of sensor IIB, however the sensitivity increased for IIB more than

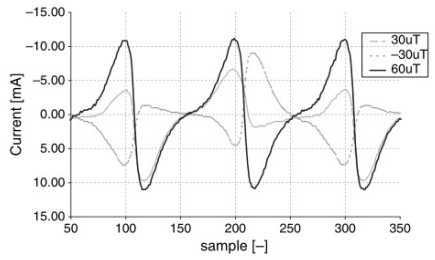

Fig. 3. Output current waveforms, as measured for ±30 μT (containing sensor feedthrough), and true output for 60 μT derived as their difference.

RESEARCH ARTICLE

Table I. Comparison of V and I mode for PCB fluxgate sensors IIB and IIIA.

	Voltage		Current	
Mode:	Sensitivity [V/T]	Nonlinearity [ppm FS]	Sensitivity [V/T]	Nonlinearity [ppm FS]
IIB	249	4830	86	2580
IIIA	750	3150	32	38500

2.6-times—this is mainly due to lower resistance of its pickup coil (1.48 Ω compared to 4.8 Ω for sensor IIIA).

3.2. Noise

Noise figures have been measured in 6-layer cylindrical shielding and using 35670A analyzer, in the range of 0.1–10 Hz, with Hanning windowing, 200-times averaging and 95% overlap. The noise parameters were similar to the voltage mode—for sensor IIB we measured 60 pTrms/$\sqrt{}$Hz @ 1 Hz (Fig. 5). The total band noise slightly decreased from approx. 900 pT down to 675 pTrms in the 0.1–10 Hz band. The current-to-voltage converter therefore did not introduce excessive noise. This noise level is lower than that of most of the orthogonal fluxgates of similar size. Only fundamental-mode orthogonal fluxgate described by Ref. [14] has a noise of 20 pTrms/$\sqrt{}$Hz. The mentioned sensor has however 600 turns of wire-wound coil and it has large temperature offset drift, moreover due to the nature of the operation the effect of perming is questionable.

3.3. Linearity

Linearity measurements gave interesting results—in the voltage mode, the sensor IIB was previously found less linear, than sensor IIIA. However, this was opposite in the current-output mode. Sensor IIIA with long pick-up coil and high number of turns (higher resistivity) worsened from 0.3% down to 3.8% nonlinearity of 100 μT

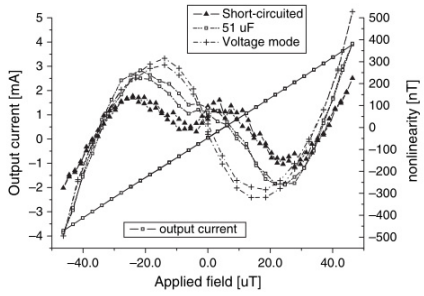

Fig. 4. Sensor IIB nonlinearities—voltage and current mode.

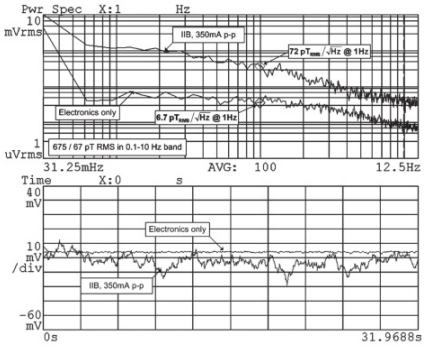

Fig. 5. Noise parameters of IIB (top trace) and electronics only (excitation disabled—bottom trace).

full-scale. On the contrary, the linearity error of sensor IIB (short pick-up coil in the middle, low resistance) dropped to one half: from 0.5% in voltage mode we achieved 0.25% in short-circuited mode (Fig. 4). For this sensor we also investigated the effect of output tuning with serial capacitor of 4 μF which was insufficient to short-circuit the pick-up coil—due to nonlinear nature of the output tuning, the linearity decreased down to 2.1%.

4. CONCLUSIONS

When considering current-output regime of PCB fluxgate sensors, we found that it can bring advantage in linearity for sensor with very low number of turns and short pick-up coil located in the middle of the core, where the nonlinearity was decreased to one half (0.23% compared to 0.5%). We found the sensitivity to be dependent on the excitation current. As the noise parameters remain unchanged and sensitivity is very high (consider voltage equivalent with 1200 Ohm which is 120 000 V/T in open loop for sensor IIB), the short-circuited mode can be advantageous mainly for miniaturized (PCB) fluxgate sensors, which can otherwise in voltage mode suffer from low number of turns and short pick-up coils in terms of linearity and sensitivity. The achieved parameters are sufficient for precise compass application of the PCB fluxgate sensors.[15]

Acknowledgments: This work was supported by the Grant Agency of Czech Republic, No. 102/08/0743.

References and Notes

1. Y. Nishio, F. Tohyama, and N. Onishi, *Meas. Sci. Technol.* 18, 2721 (**2007**).
2. H. O'Brien, P. Brown, T. Beek, C. Carr, E. Cupido, and T. Oddy, *Meas. Sci. Tech.* 18, 3645 (**2007**).

RESEARCH ARTICLE

3. O. Dezuari, E. Belloy, S. E. Gilbert, and M. A. M. Gijs, *Sens Act. A: Physical* 81, 200 **(2000)**.
4. A. Baschirotto, E. Dallago, P. Malcovati et al., *IEEE Transactions on Instrumentation and Measurement* 56, 25 **(2007)**.
5. W. Y. Choi and J. O. Kim, *Two-Axis Micro Fluxgate Sensor on Single Chip Microsystem Technologies* 352 **(2006)**.
6. P. M. Drljaca, P. Kejik, F. Vincent, D. Piguet, and R. S. Popovic, *IEEE Sens. J.* 5, 909 **(2005)**.
7. J. Kubik, L. Pavel, and P. Ripka, *Sens. Actuators, A* 130, 184 **(2006)**.
8. F. Primdahl, J. R. Petersen, C. Olin, and K. H. Andersen, *J. Phys. E: Sci. Instrum.* 22, 349 **(1989)**.
9. F. Primdahl, P. Ripka, J. R. Petersen, and O. V. Nielsen, *Meas. Sci. Technol.* 2, 1039 **(1991)**.
10. P. Ripka and F. Primdahl, *Sens. Actuators, A* 82, 160 **(2000)**.
11. H. S. Park, J. S. Hwang, W. Y. Choi, D. S. Shim, K. W. Na, and S. O. Choi, *Actuator A - Phys.* 114, 224 **(2004)**.
12. C. Hinnrichs, J. Stahl, K. Kuchenbrandt, and M. Schilling, *IEEE Trans. Magn.* 37, 1983 **(2001)**.
13. L. Perez, I. Lucas, C. Aroca et al., *Sens Act. A - Physical* 130, 142 **(2006)**.
14. E. Paperno, *Sens. Act. A* 119, 405 **(2004)**.
15. J. Vcelák, V. Petrucha, and P. Kašpar, *Sensor Lett.* 5, 279 **(2007)**.

6.2 The PCB $\partial B_x/\partial y$ gradiometer

The following paper *"PCB Fluxgate Gradiometer Measuring dB_x/dy"* [R1] was published in Journal of Electrical Engineering in 2010 after presenting at the "Magnetic Measurements 2010" conference as a majority work of the author. The motivation was investigating the performance of the $\partial B_x/\partial y$ gradiometer used in [J11]. Aspects of the construction of the $\partial B_x/\partial y$ gradiometer are discussed and a new concept with a common feedback coil is investigated. The noise obtained was as low as 3.7 $nT \cdot m^{-1} \cdot Hz^{-0.5}$ @ 1 Hz for a 20-mm gradiometric base.

Journal of ELECTRICAL ENGINEERING, VOL 61. NO 7/s, 2010, 7-9

PCB FLUXGATE GRADIOMETER MEASURING dB_x/dy

Michal Janošek* — Pavel Ripka*

In this paper, we investigated a dB_x/dy gradiometer formed by PCB fluxgate sensors stacked together with a gradiometric base of 20 and 10-mm, respectively. We discuss several possible arrangements of the gradiometer with the emphasis to a common compensating coil wound around the two sensors, which can be in a novel configuration also used for as a gradient pick-up coil. The 1-Hz noise power spectral density of the 20-mm-base gradiometer was found as 3.7 nT/m/√Hz and it increased to 8.2 nT/m/√Hz when reducing the gradiometer base to 10 mm.

Keywords: fluxgate sensor, printed circuit board, pulse excitation, gated integrators, signal extraction, magnetometer

1 INTRODUCTION

Fluxgates made with printed-circuit-board technology (PCB) have potentially low noise and temperature drift to fulfil the requirements for a small-size tensor gradiometer for satellite projects such as LISA [1]. Their advantage for this application is that they are flat (<1mm) and thus allow forming dB_x/dy type gradiometer easily.

Measuring a dBx/dy gradient can be advantageous in many other application situations. In [2], the authors used two fluxgate sensors in dB_x/dy configuration to suppress the environmental noise and increase the sensitivity in magnetorelaxometry-based detection of nanoparticles. An array of CMOS-integrated dB_x/dy fluxgate gradiometer for the purpose of NDT was presented in [3].

1st-order gradients with PCB sensors and 1-mm gradiometric base were already measured in a device developed for the detection of magnetic markers [4]. The short gradiometric base allowed for high spatial resolution, however, it degraded the noise performance (in the order of 10 $nT_{RMS}/m/\sqrt{Hz}$ @1Hz).

2 THEORETICAL ASPECTS

2.1. Gradient sensitivity, noise

The arrangement of a dB_x/dy gradiometer is evident, Fig.1 – two sensors with a sensitive axis in *x*-direction are placed in a distance *d* (gradiometric base) to measure the dB_x/dy component of the magnetic field – the most straightforward solution with fluxgate sensors is to use two phase-sensitive detectors (PSD's) and subtract their outputs.

Let us have two sensors A and B, with sensitivities S_A and S_B, gradiometric base of *d*, and a gradient field with values B_{xA} and B_{xB} in a distance *d*. Then, we can write for the gradient (derivative approximation for small *d*)

$$\frac{d(B_x)}{dy} = \frac{B_{xB} - B_{xA}}{d}. \tag{1}$$

The voltage output of the two sensors sensing the two field values of B_{xA} and B_{xB} is then

$$\Delta V = B_{xB} S_B - B_{xA} S_A \tag{2}$$

The sensitivity to gradient can be then expressed as

$$S\left[\frac{d(B_x)}{dy}\right] = \frac{B_{xB} S_B - B_{xA} S_A}{B_{xB} - B_{xA}} d\,. \tag{3}$$

The sensors need to be astatized, *ie* the sensitivities matched, in order to suppress homogeneous field response and increase gradient sensitivity. Then, using one field sensitivity *S*, we can write for sensitivity on gradient

$$S\left[\frac{d(B_x)}{dy}\right] = \frac{(B_{xB} - B_{xA})S}{B_{xB} - B_{xA}} d = Sd \tag{4}$$

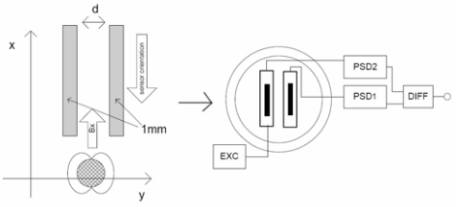

Fig. 1. Configuration of a fluxgate sensor measuring dBx/dy – layout and block diagram of simplest signal-processing

It is obvious that for short gradiometric bases, the sensitivity is low, and consequently the field noise is high. The gradient noise depends on the noise values of individual sensors B_N and correlation between them. If there is no correlation, we can write (in field units)

$$N\left[\frac{d(B_x)}{dy}\right] = \frac{\sqrt{\left(B_{NB}{}^2 + B_{NA}{}^2\right)}}{d}. \tag{5}$$

For matched sensors, the gradient noise is given by

* Department of Measurement, Czech Technical University, Faculty of Electrical Engineering, Technická 2, 166 27 Praha, Czech Republic; janosem@fel.cvut.cz

ISSN 1335-3632 © 2010 FEI STU

$$N\left[\frac{d(B_x)}{dy}\right]=\frac{\sqrt{2}\cdot B_N}{d}. \quad (6)$$

From (6), we can see that the equivalent gradient noise increases with decreasing the gradiometric base d.

2.1 Alternative sensor arrangements for measuring the dB_x/dy type gradient

The disadvantage of the arrangement in Fig. 1 is the large common-mode field seen by both sensors when recovering small horizontal gradients. Although feedback-compensating mode of both sensors can be used, there are disadvantages: short gradiometric bases (tens of mm) cannot be used because of mutual coupling of the compensating fields of respective sensors, and, the signal processing chain still has to have large dynamic range to recover the gradient reading. This was verified with the PCB sensors used in [4].

With the use of a common coil, wound around the two sensors (Fig. 3), new ways to measure the dB_x/dy gradient are possible.

As seen in Fig. 3(a), the output of one sensor can be used to field-compensate its reading with the help of the common coil. In this case, the second sensor senses only the field gradient as most of the common large field is compensated by means of the common coil.

The circuit in Fig. 3(b) adds the possibility to compensate for the homogeneous (average) part of the field. Outputs of the two PSD's are summed (yielding the homogeneous part), this signal is the control signal of the feedback loop. The ½ part of the averaging term is simply part of the feedback-loop gain, so the PSD outputs can be taken directly without any correction for it. The difference between the two sensors is then the dB_x/dy gradient.

Finally, we introduce an original approach of using a common pick-up coil - as seen in Fig. 3(c). The two sensors are excited in opposite directions: in this manner the common flux cancels and only differential flux due to the field gradient can be sensed by the common pick-up coil. The disadvantage of this approach is the large air flux decreasing the sensitivity; however, this configuration is particularly suited for Vacquier sensors: by switching the polarity of the excitation coils, measuring both homogeneous field and dB_x/dy gradient would be possible with no additional wiring.

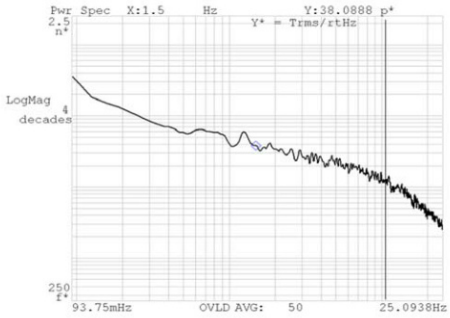

Fig. 2. Noise of individual PCB fluxgate sensor used in the gradiometer.

3 EXPERIMENTAL RESULTS

3.1 The used sensors and their arrangement

We used PCB fluxgate sensors with race-track core, which are a direct development of the sensors presented in [5]. The overall dimensions of each of the sensors are 35x16x1 mm, the sensor core is an amorphous material of Vacuumschmelze, type 6025F. We used this material because of its perspective for low noise; however large excitation current had to be used because of the low permeability of the material (up to 3.6 A p-p with 25% duty-cycle in pulse mode). The sensor noise is shown in Fig. 2 – the 1/f dependence is evident and for frequencies above 20 Hz, the field noise is below 10 pT.

To form the gradiometer, two of the PCB sensors were arranged with a gradiometric base of 20 and 10-mm, respectively (Fig. 1). The larger gradiometric base was chosen to verify the noise parameters; 10-mm base was used together with the common pickup/compensating coil.

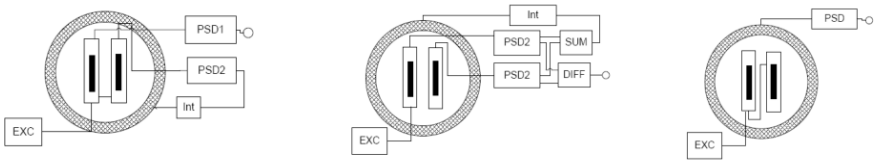

Fig. 3. Special cases of gradiometric arrangement with one common coil – compensating the field sensed by one fluxgate sensor (a), compensating the homogeneous field (b) and serving as pick-up coil for sensors with reversed excitation (c)

3.2 Gradient noise with 20-mm gradient base

We measured the gradient noise by recalculating the field noise by the factor of 1/*d*. The noise was measured in a 6-layer Permalloy shield with Agilent 3570A FFT signal analyzer. The sensors worked in open loop, similar results were obtained for either subtracting outputs of two PSD's (Fig. 4), or for directly subtracting the sensor's output voltages at the lock-in amplifier input. Feedback-compensating mode of both sensors was not used, because of evident mutual influence of the feedback fields. The combined noise spectra of the gradiometer in the range of 100 mHz up to 200 Hz are shown in Fig. 4, showing the noise of 300pT$_{rms}$/m/√Hz at 200 Hz and 3.7 nT$_{rms}$/m/√Hz @ 1Hz. As for astatization of the sensors, their open-loop sensitivities were matched by tuning each sensor output voltage.

3.3 Gradient noise 10-mm base and a common compensating coil

In this measurement, the sensors were arranged according to Fig. 3(a). The gradient compensating coil was fed by an integrator consisting of AD8671 operational amplifier and a second SR-830 lock-in amplifier with Fast-X output served as null-detector in the feedback loop using the second sensor. The common coil was wound around both sensors with 200-turns and 30-mm diameter. The gradient response was taken from the first sensor, whose output was demodulated again with SR830. The gradient noise was measured as 8.2 *n*T$_{RMS}$/m/√Hz @ 1 Hz, thus we can conclude that the noise performance scaled approximately with decreasing the gradiometric base and was not further deteriorated by the compensating feedback-loop.

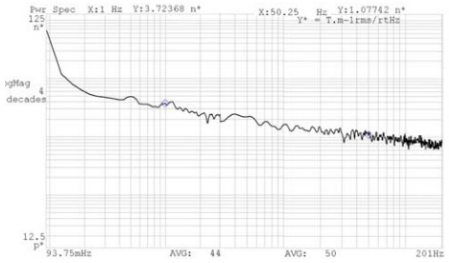

Fig. 4. dB_x/dy gradient noise – two PSD outputs subtracted by analog circuitry

3.4 Other configurations

We investigated the novel setup as described in Fig 3(c). The gradient sensitivity was determined by an indirect method – first, the sensitivity of the respective sensor in homogeneous field with that coil was obtained, then it was recalculated to gradient sensitivity according to (4). However, the noise degradation was too high in comparison to other setups (in the order of one magnitude). It was caused by the low sensitivity of the device – preamplifier noise of the lock-in amplifier was dominating (with 5nV/√Hz white noise of the detector, we need a sensitivity of at least of 0.5 V/T/m to reach 10 nT/m/√Hz gradient noise). In the future work, response of Vacquier sensors should be investigated, as they allow much higher coupling of the pick-up coil to the differential flux caused by field dBx/dy gradient, increasing the sensitivity of the sensor.

4 CONCLUSIONS

PCB sensors can perform well when arranged to a dBx/dy type gradiometer, taking the advantage from their flat design minimizing the mutual coupling of the external field-dependent flux (the used core is only one 25um sheet of amorphous material). For a gradiometer with 20-mm-base we measured 1-Hz noise power-spectral density as low as 3.7 nT/m/√Hz. Such noise is directly comparable to that of flat-coil SQUID gradiometer presented in [6] with an area of 200 mm^2, which is similar to the occupied area of the PCB gradiometer head. We also presented a novel configuration of the gradiometer with only one pick-up coil, which should be particularly suitable for Vacquier sensor designs – however those were not investigated in this work. Gradiometer astatization is another important factor and thus the feasibility of each setup to suppress the parasitic homogeneous field response should be further investigated. A highly-homogeneus coil arrangement has to be used to provide negligible field gradient in *y*-direction.

Acknowledgement

This work was supported the by the Czech Ministry of Education research program No MSM6840770012 and by the grant No 10/205 of the Czech Technical University.

REFERENCES

[1] RIPKA, P. – JANOŠEK, M.: Advances in Magnetic Field Sensors, IEEE Sens. J. **10** (2010), 1108-1116

[2] LUDWIG, F. – MÄUSELEIN, S. – HEIM, E. –SCHILLING, M.: Magnetorelaxometry of magnetic nanoparticles in magnetically unshielded environment utilizing a differential fluxgate arrangement, Rev. Sci. Instrum. **76** (2005), 106102

[3] GRÜGER, H.: Array of miniaturized fluxgate sensors for non-destructive testing applications, Sens. Act. A **106** (2003), 326–328

[4] JANOŠEK, M. - RIPKA, P. - PLATIL, A.: Magnetic Markers Detection Using PCB fluxgate array, J. Appl. Phys. **105** (2009), 7E717

[5] JANOŠEK, M. - KUBÍK, J. - RIPKA, P.: Magnetometer with Pulse-Excited Miniature Fluxgate Sensor, J. Elec. Eng. **57** (2006), 80-83

[6] KONG, X.Y. – NAKATANI, Y. – YUTANI, A. – MAKI, T. – ITOZAKI, H.: First-order high-T$_C$ SQUID gradiometer, Phys. C: Supercond. **468** (2008), 1946-1949

Received 30 September 2010

6.3 Field mapping with the PCB fluxgate gradiometer

A field-mapping instrument was developed using the PCB sensors – measuring the normal field component and the $\partial B_x/\partial y$ gradient component– see Fig. 6.3. The gap between the two PCB sensors could be held at 1-mm with the help of two washers. The PCB fluxgate sensors were operated in open-loop.

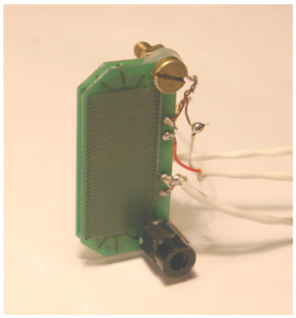

Fig. 6.3 – The PCB $\partial B_x/\partial y$ fluxgate gradiometer

The first mapping trials were carried out by a bachelor student supervised by the author [Mráz 2008], who was able to use the gradiometer for magnetic mapping of a 1-USD banknote which is using magnetic ink [Rusanov 2009]. The sensor liftoff was kept at 5-mm and the scanning step of the X-Y positioning device was 2 mm – the resulting image is shown in Fig. 6.4. The overlay of the gradient data and the scanned scene was later improved by using a smart camera, which provided the coordinates of the measurement [Pribula 2011].

The following article *"Magnetic markers detection using PCB fluxgate array"* [J11] was published in Journal of Applied Physics in 2009. The author describes the performance of a scanning PCB gradiometer of $\partial B_x/\partial y$ type, where the test objects were either a superparamagnetic particle solution excited by an AC field or a magnetic-ink banknote with no field excitation. The author constructed the fluxgate gradiometer and carried out most of the presented measurements excluding the banknote mapping.

Fig. 6.4 – The mapped magnetic field gradient – 5 mm liftoff – above the 1 USD banknote. The 20 nT difference signal corresponds to 20 nT·mm^{-1} gradient. From [Pribula 2011].

JOURNAL OF APPLIED PHYSICS **105**, 07E717 (2009)

Magnetic markers detection using PCB fluxgate array

M. Janosek,[a] P. Ripka, and A. Platil
Department of Measurement, Faculty of Electrical Engineering, Czech Technical University in Prague, Technicka 2, 166 27 Praha, Czech Republic

(Presented 12 November 2008; received 22 September 2008; accepted 9 December 2008; published online 20 March 2009)

We used an array of race-track fluxgate sensors, manufactured with printed circuit board (PCB) technology, forming a sensor head for detection of ferromagnetic and paramagnetic markers. The sensors were arranged perpendicularly to the measuring plane and we measured the difference of their output, giving us the horizontal gradient of normal component of the measured field. Due to the close match of the sensor's parameters, subtraction of the fluxgate output signals could be done directly at the input of a lock-in amplifier, increasing the signal-to-noise ratio for small gradients. When moving the sensor head, we were able to map field gradients smaller than 6 nT/mm, which was verified while measuring the magnetic markers on a dollar bill, while suppressing the background field by a factor of 5. In a line-scanning mode, we scanned a marker formed by a 0.2 mm diameter Permalloy wire in a distance of up to 10 mm. With the help of perpendicular ac excitation at 30 Hz, we were able to detect a 0.1 ml Endorem iron-oxide superparamagnetic marker at 2 mm; volume of 0.6 ml was detectable at 10 mm. © *2009 American Institute of Physics*. [DOI: 10.1063/1.3074780]

I. INTRODUCTION

In contrast to magnetic imaging, where the spatial resolution is the main parameter, e.g., Hall scanning probe microscopy,[1] detection of magnetic markers requires increased reading distance. Reading distance, which was used by Abdul *et al.*[2] to observe domain walls in ferromagnetic material in ac mode with a Hall sensor, was 0.28 mm. It is always difficult to maintain this small gap, while moving the sensor head or the object under test, which can have an uneven surface. Increasing the gap requires sensors with higher sensitivity (Giant Magnetoresistors (GMR), Anizotropic Magnetoresistors (AMR), and fluxgate), at the cost of losing spatial resolution. In dc mode, it is possible to measure the remanent magnetization field of the magnetic markers, which can be a strip of amorphous material or an array of ferrimagnetic particles in printing ink. Detecting of superparamagnetic particles in biomedical markers requires ac excitation, as these particles have no remanent field. The resulting field values can be lower than 1 nT in reading distance of several millimeters. These requirements for precise measurements in the presence of ambient field clearly favor fluxgate sensors.[3,4] Having a suitable shape, they can be used because of their high resolution, superior dc stability, and low noise at room temperatures. They also do not suffer from the large cross-field effect unlike the AMR sensors, used, e.g., by Tumanski and Linszka;[5] this allows using of perpendicular excitation fields. Slim PCB fluxgate sensors allow a close spacing of the sensors in the one-dimensional (1D) gradiometric array and thus high spatial resolution, comparable to that used by Grüger,[6] who integrated an array of fluxgate sensors with a pitch of 500 μm. The good repeatability of sensor's parameters, achieved by the PCB manufacturing process, guarantees a good balance of the gradiometer.

II. SYSTEM SETUP

We used PCB race-track fluxgate sensors of our design, with the size of 33 mm × 15 mm, thickness of 1 mm, 68 turns of pick-up coil, 30 turns of excitation coil, operated at 10 kHz excitation signal, and sensitivity of 460 V/T. They form a sensor head, which was placed on a movable nonmagnetic arm allowing positioning in the two-dimensional plane. We used three (or two) PCB fluxgate sensors in a configuration as shown in Fig. 1. The size of the sensor head is even smaller than the single gradiometric racetrack sensor used by our laboratory in dc magnetopneumography experiments.[7] The sensitive axis is perpendicular to the measurement plane, so we are measuring the horizontal gradient of the normal field component. The sensor head is less sensitive to misalignment of the sensors' axes to the normal

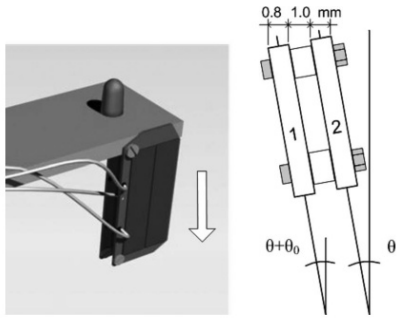

FIG. 1. Sensor configuration. The sensors are fastened together, eliminating differential tilt angle θ_0.

[a]Author to whom correspondence should be addressed. Tel.: +(420) 2 2435 3964. FAX: +(420) 2 3333 9929. Electronic mail: janosem@fel.cvut.cz.

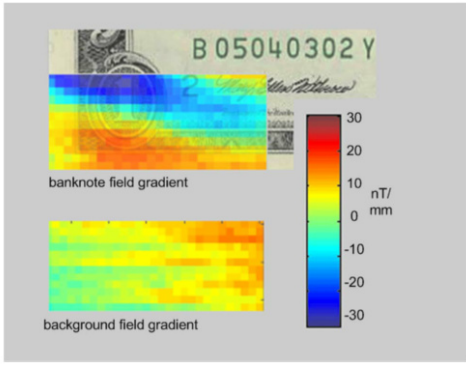

FIG. 2. (Color online) Magnetic field gradient measured 5 mm above a 1 US dollar bill overlaid with the measured area. The scanning step was 2 mm, and the bottom graph depicts background field gradient.

vector, as both of the sensors are at the same angle to the measuring plane. As the design of the sensors is flat with precisely drilled support holes, the possible error due to cross-sensor misalignment is minimal by reducing the θ_0 and φ_0 angles (tilt and yaw) in the gradiometric equation

$$B_{\text{tot}} = (B + \Delta B)\sin(\theta + \theta_0)\cos(\varphi + \varphi_0). \quad (1)$$

Because the sensor spacing is only 1 mm and the sensor's center is approximately at 15 mm above the measuring plane when measuring in direct contact with the object, the difference of sensors' readings gives almost precise information of the measured gradient (e.g., in Ref. 3, there is a derived correction term that depends on sensor spacing d and distance z from the measured dipole; for $d/z \ll 1$, the correction term is negligible and the measured difference is a true gradient reading).

III. SCANNING OF FERROMAGNETIC MARKERS

Operating in unshielded environment brings the problems of large bias fields including their variations. The computation of the gradient suffers from the stability of the magnetometer channels and the resolution of the data-acquisition system becomes critical. When the use of low-cost data acquistion modules is desired, the direct gradiometric configuration can help to suppress the large bias field and increase the resolution.[3] The signal is being fed to a difference amplifier and a second-harmonic detector processes the difference. In our case, a Signal-Recovery 7265 lock-in amplifier and a 16 bit NI-USB 9215 data-acquisition module were successfully used. The sensors were placed 5 mm above the 1 US dollar banknote, and the small area around the bottom-left corner with sign "1" was examined. The repeatability of the results was excellent, together with background gradient suppression of approximately 1:5 in average, which is a good result for an unshielded environment (Fig. 2). The obtained difference was ±30 nT full-scale, giving a full-scale horizontal gradient of ±30 nT/mm. These good results in direct configuration could be obtained because of the well-matching parameters of PCB fluxgate sensors.

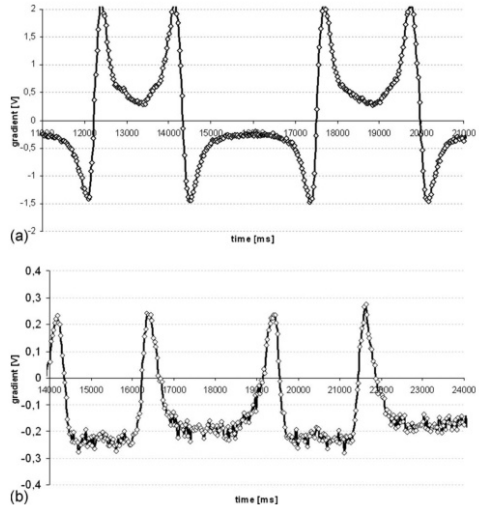

FIG. 3. Measured gradients in the closest (upper) and 10 mm distance (lower) when sweeping the sensor head around a 0.2 mm diameter Py wire.

As one of the possible applications is scanning of magnetic bar code, we tested the line (1D) resolution of the scanning head with two sensors spaced by 1 mm. One axis of the positioning device has been driven with a triangular waveform, sweeping linearly the sensor head across a 0.2 mm thin Permalloy (NiFe) wire. In the "zero distance" (2 mm gap between the sensor core and the object under test) the wire marker was easily detectable [Fig. 3(a)]. The wire was still detectable in a distance of 10 mm; however, the dipole character of the field was not observed anymore [Fig. 3(b)]. The zero distance still corresponds to 2 mm due to the PCB technology of the sensor. We tried also to use three sensors with a three-channel magnetometer of our design and computed the two adjacent gradients by software, but the resolution of the system was not sufficient, being mainly limited by the data-acquisition module.

IV. DETECTING OF SUPERPARAMAGNETIC MARKERS

Superparamagnetic particles are often used in biomedical applications.[8] ac excitation field and Superconducting Quantum Interference Device (SQUID) gradiometer have been used to locate superparamagnetic markers in a hospital operating theater to detect breast cancer sentinel lymph nodes. Our aim is to replace SQUID with a more practical room-temperature fluxgate, and not to operate in pulse mode.[4] We used the low cross-field sensitivity of race-track fluxgate sensors and arranged the system according to Fig. 4, with a sensor spacing of 2 mm (decreasing sensor spacing decreases sensitivity in gradient configuration; however, the resolution starts to be limited by the noise of the sensors). First lock-in amplifier (Stanford Research Systems 830) served as a second-harmonic detector, while the second one (Signal-Recovery 7265) supplied the low frequency signal

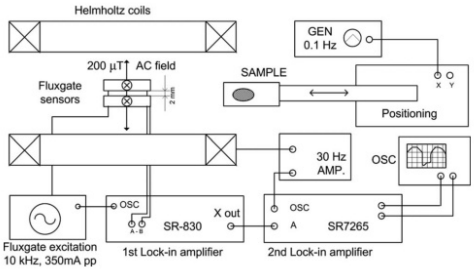

FIG. 4. System setup for detection of biomedical markers.

for external excitation field and detected the ac magnetic field as measured differentially by the two fluxgate sensors. The field of 200 μT was applied using the Helmholtz coils. The sensors were carefully aligned to minimize the cross-field effect, and we measured the normal field component due to the magnetization of the particles in the marker.

We used a volume of 0.6 ml (0.15 μmol), 15.8 mg/ml Endorem, which is basically a colloidal solution of iron-oxide particles in water, widely used for magnetic resonance imaging of tumors. The container with the particles has been swept in 5 mm vertical distance under the reading head, consisting again of two fluxgate sensors in differential setup. The marker could be clearly identified when measuring the imaginary part of the lock-in output, and the maximum distance to detect the particles has been measured as 10 mm (see Fig. 5). We decreased the excitation frequency from 200 Hz down to 30 Hz, where the signal-to-noise ratio was found as highest. The detected difference field value, when computed from the sensitivities of the two lock-in amplifiers, was 540 pT p.-p. in 5 mm distance, and 400 pT in 10 mm distance (Fig. 5), which gives gradients of 270 and 200 pT/mm, respectively. The sample was further decreased; we dropped 0.1 ml (0.025 mmol) of the solution on a cotton-wool, forming the phantom. In the distance of 2 mm, we were again able to detect the marker (Fig. 6). For larger distances, the signal-to-noise ratio was too low.

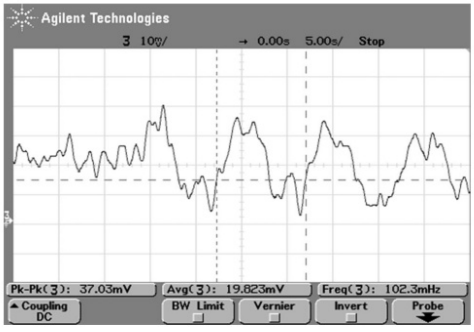

FIG. 5. 0.6 ml sample at 10 mm distance. Noise in the left side corresponds to a difference of 50 pT p.-p., and marker response in the right side to 400 pT p.-p.

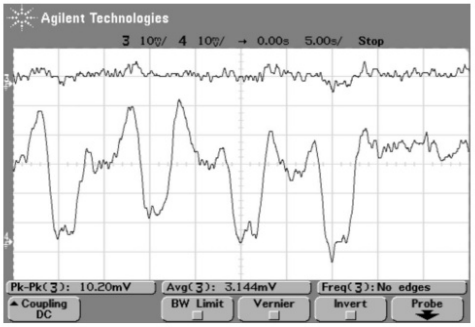

FIG. 6. Signal from a 0.1 ml Endoreme phantom at 2 mm distance from the sensors. Difference field due to the marker corresponding to 370 pT p.-p. The upper trace is the real part for comparison.

The sensor's noise (~100 pT p.-p.) can be clearly identified in the static part of the figures, with the sweeping disabled. In static mode, when the sample is not moved or moved very slowly, the drift of the sensors and the electronics has to be kept as low as possible.

V. CONCLUSION

The resolution of the PCB fluxgate sensors in dc gradiometric mode was better than 6 nT/mm, which allowed mapping the remanent field of magnetic ink used in a banknote at the distance of 5 mm. At the same distance, we were able to detect dipole character of a cut 0.2 mm Py wire. At 10 mm distance, the spatial resolution starts decreasing due to closure of the flux lines; however, the presence of Py wire could be still easily detected. Finally, we were able to detect 0.025 mmol of superparamagnetic Endorem particles on a distance of 10 mm, when applying external, perpendicular 200 μT ac field of 30 (200) Hz. Our fluxgate gradiometer thus may replace SQUID gradiometer in routine breast cancer operations; increasing the number of elements in the array would allow larger S/N ratios than the achieved ones.

ACKNOWLEDGMENTS

We thank Professor Quentin A. Pankhurst, London Centre for Nanotechnology, University College London for providing Endorem samples. This work has been supported by the CTU Grant No. CTU0807513, Czech Grant Agency grant No. GA102/08/0743 and by the Ministry of Education research program No. MSM6840770012.

[1]A. Oral and S. J. Bending, Appl. Phys. Lett. **69**, 1324 (1996).
[2]J. Abdul, A. J. Moses, and P. I. Williams, EMSA 2008 Book of Abstracts, 2008 (unpublished), p. 52.
[3]J. M. G. Merayo, J. R. Petersen, O. V. Nielsen, F. Primdahl, and P. Brauer, Sens. Actuators, A **93**, 185 (2001).
[4]F. Ludwig, E. Heim, S. Mauselein, D. Eberbeck, and M. Schilling, J. Magn. Magn. Mater. **293**, 690 (2005).
[5]S. Tumanski and A. Liszka, J. Magn. Magn. Mater. **242–245**, 1253 (2002).
[6]H. Grüger, Sens. Actuators, A **106**, 326 (2003).
[7]P. Ripka and P. Navratil, Sens. Actuators, A **60**, 76 (1997).
[8]Q. A. Pankhurst, J. Connolly, S. K. Jones, and J. Dobson, J. Phys. D **36**, R167 (2003).

7 A gradiometer with AMR sensors

The AMR sensors evaluated here were Honeywell HMC 1001 and NXP (ex Philips) KMZ 51, both of them off-the-shelf products. Their performance in magnetometer and compass applications was studied in [Zimmermann 2005] and [Včelák 2006]. The HMC 1001 excels in low noise, but due to its low anisotropy field it suffers from high crossfield error (Section 5.1). Both of these sensors benefit from using the so-called "flipping" technique [Vopálenský 2003], where the magnetic state of the permalloy strip is restored by a strong magnetizing pulse of short duration (in the order of 10 – 100 μs).

It must be stated that an AMR magnetometer by far does not approach the precision of fluxgate sensors [Ripka 2010] – the typical offset temperature coefficient is between 2-10 $nT \cdot K^{-1}$ depending on sensor type and signal processing [Platil 2003], [Ripka 2013] – see Fig. 7.2. However, AMR sensors offer the following advantages in gradiometer construction:

- A minimum gradiometric base according to the packaging size of the gradiometer. In the case of KMZ 51, the package size is 5 mm – see Fig. 7.1. The minimum length of the AMR element ensures minimal error if we assume that the field is spatially integrated across magnetic element length [J13].
- The current consumption can be kept low without flipping or when using low-frequency flipping (30 mW for unflipped and 100 mW for flipped KMZ 51).
- AMR magnetometers were successfully tested and used in a space environment [Michelena 2010].

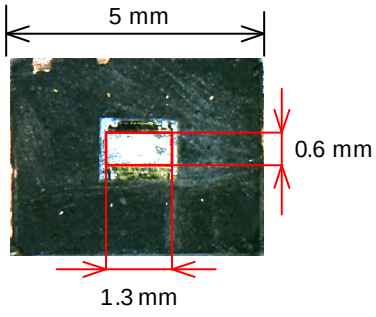

Fig. 7.1– The size of the KMZ51 active element after disassembling its package. From [Janošek 2014]

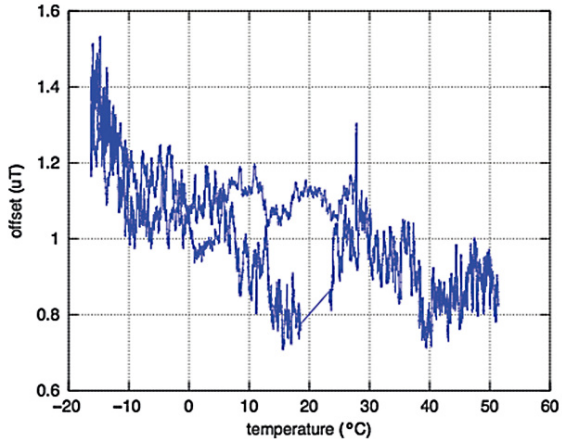

Fig. 7.2 – Complex temperature dependence of flippped KMZ 51 offset. From [Ripka 2013]

7.1 CW metal detector with AMR gradiometers

The first paper below named *"CW Metal Detector Based on AMR Sensor Array"* [W3] is a proceeding paper of the 2011 IEEE Sensors conference. A gradiometric 4×4 array constructed with KMZ51 sensors, each $\partial B_z/\partial z$ gradiometer having a gradiometric base of 40-mm, is presented in article. The two gradiometer sensors are placed in such a way that the excitation field inhomogeneity is symmetric to both of them, and the excitation field can therefore be compensated using the internal compensating coils of the sensors. The author's original idea of an array of $\partial B_z/\partial z$ gradiometers with a feedback-compensated AC excitation field was realized in a master's thesis of [Vyhnánek 2011] under the author's supervision and an improved version of the detector was presented at the conference. As for the article, the author took care about synthesis of the results and their presentation, while most of the measurements were conducted by Mr. Vyhnánek.

The second following article *"AMR gradiometer for mine detection"* [J2] published in Sensors and Actuators in 2012 is an extended version of the previous conference proceedings article, explaining mainly the principle of the homogeneous field compensation in the gradiometer and brings in-depth evaluation of its performance. The major author was Jan Vyhnánek, then a junior PhD. student at the author's group. The author's contribution was mainly in supervising the measurements, suggesting improvements to the measurement setup and revising the text.

The instrument described in the following papers was later developed by a broader-based research group into a real-time linear-array scanning device for detecting of concealed structures in civil engineering [Zikmund 2013]. In Fig. 7.3, the results of real-time scans of underfloor structures are shown (the scans cover an area of 60×140 cm^2).

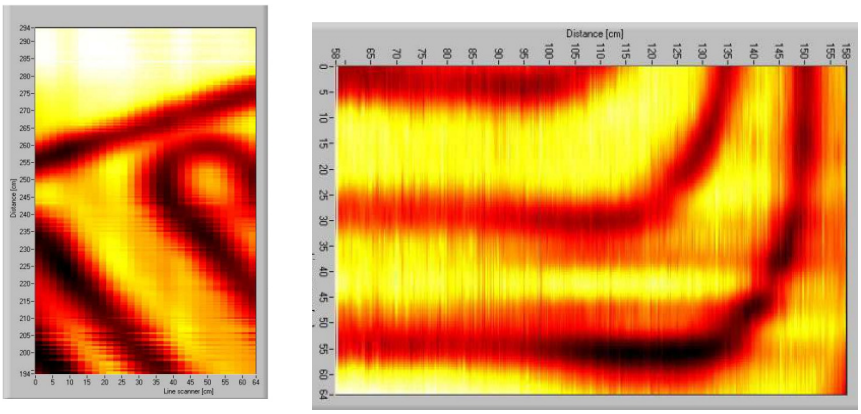

Fig. 7.3 - The 2-D scans of underfloor heating pipes – ferrous (left) and aluminium (rotated, right) – from [Vyhnánek 2014]

CW Metal Detector Based on AMR Sensor Array

M. Janosek, J. Vyhnanek and P. Ripka
Dept. of Measurement, Faculty of Electrical Engineering
Czech Technical University in Prague
PRAHA 6, Czech Republic
Email: janosem@fel.cvut.cz

Abstract— We developed an eddy-current metal detectors with Anisotropic Magnetoresistors (AMR's) arranged in a 4x4 array. The magnetoresistive sensors in a gradiometric configuration are sensing the vertical component of the magnetic field – either originating from magnetized ferromagnetic bodies or induced by 1-kHz, alternating continuous-wave excitation. The AMR's are arranged so that the homogeneous Earth's field and the large excitation field can be suppressed. The mine-detector was constructed as a standard portable device. The presented results show that the performance is limited by the noise of the selected magnetoresistive sensor. If the size of the sensor array was increased, the system could form an advanced mine-detector for quick, large-scale demining purposes.

I. INTRODUCTION

Modern metal detectors should not be only very sensitive, but also very selective and be able to compensate the influence of soils containing ferromagnetic particles as well as electrically conducting medium when working in wetlands and shallow waters. A pick-up coil is practically the only sensor used to detect field variations caused by eddy currents in a conducting object. It would be very desirable to replace it by a smaller sensor, which would give better spatial resolution and allow arranging of the sensors in scanning arrays for speeding up the detection process [1].

Magnetoresistive sensors are the favorite for this purpose as they became readily available and low-cost. A fluxgate sensor might be used too [2], but the excellent noise performance of a fluxgate is traded off for its complexity, cost and size.

The main advantage of an AMR is its small size, which allows to achieve much higher spatial resolution compared to the traditional pick-up coil. When compared to other magnetoresistive sensors (GMR, SDT), AMRs have an advantage of low DC magnetic noise. Drawbacks of AMRs compared to the pick-up coils are however numerous: increased power consumption, 1/f noise, non-linearity, perming, and necessity of periodical flipping.

In [3], authors described an advanced, eddy-current handheld mine-detection system with SDT sensors using pulsed excitation. The device was quite complex, however we are not aware of any real-world performance data. As the low frequency noise of the SDT sensors is too high, it did not allow for including the DC magnetic response.

II. DESCRIPTION OF THE METAL DETECTOR

Our metal detector is based on an array of 16 AMR gradiometers, arranged in a 4x4 matrix, sharing a common continuous-wave excitation coil. The metal detector is able to sense the AC response to the excitation field and the DC magnetic field, decomposed in 4 components. All of them are available at one moment: Re and Im component of the AC response, DC field gradient and DC homogeneous field (mainly for calibration and verification purposes).

The electronics of the mine-detector is built on a modular base with 19 blocks – the flipping generator, CW amplifier, 8 two-channel signal-processing blocks and finally the data-transfer module (Fig. 1). On the search-head, the 16 gradiometers with KMZ51 sensors in 4-cm distance are arranged in a 4x4 matrix. The size of the search head is approx 35 cm in diameter (Fig. 2A), the coil generates a 1-kHz AC field of 150 μT amplitude.

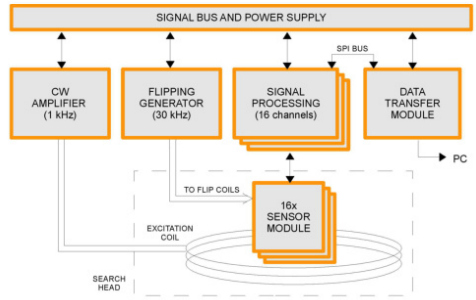

Figure 1. Building blocks of the mine-detector

For a reliable operation the sensors should be periodically flipped, otherwise the stable monodomain state could be corrupted by field or temperature shocks and performance of the sensor would deteriorate. The flipping frequency (30 kHz)

978-1-4244-9289-3/11/$26.00 ©2011 IEEE

was relatively high to avoid overlap with signals resulting from the main excitation field of 1 kHz.

Every signal-processing channel consists of the respective synchronous detectors (30 kHz, 1 kHz Re and Im), a PI feedback regulator, amplifiers and filters. Each 2 channels share a 24-bit delta-sigma AD converter ADS1278 (Fig. 2B) with 96 samples/second, giving 48 Hz alias-free bandwidth. The Earth's field and most of the 1 kHz excitation field are compensated using the internal feedback coils of the KMZ51 by the negative feedback-loop with the "distant" sensor as reference. The detailed principle of each gradiometer was described by the authors in [4].

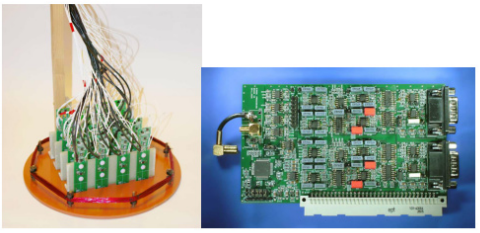

Figure 2. *A* – the sensor head with 4x4 matrix, *B* – electronic with 2 channels. The upper sensor is the "distant", the lower "close" sensor is hidden in the search-head frame to be as close as possible to scanned object

The data from all 16 channels (64 values) are simultaneously transmitted using daisy-chaining via USB to the host computer for postprocessing in LabView environment.

III. LABORATORY RESULTS

A. *Noise performance*

Noise performance was tested with one of the gradiometers. After increasing the flipping pulses to 2.9A peak-peak [6, 7], we obtained 1-kHz noise of 200 pT/√Hz (limits detection of diamagnetic objects) and 2 nT/√Hz at 1 Hz (DC field response of ferromagnetic objects). The noise figures are shown in detail in [4] and correlate with those published in [8] – as we did not find any significant coherence between the two AMR sensors noise, the influence of the common current-source was negligible. For the perspective use of an AMR with lower noise (HMC1001 was shown to have 15 pT/√Hz @ 1 kHz [9]), we face two problems:

- the noise of the electronics is 150 pT/√Hz at 1 kHz, and is mainly limited by the noise of the instrumentation amplifier sensing the bridge output.
- the internal feedback-coil constant of HMC1001 is low, excessive current would be needed for each channel to compensate Earth's field

The solution of the electronic noise is only by increasing the AMR gain (by applying larger supply voltage – up to 8V for KMZ51, up to 10V for HMC1001) or by selecting a better instrumentation amplifier.

As the compensating current of the HMC1001 is tens of mA's for the Earth's field, the power consumption of the device would significantly increase (the feedback coil constant of KMZ51 is 10x larger), causing further problems in power consumption of a portable instrument

Further reduction of the noise is possible by averaging: for 1 second, we should be able to lower the noise 10x as we are sampling at 100 samples/s. It was however not used as we required dynamic performance of the detector.

B. *Response to test object*

Figures 4 and 5 show the response in 3, 6 and 9-cm depth to an empty Kalashnikov shell, which was moved in a 5-cm grid below the sensing head (Fig. 3). It can be seen that for the steel shell, the DC response is 3-orders of magnitude larger; however both the DC response and Im part of the AC response are similar, allowing to identify the position of the shell with a single scan (Fig. 6).

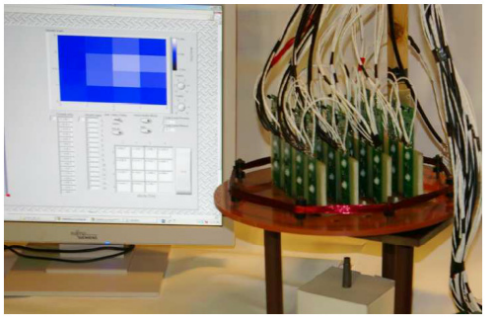

Figure 3. Measuring the response to the test object

During tests, it turned out that even for measuring field "gradient", the response of distant objects is $1/r^3$ and not $1/r^4$: in most cases the response falls quickly enough so that the "distant" sensor measures only Earth's field or the excitation field, and does not see the object's response measured with the "close" sensor (Fig. 2A).

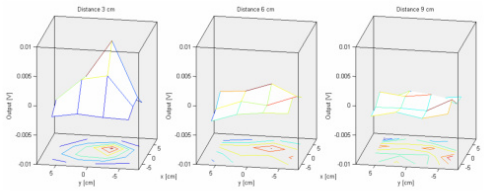

Figure 4. IM part of the AC response –Kalashnikov shell in 3, 6 and 9-cm depth

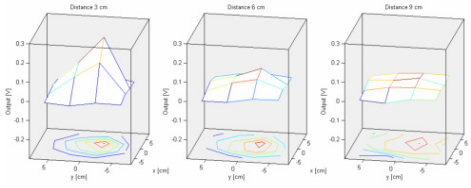

Figure 5. DC response – Kalashnikov shell in 3, 6 and 9-cm depth

The maximum detection depth of the steel shell was 13 cm and of an 5x5cm aluminum plate it turned out to be 20-cm. In both cases, the sensor noise was the limiting factor.

IV. FIELD TEST

To exclude the laboratory noise, the mine-detector was rearranged to a portable, battery-powered device. However due to large power consumption (~20W) and moderate weight (5kg), the portability was somehow affected (Fig. 6A). For a real-world application, it turned out that an average of all 16-sensors was helpful to create an thresholded alarm, and that the position of the sensing head should be determined in some means [10] to incorporate averaging during multiple sweeps. Fig. 6B shows the response to sweeping over Khalasnikov shell with decreasing distance from 20 cm down to 1cm.

V. CONCLUSION

The presented mine-detector shows that it is possible to build a CW-metal detector with AMR sensors – the main problem of compensating the excessive excitation field amplitude was solved. The 4x4 array of gradiometers proved usable for small, shallow objects, for more distant targets an average from all 16 sensors was helpful. As the mine-detectors is able to produce 4 physically meaningful outputs from each channel, the system is overdetermined and it should be possible to improve the detection performance by mathematical postprocessing, which is out of scope of this paper.

The detection depth is mediocre, a noise reduction of at least one magnitude is needed. This is possible with another type of AMR sensor, however the power consumption would then disqualify this type of mine-detector from being portable. In this case re-arranging the sensing head to a larger array, or a single-line scanner, would allow to create a highly efficient, large-scale detection system, which could be towed or moved by other means.

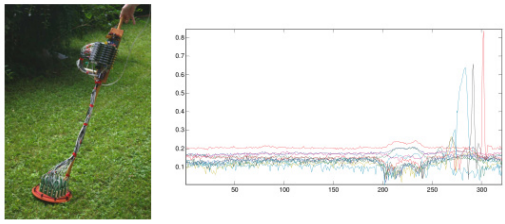

Figure 6. *A* – the portable version of mine-detector during field tests, *B* – 16-ch response to sweeps 20 to 1 cm above a steel shell (highlighted with $\sqrt[3]{|y|}$)

REFERENCES

[1] H. H. Nelson and J. R. McDonald, "Multisensor towed array detection system for UXO detection", IEEE Transactions on Geoscience and Remote Sensing, Vol. 39, No. 6, pp. 1139-1149, 2009

[2] Y. Zhang, M. Steiger, A. D. Hibbs, R. E. Grimm and T. A. Sprott, "Dual-mode, Fluxgate-Induction Sensor for UXO Detection and Discrimination", Journal of Environmental & Engineering Geophysics, Vol. 15, p. 51-64, June 2010.

[3] R. Wold, C.A. Nordnlan, E.M. Lavely, M. Tondra, E. Lange and M. Prouty, "Development of a handheld mine detection system using a magnetoresistive sensor array", Proc. SPIE, vol. 3710 (1), pp. 113-123, 1999.

[4] J. Vyhnanek, M. Janosek and P. Ripka, "AMR gradiometer for mine detection and sensing", Proceedings of Eurosensors XXV, September 2011, accepted.

[5] N. A. Stutzke, S.E. Russek, D. P. Pappas, M. Tondra, "Low-frequency noise measurements on commercial magnetoresistive magnetic field sensors", Journal of Applied Physics, Volume 97, Issue 10, pp. 10Q107-10Q107-3, 2005.

[6] P. Ripka, M. Vopalensky, A. Platil, M. Döscher, K. -M. H. Lenssen and H. Hauser, "AMR magnetometer". Journal of Magnetism and Magnetic Materials 254-255, pp.639-641, 2003

[7] H. Hauser, P.L. Fulmek, P. Haumer, M. Vopalensky and P. Ripka, „Flipping field and stability in anisotropic magnetoresistive sensors", Sensors and Actuators A, Vol. 106, pp. 121-125, 2003

[8] E. Zimmermann, A. Verweerd, W. Glaas, A. Tillmann and A. Kemna, "An AMR sensor-based measurement system for magnetoeletrical resistivity tomography", IEEE Sensors Journal, Vol. 5, no. 2, pp. 233-241, April 2005

[9] D. F. He, M. Tachiki, and H. Itozaki, "Highly sensitive anisotropic magnetoresistance magnetometer for Eddy-current nondestructive evaluation", Review of Scientific Instruments, Vol 80, pp. 036102, 2009

[10] H. Krüger and H. Ewald, Handheld metal detector with online visualisation and classification for the humanitarian mine clearance, IEEE Sensors, 2008 Proceedings, pp.415-418, Oct. 2008

Sensors and Actuators A 186 (2012) 100–104

Contents lists available at SciVerse ScienceDirect

Sensors and Actuators A: Physical

journal homepage: www.elsevier.com/locate/sna

AMR gradiometer for mine detection

Jan Vyhnánek*, Michal Janošek, Pavel Ripka

Czech Technical University in Prague, Faculty of Electrical Engineering, Dept. of Measurement, Technická 2, 166 27 Prague, Czech Republic

ARTICLE INFO

Article history:
Received 6 October 2011
Received in revised form 10 February 2012
Accepted 2 March 2012
Available online 29 March 2012

Keywords:
Mine detection
Magnetic sensors
AMR
Gradiometer
Eddy currents

ABSTRACT

Anisotropic magnetoresistors (AMRs) are used to build an advanced mine detector. The sensing head involves a gradiometric pair of AMR sensors and a continuous-wave driven excitation coil, so the gradiometer is capable of detection of ferromagnetic materials as well as diamagnetic metals. The sensors are specially arranged to suppress the large AC-excitation field, so the mine detector senses both DC and AC field gradient responses of the object of interest. Being limited by the sensor and electronics noise of 268 pT/$\sqrt{\text{Hz}}$ at 1 kHz, we were able to detect a 50 mm × 50 mm × 1.5 mm aluminum test object in a 20 cm depth using a 150 μT, 1-kHz excitation field.

1. Introduction

Mine detectors used for clearing landmines and other explosive remnants are in most cases specialized metal detectors constructed to reveal even minimum metal mines in electromagnetically difficult soils. They are nearly exclusively based on eddy currents and use induction coils for sensing the metallic parts of mines. They detect conducting objects very reliably, but they fail to discriminate dangerous objects from the scrap metal. The work of deminers is often very slow, as they have to carefully excavate each concealed metal object [1].

To distinguish metal parts of mines from other metal objects the AMR gradiometer uses sensors with high spatial resolution to discriminate objects by the recognition of their shape and dimensions. This process requires scanning, which is however already performed by deminers naturally by sweeping a detector head from side to side while searching for mines. For the effectivity of the scanning process multiple sensor array should be used, as was demonstrated by non-destructive testing systems [2,3]. Sensing both DC and AC magnetic field response should contribute to better characterization of the object. Even when some parts of a ferromagnetic object have corroded and lost its conductivity, they still can be detected by steady-state magnetic fields.

The proposed gradiometer benefits from the simple design of commercially available AMR sensors and printed circuit board (PCB) technology. It can operate with a 1-kHz continuous-wave excitation field, so non-magnetic metals can be detected in the AC part of the gradiometer output in addition to ferromagnetic metals that affect the DC part. The gradiometric arrangement allows to measure the weak gradient field of the object of interest, while suppressing the strong excitation and Earth's field.

A similar mine detector with spin dependent tunneling sensors (SDT) was presented in [4], however it worked with a pulsed field and the DC noise of the SDT sensors disqualifies them from the combined DC and AC response sensing. An AMR sensor working with a harmonic excitation field was used for non-destructive testing [5] and dealt with reduction of the sensor noise as the main factor limiting the sensitivity, but it did not solve the suppression of the Earth's magnetic field needed for the DC gradient sensing.

2. Gradiometer principle

AMRs of the KMZ51 type (NXP, ex. Philips) are thin-film permalloy sensors with magnetoresistive elements configured in a full bridge and with the on-chip flipping and compensation coil. They detect the magnetic field component along the sensitive axis, the sensitivity reaches up to 130 mV/(A/m) for the maximum 8-V bridge supply. Two AMRs are arranged in the distance of 40 mm, forming a vertical dB_x/dx gradiometer (Fig. 1). The two gradiometric sensors in a SO-8 package are soldered on the PCB together with signal preamplifiers (total gain of 1000×).

As a proper mine detector needs to sense diamagnetic metals too, we added a continuous-wave driven excitation coil and solved the most difficult part of suppressing the large excitation field, which is needed for the proper detection depth. The coil is symmetric to the gradiometric sensors and it is fed with a 1-kHz

* Corresponding author.
E-mail address: vyhnajan@fel.cvut.cz (J. Vyhnánek).

0924-4247/$ – see front matter © 2012 Elsevier B.V. All rights reserved.
doi:10.1016/j.sna.2012.03.007

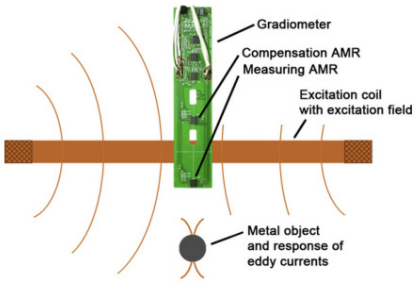

Fig. 1. Gradiometer combined with the excitation coil form the detector head. The compensating and measuring sensors of the gradiometer are symmetrically placed on both sides of the excitation coil.

harmonic signal resulting in an AC field of about 150 μT amplitude. The first (measuring) AMR sensor is located on the sensitive side of the detector head and experiences the same excitation magnetic field as does the second (compensation) sensor. Without any deformation of the excitation or Earth's field the gradiometer response is near zero, limited by the gain of the PI controller in the feedback loop (Fig. 2).

Choosing the coil diameter is not a simple task: for a given excitation current, a small coil provides stronger magnetic fields to a small distance, while a larger coil delivers weaker fields to greater distances. Coils with the diameter in the range of centimeters are used in non-destructive testing for the detection of small near-surface cracks in metals [6,7], while a coil of 1-m diameter is employed for the detection of large deeply buried bombs [1]. The selected diameter of 27 cm is a compromise and should be suitable for both minimum metal mines and bombs close to the surface; this coil diameter is also common to commercial mine detectors.

3. Gradiometer circuitry

In order to assure the magnetic state of the AMR sensors and to improve the stability of its parameters, the AMR sensors are periodically remagnetized – "flipped" at 30 kHz. The sensor field response becomes modulated (Fig. 3), therefore the signal processing is shifted to a less noisy frequency band of the amplifiers. High flipping pulses (1.5 A peak) are used in order to lower the sensor noise [8] while keeping the maximum power dissipation by a low duty-cycle.

Synchronous demodulators with the reference signal of 30 kHz provide reconstruction of the flipped output of the AMR sensors. The 30-kHz demodulation stage is followed by a sampling circuit using a switched integrator, which is inactive in the noisy time intervals, where the sensor output is recovering after a flipping

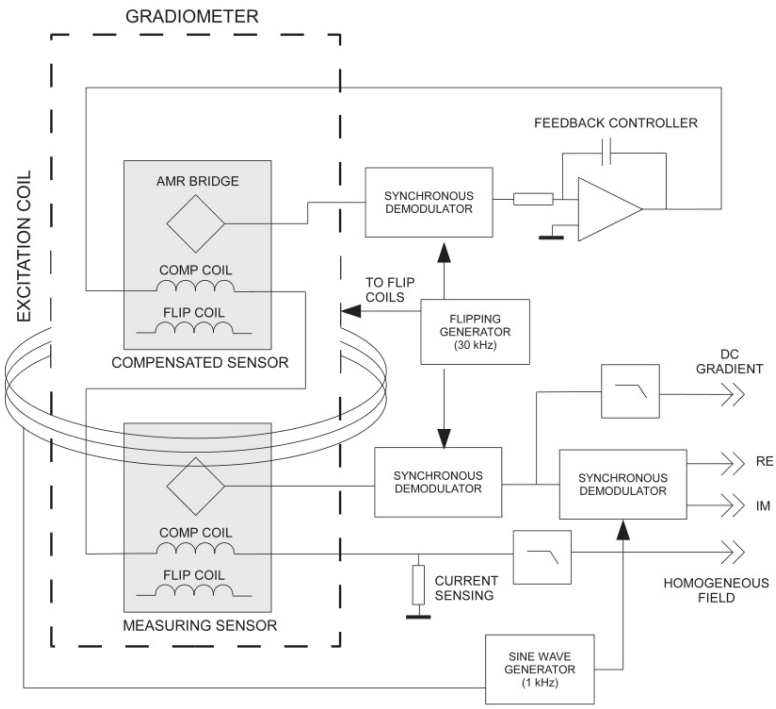

Fig. 2. Functional diagram of the gradiometer operating in the excitation coil. Gradiometric function is obtained by connecting the on-chip compensation coils of the "measuring" and "compensated" sensors in series.

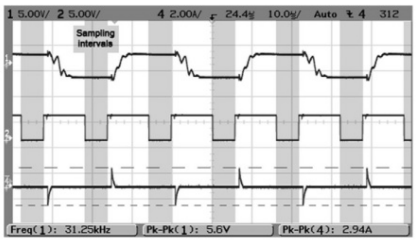

Fig. 3. Sensor output (top trace) and the reference (middle) of the switched integrator suppressing the noisy intervals after flipping pulses (bottom trace).

pulse [9]. The sensor connected to the feedback regulator is maintained in a zero magnetic field by the compensation coil current from DC up to 1 kHz. The compensating current flows through the serially connected compensating coils of both AMR sensors, so the output of the second (measuring) sensor is proportional to the magnetic field gradient. Suppressing the excitation field in addition to the suppression of the Earth's DC field by the compensator allows using higher excitation fields, therefore provides a reserve in DC gradient measurements and possibly an improvement in S/N ratio.

There are four relevant outputs of the gradiometer: the DC field, DC field gradient and the AC field gradient decomposed into the real and imaginary parts. The DC field magnitude (homogeneous part compensating both sensors) is sensed on a shunt resistor in the feedback loop and can be used for correcting for the spurious sensitivity on the Earth's field due to non-orthogonalities of the gradiometer.

4. System noise

The noise of the measuring channel, which consists of a KMZ51 sensor, an AD621 preamplifier and a 30 kHz demodulator, is shown in Fig. 4 – it was determined as 3.1 nT/$\sqrt{}$Hz @ 1 Hz and 268 pT/$\sqrt{}$Hz @ 1 kHz, respectively. When the feedback compensation is switched on (as in the normal operation), the noise increases by 19% @ 1 Hz and 38% @ 1 kHz. This roughly corresponds to a noise increase due to adding an uncorrelated noise signal with the same standard deviation, which comes from the second (compensation) AMR sensor in our case. We could confirm the lack of correlation by the coherence measurement – the compensating current did not show any

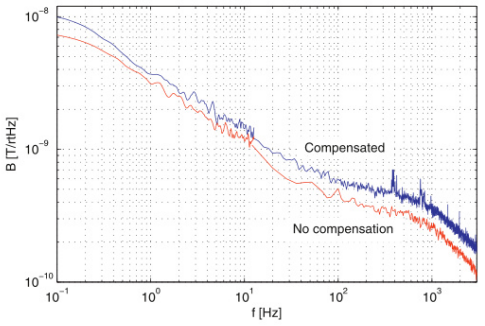

Fig. 4. Noise of the AMR sensor KMZ51 after the first demodulation (bottom trace), the influence of the feedback compensation (top trace). Noise level decrease above 1 kHz is caused by the low pass filter of the demodulator.

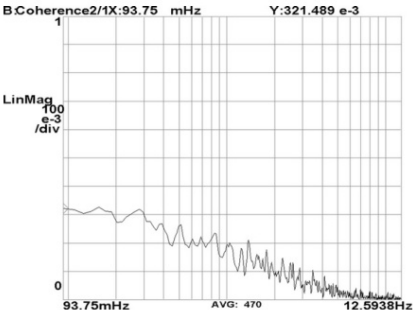

Fig. 5. Coherence of the compensating current and the measuring sensor output, the region of the near zero coherence continues up to 1 kHz.

significant coherence with the signal from the measuring sensor (Fig. 5).

The 1/f noise of the sensor dominates in DC field measurements and decreases with the frequency. At higher frequencies, the system noise can be already limited by the instrumentation amplifier noise and resistive thermal noise of the bridge elements:

$$B_N = \frac{1}{S}\sqrt{4kTR + V_{ni}^2 + \left(V_{no}/G\right)^2 + (I_{ni}R)^2/2} \quad (1)$$

The noise spectral density thus decreases with the lower resistance of the AMR bridge (R) and higher sensitivity (S), which can be augmented by a higher bridge bias voltage. The most critical parameters of the instrumentation amplifier are the input voltage noise (V_{ni}), output voltage noise (V_{no}), current noise (I_{ni}) and the gain (G). For the KMZ51 and AD621 instrumentation amplifier, this would yield 137 pT/$\sqrt{}$Hz noise spectral density which corresponds to the measured electronics noise – the 1-kHz electronic noise was 141 pT/$\sqrt{}$Hz in this case, and was mainly limited by the 10 nV noise of the instrumentation amplifier. As we did not notice any further improvement in the noise level of the KMZ51 when increasing its gain by a higher bridge supply voltage, we can conclude that even at 1 kHz we were measuring the intrinsic magnetic noise of the sensor [10].

Further improvement in the noise performance is possible by using another type of AMR sensor [11]. With the AMR sensor HMC1001 and the low-noise instrumentation amplifier INA103 we were able to achieve 33 pT/$\sqrt{}$Hz @ 1 kHz, however the power consumption disqualifies these components from the application in an advanced handheld metal detector using multiple of these gradiometers in an array.

5. Detection performance

The gradiometer output was tested on aluminum and ferrous objects in different distances. The best approximation curve for both AC and DC gradient responses resulted in x^{-3}. Compared to conventional metal detectors with an induction coil (e.g. Schiebel ATMID), the AMR gradiometer with KMZ51 sensors has still about a half of the detection depth. An aluminum object of 5 × 5 cm could be recognized from the noise level at the gradiometer AC output up to the distance of 20 cm. A ferrous nail 3 cm long and 3 mm thick could be recognized in the DC gradient signal up to the 10 cm distance.

Graphs of the spatial resolution (Fig. 6), measured with the 27-cm-diameter excitation coil, confirm that the gradiometer responds to the local magnetic field disturbance, rather than the possible changes of the excitation field caused by the changing inductance of the coil. Therefore it is possible to use an array of

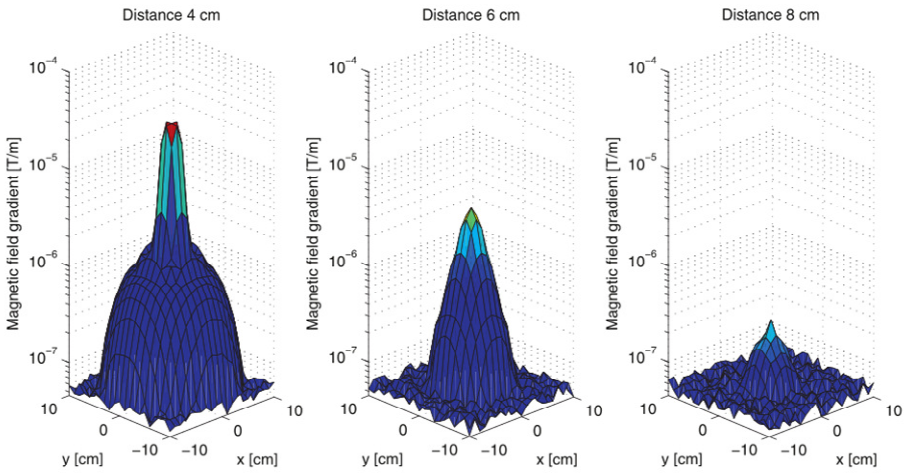

Fig. 6. Single gradiometer scans showing the spatial resolution – a 10 mm diameter stainless steel sphere at distances of 4 cm, 6 cm and 8 cm (AC gradiometer response).

gradiometers inside a single large coil (Fig. 7) – we built a prototype of such a metal detector which is a subject of further investigations [12].

However, as the AMR sensors in the gradiometer have their sensitive axes not perfectly coaxial, the gradiometer is still sensitive to homogeneous fields. Due to limited soldering accuracy and with no factory specifications of the sensitive axis deviation to the package frame of the sensor, the parasitic sensitivity will also differ for each gradiometer. For one gradiometer it was determined by calibrations to be 150 nT/50 μT (output change caused by rotation in the Earth's field). The mine detector will be operated by sweeping in the horizontal plane; therefore at higher latitudes (e.g. the most of Europe) the main part of the Earth's field is vertical to the detector head: this linear dependence can be then used for correcting of the DC response using the homogeneous field magnitude (one of the four gradiometer outputs). The AC output of the gradiometer was found not to be affected by homogeneous fields, as the excitation field direction is stable.

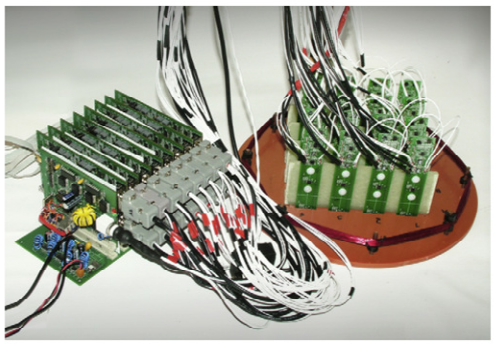

Fig. 7. The array of gradiometers with AMR sensors KMZ51 in a prototype mine detector.

6. Conclusion

The presented gradiometric mine detector uses AMR sensors of KMZ51 type for metal detection together with 1-kHz continuous-wave excitation. As the gradient response of ferromagnetic and diamagnetic objects falls with distance approximately with a $1/r^3$ rule, the most limiting factor of the maximum detection depth is the sensor noise – in our case we can detect a 50×50 mm aluminum plate up to 20 cm depth only being limited by the 268 pT/$\sqrt{\text{Hz}}$ sensor and electronics noise at 1 kHz, which translates to 6.7 (nT/m)/$\sqrt{\text{Hz}}$ gradient noise. Further improvement of the detection depth is possible when using AMR sensors with a lower noise at the cost of increased current consumption. Prospectively, the high spatial resolution of AMR sensors should allow to recognize objects by using signals from a sensor array.

Acknowledgement

This research was supported by the internal grant of the Czech Technical University in Prague, SGS10/205/OHK3/2T/13 "Compact sensors of magnetic field gradient – development and application".

References

[1] D. Guelle, A. Smith, A. Lewis, T. Bloodworth, Metal Detector Handbook for Humanitarian Demining, European Communities, 2003.
[2] D.S. Benitez, S. Quek, P. Gaydecki, V. Torres, A 1-D solid-state-sensor-based array system for magnetic field imaging of steel reinforcing bars embedded within reinforced concrete, IEEE Transactions on Instrumentation and Measurement 58 (2009) 3335–3340.
[3] S. Tumanski, A. Liszka, The methods and devices for scanning of magnetic fields, Journal of Magnetism and Magnetic Materials 242 (2002) 1253–1256.
[4] R.J. Wold, C.A. Nordman, E.M. Lavely, M. Tondra, E. Lange, M. Prouty, Development of a handheld mine detection system using a magnetoresistive sensor array, Proceedings of SPIE 3710 (1) (1999) 113–123.
[5] D.F. He, M. Tachiki, H. Itozaki, Highly sensitive anisotropic magnetoresistance magnetometer for Eddy-current nondestructive evaluation, Review of Scientific Instruments 80 (2009), 036102-1–036102-2.

[6] T. Dogaru, S.T. Smith, Giant magnetoresistance-based eddy-current sensor, IEEE Transaction on Magnetics 37 (2001) 3831–3838.
[7] R. Sikora, T. Chady, S. Gratkowski, M. Komorowski, K. Stawicki, Eddy current testing of thick aluminum plates with hidden cracks, Review of Progress in Quantitative Nondestructive Evaluation 20 (2003) 427–434.
[8] H. Hauser, P.L. Fulmek, P. Haumer, M. Vopalensky, P. Ripka, Flipping field and stability in anisotropic magnetoresistive sensors, Sensors and Actuators 106 (2003) 121–125.
[9] P. Ripka, M. Vopalensky, A. Platil, M. Doscher, K.M.H. Lenssen, H. Hauser, AMR magnetometer, Journal of Magnetism and Magnetic Materials 254–255 (2003) 639–641.
[10] N. Stutzke, S.E. Russek, D.P. Pappas, M. Tondra, Low-frequency noise measurements on commercial magnetoresistive sensors, Journal of Applied Physics 97 (2005), 10Q107-1–10Q107-3.
[11] E. Zimmermann, A. Verweed, W. Glaas, A. Tillmann, A. Kemna, An AMR sensor-based measurement system for magnetoelectrical resistivity tomography, IEEE Sensors Journal 5 (2) (2005) 233–241.
[12] M. Janosek, J. Vyhnanek, P. Ripka, CW metal detector based on AMR Sensor Array, IEEE Sensors 2011 – Proceedings, pp. 1515–1517.

Biographies

Jan Vyhnánek was born in Prague in 1987. Received the engineering degree from the Faculty of Electrical Engineering, Czech Technical University in Prague in 2011, currently a student of PhD at the Dept. of Measurement. His main fields of interest are magnetic sensors and their applications in detection of metal objects.

Michal Janošek, born in Varnsdorf in 1980, graduated from the Faculty of Electrical Engineering, CTU in Prague in 2007 at the Dept. of Measurement. He is working as a junior researcher and PhD candidate at the same department. His main research activity is the application of magnetic sensors in gradiometers and further development in PCB fluxgate sensors.

Pavel Ripka was born in Prague in 1959. He received an Engineering degree in 1984, a CSc (PhD equivalent) in 1989, Associate Prof. in 1996 and finally Prof. in 2002. He was elected the dean of the Faculty of Electrical Engineering, CTU in Prague in 2011. He continues to work at the Department of Measurement as a Professor, lecturing in Measurements, Engineering Magnetism and Sensors. His main research interests are magnetic measurements and magnetic sensors, especially fluxgate. He is a co-author of 4 books and >200 scientific papers.

7.2 Performance of the AMR in the metal detector

The following paper *"Low frequency noise of anisotropic magnetoresistors in DC and AC-excited magnetometers"* [W2] was published in proceedings of the 2013 IOP conference "Sensors & their Applications". It describes the improvement in low-frequency noise of the HMC 1001 sensor with periodic flipping and was motivated by the need of improving the scanning instrument presented above – its power consumption and noise, given by the 30-kHz flipping and the KMZ 51 noise, were sought to be improved using HMC 1001 and reducing the flipping rate or even operating the AMR sensor without flipping.

Unlike other authors, who found no improvement of the AMR noise, we have clearly shown an advantage of flipping: the noise decreased to almost one half of the level when there is no flipping. The measurements were done by J. Vyhnánek, author's contribution was in the theoretical calculations, synthesis and publication of the results.

Sensors & their Applications XVII IOP Publishing
Journal of Physics: Conference Series **450** (2013) 012031 doi:10.1088/1742-6596/450/1/012031

LOW FREQUENCY NOISE OF ANISOTROPIC MAGNETORESISTORS IN DC AND AC-EXCITED METAL DETECTORS

J Vyhnanek, M Janosek, P Ripka
Czech Technical University in Prague, Technicka 2, 166 27 Prague, Czech Republic
E-mail: vyhnajan@fel.cvut.cz

Abstract. Magnetoresistors can replace induction sensors in applications like non-destructive testing and metal detection, where high spatial resolution or low frequency response is required. Using an AC excitation field the magnetic response of eddy currents is detected. Although giant magnetoresistive (GMR) sensors have higher measuring range and sensitivity compared to anisotropic magnetoresistors (AMR), they show also higher hysteresis and noise especially at low frequencies. Therefore AMR sensors are chosen to be evaluated in low noise measurements with combined processing of DC and AC excitation field with respect to the arrangement of processing electronics. Circuit with a commercial AMR sensor HMC1001 and AD8429 preamplifier using flipping technique exhibited 1-Hz noise as low as 125 pT/√Hz. Without flipping, the 1-Hz noise increased to 246 pT/√Hz.

1. Introduction

Magnetoresistors (MR) fall between Hall sensors and induction sensors in terms of sensitivity and noise. Unlike induction sensors, MRs have the frequency response starting from DC and they are therefore favorite sensors for non-destructive testing devices which detect deeply buried cracks [1]. MRs have small dimensions and high spatial resolution which allows to build array arrangements which can be used for metal detection and object recognition [2]. They are also readily available in commercial packaging as electronic components.

The limiting factors for these applications are the noise of the sensor, gain temperature drift, hysteresis and also offset temperature drift when sensors are used at low frequencies or DC. These parameters limit the detection depth in metal detection and non-destructive testing. Noise can be generally filtered by averaging, however this affects the speed of operation and temperature drifts become more pronounced. There are generally three competing magnetoresistive technologies: giant magnetoresistive (GMR), tunneling magnetoresistive (TMR) and anisotropic magnetoresistance (AMR) sensors. In the case of GMR and TMR, the hysteresis and noise are generally higher [3] than for AMRs, which are subject of this study.

We focus on the sensor noise which disqualifies MRs in favor of induction coils, whereas other parameters speak for MRs – they have small size with high spatial resolution and they are mass produced devices available in packages for assembly in printed circuit boards, so that they can be easily used in arrays [4]. A widely used technique of improving of the AMR sensors parameters is the so called flipping – periodic remagnetization of the sensor by applying large bipolar magnetic field pulses. With the magnetization of opposite polarity the output characteristic is reversed – "flipped". Flipping was shown to improve the offset and gain temperature stability and to reduce crossfield

Sensors & their Applications XVII IOP Publishing
Journal of Physics: Conference Series **450** (2013) 012031 doi:10.1088/1742-6596/450/1/012031

sensitivity of the sensor [5]. Metal detector noise was investigated in three possible circuit arrangements with and without flipping - their effects on AC and also DC detector noise were studied.

2. Measurement setup

For experimental measurements, AMR sensor HMC1001 (Honeywell) was used. This sensor has still the best available noise specifications from the off-the-shelf magnetoresistors. It is a barber-pole sensor with MR elements with 850 ohms resistance arranged in a full bridge, featuring on-chip flipping and compensation coils for feedback operation. The sensitivity is 140 V/T for the selected supply voltage of 5.5 V. As the sensitivity is low, the contribution of the noise of the processing electronics is not negligible. Electronics noise could be removed by the crosscorrelation technique [6], it is however not practical (speed of measurement).

The typical choice for the signal processing of an AMR bridge is a low noise instrumentation amplifier (Figure 1a). We chose AD8429 with a 1 nV/√Hz input voltage noise (gain = 100x) and 1.5 pA/√Hz current noise. Due to the high common mode of the bridge, the instrumentation amplifier cannot be set to the full voltage span therefore another amplifier with the gain 10x was connected as the last stage. A similar arrangement was evaluated in [7] where the high bridge supply of 24 V was applied in order to achieve higher sensitivity and lower noise; however 24V is impractical due to sensor heating.

AMR sensor exhibits two significant types of noise: the 1/f type magnetic noise and the white thermal noise. The white magnetic noise is still some orders of magnitude below the thermal resistive noise of the bridge elements; therefore it is not further taken into account. Whereas the 1/f noise affects low-frequency measurements and depends on the manufacturing process, the white noise influencing AC measurements can be predicted by the bridge resistance and parameters of the instrumentation amplifier.

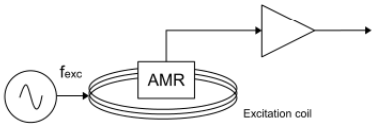

Figure 1a - Direct measurement

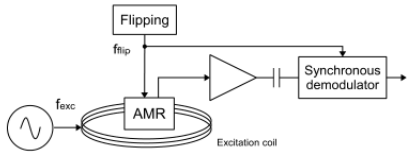

Figure 1b - Measurement setup with flipping

The commonly used method for improving the parameters of an AMR sensor is the so-called "flipping": the sensitive magnetic layer of the AMR is remagnetized in the opposite direction, thus reducing the hysteresis and eliminating the temperature offset drift of the sensor and AC electronics.

For processing the output signal in the flipped mode where the output becomes modulated, a synchronous demodulator is used – Figure 1b. The demodulator in our case includes a switched integrator which eliminates noisy spikes in signal when the sensor is being remagnetized [3] – Figure 2a.

The noise was measured with the Agilent FFT Analyzer 35670A in all cases, without any further amplification, using DC-coupling, 100 averages and a Hanning window. The sensor together with amplifier stage was placed in a 6-layer magnetic shielding can with 100.000x attenuation of the ambient magnetic field noise.

3. Experimental results

3.1. Noise of the electronics

The noise of the electronics was evaluated by connecting a dummy bridge made of resistors of the same value as the MR elements in HMC1001 (850 Ω). Figure 2b shows the noise spectrum obtained at the output of the amplifier (input of the synchronous demodulator in Figure 2a). The 1/f noise with the equivalent of B_E = 95 pT/√Hz at 1 Hz (recalculated using sensitivity S = 140 V/T) is dominantly due

Sensors & their Applications XVII IOP Publishing
Journal of Physics: Conference Series **450** (2013) 012031 doi:10.1088/1742-6596/450/1/012031

to the instrumentation amplifier noise. The white noise with the equivalent of 30 pT/√Hz results both from the bridge thermal noise and the voltage and current noise of the instrumentation amplifier.

The expected white noise of the electronics B_{EW} can be calculated as

$$B_{EW}^2 = (SV_R)^2 + (SV_N)^2 + (SRI_N)^2 \quad (1)$$

$$B_{EW} = S \cdot \sqrt{(V_R)^2 + (V_N)^2 + (RI_N)^2} \quad (2)$$

where V_R is the resistor voltage noise, V_N is the amplifier voltage noise and I_N is the amplifier current noise.

$$B_{EW} = \frac{140V}{T} \cdot \sqrt{\left(\frac{4.12nV}{\sqrt{Hz}}\right)^2 + \left(\frac{1nV}{\sqrt{Hz}}\right)^2 + \left(\frac{1.5pA \cdot 850\Omega}{\sqrt{Hz}}\right)^2} = 31.4\frac{pT}{\sqrt{Hz}}, \quad (3)$$

which matches the measured amplifier noise in Figure 2 (b).

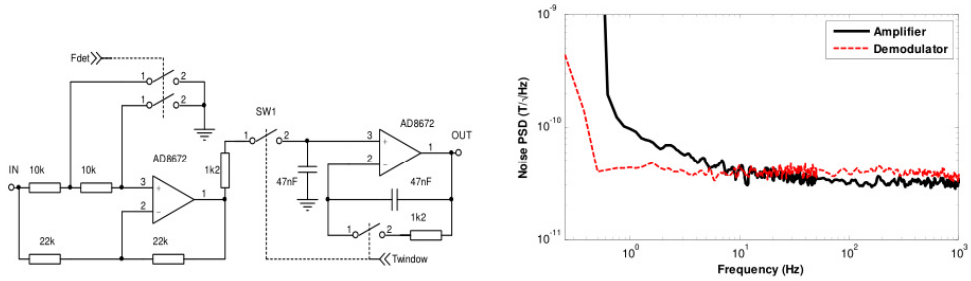

(a) (b)

Figure 2. Synchronous demodulator schematics (a) and comparison of noise of the electronics at amplifier output and demodulator output (b)

The noise of synchronous demodulator was measured at the demodulator output with a 10-kHz reference and the same dummy resistor bridge. The spectrum shows an increased white noise level of 40 pT/√Hz. This was identified as the effect of the switched integrator used in the windowing circuit with the time window set to 70%. With the time window of 100%, the white noise level was 32 pT/√Hz. In the demodulator spectrum there is no 1/f noise of the instrumentation amplifier, due to the fact, that the frequency range was shifted by the 10-kHz demodulation frequency.
Knowing the electronic noise, the noise measurements were done using three different circuit arrangements.

3.2. Direct measurement
This arrangement with simple electronics is depicted in Figure 1a. The output of the AMR bridge is directly amplified. It has the full frequency span limited only by the corner frequency of the amplifier stage. The eventual feedback compensation, which eliminates gain drift and improves linearity, can be realized with a single-opamp PI controller. In this case, the 1/f sensor noise was dominating, the total noise value B_{N1} = 246 pT/√Hz at 1 Hz (Figure 3b).
From the measured values, we can estimate the 1-Hz noise of the sensor itself (B_{S1}) as

Sensors & their Applications XVII IOP Publishing
Journal of Physics: Conference Series **450** (2013) 012031 doi:10.1088/1742-6596/450/1/012031

$$B_{S1} = \sqrt{B_{N1}{}^2 - B_{E1}{}^2} = \sqrt{246^2 - 95^2}\ \frac{pT}{\sqrt{Hz}} = 226\frac{pT}{\sqrt{Hz}} \quad (4)$$

This result is in agreement with values published in [5]. The 1-kHz white noise, which would dominate in the AC application, is approx. the same as the electronic noise - 32 pT/√Hz.
If we use this mode, a single remagnetizing pulse should be performed at least while switching on the device to assure the magnetic state of the sensor.

3.3. Modulation – flipping
The block diagram is shown in Figure 1b, the flipping current and output waveform are shown in Figure 3a. By using flipping at 10 kHz with peak-to-peak amplitude of 3.6 Amps, the output signal was modulated and shifted to the white-noise frequency range of the instrumentation amplifier. The resulting noise of 125 pT/√Hz at 1 Hz (Figure 3b) makes flipping the obvious choice for precise DC field measurements, avoiding the offsets and 1/f noise of the instrumentation amplifier. When compared to 1/f noise of the amplifier and non-flipped sensor (4), the noise clearly further decreased: flipping improved also the low-frequency noise of the magnetoresistor.

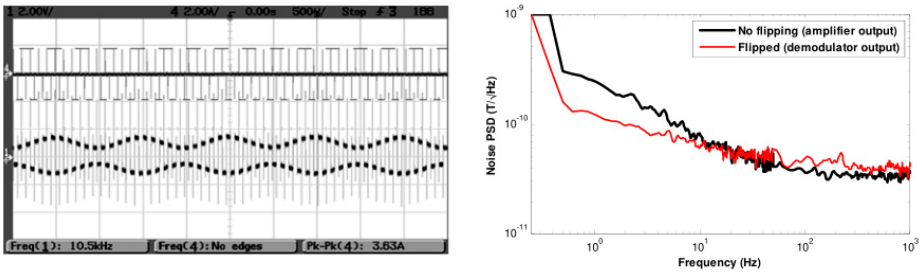

(a) (b)

Figure 3 – Modulated output signal of flipped AMR (a) and comparison of overall noise with direct measurement (b)

However, flipping is power-demanding as the narrow current pulses have to have an amplitude of several amperes in order to properly magnetize the sensitive layer and reduce the 1/f noise [5]. The maximum allowed power dissipation allows maximum flipping frequencies in the order of tens of kHz, limiting the measuring frequency range. It is however possible to use a lower flipping frequency and higher excitation frequency.

3.4. D. Sensor as rectifier
A flipped sensor can be used as a rectifier [8], basic block diagram is presented in Figure 4a. If the flipping frequency is derived from the excitation frequency, the excitation signal is synchronously rectified and the output signal looks like in Figure 4b. The excitation frequency is evaluated with a simple low pass filter connected to the output of the amplifier stage, thus eliminating complex detection circuitry.
A simple feedback compensation is however possible only for a DC range, therefore the sensor should be positioned perpendicularly to the excitation field [1]. However a disadvantage is that the offset drift and the 1/f noise of the amplifier are not eliminated even at the excitation frequency f_{exc}.

Sensors & their Applications XVII IOP Publishing
Journal of Physics: Conference Series **450** (2013) 012031 doi:10.1088/1742-6596/450/1/012031

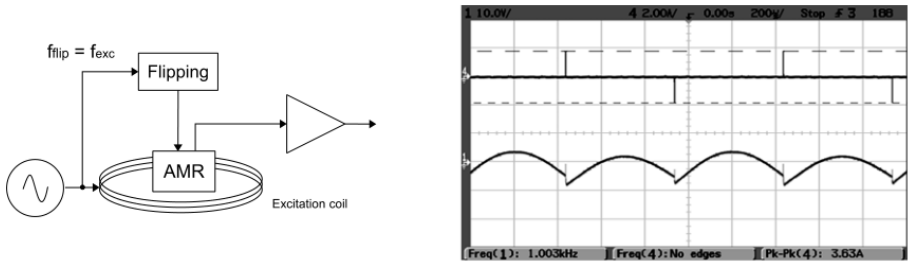

(a) (b)

Figure 4- Special arrangement with $f_{flip}=f_{exc}$ (a), and the flipping current (upper trace) and amplified sensor output (lower trace) (b)

4. Conclusion

When the AMR-based metal detector works with an AC excitation field to sense the eddy current response of metal objects and only the AC frequency response is evaluated, then the noise level is determined by the sensor white noise level and it is approximately the same for either direct measurement or for flipping with demodulator– the 1-kHz noise was about 30 pT/√Hz in both circuit arrangements.

For DC measurements, the 1/f noise of the amplifier and offset drifts of the sensor are best suppressed by flipping modulation technique. For the HMC1001 AMR sensor with 5.5 V_{DC} bridge supply and 10-kHz flipping frequency, we have found an improvement from 246 pT/√Hz 1-Hz noise with direct measurement down to 125 pT/√Hz when using flipping with appropriate demodulation. This improvement was found to be larger than simple effect of shifting the modulated signal out of 1/f amplifier noise: flipping was found to further improve the sensor low-frequency noise.

The commonly used flipping method is however power-demanding with complicated detection electronics; also the measuring frequency range is limited, which is a difficulty in NDE. The possibility of using $f_{flip}=f_{exc}$ was thus investigated: while it allowed to reduce flipping power and to simplify signal processing circuitry, the 1/f noise of the amplifier was however present in this case.

References

[1] Jander A, Smith C, Schneider R 2005 Magnetoresistive sensors for nondestructive testing and evaluation Proc. SPIE. vol. 5770 p. 1-13
[2] Wold RJ, Nordman CA, Lavely EM, Tondra M, Lange E, Prouty M 1999 Development of a handheld mine detection system using a magnetoresistive sensor array*, Proc. SPIE* vol. 3710 pp. 113-123
[3] Popovic RS, Drljaca PM, Schott C 2002 Bridging the gap between AMR, GMR, and Hall magnetic sensors *Proc. 23rd Int. Conf. On Microelectronics* vol. 1 pp. 55-58
[4] Vyhnanek J, Janosek M, Ripka P 2012 AMR Gradiometer for Mine Detection, *Sensors and Actuators,* vol. 186, pp. 100-104
[5] Hauser H, Fulmek PL, Haumer P, Vopálenský M, Ripka P 2003 Flipping field and stability in anisotropic magnetoresistive sensors *Sensors and Actuators*, vol. 106, pp. 1-3
[6] Stutzke NA, Russek SE, Pappas DP 2005, Low-frequency noise measurements on commercial magnetoresistive magnetic field sensors *J. Appl. Phys.*, vol. 97, pp. 10Q107
[7] He DF, Tachiki M, Itozaki H 2009, Highly sensitive anisotropic magnetoresistance magnetometer for Eddy-current nondestructive evaluation, *Review of Scientific Instruments*, vol. 80, pp. 036102-1 - 036102-2
[8] Tumanski S 2001, Thin film magnetoresistive sensors (IOP Publishing), pp. 78-79

8 Axial gradiometer calibration and astatization

8.1 Fluxgate gradiometer for magnetopneumography

The 6-channel fluxgate axial gradiometer, used in magnetopneumography [Tomek 2006] was originally constructed using a pair of nylon strings to hold the respective fluxgate sensors [Tomek 2009]. The low mechanical and temperature stability of the setup however limited the gradiometer performance because the measured field gradient is DC with large common mode value. The author participated in reconstruction of the probe to a rigid holder, see Fig. 8.1. The original 20-mm diameter fluxgate sensors were used and the gradiometric base of 10 cm was kept. The holder was machined from a PEEK GF-30 rod, 40 mm in diameter. The sensors were glued to precisely milled grooves. PEEK GF-30 was chosen because of its good machinability and less than 20-ppm coefficient of thermal expansion [Chu 2010]. Fig. 8.2 shows the gradiometer detail.

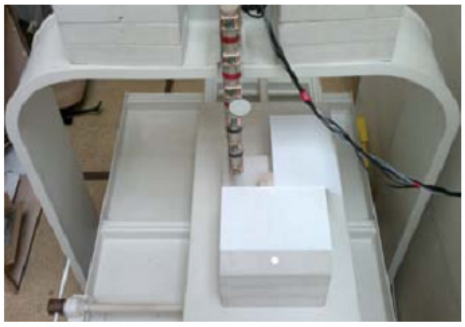

Fig. 8.1 – The gradiometer vertically placed above a non-magnetic bed, from [Platil 2013]

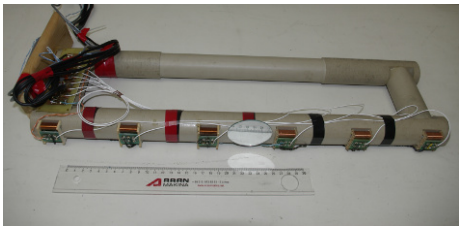

Fig. 8.2 – Detail of the 6-channel gradiometer (positioned horizontally). Z-direction is parallel to the 30-cm ruler.

8.2 Gradiometer calibration

Below, the details of scalar calibration procedure are described which did not appear in the following article [J5] due to the limit of article length.

The $\partial B_z/\partial z$ type gradiometer presented above was calibrated using a modification of the scalar calibration method [Olsen 2001, Olsen 2003, Petrucha 2009] developed by the author. Two additional perpendicular, in-plane sensors measuring B_x and B_y field component [Janošek 2009] were attached to the top of the cylindrical sensor holder. For verification of the scalar calibration results, vectorial calibration was also done in a tri-axial Braunbek coil system at Průhonice observatory (49°59'16.904"N, 14°32'24.702"E), using triangulation with the help of the central mirror (shown in Fig. 8.1). However, due to the mechanical setup of the experiment, it was possible to determine only one angle by this method. More details on the vectorial calibration setup are presented in the following paper [J5].

The coordinate system for the scalar calibration is the same as in [Olsen 2001] – angles u_1 is the misalignment angle between sensor X and sensor Y in the orthogonal (horizontal) plane. Angles u_2 and u_3 define the orientation of this plane to the ideal Z-axis, respectively, see Fig. 8.3.

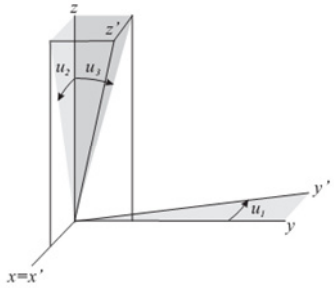

Fig. 8.3 – Coordinate system, after [Olsen 2001]

Z#	S [V·T^{-1}]	O [nT]	u1 [°]	u2 [°]	u3 [°]
1	146088	-90	1.16	-0.71	-2.37
2	146304	35	1.16	-0.60	-2.46
3	146044	-18	1.16	-0.85	-2.54
4	145638	156	1.16	-1.51	-2.97
5	146228	175	1.16	-0.50	-2.24
6	145801	-216	1.16	-1.33	-1.70

Table 1 –Calibration results for the 6 z-channels (sensitivity, offset, and three angles as of Fig. 8.4)

From one calibration sequence, we obtain six different triaxial setups, each containing X, Y and one of the six Z sensors; for each of these setups the calibrating algorithm of [Olsen 2001] is used to obtain the respective X,Y,Z sensor offsets, sensitivities and angles. The complete calibration results, not shown in the paper [J5], are given in Table 1.

The X and Y axis sensitivities (S_x, S_y), their offsets (O_x, O_y) and the u_1 angle would ideally be constant during the calibration. The X and Y sensitivities and offsets with their standard deviations from the 6 calibration were:

O_x = -2995.3 (1.9) nT O_y = -721.5 (2.3) nT
S_x = 117543.3 (2.2) V·T^{-1} S_y = 118017.8 (12.3) V·T^{-1}

Having the calibration parameters, the calibrated vector $\mathbf{B}_i$ in the orthogonal coordinate system is then calculated for each M_X, M_Y, M_{Zi} triplet (i = 1 to 6) assuming that the respective offsets O_{zi} are removed:

$$\mathbf{B_i} = \|\mathbf{S_i}\| \cdot \|\mathbf{P_i}\| \cdot \mathbf{M_i} \tag{8.1}$$

$$\begin{bmatrix} B_{Xi} \\ B_{Yi} \\ B_{Zi} \end{bmatrix} = \begin{bmatrix} S_{Xi}^{-1} & 0 & 0 \\ 0 & S_{Yi}^{-1} & 0 \\ 0 & 0 & S_{Zi}^{-1} \end{bmatrix} \cdot \begin{bmatrix} P_{11i} & 0 & 0 \\ P_{21i} & P_{22i} & 0 \\ P_{31i} & P_{32i} & P_{32i} \end{bmatrix} \cdot \begin{bmatrix} M_{Xi} \\ M_{Yi} \\ M_{Zi} \end{bmatrix} \tag{8.2}$$

Where $\mathbf{B}_i$ is the calibrated field vector, $\|\mathbf{S}\|$ is the diagonal matrix of inverse sensitivities, $|\mathbf{P}\|$ is the transformation matrix to the orthogonal coordinate system

[Olsen 2001] and $\mathbf{M_i}$ is the vector of the measured values (in arbitrary units). The gradient G_{ij} can be then calculated directly using the values of B_i and B_j (Eq. 1.11).

Using the calibrated gradiometer parameters, we have found a considerable stability problem related to temperature drifts of the respective sensor offsets and gains (Fig. 8.5).

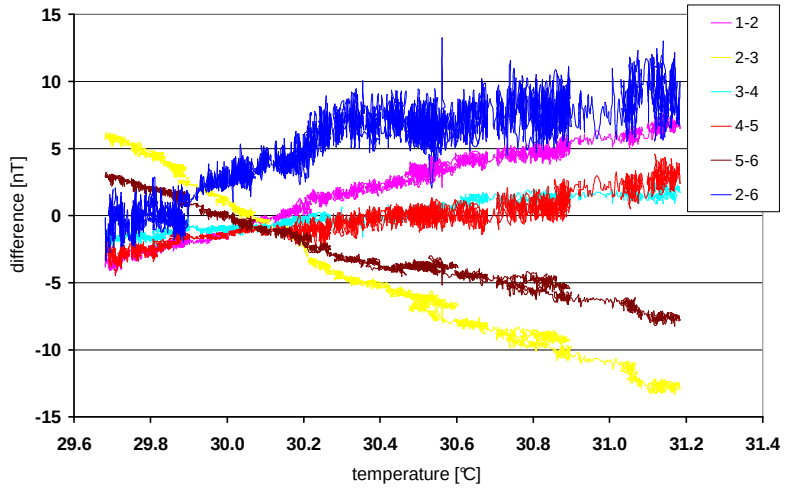

Fig. 8.5 – Sensor output differences vs. temperature show strong temperature dependence (the offsets have been removed to allow a single vertical axis)

It is evident that for a vertically-oriented probe (as in our case) even with a very low sensitivity temperature coefficient of 20 ppm·K^{-1} [Primdahl 1991], the 48,000 nT sensed will cause 1 nT·K^{-1} – or 10 nT·m^{-1}·K^{-1} – drift without taking into account any further offset drift (which is usually below 0.1 nT·K^{-1}), or the thermal expansion of the holder. As a result, either the temperature needs to be monitored or the calibration needs to be repeated when subject to large temperature changes. In the following paper, see below, due to the availability of temperature data, this effect was partially compensated by estimating the gain and offset temperature coefficients of the respective sensors.

The following paper *"Suppression of Environmental Noise in Magnetopneumography by the use of Higher Order Gradients"* [J5] was published in IEEE Transactions on Magnetics in 2012 after presenting the results at the 20th International Conference on Soft Magnetic Materials. The author performed reconstructing the gradiometer probe and its electronics and performed the two calibrations (vectorial and scalar) and astatization of the 6-probe axial gradiometer. The calibration results, after compensating on the temperature drifts described above, were then used for gradiometer astatization and calculations of higher order gradients in order to suppress the environmental noise.

IEEE TRANSACTIONS ON MAGNETICS, VOL. 48, NO. 4, APRIL 2012 1317

Suppression of Environmental Noise in Magnetopneumography by the Use of Higher Order Gradients

Jiří Tomek[1,2], Antonín Platil[1], Michal Janošek[1], Aleš Zikmund[1], and Pavel Ripka[1]

[1]Czech Technical University in Prague,Prague, Czech Republic
[2]General University Hospital in Prague, Prague, Czech Republic

Magnetopneumography is a noninvasive method for examining contamination of metal workers' lungs by ferromagnetic dusts. Our aim is to estimate not only total amount but also spatial distribution of the dust. We use fluxgate magnetometer for measuring remanent field of contaminated volume (current experiments are mostly on phantoms). For earlier experiments we used a simple 6-channel magnetometer with improvised probe holder and we used multiple first order gradients. However, geometrical and other instabilities forced us to upgrade both the mechanical assembly and the fluxgate electronics. The environmental noise from relatively close sources is apparent even in first order gradients and thus—now with more stable electronics—we evaluated second order gradients in order to obtain a better signal.

***Index Terms*—Biomagnetics, magnetic field measurement, magnetometer, noise.**

I. Introduction

MAGNETOPNEUMOGRAPHY is a diagnostic method proposed in the 1970s by Cohen [1]–[3]. The aim is to examine the amount (and spatial distribution) of ferromagnetic dust within the lungs of metal workers. The subject is first exposed to a strong dc magnetic field in order to magnetize the dust. After that, remanent magnetic field distribution above the subject's chest is measured and the data is used for estimation of the dust load.

Typically, a superconducting quantum interference device (SQUID) is used as the sensor [1]. In contrast, in our research we use much more affordable fluxgates (we are also limited to work in an unshielded environment). The setup is similar to that described in [4]. However, in our setup we use nonmagnetic glass-fiber positioning bed and a multichannel fluxgate magnetometer used as a gradiometer.

In our case, gradients are calculated in software from independent absolute field sensor data because this approach provides better sensor stability. Evaluation based on gradients helps to focus on signal from close sources (dust in lungs) while interference from distant sources like Earth's field variations is rather homogenous and thus greatly suppressed. Unfortunately, some noise from not-so-distant sources (e.g. urban traffic, electric traction) is still present.

The estimation of ferromagnetic dust load within lungs from measured magnetic data, i.e., the calculation of the *inverse problem*, is rather problematic and strongly affected by noise. In our model we work with discrete magnetic or nonmagnetic cube volumes within simplified lung phantom. We tested various approaches like neural networks [5]–[8] genetic algorithms and even direct inversion calculation [9]. Properly trained neural network provides some robustness against noise, but for target resolution better than say 10 volume elements (voxels) it has excessive demands on computer memory. Direct inversion has very small computing demands, but it is rather vulnerable to noise.

Our aim is thus to achieve better noise suppression in field measurement by evaluating higher order gradient signals instead of the simple first order gradients used so far. Fortunately, the model and the direct inversion calculation method we test are quite flexible and thus can be adapted to new types of input data.

Manuscript received August 15, 2011; accepted October 03, 2011. Date of current version March 23, 2012. Corresponding author: A. Platil (e-mail: platil@fel.cvut.cz).

Color versions of one or more of the figures in this paper are available online at http://ieeexplore.ieee.org.

Digital Object Identifier 10.1109/TMAG.2011.2172200

Fig. 1. The new robust 6-probe holder made of PEEK.

II. Setup

Our setup uses 6-channel fluxgate magnetometer with ring-core fluxgates. Initial experiments were made with improvised probe holder where individual sensors were suspended on a pair of tense plastic strings with sensors 100 mm apart [10]. That setup had limited geometrical stability and thus we replaced it with a new robust 6-probe holder made of PEEK GF-30 glass-filled material in order to achieve better stability of the gradiometer parameters—see Fig. 1.

TABLE I
COMPARISON OF RESULTS OF SCALAR (SUFFIX S) AND VECTORIAL (SUFFIX V) CALIBRATION. THE ANGULAR DEVIATIONS ARE SHOWN WITH RESPECT TO FIRST CHANNEL

CH No.	S_S [V/T]	S_V [V/T]	α_{1V} [°]	α_{2V} [°]	α_{1S} [°]
1	145998	145978	0	0	0
2	146243	146199	-0.11	-0.09	-0.09
3	145981	145881	0.15	-0.17	0.18
4	145505	145602	0.81	-0.58	0.815
5	146146	146201	-0.20	0.12	-0.285
6	145689	145674	0.63	0.69	0.66

Fig. 1 shows the vertical holder with individual fluxgates suspended above the nonmagnetic positioning bed. The gradiometric base is 100 mm. A round mirror is attached in the central part; it was used together with a laser beam for mechanical stability testing and later for calibrations. A small platform is attached on the top of the holder, with two additional perpendicular fluxgate probes (PCB racetrack type [11]) that were later used for calibration procedures and for testing of possible horizontal field variation influence on measurement.

The improved mechanical stability facilitated testing of signal stability that provided hints for further improvement of the fluxgate signal processing electronics, mainly the gain drift of individual channels. There still remains some thermal dependence caused by electronics; however, it could be compensated in data post-processing.

III. GRADIOMETER CALIBRATION

The setup (sensors and electronics) has been calibrated using scalar field method [12] where sensitivities and angular deviations of individual sensors from the reference frame were established. The whole setup with 6 gradiometer and 2 perpendicular sensors was carefully rotated in a magnetically quiet and gradient-free location; the results were simultaneously sampled at 100 Hz to avoid problems with position instability (the setup was rotated manually). The scalar value of magnetic field was monitored with an Overhauser magnetometer. The results of two consequent scalar calibrations are comparable to 15%, which still indicates some problems in location homogeneity (the required homogeneous spherical volume has over 1.2 m in diameter in this case). The results are summarized in Table I.

The scalar calibration results were independently checked by vectorial calibration using 2-m calibration coils (Pruhonice laboratory of CAS, Geophysical Institute) and a theodolite T using triangulation (Fig. 2). The gradiometer was first positioned in the middle of the coils and its position was aligned to X-axis by minimization of the AC response of perpendicular coils (y axis). The X and Y axes of the coil system have an orthogonality error better than 0.03° as estimated by scalar calibration [13]. The angular deviations were estimated in iterative steps using a simple triangulation procedure with the help of central mirror in the rotation axis. By marking the distance d from reference channel after each sensor alignment, it was possible to estimate the angular deviations α from the first channel axis. As the gradiometer was rotated only in one plane (XY), we estimated only one of the two angles—α_{1S}. Also, the rotation plane was not exactly aligned. However, the results are comparable within 18% with the angles obtained by scalar calibration (Table I).

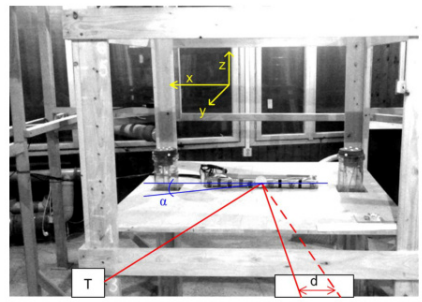

Fig. 2. Verification of the gradiometer sensors angular deviations using 2-m coil system and triangulation.

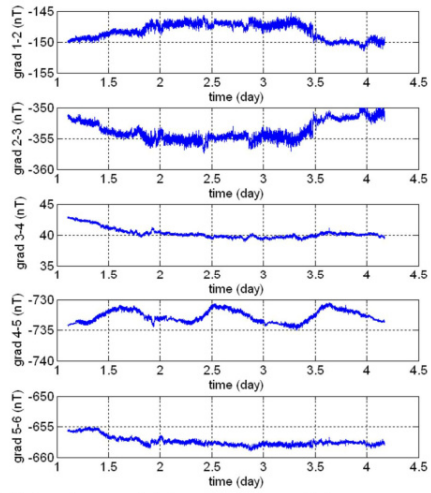

Fig. 3. Long-term record of observed first order gradients.

IV. EXPERIMENT

As we work in an unshielded environment, our setup is exposed to considerable industrial noise of urban environment (traffic, etc.), especially in daytime. The difference in readings from neighboring sensors 100 mm apart may vary by 5 nT (yielding variation in first order gradient of 50 nT/m). In the nighttime it is usually reduced to 1 nT (or 10 nT/m).

Fig. 3 shows a 3-day record of measured first order gradients in laboratory (initial warm-up period is omitted). For easier interpretation, only the difference between channels is shown (not in gradient units). The data were compensated for thermal drift using additional thermal measurement. Some channels (especially 4–5) seem influenced by horizontal field variations due to imperfect vertical orientation of sensor axis.

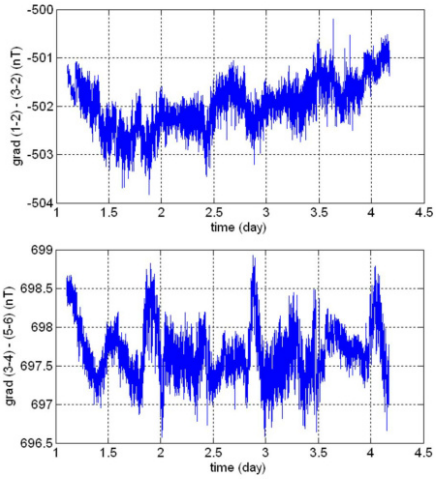

Fig. 4. Long-term record of selected second order gradients (more detailed scale).

Fig. 4 shows a detailed look of selected second order gradients (differences between channels) that provide slightly better results.

Unlike the perfect mathematical model of the setup used for testing of inversion (generation of forward model data and direct mathematical calculation or neural network inversion of them) [9], [10], the gradiometer's probes are not precisely 100 mm apart; their angular misalignment and the misalignment of the gradiometer to the bed result in serious differences in the measured data in comparison to the ideal mathematical model. We already compensate for positioning errors and for any misalignment of the phantom in the considered volume. Inversion illustrated in [9] which works perfectly on the model, even with added noise, was not capable to estimate physical phantom sources. The phantom source consisted of 2 layers with 60 cubes containing 5 elementary magnetic cubes each with magnetic moment 2400 μAm^2 measured in Helmholtz coils [14]. These elementary cubes have volume of 64000 mm^2 (side 40 mm). We have used this low resolution in order to simplify the modeling as well as phantom testing.

Compensation for all the imperfections in the setup is laborious. The solution is to prepare inverse model using real phantom testing data. This means to calibrate the setup by representative set of phantom configurations. Afterwards, the inversion should provide reasonable estimates of random distributions of magnetic cubes.

We have modeled that the inverse algorithm works well with added random noise of up to 2.6 nTp-p to the second order gradient, e.g., the gradient "(3-4)–(5-6)" has peak-to-peak amplitude 50 nT/m. The inverse algorithm when calculated with the data from the real phantom measurements, where the noise is below this value, should thus theoretically work well.

V. Discussion

Simple mathematical modeling shows that use of first order or higher order gradients cannot suppress random noise originating from individual independent measurement channels (in fact, it decreases useful signal and preserves random noise and thus signal-to-noise ratio becomes worse). However, in practice a substantial part of the observed noise is correlated between channels and therefore it can be suppressed by gradient measurement processing. We achieved moderate improvement in measurement noise by use of selected second order gradients over previous results with first order gradients.

We suppose to further reduce noise level by introducing compensation for horizontal field and then collect representative calibration data to obtain an inverse model for the real setup.

Acknowledgment

This work was supported by the research program No. MSM6840770012 "Transdisciplinary Research in the Area of Biomedical Engineering II" of the CTU in Prague, sponsored by the Ministry of Education, Youth and Sports of the Czech Republic.

References

[1] D. Cohen, "Measurements of the magnetic fields produced by the human heart, brain and lungs," *IEEE Trans. Magn.*, vol. 11, pp. 694–700, Mar. 1975.

[2] D. Cohen and I. Nemoto, "Ferrimagnetic particles in the lung, part 1: The magnetizing process," *IEEE Trans. Biomed. Eng.*, vol. 31, pp. 261–273, Mar. 1984.

[3] D. Cohen, I. Nemoto, L. Kaufman, and S. Arai, "Ferrimagnetic particles in the lung, part II: The relaxation process," *IEEE Trans. Biomed. Eng.*, vol. 31, pp. 274–285, Mar. 1984.

[4] Y. Zheng, M. Kotani, Y. Utsukawa, and T. Nakadate, "Development of a portable pneumomagnetic measurement device," *Neurol. Clin. Neurophys.*, vol. 10, pp. 1–5, Nov. 2004.

[5] J. Tomek, A. Platil, and P. Ripka, "Application of neural networks inversion in magnetopneumography," *Int. J. Appl. Electromagn. Mech.*, vol. 26, pp. 285–290, Sep. 2007.

[6] J. Tomek, A. Platil, and P. Ripka, "Magnetopneumography—Advances in measurement procedure, modeling and inversion using artificial neural networks," *Int. J. Appl. Electromagn. Mech.*, vol. 25, pp. 401–406, May 2007.

[7] P. Ramuhalli, L. Udpa, and S. S. Udpa, "Electromagnetic NDE signal inversion by function-approximation neural network," *IEEE Trans. Magn.*, vol. 38, pp. 3633–3642, Nov. 2002.

[8] M. Popov, "Data continuation for the explicit solution of an inverse biomagnetic problem," *IEEE Trans. Magn.*, vol. 38, pp. 3620–3632, Nov. 2002.

[9] J. Tomek and A. Platil, "Magnetic field inversion for magnetopneumography," *Sensor Lett.*, vol. 7, pp. 423–428, Jun. 2009.

[10] J. Tomek, A. Platil, and P. Ripka, "Multiple layer scanning in magnetopneumography," *IEEE Sensors J.*, vol. 9, pp. 383–389, Apr. 2009, 2009.

[11] M. Janošek and P. Ripka, "PCB sensors in fluxgate magnetometer with controlled excitation," *Sens. Actuators*, vol. 151, pp. 141–144, Apr. 2009.

[12] J. M. G. Merayo, P. Brauer, F. Primdahl, J. R. Petersen, and O. V. Nielsen, "Scalar calibration of vector magnetometers," *Meas. Sci. Technol.*, vol. 11, pp. 120–132, Feb. 2000.

[13] A. Zikmund and P. Ripka, "Scalar calibration of 3D coil system," *J. Elect. Eng.*, vol. 61, no. 7/s, pp. 39–41, Dec. 2010.

[14] S. R. Trout, "Use of Helmholtz coils for magnetic measurements," *IEEE Trans. Magn.*, vol. 24, pp. 2108–2111, Jul. 1988.

8.2.1 Gradiometer astatization – recalculation to orthogonal frame

In the magnetopneumography task, the gradiometer is in a fixed vertical orientation to the Earth's magnetic field, and its performance is mainly determined by the magnetic noise - its amplitude and its homogeneity. We did not find any significant improvement when using precisely astatized data and thus the results were not presented in the previous article [J5].

However, if the gradiometer is used for magnetic anomaly detection, where the gradiometer is usually moved, the calibration and subsequent astatization of the gradiometer influences its performance. Data obtained from the scalar calibration described in previous chapter and in the article were used for the gradiometer astatization – each of the Z-sensors response was recalculated to the orthogonal frame. Because of the nature of scalar calibration, where the gradiometer was rotated in Earth's magnetic field, the performance of gradiometer can be studied well using the calibration data.

Using the same naming convention as above, the 4-3 gradient (gradiometric base of 10 cm) is evaluated in Fig. 8.6. The data are from the calibration procedure, where the sensor is rotated and inclined to cover the whole sphere of angular alignment to the Earth's field vector. When the astatization is based only on calibrated sensitivities, the parasitic homogeneous response is up to 8000 $nT \cdot m^{-1}$ (corresponding to 800 nT sensor difference) if the axial (aligned) field varies in the ±40 μT range. However, if the angular misalignments are also considered, the response decreases down to ±45 $nT \cdot m^{-1}$, which corresponds to ±4.5 nT sensor difference. This remaining error is mainly due to the uncertainty of the scalar calibration – the calibration residua were up to 20 nT_{rms}, which was supposed to be caused by the gradient at the calibrating location.

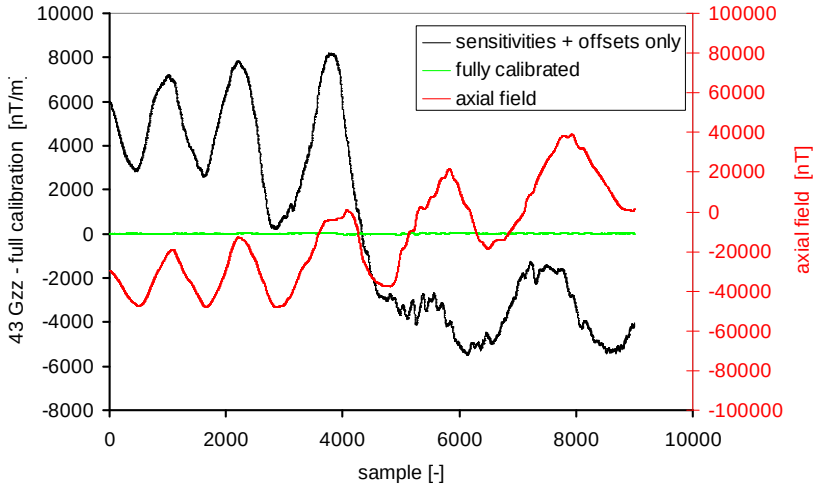

Fig. 8.6 –Effect of angular misalignments on the gradiometer residua in a homogeneous field

In order to confirm the hypothesis of a magnetic gradient at the location, the gradient was calculated for different gradiometric bases. We can use any two of the six sensors to build a "synthetic" gradiometer with a 10, 20, 30, 40 and 50-cm gradiometric base, respectively. Fig. 8.6 shows that the gradient response is almost identical for all 3 gradiometric bases with different sensors: the response is mainly due to the presence of the magnetic gradient at the calibration site. The noise modulated on gradients 6-1 and 6-2 is influenced by sensor #6: the noise was found to be due to the nearby orthogonal sensors X and Y, which used a separate electronics with a different excitation frequency [J20].

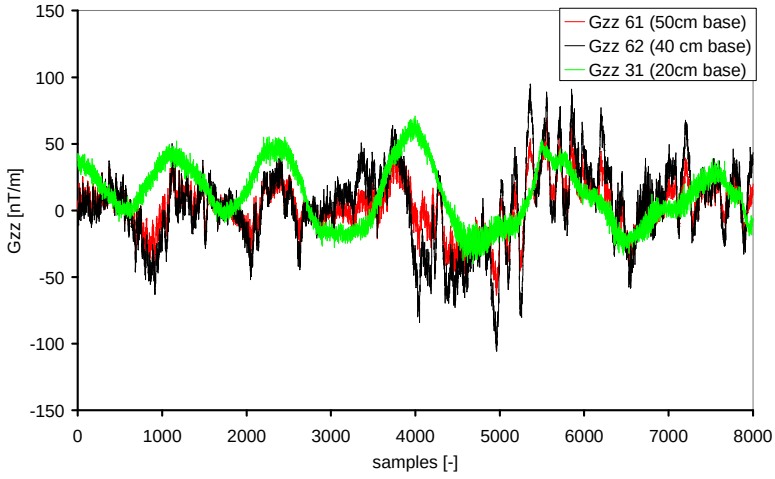

Fig. 8.7 – Essentially the same error for different bases suggests that the calibration field was not truly homogenous

8.2.2 Alternative linearized astatization

An idea used in SQUID gradiometers by [Chwala 2012] was adopted to further simplify the gradiometer calibration and astatization. Let us take magnetometer readings M_{Z1} and M_{Z2} (in engineering units, EU) from the two vertical sensors forming a gradiometer with base d, and two additional readings, M_X and M_Y, from the orthogonal sensors in the perpendicular plane (these readings are already corrected for the sensor offsets to further simplify the calculation).

We can define the uncorrected gradient $G_{ZZ} \approx \partial B_z/dz$ if no astatization was used:

$$G_{ZZ} = \frac{B_{Z1} - B_{Z2}}{d} = \frac{1}{d}\left(\frac{M_{Z1}}{S_{Z1}} - \frac{M_{Z2}}{S_{Z2}}\right) \tag{8.3}$$

Assuming that the gradient is negligibly small compared to the common-mode field, we can choose for M_Z and S_Z one of the two values to get the astatized output:

$$Gcorr_{ZZ} = G_{ZZ} - \alpha \cdot \frac{M_X}{S_X} - \beta \cdot \frac{M_Y}{S_Y} \cdot - \chi \cdot \frac{M_Z}{S_Z} \tag{8.4}$$

It is evident that precise calibration of sensitivities S_X and S_Y (EU/T) is not necessary in this case – field values can be used directly in engineering units. Also the knowledge of the Z axis sensors sensitivities is needed for estimating the raw G_{ZZ} gradient only but not for the astatization. The offsets of Z, X and Y sensors can be obtained in a magnetic shield. Let us add second-order terms in addition to the astatization of [Chwala 2012] to obtain a better fit. We get:

$$Gcorr_{ZZ} = G_{ZZ} - \begin{bmatrix} k_1 & k_2 & k_3 \end{bmatrix} \cdot \begin{bmatrix} M_X \\ M_Y \\ M_Z \end{bmatrix} - \begin{bmatrix} k_4 & k_5 & k_6 \end{bmatrix} \cdot \begin{bmatrix} M_X^2 \\ M_Y^2 \\ M_Z^2 \end{bmatrix} \tag{8.5}$$

Having a set of calibration measurements similar to that presented in [J5] in a gradient-free location, thus assuming $Gcorr_{ZZ}=0$, we get a set of equations forming a linear system

$$\begin{bmatrix} k_1 & \dots & k_6 \end{bmatrix} = \begin{vmatrix} M_X \\ \dots \\ M_Z^2 \end{vmatrix}^{-1} G_Z \tag{8.6}$$

In a set of N equations from the scalar calibration we have N values of G_{ZZ} and 6xN values of M_X, M_Y, M_Z, M_X^2, M_Y^2, M_Z^2. A least-squares method or an inverse function based on SVD decomposition was used with the same result to obtain the k_i coefficients in MATLAB. A comparison of the gradiometer response during the same scalar calibration run using the astatization with subsequent orthogonalization of the Z_1 and Z_2 readings, the linearized astatization approach of [Chwala 2012] and the proposed method with second-order terms is shown in Fig. 8.8.

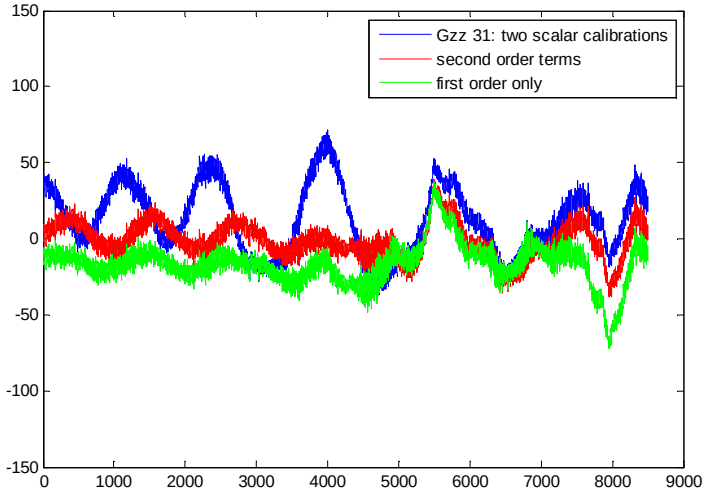

Fig. 8.8 –Astatizated gradiometer output, using two scalar calibrations (blue) and first (green) or second-order (red) linearized astatization (red)

From Fig. 8.8, it is evident that the residua from the modified astatization were even lower than of the classical approach of two calibrated Z values. The explanation lies in the uncertainty of the two scalar calibrations used for calculating the Z values.

If we consider the gradiometric base of 20 cm (sensors 3 and 1) and the 50 nT_{pp} residua for the 48,000 nT common-mode field during the calibration (Fig. 8.8), we see that the CMRR (Eq. 1.15) improved to $20\log\frac{48\cdot10^{-6}}{50\cdot10^{-9}\cdot0.2}=73dB$, even with the on-site gradient proved in Fig. 8.7.

8.2.3 Astatization using spherical misalignment angles

Another approach to astatization, which will not be evaluated here, was used by [Merayo 2001], where the two spherical misalignment angles between the Z sensors are considered.

$$G_{corr}=G-a_0+a_1B_z+a_2|B|(\theta\cos\theta_0\cos\varphi_0-\varphi\sin\theta_0\sin\varphi_0) \quad (8.7)$$

θ and φ are the misalignment angles of the second Z sensor, and θ_0 and φ_0 are the spherical angles defining the orientation of the vector with scalar value |**B**| to the first Z sensor (see Fig. 8.9).

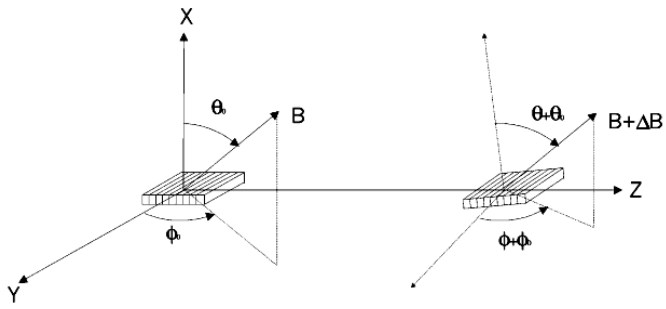

Fig. 8.9 – Definition of the spherical angles, from [Merayo 2001]

The use of Eq. 8.7 is complicated by the need to know the orientation and value of the vector **B**, and the two misalignment angles obtained either by measurement [Merayo 2001] or by a complete scalar calibration (section 8.2.1). To solve the equation, two (aligned) orthogonal X and Y sensors are again needed to establish the two θ_0 and φ_0 angles defining the vector **B** orientation. The calculation is therefore in turn more complicated than using the linear astatization approach described previously. It is however considered later in the case of a single-core gradiometer (10.6.2), where it can be simplified under certain circumstances.

9 A compact, low-noise fluxgate sensor

So far, the author has studied gradiometers using off-the-shelf 30×8×1 mm^3 PCB fluxgates [J20] and 35×30×10 mm^3 ring-core fluxgates [Cerman 2003, Tomek 2009]. However, the design parameter for a compact gradiometer was overall sensor size ‹ 20 mm and sensor noise ‹ 10 pT·Hz$^{-0.5}$ @ 1 Hz – both of the parameters are not fulfilled by any of these sensors. Further miniaturization of the sensor was therefore sought. A flat, racetrack fluxgate sensor (Fig. 9.1) and a classical ring-core sensor (Fig. 9.2) have been developed by the author. Both use an amorphous $Co_{67}Cr_7Fe_4B_{13}Si_9$ tape provided by the Institute of Physics, Slovak Academy of Sciences (SAS), Bratislava.

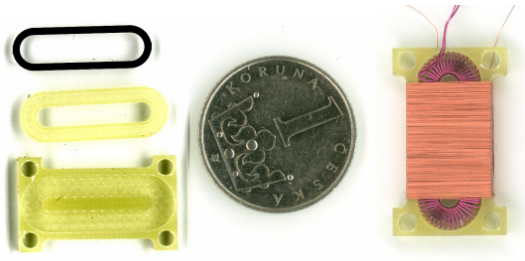

Fig. 9.1 –race-track fluxgate, the components (left) and an assembled sensor (right)

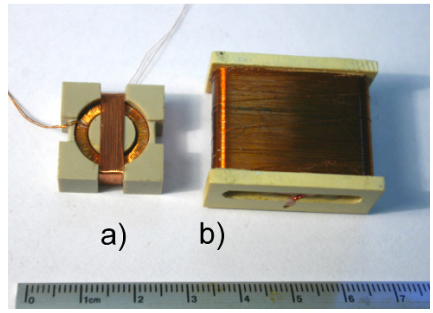

Fig. 9.2 – the ringcore sensor (a) compared with the sensor used in [Cerman 2003], [Tomek 2009] (b)

9.1 Flat race-track sensors

Race-track sensors are the most promising in terms of noise [Hinnrichs 2001]. The sensor was further miniaturized as compared to the PCB fluxgate in [J20]- the race-track core size is 8×15×0.025 mm^3 (Fig. 9.1). PCB technology was abandoned due to its high noise. The core was chemically wet-etched from the 20-mm wide amorphous tape. Unlike in the work presented in [Ripka 1993a], only single-sheet core was used in order to avoid further mechanical stresses and to keep a low demagnetization factor [Kubík 2008]. The core was fixed in a milled slot made from FR4 glass-fiber laminate using a drop of acrylic paint. Next, the excitation coil was wound around the race-track and the assembly was inserted into a 20×11×2 mm^3 milled holder made from the same material, where the pick-up/compensating coil is wound (Fig. 9.1). The offset temperature dependence, which is often a limiting parameter for fluxgate sensors, was measured in a thermostated non-magnetic shielding chamber allowing for –20°C to +80°C with a remanent field in the chamber less than 5 nT. The offset temperature coefficient was found as less than 0.05 nT·K^{-1} – see Fig. 9.3, which is a value comparable with the value of space-grade fluxgate sensors [Auster 2008]. The noise PSD was

measured as 10-12 pT·Hz$^{-0.5}$@ 1 Hz when using a 10-kHz, 600-mA p-p excitation current in the whole temperature range.

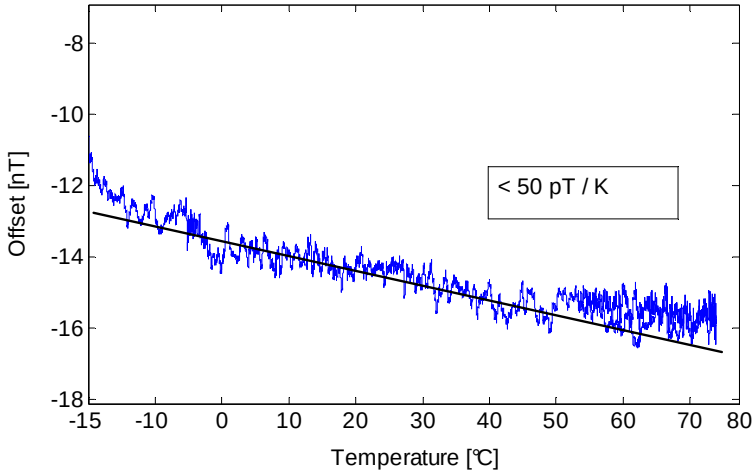

Fig. 9.3 – Offset temperature dependence of the developed race-track sensor

9.2 Tape-wound ring-core sensor

The diameter of the developed tape-wound ring-core was reduced to 12 mm. The tape cross-section was 2.5×0.025 mm^2. The magnetic ribbon was wound in a PEEK/MACOR sheath with typically 5 wraps only. After assembling the toroidal core to the machined PEEK support with the pick-up coil, the sensor was 20×20×8 mm^3 in size, see Fig. 9.2. The noise however increased up to 20 pT·Hz$^{-0.5}$ due to the size reduction - the bending stress and non-zero magnetostriction of the magnetic material [Weiner 1969, Butta 2014] certainly play a role. To lower the noise to match the state-of-the-art, perpendicular anisotropy [Nielsen 1991] was introduced by annealing. Magnetic field annealing of the ring assembly was developed and performed by SAS Bratislava, and the technology was then transferred to a dedicated laboratory at CTU in Prague. The noise after annealing decreased to 7 pT·Hz$^{-0.5}$, which is the lowest value found in the literature.

The following paper *"Field Annealed Closed-path Fluxgate Sensors Made of Metallic-glass Ribbons"* published in Sensors and Actuators in 2012 [J3], describes the development of the low-noise ring-core sensors by magnetic field annealing. Author's contribution was in designing and assembling the sensors, measuring their noise and providing feedback to the SAS group which was focused in magnetic material annealing and the MOKE analysis of the magnetic domains of each sample. MOKE analysis has also proved that annealing of the race-tracks did not bring a benefit because of the non-uniform domain structure after annealing.

Sensors and Actuators A 184 (2012) 72–77

Contents lists available at SciVerse ScienceDirect

Sensors and Actuators A: Physical

journal homepage: www.elsevier.com/locate/sna

Field annealed closed-path fluxgate sensors made of metallic-glass ribbons

Pavol Butvin[a,*], Michal Janošek[b], Pavel Ripka[b], Beata Butvinová[a], Peter Švec Sr.[a], Marek Kuzminski[c], Peter Švec Jr.[a], Dušan Janičkovič[a], Gabriel Vlasák[a]

[a] Institute of Physics, Slovak Academy of Sciences, 845 11 Bratislava, Slovakia
[b] Czech Technical University in Prague, 166 27 Praha, Czech Republic
[c] Institute of Physics, Polish Academy of Sciences, 02-668 Warszawa, Poland

ARTICLE INFO

Article history:
Received 28 April 2012
Received in revised form 30 June 2012
Accepted 2 July 2012
Available online 8 July 2012

Keywords:
Field annealing
Fluxgate sensor
Metallic glass
Sensor noise

ABSTRACT

The possibilities to improve the performance of certain fluxgate sensor types are still not exhausted. Two types of closed-path sensors – ring core and racetrack – were checked to reveal risky combination of material and construction parameters, and means to optimize the combination were tested. One-step field annealing of Co-based metallic glass was chosen to acquire low-magnetostrictive material with anisotropy required to reduce noise by favoring magnetization rotation. Locally misaligned anisotropy promoted incoherent rotation and handicapped racetrack noise performance. Despite the risk of bending stress aggravated by small – 12 mm diameter, the ring cores fared better and reproducibly achieved noise 7 pT/√Hz @ 1 Hz when thoroughly fixed an annealed in an optimal sheath. As far as we know these are the lowest noise values achieved for this size of fluxgate sensors.

1. Introduction

Fluxgate sensors (magnetometers) are still the first choice when an accurate directional measurement of low-frequency medium intensity magnetic field should be performed without the need of shielding and cryogenic temperatures. Properties of the magnetic core material and its impact on sensor performance are the main scope of this work. Magnetic anisotropy together with its response to the induction method and material handling appears to be the most important property linked to the most haunted performance parameter – the noise. Extended experience (e.g. [1,2]) suggests preferring materials with low magnetostriction [1] and low Curie temperature [3]. Co–Cr–Fe–B–Si metallic glass fulfills the demands well. Since the noise (Barkhausen noise) comes from abrupt changes of magnetic flux, it is most often attributed to an abrupt domain-wall movement and several methods to suppress it are applied [4]. Induction of strong transversal anisotropy by stress annealing came to be the first choice for metallic glasses [1] to promote the magnetization rotation to the detriment of wall movement. Nevertheless, there are inherent limitations for the tape-wound ring cores, since for the anisotropy to be uniform it has to be induced in the straight ribbon prior to winding the core. Then the ribbon is submitted to additional bending stress at core winding. The magnetostriction desired here to be zero is still tricky due to its variation with the stress [5]. To avoid this problem, we chose field annealing that enables a tape-wound core to relax significant part of the bending stress. The sensor electronics used in tested prototypes adheres to the standard principles of bipolar AC excitation and evaluation of the output signal at its second harmonic frequency. Two forms of magnetic cores were used: true closed path racetrack and tape-wound toroid with a mean field path of 3–6 cm. It should be emphasized that the diameter of the used tape-wound ring-cores is 10-mm or 12-mm, which is less than the commonly used dimensions (17–25 mm diameter). The choice of these dimensions was given by demands for miniaturization by simultaneously keeping the good noise properties. However, the small diameter amplifies not only the bending-stress related problems, but also the symmetry issues in miniature ring-cores – the sensitivity to any 2nd harmonic distortion of the excitation current is high.

1.1. Field annealing

Magnetic anisotropy with easy magnetization axis directed transversally to the sensor principal field direction is widely used not to excite domain-wall movement that easily tends to be irregular and generate noise. The simplicity of the task to provide domain walls minimally sensitive to directional external field ends at the requirement of domains and 180° walls to be oriented perpendicularly to the field. Apparently, the anisotropy should be strong. But strong anisotropy (with large coefficient K_u) results in fine domains [6,7] and so in many walls. This accentuates the demand

* Corresponding author. Tel.: +421 2 5941 0560; fax: +421 2 5477 6085.
E-mail address: pavol.butvin@savba.sk (P. Butvin).

0924-4247/$ – see front matter © 2012 Elsevier B.V. All rights reserved.
http://dx.doi.org/10.1016/j.sna.2012.07.001

Table 1
Magnetic parameters of Co-based metallic glass ribbons used in fluxgate sensor cores.

Material & condition	Magnetostriction λ_s	Curie temp. T_C [°C]	Saturation Bs [T]	HRA anisotropy [J/m³]	Permeability μ_{eff}	Noise spect. density [pTrms/√Hz] @ 1 Hz	
						RT	TOR
#1 As-cast	−5.2 e−7	270	0.53	~0	–	–	10
#1 Annealed	−6.0 e−7	282	0.55	22	6800	–	5
#2 As-cast	−2.0 e−7	282	0.61	11	16400	8	10
#2 Annealed	−5.0 e−7	291	0.63	31	5600	70	8

of domain-structure homogeneity not to provide misaligned walls. The anisotropy induced by stress annealing in Co-based metallic glasses is generally stronger [8,9] than the anisotropy by field annealing and can be, contrary to field annealing, further promoted by specific pre-annealing of the ribbon. However, the homogeneity of stress-annealing anisotropy meets with more limitations [10,11]. Apart from the macroscopic bending stress in a ringcore [12] (principally capable of inducing inhomogeneous magnetoelastic anisotropy), the straight-ribbon stress annealing itself meets with the risk of producing inhomogeneous anisotropy since the anisotropy energy is sensitive to the actual local stress applied during annealing. Due to problems with ribbon cross section geometry and the rather rough surface, it is difficult to provide an actually uniform stress. But neither the field annealing is quite risk-free in the context of annealing under inhomogeneous stress. Such a stress can come in ringcores tightly wound of as-cast ribbon if its inherent (preferentially longitudinal) relaxation or crystallization shrinkage is somehow hampered during annealing [13]. This risk tends to be negligible in a few-wrap ringcore annealed at a low temperature (<350 °C). Thus the annealing temperature requires a compromise too. Stress annealing uses higher temperature and often a pre-annealing to minimize magnetostriction coefficient [1]. Field annealing is principally limited to be performed below the Curie temperature and we did not consider looking for a simultaneous manipulation of magnetostriction. Nevertheless, field annealing omits at least one technological step (pre-annealing) and induces some domain wall stabilization [14] that is useful when low wall mobility and high start field is desired.

2. Experimental

Amorphous ribbons of $Co_{67}Cr_7Fe_4B_{13}Si_9$ alloy (#1) were prepared by planar-flow casting on air. To achieve modest difference of the Curie temperature T_C, 1 at.% of Cr was substituted by Mn in the reference alloy #2. The composition of ribbons was checked by ICP AES method. We used ribbons with 2.6/0.018 and 20/0.022 mm width/thickness. Racetracks (RT) were chemically etched from the 20 mm wide ribbon #2 center to give 2-mm "track" width and 30 mm long × 10 mm wide outer footprint (Fig. 1). The ring cores – toroids (TOR) were wound with 5–10 wraps into 10 mm inner diameter PEEK sheaths (Fig. 1). The ribbon was not glued or fixed in other means. Later, the ring cores were wound also into MACOR sheaths with 12-mm inner diameter, which were composed from two parts glued together, where the final gap for the core was 0.2 mm reducing the spring-effect of the ribbon to minimum.

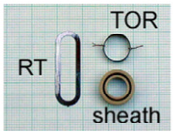

Fig. 1. Actual size ring core (TOR) and racetrack (RT) photographed on millimeter-scaled paper. The bare core was prior to inserting into sheath secured by makeshift wire fixture since no glue or welding was used. PEEK "slack" sheath is shown.

The standard field annealing used one temperature (250° or 265 °C) with the isotherm duration of 120 or 90 min and was performed in Ar atmosphere under ~10 kA/m transversal external field. Hysteresis loops were recorded on a digitizing hysteresisgraph where the sensors were excited by sine signal from a low-output-impedance amplifier. The energy density of hard-ribbon-axis (HRA) anisotropy (Table 1.) has been evaluated from saturation–remanence-loop outer cut-off area in 1st and 3rd quadrants. The noise parameters were measured in a standard fluxgate-sensor configuration with transformer-coupled, parallel-tuned excitation tank with 12-kHz driving frequency and variable excitation amplitude up to 10 kA/m p-p. The excitation winding had 120-turns of 0.2-mm-dia wire and the pickup-coil had 180-turns tuned by parallel capacitor at 2nd harmonic. A lock-in amplifier SR830 was used for the 2nd harmonic detection, its digital output was evaluated in the noise measurements. Domain structure was imaged by polarization microscope exploiting the magneto-optical Kerr effect (MOKE). Major domain magnetization direction is identified by contrast: full contrast is obtained when maximum magneto-optical sensitivity of the microscope is parallel or anti-parallel to domain magnetization. Curie temperature was determined by thermogravimetry. Etched-out circular samples were used to determine magnetostriction coefficient λ_s by calculating it from sample strain measured by a capacitance method.

3. Results and discussion

The higher T_C ribbon #2 is a 20 mm wide ribbon. When measured as full-width strip or in the etched racetrack geometry it shows slightly slant loop (HRA anisotropy ~11 J/m³) already in the as-cast state unlike ribbon #1 (see Fig. 2a). It appears that the bending stress σ slightly lowers the HRA anisotropy in the as-cast as well as in the annealed state – the loops of #2 TORs are less slant and/or display a steep low-field part (Fig. 2b). The reason of the poorly reproducible as-cast HRA anisotropy could be the as-cast structural anisotropy [15] or a creep anisotropy induced by intrinsic macroscopic stress acting in the still hot "fresh" ribbon at the end of casting. Similar resulting anisotropy is observed after no-intentional-stress annealing in some Fe–Nb–Cu–B–Si ribbons with the same sign of creep-induced anisotropy [16]. In any case, the as-cast-borne magnetic anisotropy is not homogeneous and it comprises, apart from HRA, an easy-ribbon-axis (ERA) component too.

The persisting ERA component prevents the domains to align perfectly transversally to the ribbon axis after the field annealing (see Fig. 3a, right). This is not the case of narrow ribbon #1 with its upright as-cast loop (Figs. 2a and 3a left). As seen by comparison of #1 loops in Fig. 2a and b, bending stress acting through magnetoelastic interaction induces the coexistence of HRA and ERA components. The stress appears to support preferentially the already present ERA component in ribbon #2. This is seen well by comparing Fig. 3a (right) and c. Since the strips of #2 were longitudinally cut to match the width and demagnetization factor of the

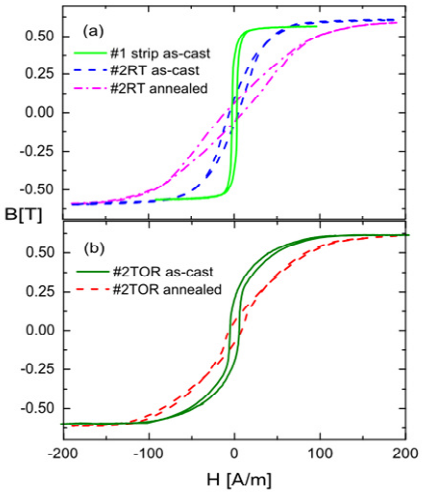

Fig. 2. Loops (1 kHz) of differently shaped samples of material #2. Loop for as-cast material #1 is plotted as reference to show different as-cast anisotropy without additional bending stress (therefore strip sample). Indicated samples were annealed at 265 °C for 90 min.

narrower #1 and the domain tilt (10° from transverse) is slightly greater than for etched RT (Fig. 3b – ~5° tilt), one can suspect remnants of shear stress to assist the ERA anisotropy component. However, the comparison of adjacent cut narrow strips with the genuine-width (20 mm) strip of ribbon #2 showed only minor differences (± 1 J/m^3) of the HRA anisotropy. This excludes a residual stress possibly induced by cutting as the reason of the observed tilt of transversal domains. Moreover the comparison shows that the field used at the field annealing saturated the ribbon transversally and did not allow different demagnetization factor to show up on 20 mm down to 2.6 mm wide ribbons.

Fig. 2a and b and especially Fig. 3c point to the bending stress as the major risk factor, which deteriorates a tilted linear loop and supports unwanted ERA anisotropy component despite of low material magnetostriction. Clear difference is seen in Fig. 4 to come from additional (applied after annealing) bending stress. The additional bending stress also disturbs the domain wall stabilization as seen by comparison of Fig. 3a (right) and c – the walls and domains visibly tilt by bending and still more tilted by longitudinal external field, the walls move easily. Different response to longitudinal field is observed without bending – it will be commented below at RT–TOR comparison.

Nevertheless, the bending stress in ring cores might not to be relaxed enough at below-T_C temperatures used at the annealing, although the "zero additional stress" loop (Fig. 4 – TOR #1P3) is already looking fine. Fig. 5a shows the comparison of field-annealed 5-wrap cores in MACOR tight sheaths (TOR #1M4) and 10-wrap core in PEEK slack sheath (TOR #1P3). The comparison was intended to identify whether the different thermal expansion of MACOR and the ribbon does not cause significant thermal stress in the core to show up consequences to the resulting anisotropy. The small difference seen between the corresponding loops does not clearly represent either the slightly different annealing or a thermal stress result. The difference rather reflects somewhat poorer reproducibility of cores annealed in slack PEEK sheaths. Three cores wound of consecutive ribbon sections and annealed in the "taut" MACOR sheaths (#1M4 is a member of the trinity) responded with practically matching loops. To test further the residual-stress suspicion, differently wound field-annealed ring cores were measured and then released from the sheath to see whether they reveal residual stress by partial unwrapping. Relatively special portion of the ribbon – bulging notably the wheel side out – has been chosen and one of the two cores – #1P4 – was wound air-side up and the other – #1P5 – wheel-side up. Notable difference is observed between the loops – Fig. 5b. Unwrapping showed up different too – the wheel-side-up core unwrapped to four times larger diameter when pulled out from the sheath whereas the air-side-up core merely doubled its diameter. One can conclude that the 265 °C annealing temperature is not enough to relax the bending stress completely and if the core is wound wheel-side up, the residual stress appears still larger. Unfortunately, we are so far not able to recognize for sure, which effects are responsible for the low-field bellies on loops of Fig. 5b.

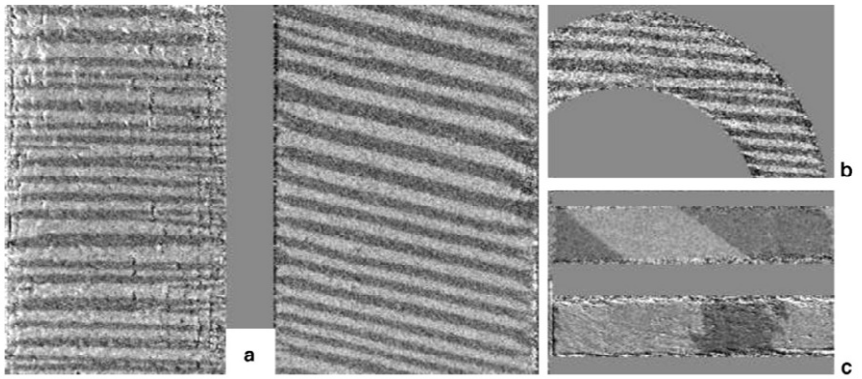

Fig. 3. Domain patterns of equally field-annealed samples: (a) full genuine width strip of ribbon #1 (left) and cut-width strip of #2 (right), (b) RT (half the magnification of (a) or (c)), (c) strip of #2 bent to TOR curvature after being annealed as straight strip: no external field (upper) and vertical bias field applied (lower). Ribbon axis always vertical, major domain magnetization horizontal for (a), (b), vertical for (c).

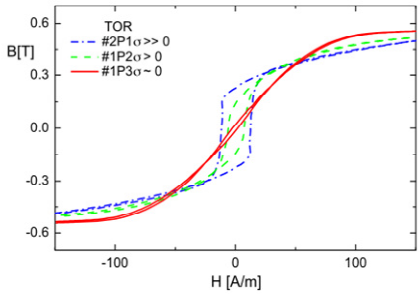

Fig. 4. Loops (40 Hz) of equally field-annealed (2 h at 250 °C) ring cores wound of equally long ribbon sections. Whereas #1P3 ring core was annealed and measured within the 10-mm-diameter sheath, the #1P2 and #2P1 ring cores were annealed as ~30-mm-diameter rings but measured inserted into equal 10-mm-diameter sheaths (after thorough diameter reduction). Note that ribbon #2 is ~20% thicker than #1.

3.1. Comparison of racetracks to toroidal cores (RT–TOR)

The most obvious difference between TOR and RT is the advantage of the latter that no bending stress is induced since a ready-to-use RT core is etched from a single planar sheet (ribbon). Fig. 6, however, shows the principal risks of a field-annealed racetrack: The U-turn part shows easy direction along the sensor exciting field, which promotes domain wall movement. Moreover, there are remnants of incoherent rotation over the whole RT – the medium black density indicates distinct areas magnetized approximately perpendicular to magneto-optical sensitivity, thus parallel to the exciting field whereas the rest area is still controlled by the induced transverse anisotropy. Due to experimental limitation – external field is directed like field to be measured, not sensor exciting field – Fig. 6 does not display the expected marked domain wall movement in U-turn part. Nonetheless we observed easy wall movement on no-field-annealed straight strip samples if external field was applied along the annealing-stabilized walls (not shown). Thus the wall stabilization significantly hampers their movement under large-angle external field, but is not efficient enough to block the wall movement under low-angle field. Recalling Fig. 2a, the RT drawbacks appear to correlate to the low-field "belly" on the loop in annealed RT. If compared to TOR, field-annealed RT performed worse (loops, noise) with slightly better as-cast results.

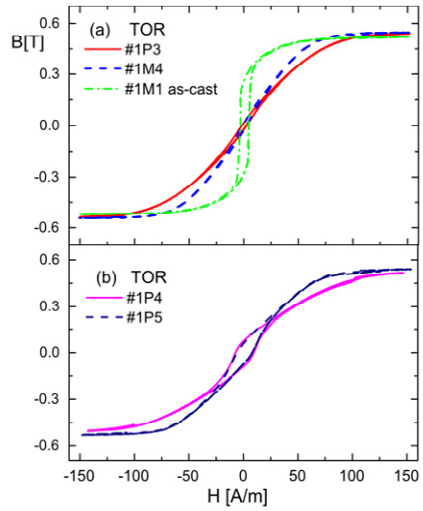

Fig. 5. Loops (200 Hz) of differently treated ring cores in different sheaths (P for PEEK, M for MACOR). (a) #1M4 represents well-reproducible "taut" sheath cores field-annealed at 265 °C compared to as-cast core #1M1 to show acquired anisotropy and to the best of "slack" sheath cores annealed at 250 °C. (b) Equally annealed (265 °C) but differently wound cores: #1P4 ribbon air side up, #1P5 wheel side up.

3.2. Noise performance

The noise performance of TOR and RT as well appears clearly to correlate with the loop shape: Worse noise comes with the more pronounced low-field steep part ("belly") of the loop. This is seen clearly if Fig. 7 is compared to the loops (Fig. 4). According to previous paragraphs, we ascribe the deterioration of a slim linear loop to domain wall movement and/or incoherent rotation promoted mainly by (additional) bending stress.

Then the loops of Fig. 5 (differently wound cores) can be correlated to the noise results too: At 3 $A_{p\text{-}p}$ excitation (10 kA/m p-p), the noise at 1 Hz amounts to 40, 30, 6.7 pT/$\sqrt{}$Hz for TOR #1P5, #1P4, #1M4, respectively. One comment for the higher T_C material #2: It never showed lower noise than #1 – the best sensor of #2 ring cores presented noise around 12 pT/$\sqrt{}$Hz @ 1 Hz, though at still larger excitation current of 4 $A_{p\text{-}p}$ (not shown). However this is not enough to claim that we confirmed the variation of noise

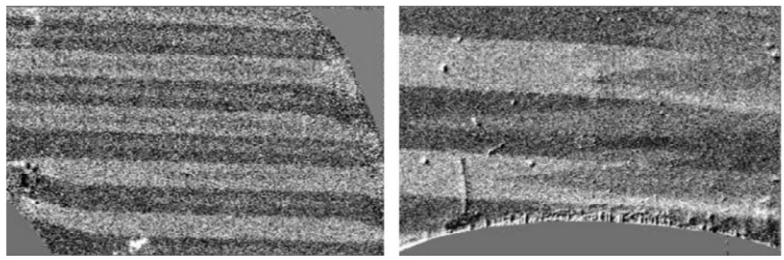

Fig. 6. Domain patterns of field-annealed RT of #2. Note 3-level black density – the medium one identifies areas magnetized at a large angle to horizontally magnetized majority domains. Left – weak vertical ac demagnetizing field leaves large-angle-magnetized domains on straight parts of RT. Right – 4× stronger field still leaves the domains on U-turn parts (but straight parts show horizontally magnetized domains only – not shown). Magnification is equal for left and right image.

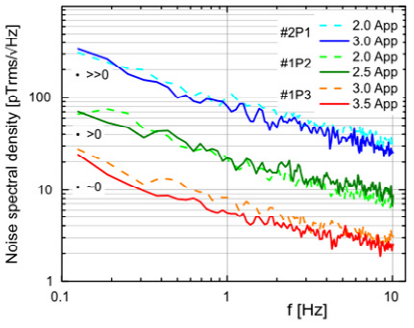

Fig. 7. Noise of FG sensors made of field-annealed ring cores (the same as in Fig. 4). Excitation field (12 kHz) scales linearly with the current quoted in the legend. Here the best noise figure – 5.5 pT/√Hz @ 1 Hz is shown by TOR #1P3.

with T_C found by Shirae [3]. The large noise figures for poorly fixed ring cores #1P4 and #1P5 point to still another factor – a stray field, which deteriorates the field symmetry and adds to the (residual) bending stress effect. Large free space was left within the PEEK sheath slot so the cores were able to move their wraps. (Wide slot aided the core withdrawal. We did not use any supporting springs.) The non-symmetric stray field can come from the ribbon ends with mismatched overlap, but is more probable to come from inhomogeneous bending stress along the core circumference, causing excessive noise. The noise of this sensor in a practical fluxgate mode could be higher also because of the large zero-field feedthrough due to core inhomogeneity, which compromised dynamic range of the second harmonic detector [17]. The poor symmetry also promotes the effect of any 2nd harmonic appearing in the excitation current. Better noise reduction by transversal field annealing is achieved in TOR if compared to RT (see Table). If ring cores are prepared thoroughly, their risks – the bending stress and poorer symmetry – can be minimized and the results are good and well reproducible. The slim linear loops displayed in Figs. 4 and 5a come from well-fixed (MACOR tight sheaths) and comprehensively wound ring cores. Reproducibility test with 5-wrap TORs (#1M2÷4) reveals equal loops and equally low noise (~7 pT/√Hz @ 1 Hz) for the three equally handled cores.

The large necessary excitation field poses already a limitation. The ensuing heating can compromise the parameter stability and it can disable the domain-wall stabilization, moreover it contributes to drift of sensor parameters. However we found it necessary for the current material to keep the saturation level deep enough to obtain low noise by applying the rule of thumb having 100× higher excitation level than the actual required field for saturation. When reaching this limit, the noise did not decrease any lower. The explanation assumed by Scouten [18] is based on macroscopic inhomogeneity in the ribbon, i.e. inclusions of magnetically hard regions. So far we have no noise-independent indication that this is the case with our ribbons. When compared to the results of Primdahl [19], we have to note that excitation level required for obtaining low noise in the case of field-annealed Co–Cr–Fe–B–Si ribbons is still higher than that for stress annealed Vitrovac 6025X used for the same purpose by the Danish group.

4. Conclusions

The few degree difference in T_C of the two alike materials studied is not enough to assess the importance of low Curie temperature for fluxgate sensor performance. However, low T_C poses certain risk for field-annealed ring cores not to provide optimal residual bending stress relaxation. The noise of field-annealed racetrack tapes was found higher after field-annealing due to the presence of longitudinal anisotropy in the U-shaped ends of the racetrack, which is inherent to the geometry. If we conclude the progress for the 10/12-mm ring-cores, we can state that:

- The potential of rapidly quenched ribbons for use in FG sensors is still not exhausted.
- Field annealing is a viable and competitive option to promote the desired magnetization rotation provided by transversal anisotropy in order to reduce Barkhausen noise. It also allows to field-anneal an already finished core-sheath assembly, possibly lowering the manufacturing costs and minimizing handling-induced stress.
- Despite problems with ribbon free ends and high sensitivity to even harmonics in the excitation, the major difficulty of ring cores with small diameters – bending stress – can be sufficiently reduced by field annealing to enable sensor noise as low as 5.5 pT/√Hz @ 1 Hz. According to our knowledge, these are the lowest noise figures achieved for fluxgate sensors of this size so far.

Acknowledgments

The authors are grateful for partial financial support by APVV grant SK-CZ-0078-11. Slovak authors thank also to VEGA grants Nos. 2/0056/11, 2/0111/11 and to FUN-MAT Center of Excellence. Czech authors thank also to Grant No. TA01010298 by the Technology Agency of the Czech Republic.

References

[1] O.V. Nielsen, P. Brauer, F. Primdahl, T. Risbo, J.L. Jørgensen, C. Boe, M. Deyerler, S. Bauereisen, A high-precision triaxial fluxgate sensor for space applications: layout and choice of materials, Sensors and Actuators A 59 (1997) 168–176.
[2] P. Ripka, Advances in fluxgate sensors, Sensors and Actuators A 106 (2003) 8–14.
[3] K. Shirae, Noise in amorphous magnetic materials, IEEE Transactions on Magnetics 20 (5) (1984) 1299–1301.
[4] S.B. Ubizskii, L.P. Pavlyk, The pendulum-like fluxgate magnetic field sensor, Sensors and Actuators A 141 (2008) 440–446.
[5] A. Siemko, H.K. Lachowicz, Comments on the indirect measurement of magnetostriction in low-magnetostrictive metallic glasses, Journal of Magnetism and Magnetic Materials 66 (1987) 31–36.
[6] J.D. Livingston, W.G. Morris, T. Jagielinski, Effects of anisotropy on domain structures in amorphous ribbons, IEEE Transactions on Magnetics 19 (1983) 1916–1918.
[7] A. Hubert, R. Schäfer, Magnetic Domains, The Analysis of Magnetic Microstructures, Springer-Verlag, Berlin, 1998.
[8] O.V. Nielsen, Effects of longitudinal and torsional stress annealing on the magnetic anisotropy in amorphous ribbon materials, IEEE Transactions on Magnetics 21 (1985) 2008–2013.
[9] K. Závěta, O.V. Nielsen, K. Jurek, A domain study of magnetization processes in a stress-annealed metallic glass ribbons for fluxgate sensors, Journal of Magnetism and Magnetic Materials 117 (1992) 61–68.
[10] J.D. Livingston, W.G. Morris, Magnetic domains on amorphous metal ribbons, Journal of Applied Physics 57 (1) (1985) 3555–3559.
[11] F. Alves, R. Barrué, Anisotropy and domain patterns of flash stress-annealed soft amorphous and nanocrystalline alloys, Journal of Magnetism and Magnetic Materials 254–255 (2003) 155–157.
[12] L.C. de Carvalho Benyosef, G.C. Stael, M. Bochner, Optimization of the magnetic properties of materials for fluxgate sensors, Materials Research 11 (2008) 145–149.
[13] P. Butvin, M. Hlásnik, P. Duhaj, B. Butvinová, K. Záveta, L. Kraus, K. Jurek, Journal of Magnetism and Magnetic Materials 112 (1992) 359–362.
[14] P. Butvin, B. de Ronzyová, Structural relaxation and domain wall stabilization in metallic glasses, Zeitschrift Fur Physikalische Chemie-Frankfurt 157 (1988) 329–333.
[15] D. Spilsbury, P. Butvin, N. Cowlam, W.S. Howells, R.J. Cooper, Some evidence for directional atomic pair ordering in a cobalt-based metallic glass, Journal of Materials Science and Engineering A 226–228 (1997) 187–191.
[16] B. Butvinová, P. Butvin, M. Kuzminski, M. Kadlečíková, A. Ślawska-Waniewska, Indication of intrinsic macroscopic forces affecting magnetic properties of Fe–Nb/Mo–Cu–B–Si ribbons, IEEE Transactions on Magnetics 48 (4) (2012) 1340–1343.

[17] R. Petersen, F. Primdahl, B. Hernando, A. Fernandey, O.V. Nielsen, The ring core fluxgate sensor null feed-through signal, Measurement Science & Technology 8 (1992) 1149–1154.
[18] D.C. Scouten, Sensor noise in low-level flux-gate magnetometers, IEEE Transactions on Magnetics 8 (1972) 223–231.
[19] O.V. Nielsen, J.R. Petersen, F. Primdahl, P. Brauer, B. Hernando, A. Fernandez, J.M.G. Merayo, P. Ripka, Development, Construction, Analysis of the ØRSTED fluxgate magnetometer, Measurement Science and Technology 6 (1995) 1099–1115.

Biographies

Pavol Butvin studied Physics, specialized in Solid State Physics and graduated from Faculty of Natural Sciences, J.A. Comenius University Bratislava in 1971. He joined the Institute of Physics, Slovak Academy of Sciences (SAS) Bratislava the same year and he is still active there as Department Deputy Head and Principal Investigator of various projects. In 1980, he acquired his RNDr and CSc (=PhD) degrees from the University and SAS, respectively. He was a member of the group awarded by the State Prize in 1988. From 1973 on, his interests are in magnetism of metals as well as in applied research of novel magnetic materials. In the recent years, he specializes in less-common properties (impact of various types of heterogeneity on magnetic properties) of modern soft-magnetic materials.

Michal Janošek was born in Varnsdorf, Czech Republic, in 1980. Graduated from the Faculty of Electrical Engineering, Department of Measurement – Measurement and Instrumentation, Czech Technical University, Prague in 2007. Currently working towards the PhD degree at the same department. His main research activity is the application of magnetic sensors in gradiometers and magnetometers. He is a (co)author of 15 journal papers.

Pavel Ripka was awarded an Ing. degree in 1984, a CSc degree (=PhD) in 1989, and was appointed a Full Professor in 2001 at the Czech Technical University, Prague, Czech Republic. He works at the Faculty of Electrical Engineering, Czech Technical University as a Full Professor, teaching courses in electrical measurements and instrumentation, engineering magnetism and sensors. He also worked as a visiting scientist at the Danish Technical University (1990–1993), at the National University of Ireland (2001) and at the Institute for the Protection and the Security of the Citizen, European Commission Joint Research Centre, in Italy (2005/6). His main research interests are magnetic measurements and magnetic sensors, especially fluxgate sensors. He was a General Chairman of the Eurosensors 2002 Conference.

Beata Butvinová, maiden name de Ronzyová, born 1955 in Nitra (Slovakia), graduated from the Faculty of Natural Sciences, J.A. Comenius University Bratislava, from the branch of Experimental Physics – Solid State Physics in 1980. Then, she joined the Institute of Physics, Slovak Academy of Sciences Bratislava. She received her RNDr degree from Comenius University of Bratislava and CSc = PhD degree in 1981 and 1987, respectively. Her current interests are in research of soft-magnetic properties of materials prepared by rapid quenching of the melt and operates several experimental methods. From 1998 she works in IP SAS Bratislava as Senior Researcher.

Peter Švec Sr. was born in Bratislava, Czechoslovakia, in 1955, graduated from the Faculty of Electrical Engineering, Slovak University of Technology, Bratislava, specialization Solid State Physics, in 1979 and received his PhD degree in Solid State Physics in 1986 and DrSc in 2004 from the Institute of Physics of the Slovak Academy of Sciences in Bratislava, where he is till active as Department Head and Projects Leader. His research interests are physics of metals, metastable disordered systems, especially those prepared by rapid quenching from the melt, phase transitions and quantitative structure analysis on atomic-scales.

Marek Kuzmiński graduated in 1986 from the Department of Technical Physics of the Warsaw University of Technology. In 1997 he received PhD degree in physics from the Institute of Physics, Polish Academy of Sciences (IF PAN), Warsaw. Present employment is at IF PAN as Senior researcher. Current fields of interest include magnetic amorphous and nanocrystalline materials, magnetic nanowires, magnetization processes, domain structures, giant magnetoimpedance and ferromagnetic resonance.

Peter Švec Jr., born 1983 in Bratislava, graduated from the Faculty of Electrical Engineering, Slovak University of Technology, Bratislava specialization Physical Engineering, in 2008. His PhD study in Solid State Physics at the Institute of Physics of the Slovak Academy of Sciences was focused on application of methods of high-resolution structure analysis to phase transformations in metallic glasses and is to be finished 2012.

Dušan Janičković graduated from Comenius University Bratislava and acquired his RNDr degree in 1981. Since 1984 he works as Research-methods Engineer in rapid solidification technology and amorphous metals production. He supervises the Laboratory of Rapid Solidification at Institute of Physics, SAS. Current filed of interest: development of new composite amorphous materials prepared by in situ rapid solidification of the melt.

Gabriel Vlasák, born 1937 in Vinodol, Slovakia, graduated from J.A. Comenius University Bratislava (branch of Experimental Physics) and acquired his RNDr degree from the same university in 1961. He gained his CSc (=PhD) degree from Institute of Physics Slovak Academy of Sciences Bratislava in 1977. Since 1994 he works at IP SAS Bratislava as Senior Researcher. His interest is in mechanical and magnetoelastic properties of amorphous and nanocrystalline materials.

9.3 The performance of different fluxgate sensor designs

The following paper *"Effects of Core Dimensions and Manufacturing Procedure on Fluxgate noise"* [J1] was published in 2014 in Acta Physica Polonica. The author has proved that the demagnetization factor [Primdahl 1989] has a significant influence on sensor performance as the sensor size is reduced. However, it was shown in the article that the manufacturing procedure has to be taken into account when comparing different sensor designs. The measurements and simulations were partially provided by Mr. Vyhnánek and Zikmund, respectively, and the SAS authors provided the annealed tapes for the different fluxgate designs – race-track and ring-cores with two diameters.

Vol. **126** (2014) *ACTA PHYSICA POLONICA A* No. 1

Proceedings of the 15th Czech and Slovak Conference on Magnetism, Košice, Slovakia, June 17–21 2013

Effects of Core Dimensions and Manufacturing Procedure on Fluxgate Noise

M. Janošek[a,*], J. Vyhnánek[a], A. Zikmund[a], P. Butvin[b], B. Butvinová[b]

[a]Dept. of Measurement, FEE, Czech Technical University in Prague, Technická 2, 166 27 Praha, Czech Republic

[b]Institute of Physics, Slovak Academy of Sciences, Dúbravská cesta 9, 84511 Bratislava , Slovakia

The effect of demagnetizing factor and manufacturing procedure on noise of the fluxgate probes, manufactured from metallic glasses, is presented. The fluxgate probes were either tape-wound, or flat, wet-etched ringcore and race-track geometries. When combining low demagnetizing factor and high enough cross-section of the probe, a minimum in the noise dependence can be found. For 50 mm ringcores, in such minimum the noise value as low as 7 pT_{RMS} in 0.1-10 Hz frequency band was achieved, which is very low for an as-cast tape, and has not been reported before.

DOI: 10.12693/APhysPolA.126.104

PACS: 75.75.–c, 75.30.-m, 75.50.–y, 07.55.–w, 75.70.-i

1. Introduction

The coupling of internal noise of the magnetic material to the noise of fluxgate sensors, manufactured from that material is ruled according to the commonly agreed practice, by the so called demagnetizing factor of the probe. This factor can be altered by changing the geometry of the probe (Fig. 1). For tape-wound sensors, core radius can be modified or the number of tape-turns can be altered. For ring-core and race-track geometries etched from tapes, changing the width of the annulus or stacking of the cores brings similar results.

The effect of the demagnetizing factor on noise was shown by Primdahl [1] for a given ringcore diameter of 17 mm. Tape-wound racetracks, studied in [2], were also optimized by altering the race-track geometry.

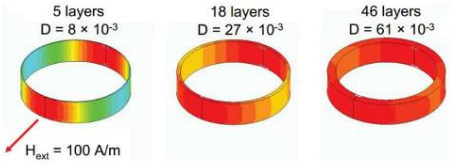

Fig. 1. Demagnetizing factor as a function of ringcore thickness (3D FEM simulation, the outer diameter (12 mm) is fixed).

However, mainly for ringcores with various diameters, the comparison is not straightforward: the bending stress, which becomes higher with smaller core diameter, is worsening the fluxgate probe noise. This can be handled either by appropriate zero-magnetostriction annealing [3], or at least by partially releasing the stresses during field annealing of the tape-wound core in its final form [4].

A different situation exists for flat cores wet-etched from a wide amorphous tape. In this case the bending stress does not affect the probe noise, however the smoothness of etching process and mainly the art of fixing the core to the bobbin influence the noise. Fluxgate probes with etched race-track cores were previously studied in printed-circuit-board (PCB) sensors; however the internal stresses due to embedding the core in the PCB laminate affected probe performance [5]. In [4] the authors have shown noise figure also for the race-track core which was not embedded in the laminate, however its performance was limited by excitation electronics. In this study, the working conditions were all the same for all studied sensors in order to facilitate the comparison of results.

2. Material and geometry selection

In this work, Vitrokov 8116 – a Co-Cr-Fe-B-Si metallic glass tape was used, with an average thickness of 20 μm and with tape widths of 2.6 mm (wound cores) and 20 mm (etched race-tracks).

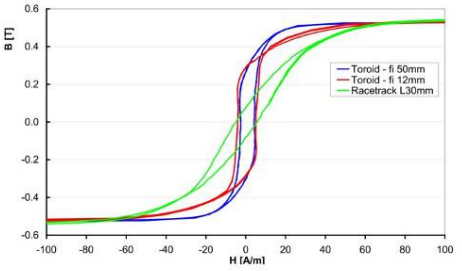

Fig. 2. *B-H* loops of the 3 core geometries.

*corresponding author; e-mail: janosem@fel.cvut.cz

For the tape-wound cores, the magnetoelastic effects can be seen by using the same material for 12 mm and 50 mm diameter (Fig. 2). From the B-H loops it is evident, that even for these tapes with magnetostriction of $\sim 1 \times 10^{-7}$ this effect is present.

As for the 2.6 mm tape width, the material did not show any appreciable macroscopic heterogeneity, which otherwise causes poorly reproducible inhomogeneous magnetic anisotropy, brought about by macroscopic stress between surfaces and interior of many Fe-based ribbons (e.g. Finemets). The absence of this heterogeneity in Co-Cr-Fe-B-Si has been verified by comparing hysteresis loops prior to and after surfaces removal when the ribbon thickness was reduced by $10 \div 15\%$ ($2 \div 3$ μm).

In the 20 mm tape however, the heterogeneity was present but still acceptable. The different B-H loop shape of the race-track in the comparison is evident but not caused by the tape macroscopic heterogeneity: the explanation lies in the as-cast anisotropy of the amorphous tape due to the manufacturing process, which is in the case of longitudinally etched race-tracks combined in both of the perpendicular branches of the race-track. An evidence for this behavior was shown in the MOKE pictures in [4].

4. Noise measurements – setup and results

The setup of electronics and operating conditions of the fluxgate probe were almost identical to that used in [4]. The resulting noise spectra for various tape thicknesses in the case of 50 mm ringcores obtained in a 6-layer magnetic shielding can, are shown in Fig. 3. To decrease the statistical error, an integral value of the noise in the frequency band of 0.1 to 10 Hz was calculated.

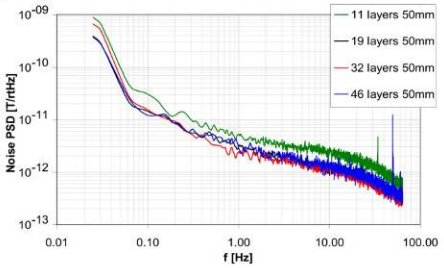

Fig. 3. Noise spectra of the 50 mm ringcore sensors.

The spectrum clearly maintains $1/f$ behaviour with lowpass filtering visible for frequencies above 12 Hz. The measuring procedure was done for the 50 mm cores in two tracks: 4 cores with different number of turns were produced and also one core was sequentially re-wound with decreased number of turns of the tape. The almost identical 50 mm results shown in Fig. 4 are thus independently obtained.

For 12 mm cores, there was a manufacturing problem of the bobbins, so only values for two demagnetizing factors are shown (5 and 10 turns). Although no dependence can be deducted, the overall increased noise, due to the bending stress is evident. This was further confirmed by the one-layer, 30 mm long race-track noise: absence of the bending stress and relatively low demagnetizing factor resulted in a noise comparable to that of 50 mm wound cores.

The results are in agreement with the behaviour found by Primdahl [1]. The noise for a given geometry slowly decreases with the decreasing demagnetizing factor up to a given minimum, from which it increases much faster.

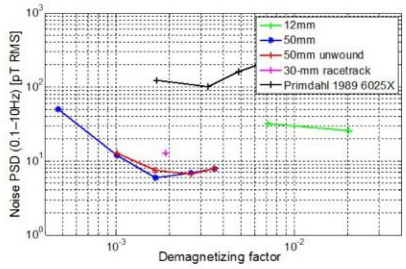

Fig. 4. Noise vs. demagnetizing factor for three geometries, including results of Primdahl for reference (he used 5, 10, 15 and 20 turns, respectively, on 17 mm diameter).

The authors offer the following explanation: as the cross-section of the magnetic material decreases in this case, also the signal-to-noise ratio of the whole sensor-electronics setup decreases, so the lower demagnetizing factor cannot bring a benefit anymore. Here the limitation was not the 5 nV lock-in amplifier noise, but rather remanent parasitic signal from unwanted even harmonics in the excitation current, which does not change when the core cross-section (and thus demagnetizing factor) is altered.

Acknowledgments

The authors are grateful for partial financial support by APVV grant SK-CZ-0078-11.

References

[1] F. Primdahl, B.Hernando, O.V. Nielsen, J.R. Petersen, *J. Phys. E: Sci. Instrum.* **22**, 1004 (1989).

[2] C. Hinnrichs, J. Stahl, K. Kuchenbrandt, M. Schilling, *IEEE Trans. Mag.* **37**, 1983 (2001).

[3] F. Primdahl, P. Brauer, J.M.G. Merayo, O.V. Nielsen, *Meas. Sci. Technol.* **13**, 1248 (2002).

[4] P. Butvin, M. Janošek, P. Ripka, B. Butvinová, P. Švec sr., M. Kuzminski, P. Švec jr., D. Janičkovič, G. Vlasák, *Sens. Act. A* **184**, 72 (2012).

[5] J. Kubík, L. Pavel, P. Ripka, *Sens. Act. A* **130-131**, 184 (2006).

10 A gradiometer with 30-mm gradient base

10.1 The "single-core" fluxgate gradiometer

The single core gradiometer developed by the author is presented below in the article [J4] (section 10.4). However to bring an in-depth information about the problematic, the following five paragraphs briefly describe the theoretical and practical aspects which were associated with the gradiometer construction and which did not appear in the article [J4] due to its limited scope.

10.1.1 Working principle

The basic principle of the single-core fluxgate $\partial B_i/\partial i$ gradiometer involves using two (or more) pick-up coils on a common sensor core (Fig. 10.1), instead of two separate sensors. This enables the use of small gradiometric bases – below 4 cm.

According to the state-of-the-art, the sensor can be connected after Fig. 10.1a), with antiserially connected pick-up coils and a single detector as seen in [Berkman 1960] and [Mermelstein 1988]. However, this makes astatization difficult. Alternatively, the output of two PSD detectors is subtracted in accordance with Fig. 10.1b), where the PSD (ADC) gains can be altered to astatize the gradiometer.

Fig. 10.1 – A single core gradiometer with a) direct signal subtraction, b) detector difference

As rod-core (Foerster, Vacquier) fluxgate geometries tend to be noisy at their respective ends, which are not well saturated [Ripka 2001, Musmann 2010], the favorite core geometry is in this case a race-track. A race-track geometry has the advantage of a closed magnetic circuit [Ripka 1993] while preserving lower demagnetization than a ring-core.

The fact that the flux in the magnetic core is not "flattened" by its high permeability can be demonstrated by a simple FEM simulation, as shown in Fig. 10.2 and Fig. 10.3. In these figures, the magnetic flux density profile across the linear branch of the race-track path, where the pick-up coil is usually placed, is plotted in the presence of a linear, first-order gradient field of 1 $\mu T \cdot m^{-1}$. The flux density near the rounded race-track parts is influenced by the different demagnetization factor, as expected.

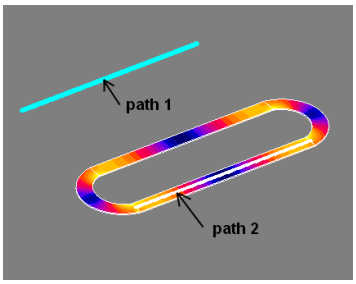

Fig. 10.2 – FEM simulation of the flux density profile in a race-track core

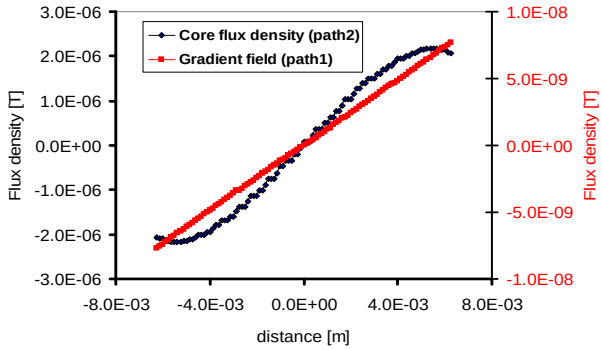

Fig. 10.3 – Results on the two post-processing paths. The applied gradient (red) and the core flux density (black) are shown.

10.1.2 Single core gradiometer noise analysis

The following results have been presented at the INTERMAG 2011 conference in Taipei under the title "*Spatial correlation of race-track fluxgate noise*".

To investigate the noise correlation across a race-track fluxgate sensor core which is suitable for single-core gradiometers, the noise profile of a 70-mm PCB-fluxgate was measured. The size was chosen for the purposes of a comparison with the sensor used by [Ripka 1997]. The excitation frequency was 10 kHz with 10 % duty-cycle pulses. The amplitude was 1 A p-p only to pronounce the inhomogeneities and defects in the core. The sensitivity change was recalculated for each position of the pick-up coil to obtain the noise in the field units. From the noise profile in Fig. 10.4, it is evident that the race-track ends are almost 3× noisier than 6 mm away in the direction of the core centre (the sensor noise in the middle was 10 pT), even when there is no bending stress as the core is etched from a single sheet.

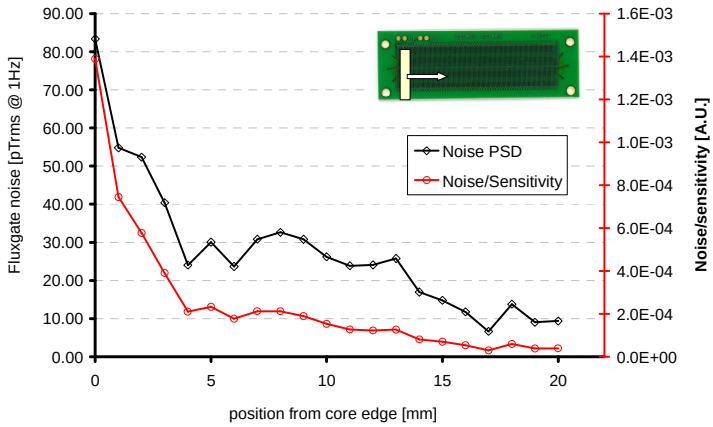

Fig. 10.4 – Race-track fluxgate spatial noise profile

There can be two reasons for noisy race-track ends:

1. The fluxgate core etched from a flat magnetic tape does not have uniform anisotropy along the excitation path due to the anisotropy of the amorphous magnetic tape, resulting from the manufacturing process [Ripka 2001].

2. The level of saturation of the round race-track ends depends strongly on the excitation turn distribution at those ends. This is demonstrated by FEM simulation in Fig. 10.5. The incremental permeability with 0.5 A excitation current applied to the two solenoidal windings (not shown here) is up to 3.4 with no turns on the round part and below 1.8 with five extra turns, respectively.

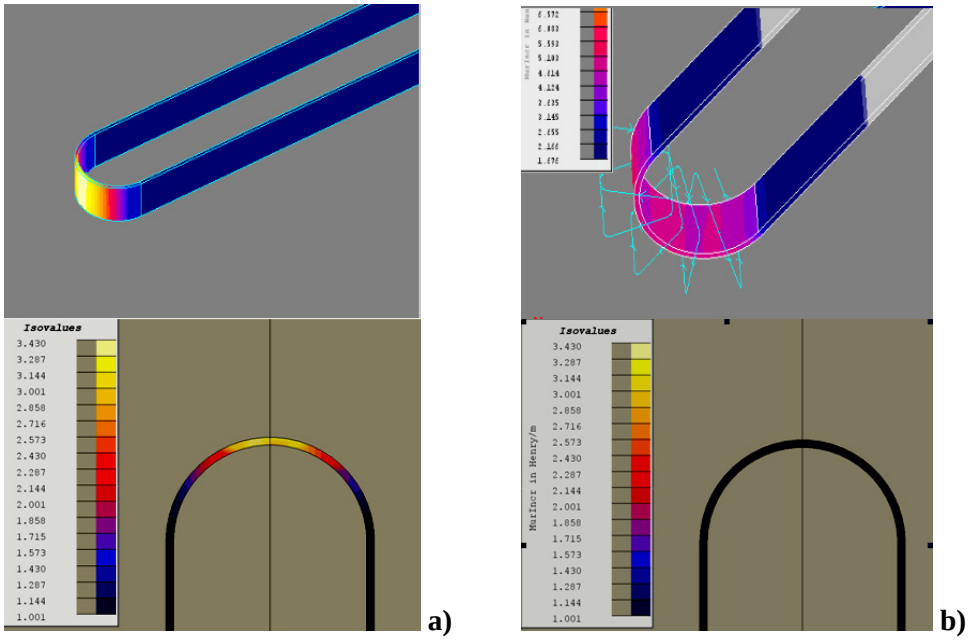

Fig. 10.5 – Incremental permeability profile for the case without excitation turns (a) and with excitation turns (b) at the round race-track ends. The saturation values are 3.4 (yellow) and 1.001 (black)

10.1.3 Noise Correlation

The performance of a gradiometer depends not only on the overall noise but also on the noise correlation at two core positions where the coils will be placed. [Buttino 1986] measured the correlation of magnetic noise on open cores. For places with correlated noise, a cross-spectral measurement technique can further suppress the core noise, as was described by [Koch 2001]. In a theoretical case, the correlated noise in a single-core gradiometer would be subtracted in this case. However, this was at the cost of computational power and also averaging, and this makes the measurement very slow.

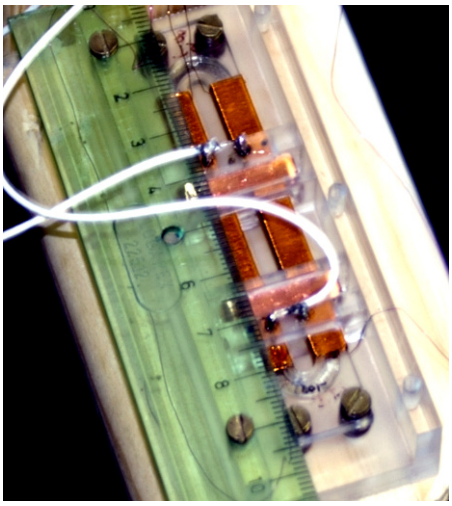

Fig. 10.6 – Race-track fluxgate set-up for coherence measurement

A similar race-track fluxgate to that used by [Ripka 1997] was manufactured, with two 150-turn pick-up coils. The coils were positioned either with the reference coil in the fluxgate centre, or at the core ends – see Fig. 10.6. As the core did not have any extra excitation turns in the round part of the fluxgate, the noise at the core-ends is quite high – it was 11 $pT \cdot Hz^{-0.5}$ @ 1 Hz at the core ends and 5 $pT \cdot Hz^{-0.5}$ @ 1Hz in the middle of the core.

The noise was measured using two SR-830 lock-in amplifiers and a dual-input Agilent 5670A FFT analyzer, applying its internal coherence function. The noise measurements were made in a 6-layer Permalloy shield – due to its attenuation of 100,000×, the DC field inside the shield was below 10 nT due to the remanence of the shield magnetic material. Thus the sensor works as if it were operating in a feedback loop (around zero).

Fig. 10.7 shows the decrease in noise coherence as coil (M) is moved away from reference coil (R) towards the edge of the core. The coherence has a 1/f character, due to the character of the fluxgate noise: at very low frequencies and thus at large noise amplitudes, the noise coherence is higher. The correlation distance, as defined by [Buttino 1986], is in turn higher, too. However for higher noise frequencies, and thus for lower noise amplitudes, the noise is more local and its coherence is already low at 10-mm coil separation.

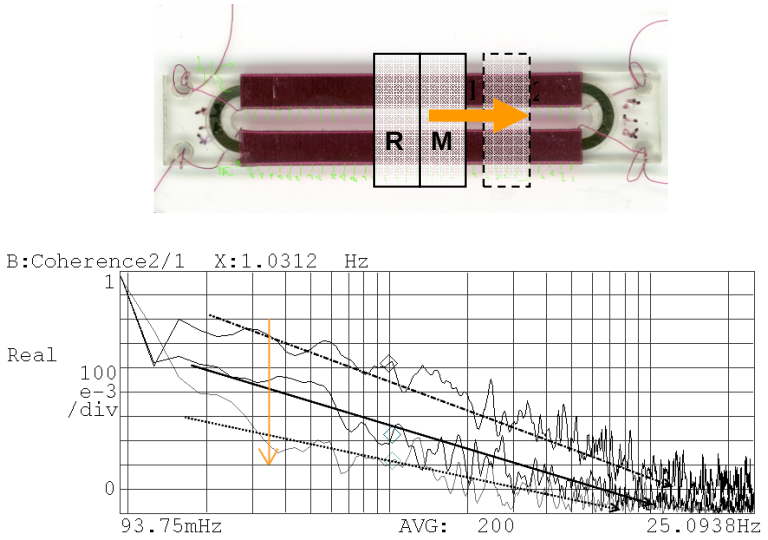

Fig. 10.7 – Noise coherence with the reference coil (R) in the center. The to the movable (M) coil increases with 5-mm steps in the arrow direction.

This was repeated for the reference coil at the fluxgate edge. The coherence for the same 5-mm steps towards the middle of the fluxgate shows the same dependency as in Fig. 10.7.

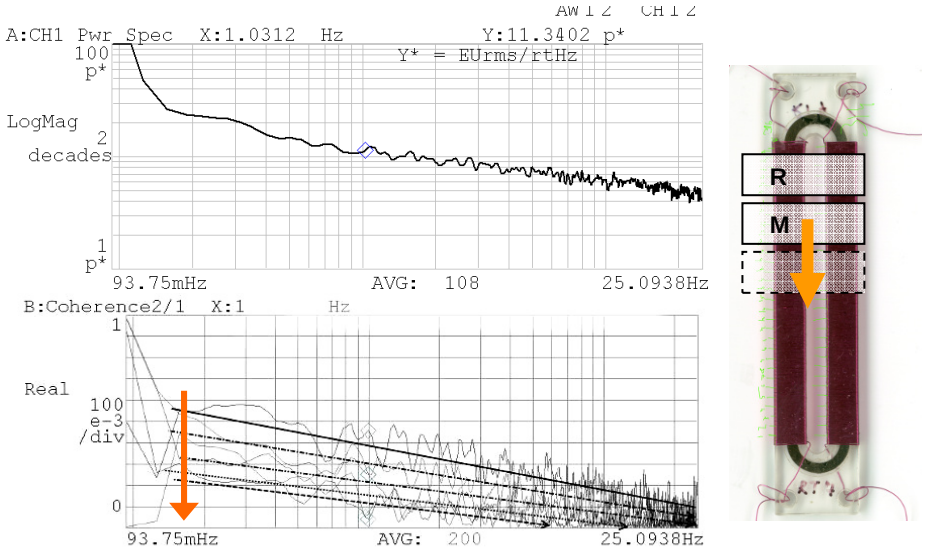

Fig. 10.8 – Noise coherence with reference coil (R) at the end of the core. The steps are again 5 mm. The noise PSD at the reference coil is plotted (in $pT_{rms}/\sqrt{Hz}$).

If the coherence is plotted as a function of the distance for the two reference coils, the graph in Fig. 10.9 is obtained. The coherence decreases much faster with the edge coil as a reference than in the case of the centre reference coil. Thus the correlation path is short for the edge reference coil. The noise is more local (i.e. from the unsaturated part of the racetrack) than in the centre: the noise in the centre tends to have a global minimum, which would be the noise limit when applying the approach by [Koch 2001].

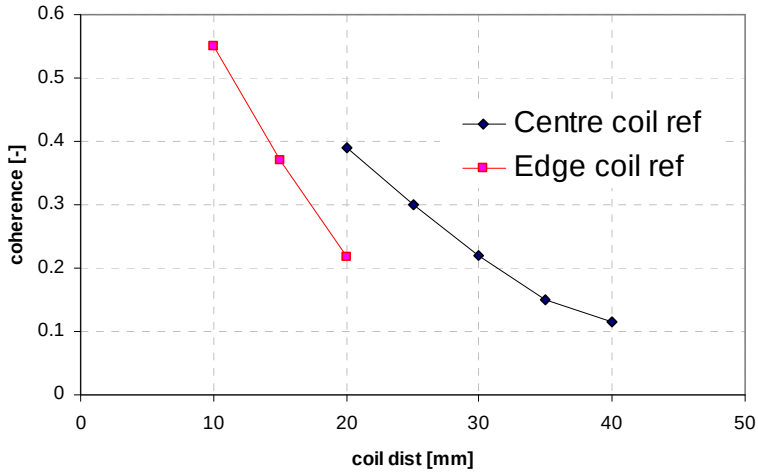

Fig. 10.9 – Coherence as a function of coil separation for the two reference coil positions

10.2 The gradient feedback coil

As the single-core gradiometers by [Berkman 1960], [Mermelstein 1988] and [Ripka 1997] operate in open-loop, a gradient-coil for gradient field feedback was designed to overcome this problem. By using a gradient feedback coil and the corresponding feedback-loop electronics, not only stable sensitivity to the magnetic gradient is assured but, in addition, the gradiometric base can also be decreased. Further, if two sensors are used in the gradiometer, the gain of the gradiometer with gradient feedback coil does not depend on the position of the two sensors.

Gradient coils are extensively used in medicine, but their design tends to be complicated [Turner 1993]. For example, [Pouladian-Kari 1990] designed a coil with different diameters for each coil segment. Unlike these designs, a simplified gradient coil was designed, see Fig. 10.10 [J4]. The diameter of the gradient coil is uniform and the coil is discretized in a number of sections with a different number of turns. The sections were manufactured by lathe-turning, and the number of turns

in each coil section varied in a nearly-linear dependence on the distance from the centre of the coil. The coil was 10 mm in diameter and 40 mm in length, and the groove-width was 1 mm.

An already existing race-track fluxgate sensor developed at TU Braunschweig [Rühmer 2009] was inserted into the manufactured gradiometric coil - Fig. 10.10 b). The coil was used not only for feedback but also for signal pickup, and thus enabled a fluxgate magnetometer to be converted to a fluxgate gradiometer.

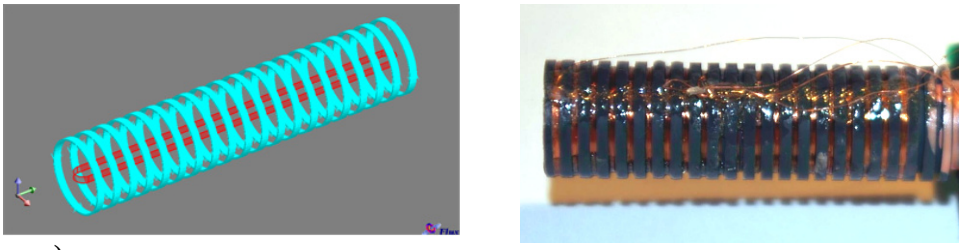

a) b)

Fig. 10.10 – Gradient feedback coil – the design (a) and the manufactured coil (b)

The field nonlinearity is below 2% at the edges when using an optimized series of coil turns (one half had 65, 42, 35, 29, 24, 20, 16, 11, 7, 3) – see Fig. 10.11. The coil constant determined from FEM simulation was 1.38 $(T \cdot m^{-1}) \cdot A^{-1}$.

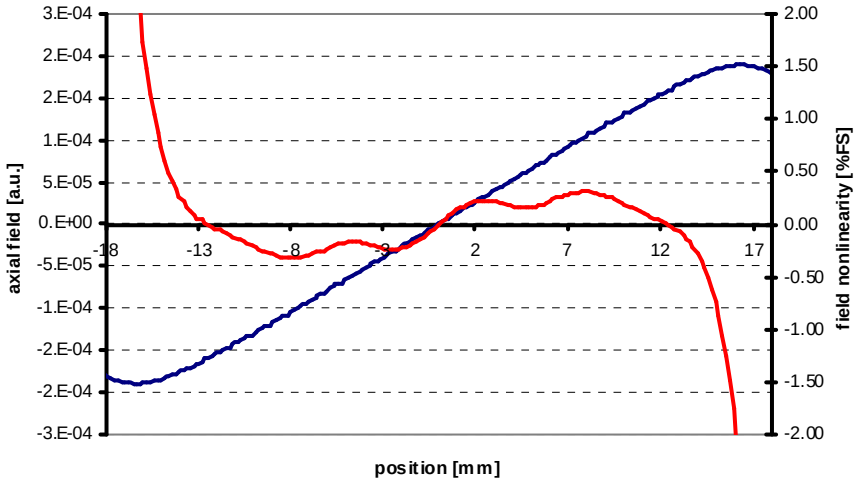

Fig. 10.11 - Gradient coil field profile (blue) and non-linearity (red)

10.3 Calibrating coils

The gain of a gradiometer with a gradient coil has to be determined by calibration using a known gradient field source. Gradient calibrating coils (Maxell-pair) have been designed and custom built at TU Braunschweig, see Fig. 10.12 - G. A four-coil system [Kirschwink 1992] for creating a homogeneous field (H) shared the same 0.44×0.44×0.47 m^3 coil frame.

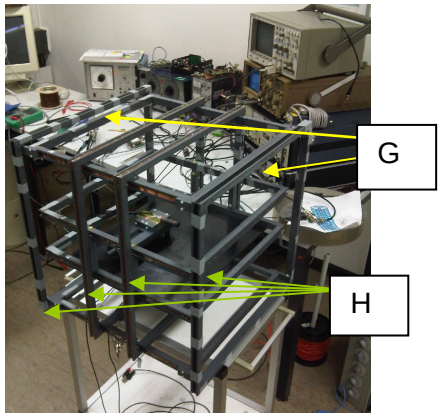

Fig. 10.12 – The structure of the calibration coils

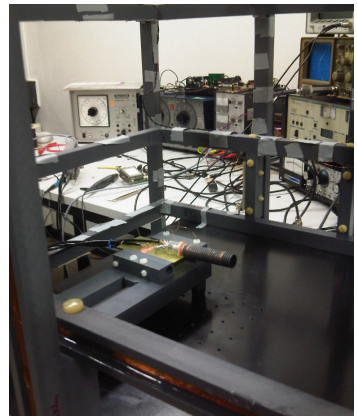

Fig. 10.13 – The single-core gradiometer during calibration

The coil constants (K_H=122 μT·A^{-1}, K_G=78 μT·m^{-1}·A^{-1}) were obtained by FEM modeling, and were verified by measurements with a calibrated solenoid – see Fig. 10.14 and Fig. 10.15. For the homogeneous coil, the area with ±1000 ppm homogeneity was 170×100 mm^2. This is more than twice the value for Helmholtz coils of comparable size. High field homogeneity is required for astatizing a gradiometer and for measuring gradiometer CMRR.

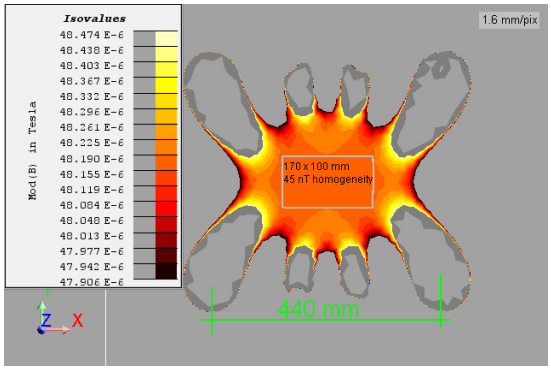

Fig. 10.14 – The field profile of the homogeneous coils. Colour map scale is 500 nT.

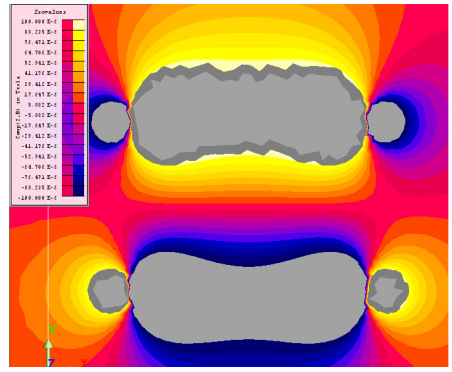

Fig. 10.15 – Field profile of the gradient coils. The colour map scale is ±100 μT

10.4 Single-core gradiometer with gradient feedback loop

Using the gradient feedback coil, the author proposed the feedback operation of the gradiometer. In addition, unlike in previous designs, an additional feedback coil is used to suppress also the large homogeneous field: the large common-mode caused by the homogeneous Earth's field is reduced and, as the core is kept in the nearly zero-field, the inhomogeneities of the magnetic core play a minor role in gradiometer astatization.

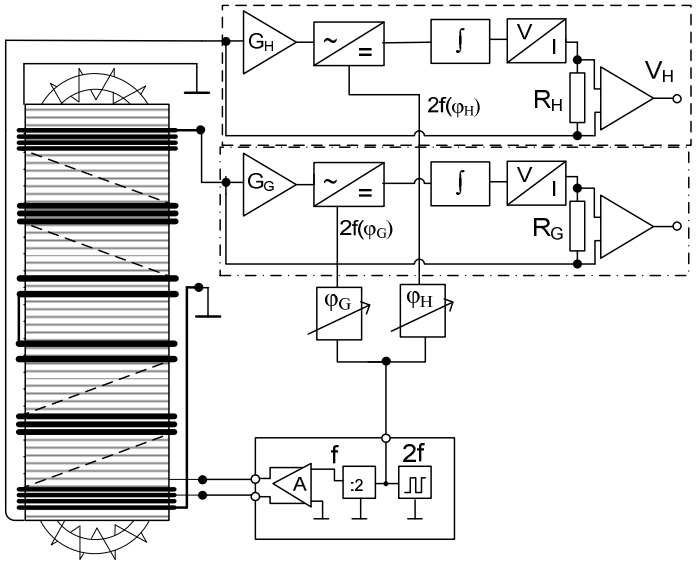

Fig. 10.16 – A single core gradiometer with gradient feedback, redrawn from [P1]

The principal circuit of the gradiometer, which has been patented by the author [P1] is shown in Fig. 10.16. The two electronics (gradient and homogeneous) work simultaneously with their respective feedback (and also pick-up) coils compensating the homogeneous field and the magnetic field gradient. The feedback loop (gradient or homogeneous) is facilitated using a V/I converter, and the output voltage of each channel is proportional to the feedback current, sensed on resistor R, which is a typical circuit for feedback-operated fluxgate magnetometer [Ripka 2001].

The following paper "*Single-core fluxgate gradiometer with simultaneous gradient and homogeneous feedback operation*" [J4] was published in Journal of Applied Physics in 2012 after presenting at the 56th Conference on Magnetism and Magnetic Materials. It describes the construction and the performance of the feedback-loop operated single-core gradiometer developed during the author's stay at TU Braunschweig in 2011. The author provided a major contribution to the publication both in the theoretical part and experimental results.

JOURNAL OF APPLIED PHYSICS **111**, 07E328 (2012)

Single-core fluxgate gradiometer with simultaneous gradient and homogeneous feedback operation

Michal Janosek,[1,a)] Pavel Ripka,[1] Frank Ludwig,[2] and Meinhard Schilling[2]
[1]*Czech Technical University, Faculty of Electrical Engineering, Department of Measurement, Technicka 2, 166 27 Praha, Czech Republic*
[2]*Institut für Elektrische Messtechnik und Grundlagen der Elektrotechnik, TU Braunschweig, 381 06 Braunschweig, Germany*

(Presented 2 November 2011; received 23 September 2011; accepted 9 November 2011; published online 6 March 2012)

A novel configuration of a single-core gradiometer, utilizing both homogeneous and gradient feedback operation, is presented. The fluxgate gradiometer comprises of a standard pick-up/feedback coil and an additional gradient pickup/feedback coil with two separate electronic blocks. The 40-mm-long gradient coil is concentric and coaxial with the homogeneous pickup/feedback coil: the gradient coil assembly was slipped over an already existing race-track fluxgate sensor. The gradient coil works as a pick-up coil and it also generates the compensating field which well approximates a first-order gradient field with zero spatial-mean value. Together with the compensating field from the homogeneous feedback coil, it is thus always possible to measure in two independent feedback loops the homogeneous and gradient field components. The 1/f gradient noise is 4 nT/m/$\sqrt{\text{Hz}}$ @ 1 Hz, and it can be further improved by separating the gradient feedback and compensating coil. © *2012 American Institute of Physics*. [doi:10.1063/1.3676238]

I. INTRODUCTION

A common type of magnetic gradiometer with fluxgate sensors uses two separate sensor heads, either using two single-axis sensors,[1] or two orthogonal triplets.[2] In both of these cases, the fluxgate sensors typically work in a compensating feedback. The so-called gradiometric base, which is the distance between individual sensor heads, affects resolution and noise when measuring the magnetic field difference and it also defines the rate of approximation of the measured value to the magnetic field gradient. The gradient base is however limited to certain minimum distance (usually tens of centimeters), which is determined mainly by mutual interaction of feedback-compensated sensors.

If the gradiometer is used for suppressing of interfering fields during measurements of weak, point-like sources (e.g., magnetic nanoparticles in medicine), the excessive length of the gradiometric base does not allow to efficiently suppress close sources of interference.[3] Also, it is difficult to measure the magnetic field gradient with a good rate of approximation in the presence of higher-order gradients or if the gradient is weak (i.e., when the reading of the distant sensor is buried in noise). In addition, the angular deviation between the sensor heads results in gross measurement error, and therefore very stable fixture of the sensors is required.

A so-called "single-core" fluxgate gradiometer, i.e., a gradiometer using a single fluxgate sensor and two or more pick-up coils along its core, allows to shorten the gradiometric base. These gradiometers measure the axial gradient of magnetic field and they have been introduced in 1960s.[3] The single-core gradiometer principle was since then used in a rod-type fluxgate gradiometer[4] with separate signal processing blocks, and a race-track type was presented with the pick-up coils antiserially connected.[5] As these gradiometers were operated in an open-loop, their parameters were unstable with temperature and time. In this paper, we introduce a gradient feedback using a special gradient coil. It allows, together with the standard homogeneous feedback, to create a single-core fluxgate gradiometer/magnetometer with promising parameters.[6]

II. SINGLE CORE GRADIOMETER THEORY

If the uniaxial first-order gradient field is measured by two separate and coaxial fluxgate elements of length l, originating at the coordinates L_1 and L_2, respectively, as shown in Fig. 1, we can write[3]

$$\frac{\partial H}{dx} = \frac{dH}{dx} \cong \frac{dH}{L_2 - L_1} = \frac{\int_{L_1}^{L_1+l} H(x)dx - \int_{L_2}^{L_2+l} H(x)dx}{l(L_2 - L_1)}. \quad (1)$$

If the two fluxgate elements are joined together so that the coils share one common fluxgate core ($L_1 + l = L_2$), the single-core gradiometer is established (Fig. 1). Equation (1) is valid also for this case.

The distance $(L_2 - L_1)$ is the "gradient base," d. It is evident that the approximation is approaching the derivative definition only for a very short gradient base. Assuming that each of the two pickup coils is measuring an average of the magnetic field (its integral over the coil length l) with a sensitivity S [V/T] and outputs a voltage V, we can write

$$\frac{1}{d}\left(\frac{V_1}{S_1} - \frac{V_2}{S_2}\right) = \frac{dH}{dx}. \quad (2)$$

a)Author to whom correspondence should be addressed. Electronic mail: janosem@fel.cvut.cz. Fax : +(420) 2 3333 9929.

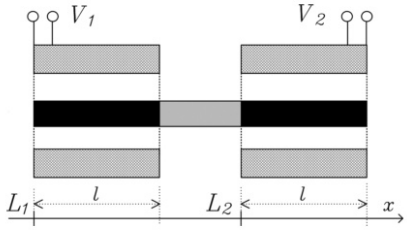

FIG. 1. The coaxial fluxgate gradiometer—two separate core elements, or a single-core type if the two cores are joined.

If the gradiometer is perfectly astatized, i.e., if the two sensitivities are known or equal, the gradiometer output can be rewritten to a simple equation

$$(V_1 - V_2) = S \cdot d \cdot \frac{dH}{dx}. \tag{3}$$

III. THE GRADIENT FEEDBACK

We introduce a gradient-feedback loop, compensating the measured first-order-gradient field. The use of two flux-locked feedback loops in the two pick-up coils would be possible, but they would influence each other and finally the gradiometer output would be difficult to interpret. Suitable coils are already used in MRI,[7] but we found them difficult to manufacture. We thus designed a gradient coil of different type: it consists of equidistant sections of equal width, where the number of turns N in the respective sections almost linearly decreases to the coil center and, after reversing the winding direction in the middle, again increases to the coil end (Fig. 2). The coil bobbin could be easily manufactured by lathe-turning.

In order to increase simplicity and also geometrical stability, this coil is also used as a gradient-pickup coil. For calculating the theoretical output, the Eq. (1) is now rewritten

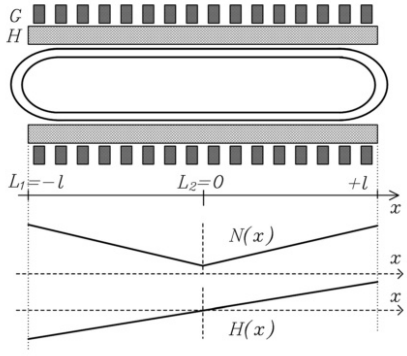

FIG. 2. The single-core gradiometer with homogeneous (H) and gradient feedback coil (G). The number of turns of gradient coil $N(x)$ and gradient field $H(x)$ are shown.

according to Fig. 2, $L_1 = -l$, $L_2 = 0$ and the gradient base $d = (L_2 - L_1) = l$. We further assume that the sensitivity between $\langle -l,0\rangle$ and $\langle 0,l\rangle$ (depending on the number of turns) is a linear function of the position, thus, we can define its spatial derivative $dS(x)/dx = \pm s$. Analogically if the measured field H is only a linear function of x, $\partial H(x)/\partial x = dH(x)/dx = g$. The output voltage V of the gradient pickup coil can be then written as

$$\begin{aligned} V &= \frac{1}{l^2}\left[\int_{-l}^{0} S(x)H(x)dx - \int_{0}^{l} S(x)H(x)dx\right] \\ &= \frac{1}{l^2}\left[\int_{-l}^{0} (-sx \cdot gx)dx - \int_{0}^{l} (sx \cdot gx)dx\right], \end{aligned} \tag{4}$$

and after simple calculation and substitution for $g = \partial H(x)/\partial x$ the output can be rewritten as

$$V = \frac{2}{3} \cdot \frac{\partial H}{\partial x} \cdot s \cdot d. \tag{5}$$

The number of turns of the gradient coil was determined by optimizing the linear series with finite element modeling (FEM) in the *Flux3D* software package in order to obtain best linearity. The 40-mm long gradient coil consisted of 20 sections—the section width was 0.2 and the pitch 1.8 mm. The gradient coil diameter was 10 mm, the coil sections with twice 65, 42, 35, 29, 24, 20, 16, 11, 7, and 3 turns were wound with 0.056 mm diam copper wire (Fig. 3). The gradient coil constant was determined by the FEM analysis as 1.38 $(\mathrm{T.m}^{-1}).\mathrm{A}^{-1}$, and was later verified experimentally by calibrations.

The coil support was swept over an existing tape-wound race-track fluxgate sensor with homogeneous feedback and separate pick-up and feedback coils.[8] The dual electronics is a common type with an integrating regulator in the feedback loop. Both electronics share the same reference signal, however the phase adjustment is done separately: we found it necessary in order to keep the feedback loops stable.

The single-core gradiometer is usually influenced by core inhomogenities, causing false response to homogeneous fields even after careful astatization.[5] We observed that the simultaneous use of a homogeneous feedback loop decreased this effect by keeping the core in zero-average field.

IV. GRADIOMETER PARAMETERS

A coil system producing coaxial gradient and homogeneous field was used for the calibrations. The rectangular

FIG. 3. The fluxgate gradiometer shown with 1-cent coin.

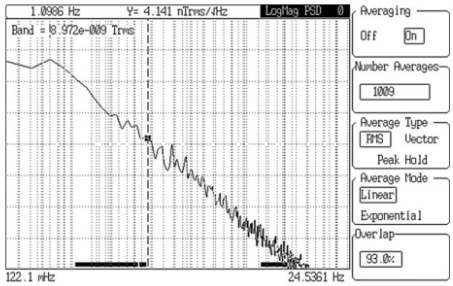

FIG. 4. Noise spectral density of the gradiometer.

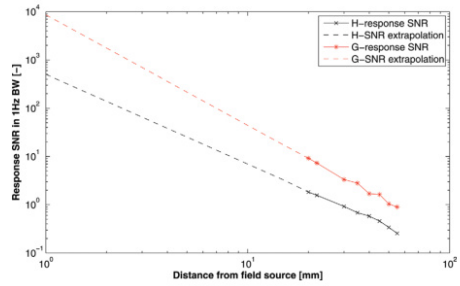

FIG. 5. (Color online) The SNR in 1-Hz bandwidth for homogeneous and gradient readings for a dipole source in an unshielded environment (in log-log scale).

4-coils system[9] assured high field homogeneity. The gradient coil of Maxwell-pair type shared the outer two coil supports of the homogeneous system. During calibration, the gradiometer was positioned to the geometric center of the coils, thus not influencing homogeneous reading by applied gradient field. A quasistatic field (4 Hz) was used for the calibrations.

The sensitivities of the gradiometer were determined as 0.17 $V{\cdot}\mu T^{-1}$ and 0.163 $V{\cdot}(\mu T{\cdot}m^{-1})^{-1}$ and agreed with the coil-constants of both feedback-loop coils. The sensitivity of homogeneous reading on gradient field was found as negligible, but the parasitic sensitivity of gradiometric reading on homogeneous field was significant - 0.2 $(nT.m^{-1}){\cdot}nT^{-1}$. However, as this dependence was found to be linear and the homogeneous field value is measured simultaneously, it should be possible to compensate for this effect.

The noise of the gradiometer was measured in a 6-layer Permalloy shielding can, the noise spectral density is shown in Fig. 4. The 1-Hz noise of 4 $nT{\cdot}m^{-1}/\sqrt{Hz}$ is higher than expected, and should not be influenced by the 10 $pT/\sqrt{Hz}$ "homogeneous" noise of the magnetometer which was used to build the gradiometer. The sensitivity to gradient of 14 $V{\cdot}(T{\cdot}m^{-1})^{-1}$ means that the noise level is already influenced by the electronic noise. Further increasing the sensitivity by increasing the number of turns is, however, possible only when splitting the gradient coil to separate feedback and pickup coils, since its coil constant is already very high: for 1 $nT.m^{-1}$ field gradient, a current of only 0.7 nA is needed.

V. EXPERIMENTAL RESULTS

The gradiometer performance was verified with a 22-turn, 9-mm diam and 3 mm long coil representing a dipole-like source, in an unshielded laboratory environment. The 20-Hz, 50 μA_{rms} coil current resulted in a dipole moment of approximately 0.07 $\mu A.m.^2$ The fluxgate sensor was positioned coaxially to the source and the distance was increased in 5-mm steps from the minimum distance of 20-mm required for true $1/r^3$ field dependence. The signal-to-noise ratio (SNR) was measured for both the homogeneous and gradient output in a 1-Hz bandwidth. Figure 5 shows that the SNR ratio of 10 could be maintained for more than doubled distance in the case of gradiometric output. The power-law extrapolation of the results (Fig. 5, dashed trace) confirms the feasibility of the gradiometer for measuring the response of weak, point-like sources in an unshielded environment.

VI. CONCLUSION

We have presented a single-core gradiometer with both homogeneous and gradient feedback operation, with a gradient base of 40 mm. The linear parasitic sensitivity to homogeneous fields, which is inherent to single-core fluxgate gradiometers, can be reduced by knowing both the homogeneous and gradient field value. The gradiometer noise of 4 $nT{\cdot}m^{-1}/\sqrt{Hz}$ maintains 1/f character over the whole 20-Hz frequency range and it can be further lowered by, e.g., separating the gradient pickup and feedback coil into two coils of different number of turns, allowing to gain on sensitivity. We confirmed that the gradiometer is feasible for measurements of weak point-like sources where minimum sensor distance is required, i.e., in magnetorelaxometry of magnetic nanoparticles.[10] Further suppression of the unshielded, environmental noise could be achieved by simultaneous numerical corrections of the gradient output signal for parasitic sensitivity to homogeneous fields.

ACKNOWLEDGMENTS

Substantial part of this work has been supported by the International Graduate School of Metrology at Technische Universität Braunschweig, Germany, during the author's stay in 2010. The author also acknowledges the support of the Grant Agency of the Czech Republic under the Grant No. GD102/09/H082 - Sensors and intelligent sensor systems.

[1]J. M. G. Merayo, J. R. Petersen, O. V. Nielsen, F. Primdahl, and P. Brauer, Sens. Actuators A **93**, 185 (2001).
[2]J. M. G. Merayo, P. Brauer, and F. Primdahl, Sens. Actuators A **120**, 71 (2005).
[3]R. J. Berkman, Avtomaticheski kontrol i izmeritelnaya technika **4**, 157 (1960), in Russian.
[4]M. D. Mermelstein and A. Dandridge, Electron. Lett. **26**, 501 (1990).
[5]P. Ripka and P. Navratil, Sens. Actuators, A **60**, 76 (1997).
[6]M. Janosek and P. Ripka, EU patent 2388608 (2011).
[7]J. F. Schenck, U.S. patent 4,617,516 (1983).
[8]R. Piel, F. Ludwig, and M. Schilling, Sensor Letters **7**, 317 (2009).
[9]J. L. Kirschvink, Biolectromagnetics **13**, 401 (1992).
[10]F. Ludwig, E. Heim, and M. Schilling, J. Appl. Phys. **101**, 113909 (2006).

10.5 The dual-core feedback-loop operated gradiometer

The high noise – 4 $nT \cdot m^{-1} \cdot Hz^{-0.5}$ – of the single-core gradiometer described in [J4] was found to be caused by:

- Low sensitivity of the gradient coil when used as a sensing coil: 14 $V \cdot (T \cdot m^{-1})^{-1}$ sensitivity and 5 nV input amplifier white noise leads to approx. 0.4 $nT \cdot m^{-1} \cdot Hz^{-0.5}$ white noise.
- The high constant of the gradient coil: for compensating 1 $nT \cdot m^{-1}$, only approx. 0.7 nA compensating current was needed, which is well within the noise of the operational amplifiers.
- The noisy race-track ends were sensed by the gradient coil (this took place where the number of turns of the combined sensing/compensating coil was highest). Due to the low correlation the noise is not suppressed.

The first and second noise sources are coupled together, so the design of the gradient coil, if it is to serve both for signal pick-up and for signal compensation, is a trade-off. In order to overcome the problems of the single-core gradiometer, a classical "dual-core" gradiometer, was proposed with two ring-core fluxgate sensors, but using the gradient feedback coil, see Fig. 10.17 [Janošek 2011]. Because two separate fluxgate sensors are used, their gains can be controlled and the noise correlation is kept to a minimum. The ring-core sensors that were developed and used in the gradiometer also have the advantage of low noise (Chapter 9).

The two cores as shown in Fig. 10.17 and Fig. 10.18 are placed in the milled bobbin (8), where homogeneous and gradient feedback coils are wound - Fig. 10.19 and Fig. 10.20. Pick-up coils 14 and 24 serve as sense coils only. The signals for the error detector of the gradient and homogeneous feedback loops are obtained by summing or subtracting the (phase sensitive) rectified pick-up signals of the respective coils.

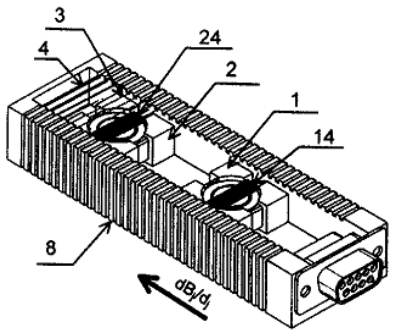

Fig. 10.17 – The dual-core gradiometer - from [Janošek 2011].

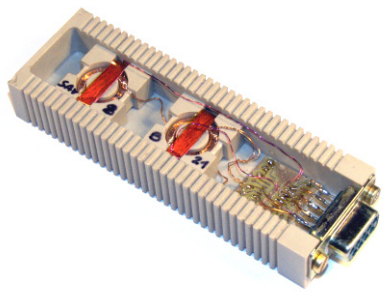

Fig. 10.18 – The sensor head milled from PEEK GF30, before winding the respective feedback coils.

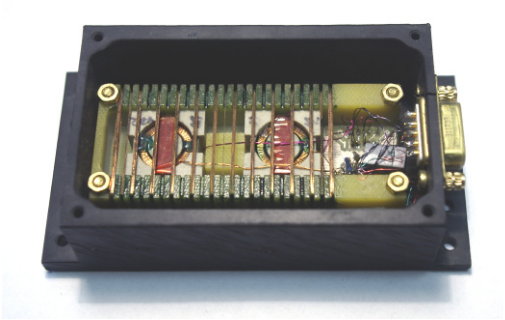

Fig. 10.19 – Gradiometer head #1 milled with a FR4 coil bobbin.

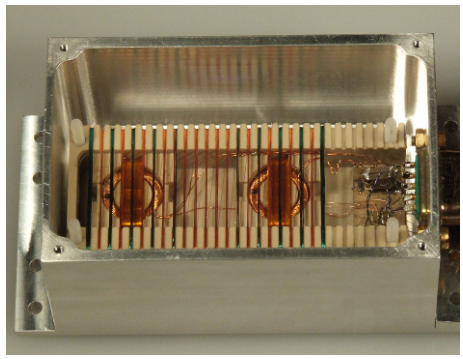

Fig. 10.20 – Gradiometer head #2, using the PEEK bobbin, H feedback coil (orange wire) not yet optimized.

The number of turns of the gradient s coil was optimized by FEM simulation. The number of milled grooves was 23. The homogeneous feedback coil was also optimized to provide better field flatness than a regular solenoid: instead of uniform turns density, the number of turns of the homogeneous feedback coil was 54, 4, 28, 0, 28, 0, 28, 0, 28, 0, 27, 1 (and vice-versa) which resulted in H-feedback nonlinearity less than 0.5% (Fig. 10.21).

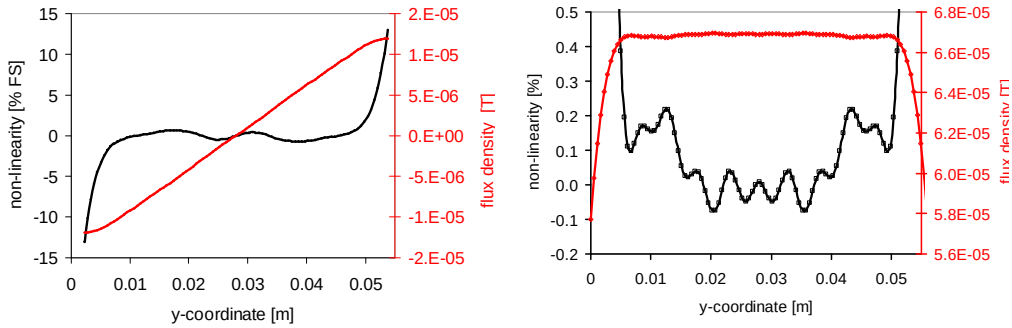

Fig. 10.21 – The field profile and the non-linearity of the gradient coil (left) and the homogeneous coil (right) – from FEM simulation in FLUX 3D

The gradiometer operation was verified in a MATLAB Simulink, confirming that in the feedback-loop operation (assuming an ideal controller - integrator - in the feedback), the gradiometer gain is independent of the individual sensor gains and their position, as long they stay in the linear region of the gradient coil. This is an inherent advantage over any other gradiometer structure with separate sensors or sensor elements [Sasada 2014, Griffin 2012]. It was also found that the offsets in

the summing and subtracting circuits should be kept low, otherwise a large gradiometric offset arises. This was later verified on the constructed gradiometer.

The gradiometer has been constructed by collaboration with CSRC s.r.o. company in the frame of a project of Technology Agency of the Czech Republic – the power supply and FPGA-driven excitation board was provided by the company [CSRC 2013].

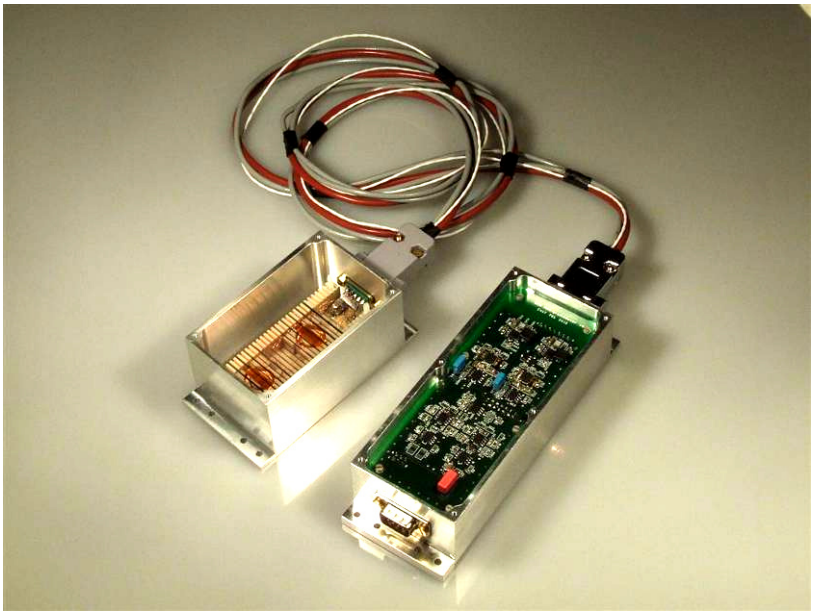

Fig. 10.22 – The gradiometer head with the gradiometer electronics

The next proceedings paper *"Dual-core fluxgate gradiometer with gradient feedback"* [W1] was presented at the 2013 IEEE Conference on Sensors. The paper describes the structure and the operation of a dual-core gradiometer and the parameters – noise and parasitic sensitivity to homogeneous fields – are determined. We were able to astatize the gradiometer in a specific orientation to the Earth's field requiring only the information about the homogeneous field in the gradiometer axis which is provided by the gradiometer anyhow. Because of limited scope of the proceedings paper, the relation of the proposed astatization to the method introduced in [Merayo 2001] is not shown - it is given in the next paragraph. The gradiometer parameters have been later improved by increasing the gradiometric base from 20 to 30 mm. The author's contribution was in the gradiometer design, its astatization and field measurements, together with synthesis of the results.

Dual-core fluxgate gradiometer with gradient feedback

Michal Janosek, Antonin Platil, Jan Vyhnanek
Dept. of Measurement, Faculty of Elec. Eng.
Czech Technical University in Prague
Prague, Czech Republic

Jan Brinek

Czech Space Research Centre Ltd.
Brno, Czech Republic

***Abstract*—A fluxgate magnetic gradiometer with two fluxgate sensors and gradient feedback loop is presented. The two feedback coils, gradient and homogeneous, are common to both fluxgate sensors. The signal from the two sensors acts as regulating input in the two feedback loops, improving stability of the gradiometer. The presented gradiometer overcomes the problems of state-of-the art gradiometers which do not allow to decrease the sensor spacing. Because the information about homogeneous field is also available at the gradiometer output, it is possible to astatize the gradiometer. The presented gradiometer has a gradient base of 20-mm with overall sensor head size of 10-cm only and its noise is less than 1.1 nT/√Hz @ 1 Hz.**

I. INTRODUCTION

A small and sensitive gradiometer finds usage i.e. in road traffic regulation, scanning for buried ferromagnetic targets or in geophysical and geological exploration, when the information about the depth of a ferromagnetic target (e.g. meteorite) or position (head of a drilling machine) is needed. Small dimensions of the gradiometer head (<10 cm) are needed either by space limitation or if magnetic gradient is needed for position or other calculations (derivative approximation effect).

The state-of-the-art axial gradiometers are using two independent fluxgate sensors with own feedbacks [1]. However this brings several fundamental problems: the feedback coils tend to influence each other, so the sensor spacing - gradient base – is limited to tens of centimeters and larger; and more importantly, the geometric stability of the two sensor axes is of a great importance, pronouncing larger gradient bases. A solution for compensating of geometric errors would be using two triaxial sensor heads [2], allowing - after calibration –a possibility for compensating of angular errors, however keeping the problem of influencing feedbacks.

The so called single-core gradiometers [3, 4] can have the gradient base smaller than 40-mm. They are however limited by instability of parameters due to open loop operation, sensitivity to homogeneous field was found as high [5]. The problems of open loop operation single-core gradiometers were addressed by introducing gradient feedback coil by the authors [6]. However the single-core gradiometer tended to be noisy (3 nT/m/√Hz @ 1Hz) because of the correlation of magnetic flux in the core. This limitation is now addressed by the authors using two separate ringcore fluxgate sensors and an appropriate signal processing electronics.

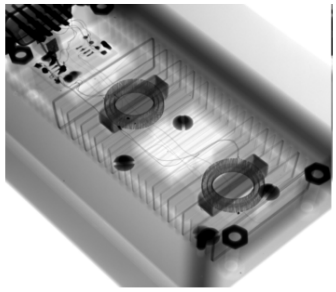

Figure 1. X-ray image of the gradiometer sensor head

II. GRADIOMETER CONSTRUCTION

A. Sensors and coils construction

The sensors cores are constructed using cobalt base amorphous tape which is wound in a 12-mm diameter MACOR bobbin and subsequently annealed in magnetic field to lower the sensor noise [7]. The ring cores are placed in a cubic holder, where the respective pickup coils are wound. The finished sensors are placed with 20-mm spacing in the fiberglass feedback coil holder – see Figure 1. The feedback coils – gradient and homogeneous one – are wound on top of each other using the grooves in the holder. There are 23 grooves and the number of turns of each of the two feedback coils was optimized using FEM modeling in FLUX3D software, in order to obtain clean homogeneous and gradient response. The homogenous feedback coil design is of great importance, because due to the 20- mm sensor spacing only fractions of per-cent nonlinearity are tolerable to avoid errors due to gradient generated in the homogenous feedback coil. The gradient coil design is similar to [6] as can be seen in the X-ray image in Figure 1, only the number of turns has been optimized.

978-1-4673-4642-9/13/$31.00 ©2013 IEEE

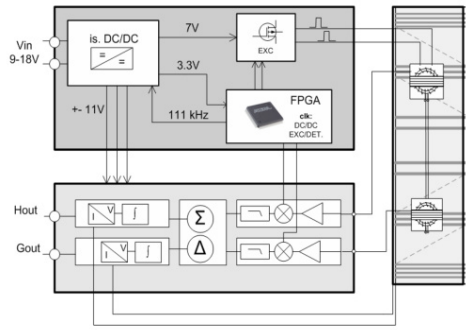

Figure 2. Block diagram of the gradiometer

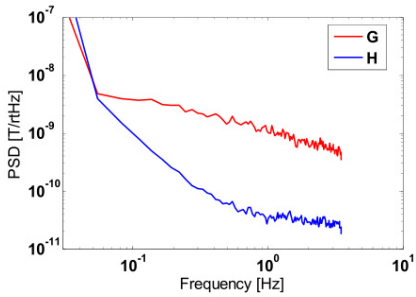

Figure 3. Noise of G and H channel of the gradiometer

B. *Principle of operation*

The gradiometer operation relies on two independent feedbacks for gradient and homogeneous component of the axial field. The block diagram in Figure 2 shows the basic electronic blocks of the gradiometer – the excitation, DC/DC and phase signals for detection electronics are derived in the FPGA module. The fluxgate excitation uses H-bridge with transformer and parallel-tuned excitation circuit, the detection uses full-wave phase-sensitive rectification. The error signals for the PI regulator of the respective feedback circuits are derived from the sum (homogeneous feedback) or difference (gradient feedback) of the two demodulated sensor outputs.

C. *Gradiometer parameters*

The analog outputs of ±10 V correspond to ±100 μT in homogeneous channel and ±52 μT/m in gradient. The calibration was performed using Maxwell-coil pairs for gradient field and Meritt-type coils for homogenous field.

The gradiometer was constructed as a two component system – electronics and sensor head are interconnected with 3-m long sensor cable, to avoid gradients from the electronic components. The gradiometer sensor head overall size is 10 cm x 5 cm. The power consumption of about 2 Watts is mainly governed by high excitation level of the fluxgate sensors (3A peak to peak): if higher sensor noise would be tolerable, the power consumption can drop to one half.

III. EXPERIMENTAL RESULTS

A. *Noise performance*

Noise was measured in a cylindrical 4-layer Permalloy shielding can in laboratory conditions. The results shown in Figure 3 show that the noise of gradient channel is 1.1 nT/m/√Hz @ 1 Hz. The 1-Hz noise PSD is 3x better than previously reported in [6] in the case of single-core gradiometer. Noise can be further improved by using low noise instrumentation amplifiers sensing the feedback current (currently INA129).

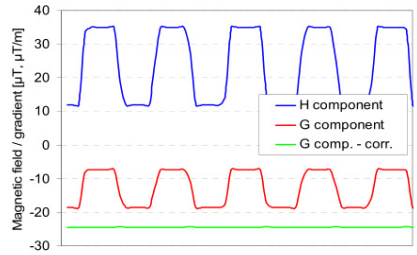

Figure 4. Gradiometer astatization in calibrating coils

B. *Gradiometer astatization – response to homogeneous component*

The gradiometer was astatized in laboratory condition using 0.45-m large Merrit-type coils with high homogeneity. It was possible to suppress the sensitivity to the applied homogeneous field almost completely by using a simple correction assuming that the homogeneous feedback coil still creates field gradient. The blue trace in Figure 4 represents the homogenous field applied (and measured), the red trace shows (raw) gradient response G and the green trace shows G_{corr} which is the result after the correction using the information about homogeneous field H using k=0.45:

$$G_{corr} = G - G' = G - H \cdot k$$

However, it has been found that this astatization is valid only for in-plane measurements, i.e. when the sensitive axis is parallel to measured vector. When the gradiometer was subject to movement in homogenous Earth's field vector in a magnetic observatory in a clean and homogeneous environment, there was still significant response to homogeneous fields.

It was assumed that the remaining response is governed by the tilt of one of the two sensors in the head.

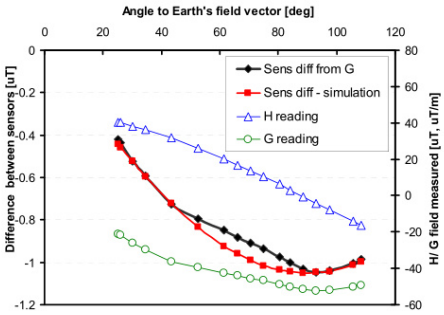

Figure 5. Sensor difference due to H field caused by mutual sensor tilt

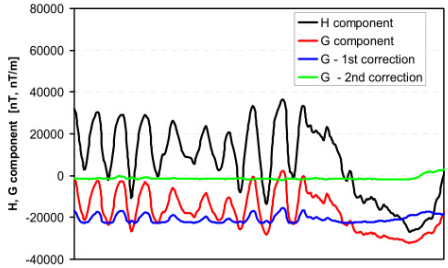

Figure 6. Real world measurement – effect of the 2 corrections

To verify this hypothesis, the gradiometer was placed on a non-magnetic theodolite and vertically rotated in the direction of Earth's field vector by 90 degrees (limited by the theodolite construction). The *H* reading follows the cosine and *G* reading sine dependency – see Figure 5. If we recalculated the *G* reading by gradient base of 20-mm, the resulting difference measured by the two sensors (due to the tilt of one of them) varies between -0.4 to -1 μT depending on orientation to the Earth's field vector.

If we define α as an angle defining sensitive axis orientation to the vector $\vec{H}$ measured, we can introduce the misalignment angle (tilt) σ of the second sensor in the sensing head. The remaining parasitic gradient response G'' will be then:

$$G'' = \sin(\alpha) \cdot \left|\vec{H}\right| \cdot tg(\sigma) \cdot 50$$

For an assumed tilt of 1.45°, the calculated sensor difference follows the measured values (the "flat region" apparent on measured data was found to be caused by approach to saturation due to high gradient reading).

If the angle of the gradiometer probe sensitive axis to the field vector and also field amplitude are known, it is easy to perform the corrections on G' and G''. In the case of Earth's field, the angle can be calculated.

C. Real-world measurements

Real-world measurements were performed in a public park, where the Earth's magnetic field was homogeneous enough, allowing to apply the suggested corrections on gradiometer response. The gradiometer was "waved" in several different positions to the Earth's field vector. The measured values are shown in Figure 6. It can be seen that after the first corrections on G', there is still significant response to homogeneous field. The second correction on G'' used a rough calculation of the orientation to Earth's field vector using the H value. The resulting trace shows good suppression to homogeneous field if both corrections are applied. However, as the orientation to the field vector could not be apriori known in other cases, it might be helpful adding another 2 orthogonal axes to the gradiometer, which would give information about the orientation.

ACKNOWLEDGMENT

The authors acknowledge the support of the Technology Agency of Czech Republic under the project number TA01010298.

REFERENCES

[1] J. M. G. Merayo et al., "A Portable Single Axis Magnetic Gradiometer", Sensors and Actuators A: Physical, Vol. 93, Issue 3, pp. 185-196, 2001

[2] J. M. G. Merayo, P. Brauer and F. Primdahl, "Triaxial fluxgate gradiometer of high stability and linearity", Sens. Actuators A 120, 71(2005).

[3] R. J. Berkman, Avtomaticheski kontrol i izmeritelnaya technika 4, 157 (1960), in Russian

[4] M.D. Mermelstein and A. Dandridge, "Metallic glass ribbon probe for the measurement of the magnetic field, first and second order field gradients", .Electron. Lett. 26, 501 (1990)

[5] P. Ripka and P. Navratil, "Fluxgate sensor for magnetopneumometry", Sensors and Actuators A: Physical, Vol. 60, Issues 1-3, 76-79 (1997)

[6] M. Janosek, M. Ludwig, F. Schilling and P. Ripka, "Single-core fluxgate gradiometer with simultaneous gradient and homogeneous feedback operation", Journal of Applied Physics Vol. 111, No. 7, pp. 07E328-1-07E328-3 (2012)

[7] P. Butvin, M. Janosek, P. Ripka, B. Butvinova, P. Svec Sr., M. Kuzminski, P. Svec Jr., D. Janickovic and G. Vlasak, "Field annealed closed-path fluxgate sensors made of metallic-glass ribbons", Sensors and Actuators A 184, 72-77 (2012)

10.6 Astatization

10.6.1 Simplified astatization in detail

The previous paper [W1] presented a simple algorithm for astatization of the gradiometer with gradient feedback, which was derived experimentally. We showed that for a specific orientation of the probe in the Earth's field, information about the homogeneous field H is sufficient to astatize the gradiometer up to a certain level. Because of the limited scope of the published paper, additional information is supplied below which shows the relation with the astatization approach of [Merayo 2001].

For two-sensor gradiometer astatization, we can consider the Equation 8.7, where G'' - as defined in [W1] - is the error term due to sensor misalignments:

$$G'' = a_2 |B| (-\varphi \sin\theta_0 \sin\varphi_0 + \theta \cos\theta_0 \cos\varphi_0) \tag{10.1}$$

However, if we keep angle φ_0 near to 90° using the coordinate system of [Merayo 2001], i.e. if the probe orientation in the Earth's field is N-S as in [W1] , we arrive at:

$$G'' \cong -a_2 |B| (\varphi \sin\theta_0) \tag{10.2}$$

Finally, we arrive at an almost identical equation, which was found in [W1] (assuming that the angle φ is constant):

$$G'' \cong |B| \cdot \sin\theta_0 \cdot K \tag{10.3}$$

Angle θ_0 can be calculated, when we know the (approximate) Earth's field flux density scalar value B_E (approx. 48,000 nT in our location) and we have appropriate information about the homogeneous field measured by the homogeneous channel of the gradiometer B_H :

$$\theta_0 = \cos^{-1} \frac{B_H}{B_E} \tag{10.4}$$

This simple astatization can be applied e.g. in UXO detection. The CMRR of the gradiometer can be then improved without using an orthogonal X-Y sensor pair, if the scanning direction is maintained North-South and if this direction is kept during scanning.

10.6.2 Full astatization

If the gradiometer is to be moved freely in the Earth's field, the condition of simplified astatization (10.6.1) cannot be fulfilled and thus full astatization (8.2.1) is essential. Also in this case, two orthogonal sensors have been added; in the form of an additional digital magnetometer (Fig. 10.23), which was developed in the scope of a Technology Agency project [CSRC 2013].

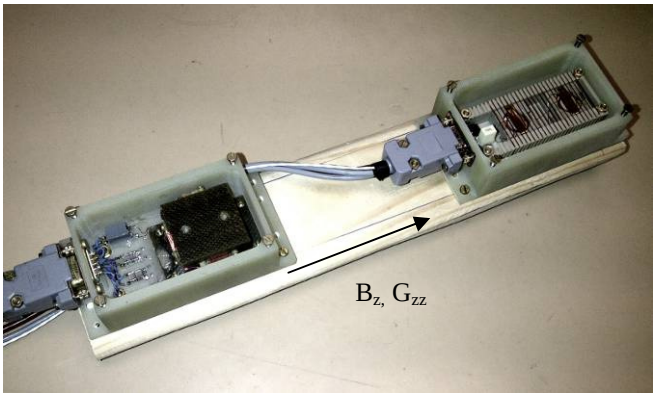

Fig. 10.23 – Assembly of the gradiometer (right) and magnetometer (left) used for astatization

The gradiometer output was digitized with the spare 4th channel of the 24-bit A/D converter of the digital magnetometer. Information about the homogeneous field was used from the gradiometer: B_X and B_Y were sensed by the magnetometer head, and the B_Z component was the component compensated by the gradiometer homogeneous feedback coil. Astatization was carried out at the former geophysical observatory in Průhonice park with a low field gradient (estimated by scalar measurement « 10 nT·m^{-1}) and low magnetic field disturbances (< 5 nT p-p). The astatization used the simplified term introduced by Eq. 8.5 in section 8.2.2.

$$Gcorr_{ZZ} = G_{ZZ} - \begin{bmatrix} k_1 & k_2 & k_3 \end{bmatrix} \cdot \begin{bmatrix} M_X \\ M_Y \\ M_Z \end{bmatrix} - \begin{bmatrix} k_4 & k_5 & k_6 \end{bmatrix} \cdot \begin{bmatrix} M_X^2 \\ M_Y^2 \\ M_Z^2 \end{bmatrix} \qquad (10.5)$$

M_X, M_Y and M_Z were obtained directly as the A/D converter output (the range of 24 bits was roughly equivalent to ±75 μT). Fast sampling of the magnetometer (200 Sa/s) enabled precise calibration even when the rotations were performed manually. The gradiometer raw output G_{ZZ} was obtained in gradient units using the calibrated gradient sensitivity S_G = 190,000 (V·T^{-1})·m^{-1}.

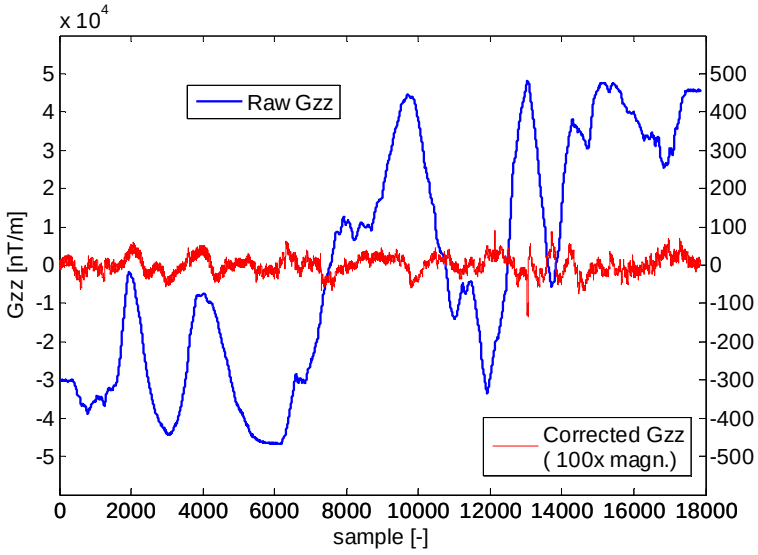

Fig. 10.24 – The result of full astatization of the dual-core gradiometer

After astatization, the response of the gradiometer to a homogeneous field was less than 50 nT p-p for full movement in the Earth's field, see Fig. 10.24. This corresponds to approx. 90 dB CMRR (the gradiometric base is 30-mm).

10.7 Field trials with the gradiometer

In addition to measuring the gradiometer noise and astatizing it, several field trials were conducted using the dual-core gradiometer. Fig. 10.25 shows the results of a "walking trial" simulating the gradiometer as a UXO detector. The target (a bunch of house keys) was passed with the gradiometer probe 20 cm above it from several directions, holding the probe approximately vertical by hand.

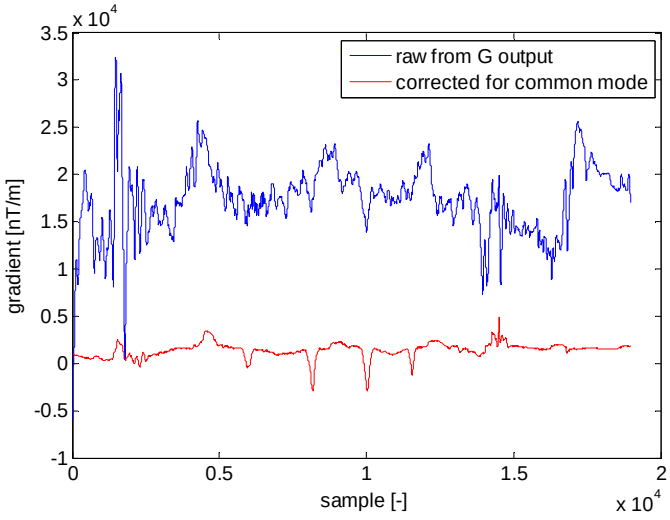

Fig. 10.25 – The "walking trial" demonstrates the necessity of astatization

The trial was conducted in a public park, surrounded by heavy DC traction traffic (an underground railway, a light railway). It can be seen that, even for this small movement, astatization is essential to obtain meaningful results. The baseline is not straight, because there is a DC gradient present at the location.

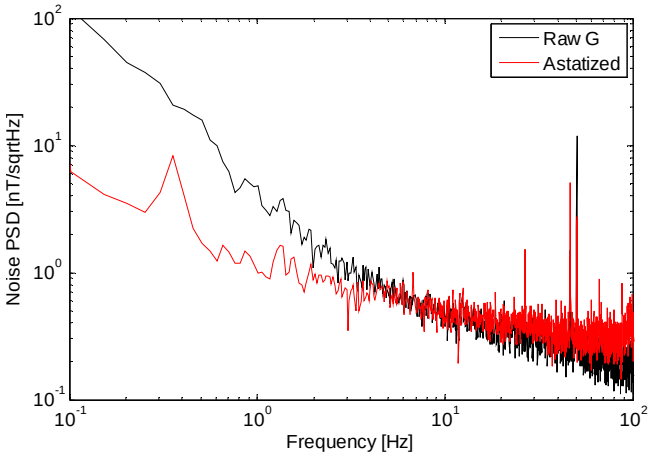

Fig. 10.26 – Gradient noise at the location

The gradient noise measured at a location of this kind provides interesting information. The probe was kept fixed, and the output was logged for 2 minutes. The noise spectra in Fig. 10.26 show that astatization improves the noise floor of the gradiometer below 1 Hz. At 1 Hz the noise is already comparable to that measured in a magnetic shield [W1].

The time-domain comparison is shown in Fig. 10.27. Even for a fixed position of the gradiometer, a high level of low-frequency homogeneous noise (from distant sources) deteriorates the performance, when astatization is not applied, due to its low CMRR – up to 600 nT p-p was observed. However the astatized gradiometer exhibits about 20 nT p-p noise only (its drift was caused by non-ideal fixation).

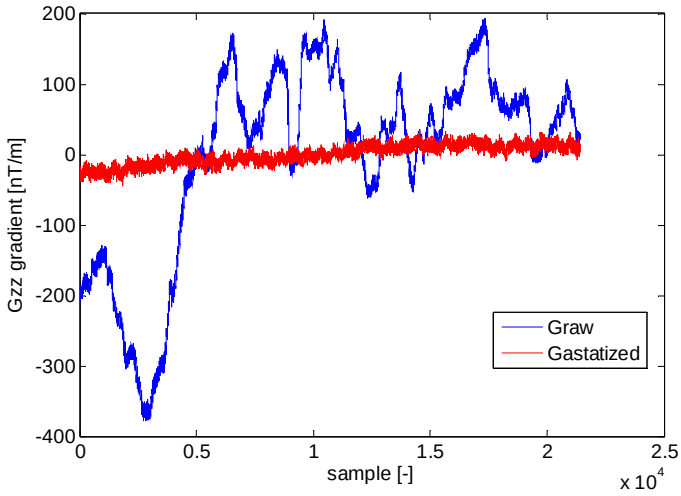

Fig. 10.27 – The same data as for Fig. 10.26, in the time domain

Another trial was carried out at the Průhonice observatory, with low magnetic field disturbances and a low magnetic gradient. The test target (horizontally placed pliers) was scanned with the gradiometer head located vertically in an orthogonal grid with a vertical distance (lift-off) to target of 5 cm and 30 cm, respectively. The probe was positioned manually in a two-dimensional grid. The results are shown in the Fig. 10.28 both for the raw gradiometer reading and for the numerically astatized gradiometer. For the lowest lift-off, the strong source can be detected easily with the gradiometer, without any astatization. However, astatization is essential for the largest lift-off.

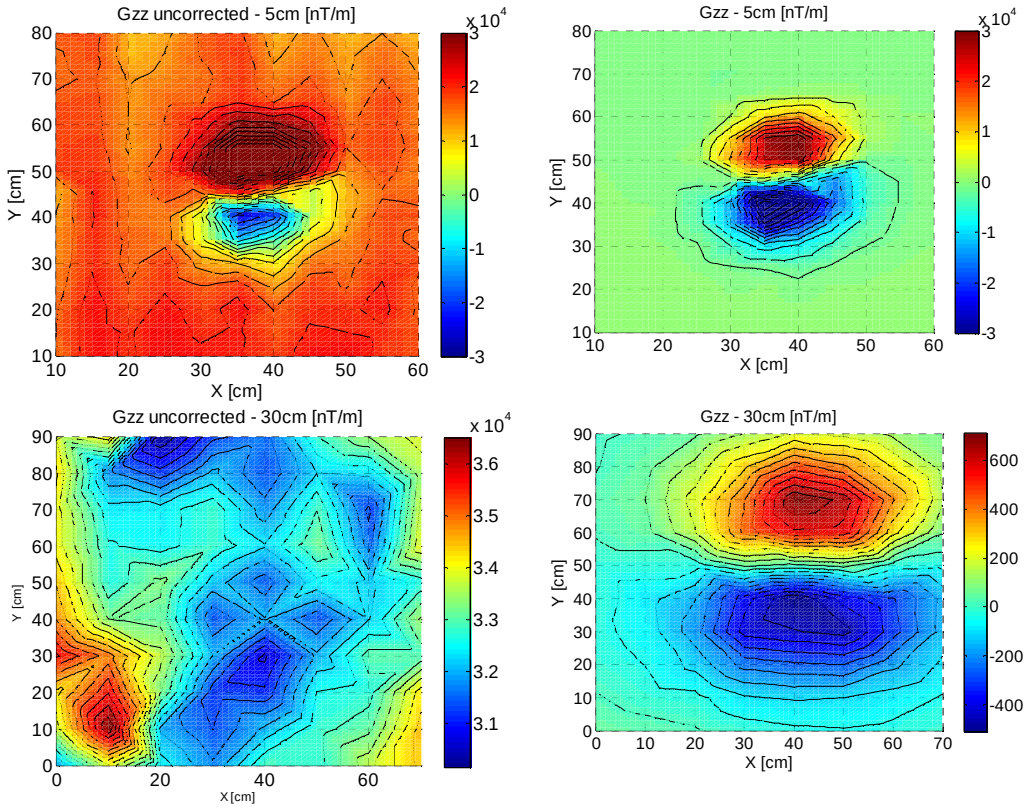

Fig. 10.28 - The raw and astatized output for a lift-off of 5 (top) and 30 cm (bottom)

11 Tensor gradiometer proposal

A standard approach for creating a tensor gradiometer would be to use three or more triaxial sensor heads with the sensors that we have developed to create the full-tensor gradiometer [Pei 2009]. This is already possible using the magnetometer presented in [CSRC 2013]. The size of developed low-noise fluxgate sensors however allows the gradiometer head to be miniaturized.

The solution presented in [Huang 2010] is promising, but a disadvantage is the non-uniqueness of the gradiometer base of the respective axes. Instead, a modification using 10 sensors is proposed below. If the sensors are of the race-track type (Chapter 9.1), the sensor head can be constructed according to Fig. 11.1. A similar design was presented in [Griffin 2012] but they used open-core Vacquier fluxgates working in open-loop. In our case, race-track sensors are preferred because they have lower power consumption than the ring-core sensors that have been developed.

According to Fig. 11.1, the five independent components are sensed with the following sensor pairs:

$\partial B_x/\partial x$, $\partial By/\partial y$	2-9, 4-6
$\partial B_x/\partial y$	5-7
$\partial B_z/\partial x$, $\partial Bz/\partial y$	1-10, 3-8

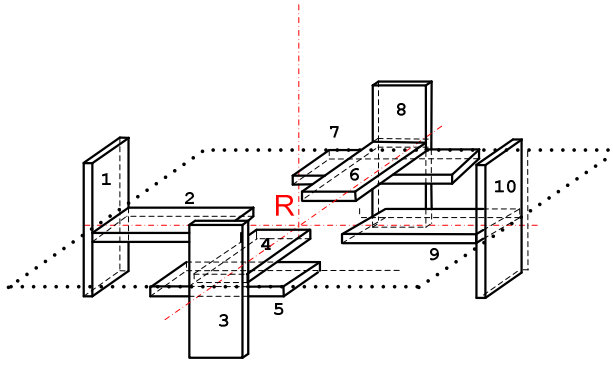

Fig. 11.1 – The tensor gradiometer head with race-track sensors

The 20-mm length of the race-tracks will allow 46×46×46 mm^3 sensor head size (the size limit of LISA gradiometer), if sensors 2,9 and 4,6 overlap. Otherwise the sensor head is limited to approx. 60×60×30 mm^3 due to the sensor length of 20-mm.

12 Conclusions

This thesis has addressed the research topics associated with the development and construction of a compact, low-noise magnetic gradiometer suitable for the space environment. A low gradiometric base is required due to constructional constraints and the need for a precise estimate of the magnetic gradient. Another advantage of a short base is better suppression of disturbing signal from distant sources when detecting the fast-decaying response of small magnetic field sources. With the help of the developed, compact, low-noise fluxgate sensors, the main thesis goal was achieved – a novel gradiometer with 30-mm gradiometric base and noise of 1 $nT \cdot m^{-1} \cdot Hz^{-0.5}$ @ 1 Hz has been successfully developed, astatized and tested. The novel and unconventional concept of simultaneous gradient and homogeneous feedback overcomes most of the problems of state-of-the-art compact gradiometers of this type. The astatization allowed to increase the gradiometer CMRR up to 90 dB. The construction of a full-tensor gradiometer has been also proposed, with the novel race-track fluxgate sensors that have been developed and tested. They are also small enough to fulfil the sensor head size requirement of 46×46×46 mm^3 for the LISA mission.

The novel gradient-feedback operated gradiometers that I have developed in the thesis are applicable in UXO detection, in archaeology, and in biomedicine, where the gradiometers are faced by high common-mode fields. In addition, the parameters of developed magnetic sensors (mainly the noise and offset) have been tested in an extended temperature range, and their suitability for space-grade applications has been confirmed.

12.1 Achieved objectives

I. *Magnetic sensor selection and evaluation.* AMR and fluxgate sensors have been selected as the best candidates, both suitable for space environment, based on a review article I have co-authored (Chapter 4). I have studied the crossfield response for both fluxgate and AMR's (Chapter 5). I have studied the high crossfield response of PCB fluxgates with planar, etched cores and addressed its origin for the first time (section 5.2). I have also participated in deriving a novel algorithm to suppress the crossfield response of AMR's.

II. *Gradiometer performance with available magnetic sensors.* I have developed an original $\partial B_x/\partial y$ PCB fluxgate gradiometer for magnetic field mapping (Chapter 6) and a novel mine-detector with AC excitation based on a 4×4 array of $\partial B_z/\partial z$ AMR gradiometers (Chapter 7). Performance of both instruments has been studied and evaluated; I have found the magnetic sensor noise as a limiting factor for both sensor types.

III. *Gradiometer astatization.* I have studied suitable astatization techniques for a state-of-the art fluxgate gradiometer with 10-cm gradiometric base (Chapter 8). I have proposed an original, linearized astatization method, which later allowed for CMRR of up to 90 dB in the case of the compact gradiometer with 30-mm gradiometric base (section 10.6).

IV. *A compact, low-noise magnetic sensor.* To meet the main thesis goal, I have developed two miniaturized low-noise fluxgate sensors - a novel, $20\times11\times2$ mm^3 race-track and a $20\times20\times8$ mm^3 ring-core sensor (Chapter 9). Field annealing of the 12-mm diameter ring-core enabled its magnetic noise to be decreased down to 7 pT·Hz$^{-0.5}$ @ 1 Hz - this is the lowest noise of sensor of this size and type found in literature. I have also tested the parameters of the developed sensors (noise, offset) in an extended temperature range and confirmed their suitability for space-grade applications. The size of the developed sensors allowed to reduce the gradiometric base below 40 mm and also to propose a $46\times46\times46$ mm^3 full-tensor gradiometer.

V. *Further development of the single-core gradiometer concept.* I have focused on this objective in a substantial part of the thesis (Chapter 10). For the first time, I have studied the noise profile and correlation in a single-core fluxgate gradiometer (section 10.1). I have proposed a novel, original concept of gradient feedback, which I have later implemented in two gradiometer types in order to overcome the stability problems of the state-of-the-art, compact instruments (section 10.2). The "single-core" gradiometer had a gradiometric base of 40-mm and the novel "dual-core" gradiometer with 30-mm base has finally met the noise requirement of 1 nT·m^{-1}·Hz$^{-0.5}$@ 1 Hz (section 10.5). I have carried out gradiometer astatization with the novel method and have presented real-world measurements (section 10.7).

12.2 Outlook

The gradiometers developed within the framework of the thesis should be considered as a proof-of-concept. Several further improvements and modifications would be beneficial for operational use, as was already done in the AMR gradiometer which was converted for detection of concealed structures in civil engineering [Zikmund 2013].

As an example, the developed axial gradiometers with gradient-coil feedback compensation can be improved by integrating the X and Y orthogonal sensor pair (used for astatization) directly into the gradiometer head. This would establish a ready-to-use instrument. It would also be possible to use a sensor with inferior parameters (a two-axis AMR magnetometer) for this purpose.

Further, the size of the dual-core gradiometer head could be possibly reduced by using a different manufacturing process (circular-shaped feedback coils, as in the case of a single-core gradiometer). Our racetrack sensor, which has been proposed for the tensor gradiometer due its low power consumption, could also be used in the axial gradiometer. This would lower its power consumption and mass.

As the construction of the full-tensor LISA gradiometer was assigned by ESA to another institute [Griffin 2012], rather the development of the suitable sensors than the construction of full tensor gradiometer was accented in the thesis. However, the full tensor gradiometer proposed in Chapter 11 is currently under development by the author in the framework of a Technology Agency of the Czech Republic project and its performance with the developed miniature sensors will be tested.

Finally, there is still a wide area of research in reducing the dimensions and possibly also the noise of fluxgate sensors which was apparent during the development of the low-noise sensors presented in the thesis. For example, recent advances in so-called fundamental-mode fluxgate sensors could benefit the construction of gradiometers which was recently proved by [Sasada 2014]. The material properties of classical, parallel fluxgates are usually improved by magnetic annealing as was shown in the presented work. However since the advent of amorphous magnetic materials in the late 1980's, only a limited number of annealing techniques and recipes have been developed which really lower the noise of fluxgate sensors with amorphous cores [Nielsen 1991], [Musmann 2010], [J3]. With the recent development of magnetic materials, improvements in the magnetic noise of fluxgate sensors can be anticipated in the future - nanocrystalline alloys with their inherent temperature stability are promising for fluxgate cores [Butvin 2010]. However a suitable annealing technique, bringing their noise to the level of amorphous ones, is yet to be found.

13 References

[Allen 2005] ALLEN, G. L., et al. Initial evaluation of the new real-time tracking gradiometer designed for small unmanned underwater vehicles. In: *OCEANS, 2005. Proceedings of MTS/IEEE*. IEEE, 2005. p. 1956-1962.

[Anderson 2002] ANDERSON J. et al. Magnetic Anomaly Sensing for Landmine Alternative System. *National Defense Industrial Association Conference 2002*, Mines, Demolition and Non-Lethal, Tampa (FL) 2002

[Auster 2000] AUSTER H. U. Kalibrierung von Fluxgate Magnetometern mittels Relativbewegungen zwischen Sensor und Magnetfeld (in German). *Dissertation, Technische Universität Braunschweig, 2000*, p. 39.

[Auster 2008] AUSTER, H. U., et al. The THEMIS Fluxgate Magnetometer. *Space Science Reviews*, 2008, 141.1-4: 235-264.

[Beiki 2012] BEIKI, M., et al. Estimating source location using normalized magnetic source strength calculated from magnetic gradient tensor data. *Geophysics*, 2012, 77.6: J23-J37.

[Berkman 1960] BERKMAN, R. About a New Type of a Magnetomodulation Transducer for the Measurement of a Magnetic Field Gradient (in Russian). *Avtomaticheski kontrol i izmeritelnaya technika, 1960*, 4:157-162

[Bevan 2013] BEVAN, B. W.; SMEKALOVA, T.N. Magnetic Exploration of Archaeological Sites. Good Practice in Archaeological Diagnostics. *Springer International Publishing*, 2013. p. 133-152.

[Boháková 2003] BOHÁKOVÁ, F.; ŠIMÁČEK, I. SQUID magnetopneumography used to estimate the ferromagnetic particle content in the human lungs. *Journal of Magnetism and Magnetic Materials, 2003*, 267.3: 357-365.

[Braginski 2009] BRAGINSKI, A. I., GORDON B.D. Recent SQUID Activities in Europe, Part II: Applications. *IEEE/CSC & ESAS EUROPEAN SUPERCONDUCTIVITY NEWS FORUM (ESNF)* 2009, 9: 1-40.

[Brauer 1997] BRAUER, P., et al. Transverse field effect in fluxgate sensors. *Sensors and Actuators A: Physical*, 1997, 59.1: 70-74.

[Butta 2014] BUTTA M. et al., Influence of magnetostriction of NiFe electroplated film on the noise of fluxgate. *INTERMAG 2014 conference*, Dresden, 2014.

[Buttino 1986] BUTTINO, G.; CECCHETTI, A.; POPPI, M. Propagation of reversible magnetization changes along ferromagnetic amorphous ribbons. *Magnetics, IEEE Transactions on*, 1986, 22.4: 301-305.

[Butvin 2010] BUTVIN, Pavol, et al. Application Potential of Nanocrystalline Ribbons Still Pending. *Journal of Electrical Engineering*, 2010, 61.5: 264-270.

[Campbell 2003] CAMPBELL, Wallace H. Introduction to geomagnetic fields. *Cambridge University Press*, 2003, p. 215.

[Cerman 2003] CERMAN, A., et al. Precise Magnetic Sensors and Magnetometers for Military and Space Applications. *Sensors & Transducers*, 2003, 38:54-58.

[Chu 2010] CHU, X. X., et al. Mechanical and thermal expansion properties of glass fibers reinforced PEEK composites at cryogenic temperatures. *Cryogenics*, 2010, 50.2: 84-88.

[Chwala 2012] CHWALA, A., et al. Full Tensor SQUID Gradiometer for airborne exploration. *ASEG Extended Abstracts*, 2012, 2012.1: 1-4.

[Clark 2012] CLARK D.A., New methods for interpretation of magnetic vector and gradient tensor data I: eigenvector analysis and the normalised source strength. *Exploration Geophysics*, 2012, 43:267-282

[CSRC 2013] Czech Space Research Centre s.r.o., Czech Technical University in Prague, Triaxial magnetometer with high resolution. *Online: http://www.csrc.cz/index.php/en/projects/ongoing-projects/127-magnetometer*

[Enpuku 2003] ENPUKU, K., et al. High T c SQUID system and magnetic marker for biological immunoassays. *Applied Superconductivity, IEEE Transactions on*, 2003, 13.2: 371-376.

[Forster 1983] FORSTER, F.M., 1983. Means for Achieving Parallelism of the Magnetic Axes of a Differential Magnetic Field Probe. *Patent*. US 4384253 A

[Griffin 2012] GRIFFIN, D. K., et al. Design and calibration of a compact low-noise magnetic gradiometer. In: *Aerospace EMC, 2012 Proceedings ESA Workshop on*. IEEE, 2012. p. 1-6.

[Grüger 2003] GRÜGER, H. Array of miniaturized fluxgate sensors for non-destructive testing applications. *Sensors and Actuators A: Physical*, 2003, 106:326-328

[Hinnrichs 2001] HINNRICHS, C., et al. Dependence of sensitivity and noise of fluxgate sensors on racetrack geometry. *Magnetics, IEEE Transactions on*, 2001, 37.4: 1983-1985.

[Hochreiter 2000] HOCHREITER J., SCHROTTMAYER D. DIMADS— Digital Magnetic Anomaly Detection System. *Preparation, Properties, and Applications of Thin Ferromagnetic Films*, Vienna, June 2000:39-43

[Huang 2010] HUANG, Yu; SUN, Feng; HAO, Yan-ling. Simplest magnetometer configuration scheme to measure magnetic field gradient tensor. In: *Mechatronics and Automation (ICMA), 2010 International Conference on*. IEEE, 2010:1426-1430.

[Ida 2004] IDA, N., *Engineering Electromagnetics*, 2nd ed., Springer, p. 507

[Janošek 2007] – Magnetometr s miniaturními senzory fluxgate (in Czech). Diploma thesis, *Czech Technical University in Prague*, 2007.

[Jennrich 2009] JENNRICH, O. LISA technology and instrumentation. *Classical and Quantum Gravity*, 2009, 26.15: 153001.

[Kirschwink 1992] KIRSCHVINK, J. L. Uniform magnetic fields and double‐wrapped coil systems: improved techniques for the design of bioelectromagnetic experiments. *Bioelectromagnetics*, 1992, 13.5: 401-411.

[Koch 2001] KOCH, R. H.; ROZEN, J. R. Low-noise flux-gate magnetic-field sensors using ring- and rod-core geometries. *Applied Physics Letters*, 2001, 78.13: 1897-1899.

[Kubik 2005] KUBIK, J., et al. Low-power PCB fluxgate sensor. In: *Sensors, 2005 IEEE*. IEEE, 2005:432-435.

[Kubík 2006] KUBÍK, J.; VČELÁK, J., RIPKA, P. On cross-axis effect of the anisotropic magnetoresistive sensors. *Sensors and Actuators A: Physical*, 2006, 129.1: 15-19.

[Kubík 2007] KUBÍK, J., JANOŠEK, M.; RIPKA, P. Low-power fluxgate sensor signal processing using gated differential integrator. *Sensor Letters*, 2007, 5.1: 149-152.

[Kubík 2008] KUBÍK, J.; RIPKA, P. Racetrack fluxgate sensor core demagnetization factor. *Sensors and Actuators A: Physical*, 2008, 143.2: 237-244.

[Kuckes 1994] KUCKES, A. F., Vector Magnetics Inc., Alternating and static magnetic field gradient measurements for distance and direction determination, *Patent US 5305212 A*, 1994.

[Kumar 2005] KUMAR, S., et al. Real-Time Tracking Gradiometer for use in an autonomous underwater vehicle for buried minehunting. In: *OCEANS, 2005. Proceedings of MTS/IEEE*. IEEE, 2005. p. 2108-2111.

[Leitao 2013] LEITÃO, D. C., et al. Magnetoresistive Sensors for Surface Scanning. In: *Giant Magnetoresistance (GMR) Sensors*. Springer Berlin Heidelberg, 2013. p. 275-299.

[Ludwig 2005] LUDWIG, F., et al. Magnetorelaxometry of magnetic nanoparticles in magnetically unshielded environment utilizing a differential fluxgate arrangement. *Review of Scientific Instruments*, 2005, 76.10: 106102.

[Merayo 2001] MERAYO, José MG, et al. A portable single axis magnetic gradiometer. *Sensors and Actuators A: Physical*, 2001, 93.3: 185-196.

[Merayo 2005] MERAYO, J.MG; BRAUER, P.; PRIMDAHL, F. Triaxial fluxgate gradiometer of high stability and linearity. *Sensors and Actuators A: Physical*, 2005, 120.1: 71-77.

[Michelena 2010] MICHELENA, M. D., et al. COTS-based wireless magnetic sensor for small satellites. *Aerospace and Electronic Systems, IEEE Transactions on*, 2010, 46.2: 542-

[Mohamadabadi 2013] – MOHAMADABADI, K., COILLOT, C., HILLION, M.. New Compensation Method for Cross-Axis Effect for Three-Axis AMR Sensors. *Sensors Journal, IEEE*, 2013, 13: 1355-1362.

[Mráz 2008] MRÁZ, J. Detekce magnetických značek (in Czech). Bachelor thesis, *Czech Technical University in Prague*, 2008.

[Musmann 2010] MUSMANN, Günter (ed.). Fluxgate magnetometers for space research. *BoD–Books on Demand*, 2010.

[Nielsen 1991] NIELSEN, O. V., et al. Analysis of a fluxgate magnetometer based on metallic glass sensors. *Measurement Science and Technology*, 1991, 2.5: 435.

[Olsen 2001] OLSEN, N., et al., 2001. In-Flight Calibration Methods Used For The Ørsted Mission. In: *Ground and In-Flight Space Magnetometer Calibration Techniques, ESA SP-490*.

[Olsen 2003] OLSEN, N., et al. Calibration of the Orsted vector magnetometer. *Earth Planets and Space*, 2003, 55.1: 11-18.

[Pankhurst 2003] PANKHURST, Quentin A., et al. Applications of magnetic nanoparticles in biomedicine. *Journal of Physics D: Applied Physics*, 2003, 36.13: R167.

[Pant 1996] PANT, Bharat B.; CARUSO, Mike. Magnetic sensor cross-axis effect. *AN-205, Honeywell*, 1996.

[Pelkner 2011] PELKNER, M., et al. Flux leakage measurements for defect characterization using a high precision 3-axial GMR magnetic sensor. In: *AIP Conference Proceedings*-American Institute of Physics. 2011. p. 380.

[Petrucha 2007] PETRUCHA, V. An Improved Version of the Fluxgate Compass Module. *Acta Polytechnica*, 2007, 47.4-5.

[Petrucha 2009] PETRUCHA, Vojtech, et al. Automated system for the calibration of magnetometers. *Journal of Applied Physics*, 2009, 105.7: 07E704.

[Pei 2009] PEI, Y. H.; YEO, H. G. UXO survey using vector magnetic gradiometer on autonomous underwater vehicle. In: *OCEANS 2009, MTS/IEEE Biloxi-Marine Technology for Our Future: Global and Local Challenges*. IEEE, 2009. p. 1-8.

[Platil 2003] PLATIL, A., et al. Precise AMR magnetometer for compass. In: *Sensors, 2003. Proceedings of IEEE*. IEEE, 2003. p. 472-476.

[Platil 2010] PLATIL, A. Sensors and gradiometers for magnetopneumography. Habilitation thesis, *Czech Technical University*, 2010, p. 13.

[Platil 2013] PLATIL, A., et al. Magnetopneumography Using Optical Position Reference. *Sensor Letters*, 2013, 11.1: 69-73.

[Pouladian-Kari 1990] POULADIAN-KARI, R. A new multi-concentric coil arrangement for producing a near-linear gradient of axial magnetic field. *Measurement Science and Technology*, 1990, 1.12: 1377.

[Primdahl 1989] PRIMDAHL, F., et al. Demagnetising factor and noise in the fluxgate ring-core sensor. *Journal of Physics E: Scientific Instruments*, 1989, 22.12: 1004.

[Primdahl 1991] PRIMDAHL, F., et al. The sensitivity parameters of the short-circuited fluxgate. *Measurement Science and Technology*, 1991, 2.11: 1039.

[Primdahl 2006] PRIMDAHL, F., et al. In-flight spacecraft magnetic field monitoring using scalar/vector gradiometry. *Measurement Science and Technology*, 2006, 17.6: 1563.

[Ripka 1993a] RIPKA, P. Race-track fluxgate sensors. *Sensors and Actuators A: Physical*, 1993, 37: 417-421.

[Ripka 1993b] RIPKA, P.; DRAXLER, K.; KAŠPAR, P. Race-track fluxgate gradiometer. *Electronics Letters*, 1993, 29.13: 1193-1194.

[Ripka 1997] PLATIL, A., et al. Fluxgate can replace SQUID for Lung Diagnostics. In: *Sensors, 2002. Proceedings of IEEE*. IEEE, 2002. p. 321-324.

[Ripka 2000] RIPKA, P.; PRIMDAHL, F. Tuned current-output fluxgate. *Sensors and Actuators A: Physical*, 2000, 82.1: 161-166.

[Ripka 2000b] RIPKA, P.; BILLINGSLEY, S. W. Crossfield effect at fluxgate. *Sensors and Actuators A: Physical*, 2000, 81.1: 176-179.

[Ripka 2001] RIPKA, P.l. Magnetic sensors and magnetometers. *Artech House*, 2001. ISBN 1-58053-057-5.

[Ripka 2002] RIPKA, P.; HURLEY, W. Excitation tuning in fluxgate sensors. In: *Instrumentation and Measurement Technology Conference, Proceedings of the 19th IEEE*. IEEE, 2002. p. 677-680.

[Ripka 2009] RIPKA, P.; BUTTA, M. Origin of the crossfield effect in AMR sensors. *Sensor Letters*, 2009, 7.3: 259-262.

[Ripka 2010] RIPKA, P.; JANOŠEK, M. Advances in Magnetic Field Sensors. *Sensors Journal, IEEE*, 2010, 10.6: 1108-1116.

[Ripka 2012] RIPKA, P., JANOŠEK, M., PETRUCHA, V. Research and development of magnetic gradient sensor for Vector Magnetics, *contract research report*, 2012

[Ripka 2013] RIPKA, Pavel; BUTTA, Mattia; PLATIL, Antonin. Temperature Stability of AMR Sensors. *Sensor Letters*, 2013, 11.1: 74-77.

[Rusanov 2009] RUSANOV, V., et al. Mössbauer and X-ray fluorescence measurements of authentic and counterfeited banknote pigments. *Dyes and Pigments*, 2009, 81.3: 254-258.

[Rühmer 2009] RÜHMER, D., et al. Magnetic relaxation imaging with a fluxgate sensor scanner. In: *SENSOR 2009 Proceedings* , Volume II, 2009, 29-33.

[Rühmer 2012] RÜHMER, D., et al. Spatial and field resolution of wire-wound fluxgates in magnetic dipole fields. *Sensors and Actuators A: Physical*, 2012, 173.1: 30-35.

[Sasada 2002] SASADA, I. Orthogonal fluxgate mechanism operated with dc biased excitation. *Journal of Applied Physics*, 2002, 91.10: 7789-7791.

[Sasada 2014] SASADA I., HARADA S. Fundamental mode orthogonal fluxgate gradiometer. *INTERMAG 2014 conference*, Dresden, 2014.

[Schneider 2013] SCHNEIDER, M., et al. Inversion of geo-magnetic full-tensor gradiometer data. *Journal of Applied Geophysics*, 2013, 92: 57-67.

[Schmidt 2006] SCHMIDT, P. W.; CLARK, D. A. The magnetic gradient tensor. Its properties and uses in source characterization. *The Leading Edge*, 2006, 25.1: 75-78.

[Seki 2009] SEKI, Y., et al. Demonstration of unshielded fetal magnetocardiography system using two-dimensional gradiometers. *Applied Superconductivity, IEEE Transactions on*, 2009, 19.3: 857-860.

[Stolz 2001] STOLZ, R., et al. Long baseline thin film SQUID gradiometers. Applied *Superconductivity, IEEE Transactions on*, 2001, 11.1: 1257-1260., 2001, 11: 1257 – 1260

[Stolz 2000] STOLZ, R., et al. Long baseline thin film SQUID gradiometers. Applied *Superconductivity, IEEE Transactions on*, 2001, 11.1: 1257-1260.

[Stolz 2006] STOLZ, R., et al. Magnetic full-tensor SQUID gradiometer system for geophysical applications. *The Leading Edge*, 2006, 25.2: 178-180.

[Stroink 1982] STROINK, G.; DAHN, D.; BRAUER, F. A lung model to study the magnetic field of lungs of miners. *Magnetics, IEEE Transactions on*, 1982, 18.6: 1791-1793.

[Sunderland 2007] SUNDERLAND, A., et al. Reducing the magnetic susceptibility of parts in a magnetic gradiometer. *arXiv*:0709.1323, 2007.

[Sunderland 2008] SUNDERLAND, A., et al. Direct string magnetic gradiometer for space applications. *Sensors and Actuators A: Physical*, 2008, 147.2: 529-535.

[Sunderland 2009] SUNDERLAND, A., et al. Differential readout for a magnetic gradiometer. *Sensors and Actuators A: Physical*, 2009, 153.1: 5-12.

[Tomek 2006] TOMEK, J., et al. Application of fluxgate gradiometer in magnetopneumography. *Sensors and Actuators A: Physical*, 2006, 132.1: 214-217.

[Turner 1993] TURNER, R. Gradient coil design: a review of methods. *Magnetic Resonance Imaging*, 1993, 11.7: 903-920.

[Včelák 2006] VČELÁK, J., et al. Errors of AMR compass and methods of their compensation. *Sensors and Actuators A: Physical*, 2006, 129.1: 53-57.

[Vopálenský 2003] VOPÁLENSKÝ, M.; RIPKA, P.; PLATIL, A. Precise magnetic sensors. *Sensors and Actuators A: Physical*, 2003, 106.1: 38-42.

[Vyhnánek 2014] VYHNÁNEK, J. Minohledačka s AMR gradiometry (in Czech). Diploma thesis, *Czech Technical University in Prague*, 2011.

[Vyhnánek 2014] VYHNÁNEK, J., et al. Metal detector for visualization of concealed construction. *EMSA 2014 book of abstracts*, EMSA 2014 conference, Vienna 2014.

[Weiner 1969] WEINER, M. Magnetostrictive offset and noise in flux gate magnetometers. *Magnetics, IEEE Transactions on*, 1969, 5.2: 98-105.

[Wiegert 2007] WIEGERT, R., OESCHGER, J.; TUOVILA, E. Demonstration of a novel man-portable magnetic STAR technology for real time localization of unexploded ordnance. In: *OCEANS 2007*. IEEE, 2007: 1-7.

[Wecker 2006] WECKER, J., et al. Magnetic Properties. *Springer Handbook of Materials Measurement Methods*, 2006, 485-529.

[Zikmund 2013] ZIKMUND A., VYHNÁNEK J., JANOŠEK M. AC/DC Linear Magnetic Scanner for Building Industry. *IEEE Sensors conference, Baltimore* (MD) 2013.

[Zimmermann 2005] ZIMMERMANN, E., et al. An AMR sensor-based measurement system for magnetoelectrical resistivity tomography. *Sensors Journal, IEEE*, 2005, 5.2: 233-241.

14 Publications of the author

14.1 Thesis related

14.1.1 Articles in peer-reviewed journals (SCI/SCI-E):

[J1] JANOŠEK, M., VYHNÁNEK, J. et al. Effects of Core Dimensions and Manufacturing Procedure on Fluxgate Noise. *Acta Physica Polonica A.* 2014, 126.1: 104-105

[J2] VYHNÁNEK, J.; JANOŠEK, M.; RIPKA, P. AMR gradiometer for mine detection. *Sensors and Actuators A: Physical*, 2012, 186: 100-104.

[J3] BUTVIN, P., JANOŠEK, M. et al. Field annealed closed-path fluxgate sensors made of metallic-glass ribbons. *Sensors and Actuators A: Physical*, 2012, 184: 72-77.

[J4] JANOŠEK, M., et al. Single-core fluxgate gradiometer with simultaneous gradient and homogeneous feedback operation. *Journal of Applied Physics*, 2012, 111.7: 07E328.

[J5] TOMEK, J., PLATIL, A., JANOŠEK, M., ZIKMUND, A. Suppression of Environmental Noise in Magnetopneumography by the Use of Higher Order Gradients. *Magnetics, IEEE Transactions on*, 2012, 48.4: 1317-1319.

[J6] PRIBULA, O.; JANOŠEK, M.; FISCHER, J. Optical Position Sensor Based on Digital Image Processing: Magnetic Field Mapping Improvement. *Radioengineering*, 2011, 2011.20: 55-60.

[J7] RIPKA, P.; JANOŠEK, M. Advances in Magnetic Field Sensors. *Sensors Journal, IEEE*, 2010, 10.6: 1108-1116.

[J8] JANOŠEK, M.; BUTTA, M.; RIPKA, P. Two sources of crossfield error in racetrack fluxgate. *Journal of Applied Physics*, 2010, 107.9: 09E713.

[J9] RIPKA, P.; JANOŠEK, M.; BUTTA, M. Crossfield sensitivity in AMR sensors. *Magnetics, IEEE Transactions on*, 2009, 45.10: 4514-4517.

[J10] JANOŠEK, M.; RIPKA, P. Current-Output of PCB fluxgates. *Sensor Letters*, 2009, 7.3: 299-302.

[J11] JANOŠEK, M.; RIPKA, P.; PLATIL, A. Magnetic markers detection using PCB fluxgate array. *Journal of Applied Physics*, 2009, 105.7: 07E717.

Accepted

[J12] SARKAR P., JANOŠEK M. et al. Study of Stress Induced Anisotropy in METGLAS. *Magnetics, IEEE Transactions on*, 2014

Submitted, under revision

[J13] JANOŠEK, M., PLATIL, A., VYHNÁNEK, J. The Effect of Sensor Size on Axial Gradiometer Performance. *Magnetics, IEEE Transaction on.* 2014.

[J14] ZIKMUND, A., JANOŠEK, M., ULVR, M., KUPEC, J. Precise calibration method for tri-axial magnetometers not requiring Earth's field compensation. *Instrumentation and Measurement, IEEE Transactions on,* 2014.

14.1.2 Patents

[P1] JANOŠEK, M., RIPKA, P. Fluxgate sensor circuit for measuring the gradient of a magnetic field. Patent, *European Patent Office*, EP2388608. 2013-08-09.

[P2] JANOŠEK, M., RIPKA, P. A fluxgate sensor-based circuit for measuring of magnetic field gradient. Patent. *Industrial Property Office of the Czech Republic*, 302564. 2011-06-02. (in Czech).

[P3] JANOSEK, M, Gradiometer with two ferromagnetic probes. Utility model, *Industrial Property Office of the Czech Republic*, No. 23385.

14.1.3 Articles in peer-reviewed journals:

[R1] JANOŠEK, M., RIPKA, P. PCB Fluxgate Gradiometer Measuring dB_x/dy. *Journal of Electrical Engineering*, 2010, 7/s: 7-9.

[R2] RIPKA, P., JANOŠEK, M. et al. Crossfield Effect in Commercial Fluxgate and AMR Sensors. *Journal of Electrical Engineering*, 2010, 61. 7/s: 13-16

14.1.4 Conference proceedings (WoS)

[W1] JANOŠEK, M., et al. Dual-core fluxgate gradiometer with gradient feedback. In: *Sensors, 2013 IEEE*. IEEE, 2013. p. 1-3.

[W2] VYHNÁNEK, J.; JANOŠEK, M.; RIPKA, P. Low frequency noise of anisotropic magnetoresistors in DC and AC-excited metal detectors. In: *Journal of Physics: Conference Series*. IOP Publishing, 2013. p. 012031.

[W3] JANOŠEK, M.; VYHNÁNEK, J.; RIPKA, P. CW metal detector based on AMR sensor array. In: *Sensors, 2011 IEEE*. IEEE, 2011. p. 1515-1517.

[W4] VYHNANEK, J.; JANOŠEK, M.; RIPKA, P. AMR gradiometer for mine detection and sensing. *Procedia Engineering*, 2011, 25: 362-366.

[W5] RIPKA, P., JANOŠEK, M. et al. Crossfield effect in magnetic sensors. In: *Sensors, 2009 IEEE*. IEEE, 2009. p. 1860-1863.

14.1.5 Conference proceedings

[C1] JANOŠEK, M. Detection of Magnetic Markers Using Array of PCB Fluxgate Sensors. In: *Workshop 09 CTU REPORTS*. Prague, CTU, 2009.

[C2] JANOŠEK, M., PRIBULA, O. Optically Referenced 2D Magnetic Field Mapping. In: *EUROSENSORS XXII 2008*. Dresden, 2008, 247-249.

[C3] JANOŠEK, M., PLATIL, A., VYHNÁNEK, J. The Effect of Sensor Size on Axial Gradiometer Performance. *EMSA 2014 conference*, Vienna, 2014

14.2 Other author publications

14.2.1 Articles in peer-reviewed journals (SCI/SCI-E):

[J15] RIPKA, Pavel, et al. AMR Proximity Sensor With Inherent Demodulation. *Sensors Journal, IEEE*, 2014, 14.9:3119-3123.

[J16] BUTTA, M., JANOSEK, M. et al. Fine Smoothing of Conductive Substrate for Permalloy Layer Electroplating. *Acta Physica Polonica, A.*, 2014, 126.1:150-151.

[J17] PLATIL, A., et al. Magnetopneumography Using Optical Position Reference. *Sensor Letters*, 2013, 11.1: 69-73.

[J18] BUTTA, M.; SASADA, I.; JANOŠEK, M. Temperature Dependence of Offset and Sensitivity in Orthogonal Fluxgate Operated in Fundamental Mode. *Magnetics, IEEE Transactions on*, 2012, 48.11: 4103-4106.

[J19] BUTTA, M.; JANOŠEK, M.; RIPKA, P. Field-Programmable Gate Array-based fluxgate magnetometer with digital integration. *Journal of Applied Physics*, 2010, 107.9: 09E714.

[J20] JANOŠEK, M.; RIPKA, P. PCB sensors in fluxgate magnetometer with controlled excitation. *Sensors and Actuators A: Physical*, 2009, 151.2: 141-144.

14.2.2 Articles in peer-reviewed journals

[R3] TOMEK, J., et al. Magnetopneumography – Incorporation of Optical Position Reference. *Journal of Electrical Engineering*, 2012, 63.7s: 122-125.

14.2.3 Conference proceedings (WoS)

[W6] RIPKA, Pavel, et al. AMR proximity sensor with inherent demodulation. In: *Sensors, 2013 IEEE*. IEEE, 2013. p. 1-4.

[W7] BUTTA, M.; JANOŠEK, M.; RIPKA, Pavel. Coil-less fluxgate operated in feedback mode by means of dc current. *In: Sensors, 2010 IEEE*. IEEE, 2010, 639-642.

[W8] RIPKA, P, JANOŠEK, M, NOVÁČEK, P. Depth Estimation of Metal Objects. In *EUROSENSORS XXIV - Proceedings*. Linz: Elsevier BV, 2010, 280-283

14.2.4 Conference proceedings

[C4] ZIKMUND, A.; JANOSEK, M. Calibration procedure for triaxial magnetometers without a compensating system or moving parts. In: *Instrumentation and Measurement Technology Conference (I2MTC) Proceedings, 2014 IEEE.*, 473-476

[C5] Tomek, J. - Platil, A. - Janošek, M. - Pribula, O.: Magnetopneumography - Real-World Phantom Inversion. In *OIPE 2012 - 12th International Workshop on Optimization and Inverse Problems in Electromagnetism*. Gent, 2012, 248-249.

[C6] JANOŠEK, M.; ĎAĎO, S. Single-lockin detection of AC magnetic fields by fluxgate sensor. In: *Electronics Conference, 2010 Biennial Baltic*. IEEE, 2010. p. 223-226.

[C7] PLATIL, A, JANOŠEK, M. et al. Short-range Navigation of Minesweeping Detector. In *EUROSENSORS XXII 2008*. Dresden, 508-511.

14.3 Responses to author's publications

[J2] VYHNÁNEK, J.; JANOŠEK, M.; RIPKA, P. AMR gradiometer for mine detection. *Sensors and Actuators A: Physical,* 2012, 186: 100-104.

1. SHEN, Ying, et al. Flux distraction effect on magnetoelectric laminate sensors and gradiometer. *Journal of Applied Physics*, 2013, 114.13: 134104
2. LONG, L. et al. Design and fabrication of micro fiber-optic magnetic sensor. *Optics and Precision Engineering 2013*, 21 (9): 2294-2302
3. LEITÃO, D. C., et al. Magnetoresistive Sensors for Surface Scanning. In: *Giant Magnetoresistance (GMR) Sensors*. Springer Berlin Heidelberg, 2013. 275-299.
4. NIAMH N.D., Review Papers - 17th *INTERPOL International Forensic Science Managers Symposium*, Lyon, 2013
5. LIANG, Long; SHAOLONG, Zhong; YAMING, Wu. Design and Fabrication of MEMS Magnetic Sensor Based on Capacitance Detection. *Nanotechnology and Precision Engineering*, 2013, 3: 007.

[J3] BUTVIN, P., JANOŠEK, M. et al. Field annealed closed-path fluxgate sensors made of metallic-glass ribbons. *Sensors and Actuators A: Physical,* 2012, 184: 72-77.

1. LEI, Jian, et al. A MEMS-fluxgate-based sensing system for the detection of Dynabeads. *Journal of Micromechanics and Microengineering*, 2013, 23.9: 095005.
2. BUTTA, Mattia; KRAUS, Ludek. Stress-Induced Anisotropy in Electroplated FeNi Racetrack Fluxgate Cores. *Magnetics, IEEE Transactions on*, 2014, 50.4: 1-4.

[J6] PRIBULA, O.; JANOŠEK, M.; FISCHER, J. Optical Position Sensor Based on Digital Image Processing: Magnetic Field Mapping Improvement. *Radioengineering,* 2011, 2011.20: 55-60.

1. POPELKA, Jan; PACES, Pavel. Performance of smart sensors standards for aerospace applications. *Electrical Review*, 2012, 88.01a: 229-232.

[J7] RIPKA, P.; JANOŠEK, M. Advances in Magnetic Field Sensors. *Sensors Journal, IEEE,* 2010, 10.6: 1108-1116.

Cited 61 times, 50× from SCI / SCI-E journals.

Most recent citations (2014):

1. JIANG, J., KINDT, W.J. and MAKINWA, K.A.A., 2014. A Continuous-Time Ripple Reduction Technique for Spinning-Current Hall Sensors. *IEEE Journal of Solid-State Circuits*, JUL, vol. 49, no. 7, pp. 1525-1534
2. TUNG, Mai Thanh, et al. Influence of electrodeposition parameters on the magnetic and magneto-impedance properties of CoP/Cu wires. *Physica B: Condensed Matter*, 2014, 442: 16-20.
3. LI, Wei; WANG, Jinling. Magnetic Sensors for Navigation Applications: An Overview. *Journal of Navigation*, 2014, 67.02: 263-275.
4. LEEPATTARAPONGPAN, Chana, et al. A merged magnetotransistor for 3-axis magnetic field measurement based on carrier recombination–deflection effect. *Microelectronics Journal*, 2014, 45.6: 565-573.
5. ZENG, Tui, et al. Magnetic-field-sensing mechanism based on dual-vortex motion and magnetic noise. *Journal of Applied Physics*, 2014, 115.17: 17D142.
6. JENG, J.-T., et al. Vector Magnetometer with Dual-Bridge GMR Sensors. *Magnetics, IEEE Transactions on*, 2014, 50.1: 1-4.

[J8] JANOŠEK, M.; BUTTA, M.; RIPKA, P. Two sources of crossfield error in racetrack fluxgate. *Journal of Applied Physics*, 2010, 107.9: 09E713.

1. PANG, Hongfeng, et al. A new calibration method of three axis magnetometer with nonlinearity suppression. *Magnetics, IEEE Transactions on*, 2013, 49.9: 5011-5015.

[J9] RIPKA, P.; JANOŠEK, M.; BUTTA, M. Crossfield sensitivity in AMR sensors. *Magnetics, IEEE Transactions on*, 2009, 45.10: 4514-4517.

1. OUYANG, Jun, et al. Compensation method of cross-axis effect for amr sensor. In: *Electrical and Control Engineering (ICECE), 2010 International Conference on*. IEEE, 2010. p. 603-606.
2. MARKEVICIUS, V.; NAVIKAS, Dangirutis. Adaptive Thermo-Compensation of Magneto-Resistive Sensor. *Electronics and Electrical Engineering*, 2011, 114.8: 43-46.
3. LIN, Jingyu; LU, Ziguang; ZHOU, Yonghua. Electrically Powered Wire Localization System for Mobile Robots. *Sensors Journal, IEEE*, 2011, 11.10: 2197-2203.
4. OUYANG, J., et al. Measurement of the anisotropy fields for AMR sensors. In: *Electron Devices and Solid-State Circuits (EDSSC), 2011 International Conference of*. IEEE, 2011. p. 1-2.
5. TINGTING, Shao, et al. Research on error compensation algorithm of magneto-resistive electronic compass. In: *Electronic Measurement & Instruments (ICEMI), 2011 10th International Conference on*. IEEE, 2011. p. 291-293.
6. COILLOT, Christophe. New Compensation Method for Cross-Axis Effect for Three-Axis AMR Sensors. *IEEE Sensors Journal*, 2013, 13: 1355-1362.

[J10] JANOŠEK, M.; RIPKA, P. Current-Output of PCB fluxgates. *Sensor Letters,* 2009, 7.3: 299-302.

1. PETROU, J.; SKAFIDAS, P.; HRISTOFOROU, E. Electronic toll and road traffic monitoring system using 3-D field AMR sensors. *Sensor Letters*, 2013, 11.1: 91-95.

[J11] JANOŠEK, M.; RIPKA, P.; PLATIL, A. Magnetic markers detection using PCB fluxgate array. *Journal of Applied Physics*, 2009, 105.7: 07E717.

1. FICKO, Bradley W., et al. Development of a magnetic nanoparticle susceptibility magnitude imaging array. *Physics in medicine and biology*, 2014, 59.4: 1047.

[J20] JANOŠEK, M.; RIPKA, P. PCB sensors in fluxgate magnetometer with controlled excitation. *Sensors and Actuators A: Physical,* 2009, 151.2: 141-144.

1. WEISS, Eyal; PAPERNO, Eugene; PLOTKIN, Anton. Orthogonal fluxgate employing discontinuous excitation. *Journal of Applied Physics*, 2010, 107.9: 09E717.
2. SKIDANOV, Vladimir; VETOSHKO, Petr. Ultrasensitive core for magnetooptical fluxgate magnetometer with high space resolution. *Procedia Engineering*, 2010, 5: 989-992.
3. DJAMAL, M., et al. Development of fluxgate sensors and its applications. In: *Instrumentation, Communications, Information Technology, and Biomedical Engineering (ICICI-BME), 2011 2nd International Conference on*. IEEE, 2011. p. 421-426.
4. ROVATI, Luigi; CATTINI, Stefano. Zero-field readout electronics for planar fluxgate sensors without compensation coil. *Industrial Electronics, IEEE Transactions on*, 2012, 59.1: 571-578.
5. BUTTA, Mattia; SASADA, Ichiro. Orthogonal fluxgate with annealed wire core. *Magnetics, IEEE Transactions on*, 2013, 49.1: 62-65.

[W3] JANOŠEK, M.; VYHNÁNEK, J.; RIPKA, P. CW metal detector based on AMR sensor array. In: *Sensors, 2011 IEEE*. IEEE, 2011. p. 1515-1517.

1. LEITÃO, D. C., et al. Magnetoresistive Sensors for Surface Scanning. In: *Giant Magnetoresistance (GMR) Sensors*. Springer Berlin Heidelberg, 2013. p. 275-299.

[W5] RIPKA, P., JANOŠEK, M. et al. Crossfield effect in magnetic sensors. In: *Sensors, 2009 IEEE*. IEEE, 2009. p. 1860-1863.

1. COILLOT, Christophe. New Compensation Method for Cross-Axis Effect for Three-Axis AMR Sensors. *IEEE Sensors Journal*, 2013, 13: 1355-1362.

15 Abbreviations

AC	Alternating current
ADC	Analog-to-digital converter
AMR	Anisotropic magneto-resistor
CMRR	Common-mode rejection ratio
CTU	Czech Technical University
DC	Direct current
ESA	European Space Agency
FEM	Finite element method
LISA	Laser Interferometer Space Antenna (Project)
NDT	Non-destructive testing
PCB	Printed circuit-board
PSD	Power spectral density
SAS	Slovak Academy of Sciences
SDT	Spin-dependent tunneling (device)
SNR	Signal-to-noise ratio
SQUID	Superconducting quantum interference device
UXO	Unexploded ordnance